Schools of
Mechanical and Chemical Engineering

The University of Adelaide

Investigating the use of Concentrated Solar Energy to Thermally Decompose Limestone

Richard Alexander Craig

Thesis Submitted for the
Degree of Doctorate of Philosophy
May 2010

Chapter 6

Muffle Furnace Calcination Experiments

6.1 Introduction

It is generally agreed that the decomposition of limestone made from a high percentage of calcium carbonate essentially takes place in the following manner. The reaction starts at the outer surface of the stone and proceeds towards the centre in a relatively thin reaction zone. At a given instant, the centre core is un-decomposed calcium carbonate and the outer shell calcium oxide. The literature survey presented in Chapter 2 revealed that the rate-limiting step (or rate controlling mechanisms) is considered to be a combination of 1). heat transfer to the calcination front, 2). diffusion of CO_2 away from the calcination front and 3). the rate of the chemical reaction (kinetics).

The mechanisms for calcination of Penrice Angaston limestone / marble were investigated by Mallen (1956), who measured calcination rates of single samples suspended centrally within a Globar element, vertical cylinder, electric furnace. The samples were shaped into spheres, cubes or prisms ranging in size (or diameter) from 12.25mm (½“) to 50mm (2”). Mallen’s laboratory based experiments did not address the relationship between multiple marble particles nor the effects of closely packed particles. Telfer (1999) investigated the calcination of various South Australian limestone including Angaston marble as part of her sulphation mitigation experiments. Samples between 10mg and 200mg were selected from five size fractions ranging between 53μm and 1.00mm in diameter. The samples were calcined within an atmospheric thermogravimetric apparatus (ATGA) with the effects of temperature, particle size, and CO_2 partial pressure being investigated. Telfer’s (1999) resulting weight loss profiles indicate that interparticle diffusion of heat transfer to the reaction zone and release of CO_2 inhibited the rate of the calcination reaction. The relationships between particle size and sample size where not investigated further by Telfer.

The premise of these muffle furnace calcination experiments is therefore to quantify the relationships between calcination temperature, particle size and sample size (bed thickness) for small to medium sized Penrice Angaston Marble. Four sets of muffle furnace experiments were used to quantify these relationships.

The first set of experiments involved measuring the calcination rate of closely packed marble samples within a crucible bowl. These experiments quantify the effect of marble diameter on the calcination rate for closely packed particles. The second set of experiments maintained a

constant bed size (diameter) while varying the bed thickness by varying the mass of the sample. The third set of experiments were similar to the second set, but this time the mass of the sample was maintained constant with the diameter of the marble bed was varied which in turn varies the bed thickness. The second and third sets of experiments quantify the effects of bed thickness on calcination rate. The fourth set of experiments involved calcining single marble samples at two different furnace temperatures. The single particle experiments were needed because of the non uniformity in the solar simulator's radiation beam, and thus the marble bed experiments were not able to be successfully completed, which is discussed in Chapter 7. The fourth set of experiments provide a baseline case against which the effects of using radiation as the sole heating source for the same sized Penrice marble samples can be evaluated.

This chapter first describes the experimental methodologies, after which the results from the four sets of muffle furnace experiments are presented. A calculation of the calcination rates and an analysis of the chemical kinetics through the use of the Arrhenius equation are then used to evaluate and recommend conditions that can be beneficial for solar calcination.

6.2 Experimental Methodology

6.2.1 Sample Preparation and Experimental Apparatus

These calcination experiments were undertaken within an electric muffle furnace set at between 850°C and 1000°C. Nine different nominal diameter Penrice marble particles were used within the four sets of experiments. The muffle furnace temperature will be labelled using T_F and nominal diameter Penrice Angaston marble labelled with d_c. The methods used for the collection and preparation of the Penrice marble sample were described in Chapter 4. The experimental equipment used within these experiments includes the electric muffle furnace, crucible bowl, ceramic fibre refractory board and analytical balance. The specifications for this equipment are detailed in Chapter 4.

6.2.2 Crucible Bowl Experiments

The first set of muffle furnace experiments involved placing one hundred gram (100g) samples of either d_c = 0.375mm, d_c = 0.925mm, d_c = 1.850mm and d_c = 2.855mm marble into a 150ml silica "*Vitreosil*" broad base crucible bowl (without a lid as shown in Figure 6-1). The temperature of the crucible bowl was approximately 20°C (ambient temperature) when the

marble sample was placed inside it. The crucible was then placed inside the electric *Carbolite* muffle furnace which had been preheated to either T_F = 900°C or T_F = 1000°C. The furnace was preheated for a minimum of 90 minutes prior to sample insertion to ensure a steady state furnace temperature was established. Figure 6-1 presents a photo of the 'loaded' crucible bowl inside the muffle furnace set at T_F = 900°C. Also seen inside the furnace immediately above the rim of the crucible bowl are the positions of two furnace temperature monitoring thermocouples.

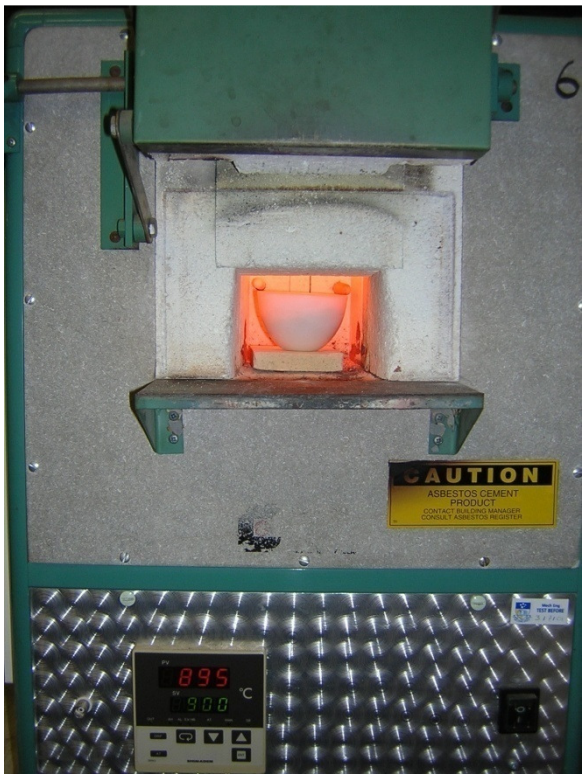

Figure 6-1: Photo of the crucible bowl inside the preheated muffle furnace.

The loaded crucible was removed from the furnace after two minutes and its mass immediately measured using the A&D GX-600 analytical balance. The mass was measured automatically at one second intervals (i.e. 1 hertz) over ten seconds, and the arithmetic mean of the ten mass measurements then calculated. This averaging was necessary because of the variation in measurement due to the convective flows around the heated crucible bowl, causing some scatter. After measurement, the crucible was returned to the muffle furnace for further heating. This measurement procedure was repeated at ten minute intervals for the remainder of the decomposition. The time results presented in this chapter do not include the weighing time of approximately 20 seconds for each measurement.

The mass loss due to the evolved carbon dioxide (m_{CO_2}) of each sample was calculated using Equation [6.1].

$$m_{CO_2} = \frac{(m_1 - m_2)}{(m_1 - m_o)} \qquad [6.1]$$

where: m_o is the mass of the clean empty crucible or refractory board
m_1 is the mass of sample and crucible or refractory board *before* heating
m_2 is the mass of sample and crucible or refractory board *after* heating

Calcination profiles, also called decomposition profiles, show the conversion of the limestone (gram) to quicklime (gram) over time (seconds). The fractional calcination profiles for the four 100 gram limestone samples at the two furnace temperatures are represented graphically in Figure 6-3.

6.2.3 Constant Bed Diameter Experiments

The second muffle furnace experimental campaign involved spreading samples of 0.375 mm, 0.925mm, 1.850mm or 2.855mm nominal diameter Angaston marble evenly over the top surface of a flat ceramic fibre refractory board 100mm square and 10mm thick. The marble samples were constrained to fit within a circle 80mm in diameter which specified the bed diameter.

Two bed thicknesses for each nominal diameter marble were used. The first bed thickness was the thickness produced by 40 gram samples of the marble. The second bed thickness was the thickness 1.5 times the marble's nominal diameter, i.e. $b_d / d_c = 1.5$.

The 40 gram sample resulted in differing bed depths for each of the four nominal diameter marble. The bed depth was directly measured using Vernier calipers, which is displayed in Table 6-1 for the four different sized marble. Also indicated is the marble bed depth as a function of the nominal stone diameter which is the measured bed depth divided by the marble particle's nominal diameter.

Table 6-1: Bed depth for the 40g marble samples placed to form an 80mm diameter bed.

Marble Nominal Diameter (mm) d_C	**Measured Bed Depth (mm) (± 0.1mm)** $b_{d,m}$	**Bed Depth as Function of Nominal Diameter** $\frac{b_{d,m}}{d_C}$
0.375	4.5	12.0
0.925	4.7	5.08
1.850	5.0	2.70
2.855	4.4	1.54

The case $b_{d,m}$ / d_c = 1.5 was directly measured using Vernier calipers, as well as being calculated using the bulk density (1425 kg/m^3 for 2:1 size ratio). This size ratio is recommended by Oates (1998, page 19). The bulk density includes the void area between each marble particle and assumes a spherical particle shape. The accuracy of the measured depth was estimated to be between ± 0.1mm and ± 1mm.

A bed thickness of 1.5 times the marble's nominal diameter was selected because it represents a typical bed thickness for Calcimatic kilns as reported by Oates (2001). Recalling Figure 1-5, which shows the annulus shaped flat bed Calcimatic kiln which used pebble sized stone and were over-fired using fuel oil or natural gas. A relatively thin and uniform limestone bed thickness (as well as good stone size ratio of up to 1:3) was found to be necessary to maintain consistent product quality.

Table 6-2 shows the nominal marble diameter, the total mass of each sample, the measured and calculated bed depths and the measured bed depth as a function of the nominal marble diameter.

Table 6-2: Bed depth and measured mass to obtain a bed thickness of 1.5 x d_c.

Marble Nominal Diameter (mm) d_C	**Measured Mass of Sample (gram) (± 0.005)** m_s	**Measured Bed Depth (mm) (± 0.1)** $b_{d,m}$	**Calculated Bed Depth (mm)** $b_{d,c}$	**Bed Depth as Function of Nominal Diameter** $\frac{b_{d,m}}{d_C}$
0.375	5	0.6	0.56	1.6
0.925	15	1.4	1.38	1.51
1.850	25	2.8	2.77	1.51
2.855	40	4.4	4.28	1.54

After loading and measuring the depth of the marble, the refractory board (with marble bed) was inserted into the preheated muffle furnace which was set to either T_F = 900°C or T_F = 1000°C. It was then removed from the furnace and the total mass measured for 10 seconds at one second intervals (1 hertz), before being returned to the furnace. These mass measurements were repeated at two minute intervals for the duration of each experiment. The arithmetic mean of the 10 second measurement was calculated to minimise the measurement noise caused by convective flows around the heated refractory board. The loss in mass was then calculated using Equation [6.1] for each measurement. The decomposition profiles for these eight experiments are seen in Figures 6-4 and 6-5.

6.2.4 Constant Mass Bed Experiments

The constant mass muffle furnace experiments were performed by spreading samples of the '**K**' and '**M**' graded (Table 4-3) Angaston marble evenly over the top surface of a flat ceramic fibre refractory board 150mm square and 10mm thick. The average diameter of the 'K' grade marble was calculated (and observed) to be approximately 10 ± 0.5mm and the 'M' grade marble approximately 3 ± 0.5mm.

The mass of each sample of the 3mm diameter marble sample was approximately 100 ± 0.01 grams while the mass of each sample of 10mm diameter marble was 200 ± 0.1 grams. The diameter of the marble bed was varied between 80mm and 150mm. Changing the diameter of the marble bed while maintaining a constant sample mass, resulted in a change in the thickness of the bed. The bed depth was directly measured using Vernier calipers, as well as being calculated using 1425 kg/m^3 as the bulk density. Table 6-3 shows the measured and calculated bed depths for the five different bed sizes. Also indicated is the

marble bed depth as a function of the stone diameter which is the measured bed depth divided by the marble particle average diameter.

Table 6-3: Measured and calculated bed depth for variations in bed diameter for the 100g, d_c = 3mm and 200g, d_c = 10mm marble samples.

Bed Diameter (mm) D_C	**Measured Bed Depth (mm) (± 0.1) for 3mm (± 1) for 10mm $b_{d,m}$**	**Calculated Bed Depth (mm) $b_{d,c}$**	**Bed Depth as Function of Nominal Diameter $\frac{b_{d,m}}{d_C}$**
d_C = 3mm Diameter			
80	14.5	12.82	4.83
100	9.1	8.05	3.03
120	6.7	5.52	2.23
140	5.1	4.01	1.70
150	4.2	3.47	1.40
d_C = 10mm Diameter			
80	28	28.09	2.80
100	20	19.78	2.00
120	16	15.6	1.60
140	12	11.7	1.20
150	10	9.68	1.00

Each sample was weighed and then spread evenly over the top surface of the refractory board. The refractory board (with marble bed) was then inserted into the preheated muffle furnace at T_F = 1000°C. Duplicating the experiments using T_F = 900°C was considered unnecessary because of the clear relationship between furnace temperature and calcination rate seen in the results from the crucible experiments.

The refractory board was removed from the furnace and the total mass measured for 10 seconds at 1 hertz, before being returned to the furnace. These mass measurements were repeated at five minute intervals for the duration of each experiment. The arithmetic mean of the 10 second mass measurement was calculated to minimise the measurement noise caused by convective flows around the heated refractory board. The loss in mass was then calculated using Equation [6.1] for each measurement. The decomposition profiles for these ten experiments can be seen from Figures 6-7 and 6-8.

6.2.5 Single Stone Calcination Experiments

The fourth set of muffle furnace experiments involved placing a single marble sample onto the surface of the ceramic fibre refractory board which was inserted it into the preheated muffle furnace set at either T_F = 900°C or T_F = 1000°C. Three marble particle sizes were used: 0.333 gram, 1.000 gram and 3.000 gram. A set of separate experiments were conducted calcining the 1.000 gram at four different T_F, namely 850°C, 900°C, 950°C and 1000°C.

Table 6-4 shows the selected stone masses, the mass tolerance of each marble particle and the calculated nominal characteristic diameter of each marble particle. The nominal characteristic diameter of each marble sample size was calculated by first computing its volume (m^3) using Equation [6.2]. The volume of the marble sample was then calculated by dividing the mass of the marble by the specific gravity (apparent density), 2720 kg/m^2, as specified by Oates (1998, pg 18).

$$V_{CaCO_3} = \frac{m_{CaCO_3}(kg)}{\rho_{CaCO_3}(kg/m^3)} \qquad [6.2]$$

Using this calculated volume, the nominal diameter was calculated using Equation [6.3] which assumes that the marble sample is spherical in shape.

$$d_C = 2 \times \left(\frac{3V_{CaCO_3}}{4\pi} \right)^{1/3} \text{ m} \qquad [6.3]$$

Table 6-4: Mass of marble and the calculated nominal characteristic diameter d_c, using Eq [6.3].

Mass of Marble (gram) m_{CaCO_3}	**Mass Tolerance (gram)**	**Nominal Characteristic Marble Diameter (mm)** $\mathbf{d_c}$
0.333	0.005	6.54
1.000	0.005	9.44
3.000	0.005	13.62

After two minutes of heating within the muffle furnace the refractory board (with marble sample) was removed and placed onto the analytical balance. The total mass was measured for 10 seconds at 1 hertz, with the arithmetic mean of the ten measurements being

calculated. The averaging was again necessary because of measurement scatter due to the convective flows around the heated refractory board. After measurement, the refractory board was returned to the muffle furnace for further heating. This measurement procedure was repeated at two minute intervals for the remaining duration of the decomposition. The loss in mass due to calcination of each sample was then calculated using Equation [6.1].

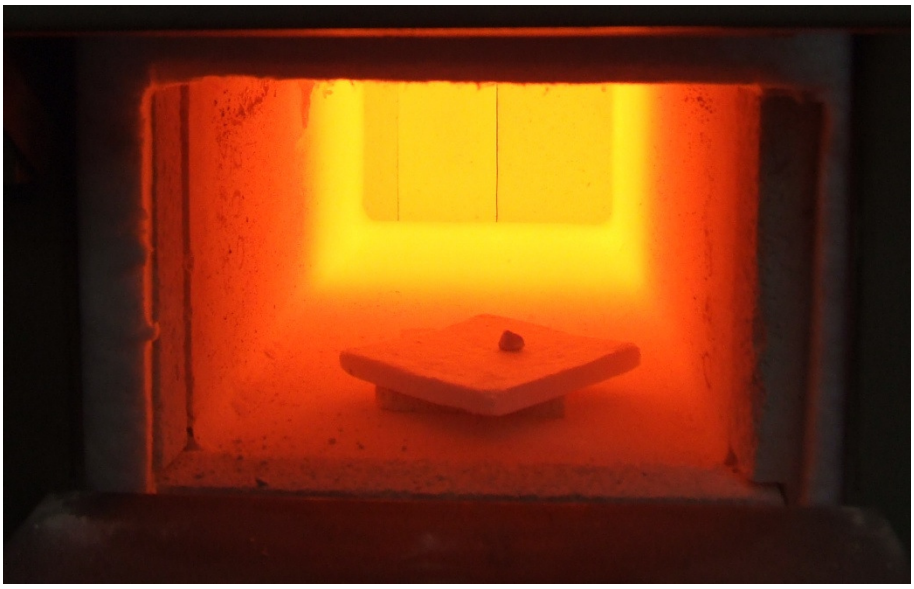

Figure 6-2: Photo of a 1.000 gram (dc = 9.44mm) Penrice marble sample placed in the muffle furnace set at T_F = 1000°C.

6.3 Results

Figures 6-3 to 6-8 show the calcination profiles for Penrice marble heated at either T_F = 900°C or T_F = 1000°C. These figures present fractional calcination, which is the fraction of CO_2 released during calcination divided by the total CO_2 within the sample. The x-axis is decomposition time given in minutes.

It should be noted that some of these figures show fractional calcination of values greater than unity, which is clearly not possible. The over-shoot is attributed to the significant upward convectional air flow which occurs around the hot ceramic fibre board when placed on the analytical balance. Additionally, there can be mass loss from the Penrice marble sample because of explosion of some stones if the heating rate is too high. Further explanations of these errors are given in Section 6.6.

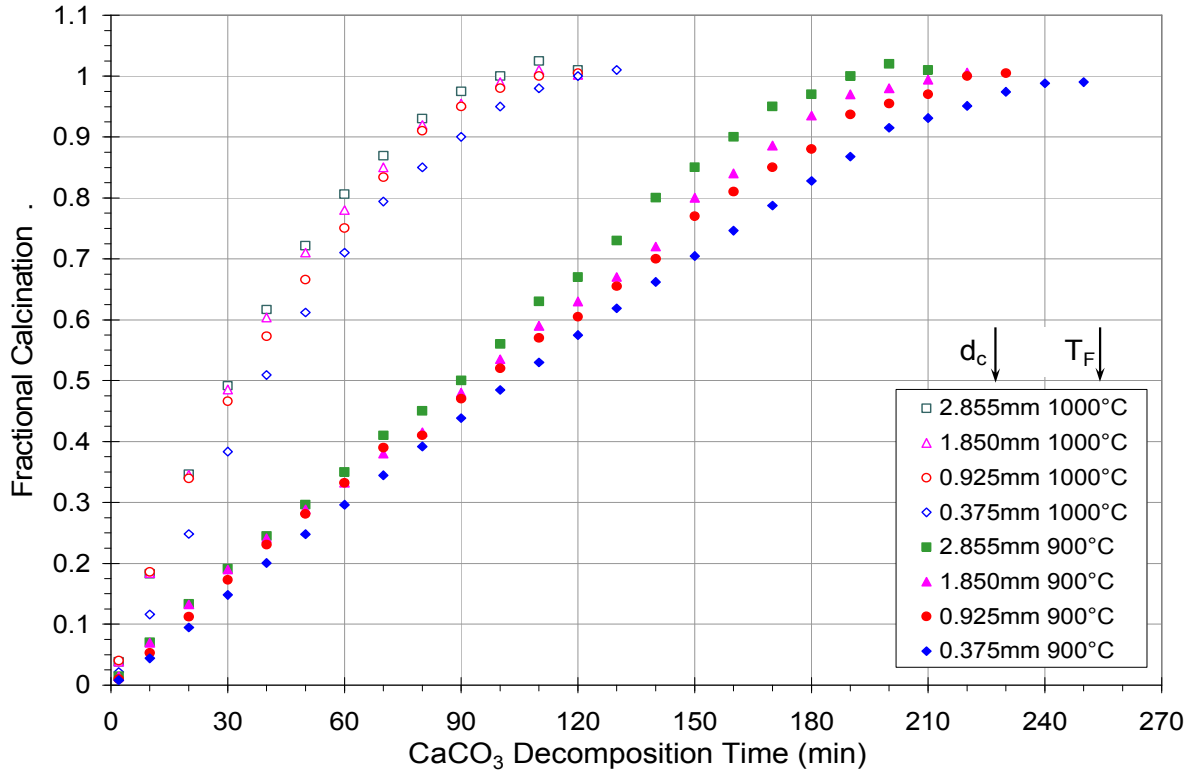

Figure 6-3: Calcination profiles of Penrice marble at T_F = 900°C and T_F = 1000°C conducted on 100g samples of four different diameters placed in a crucible in the muffle furnace.

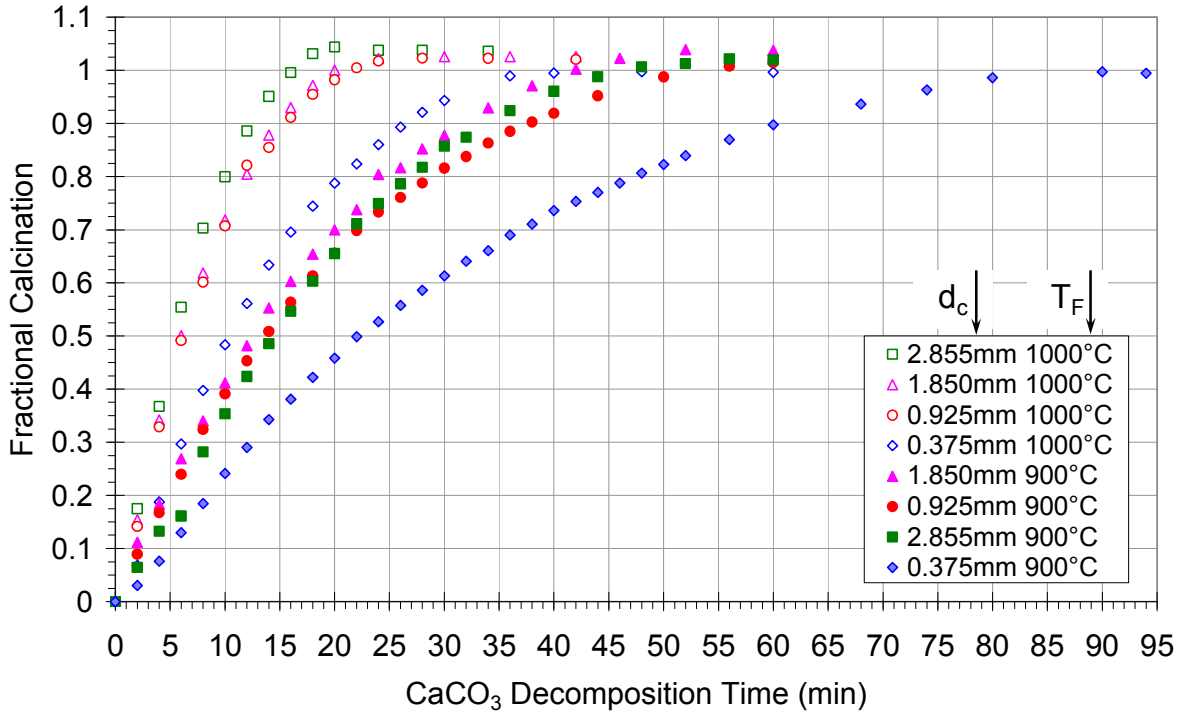

Figure 6-4: Calcination profiles of 40 gram Penrice marble at T_F = 900°C and T_F = 1000°C conducted on four different nominal diameters, spread evenly over an area of 80mm diameter in the muffle furnace.

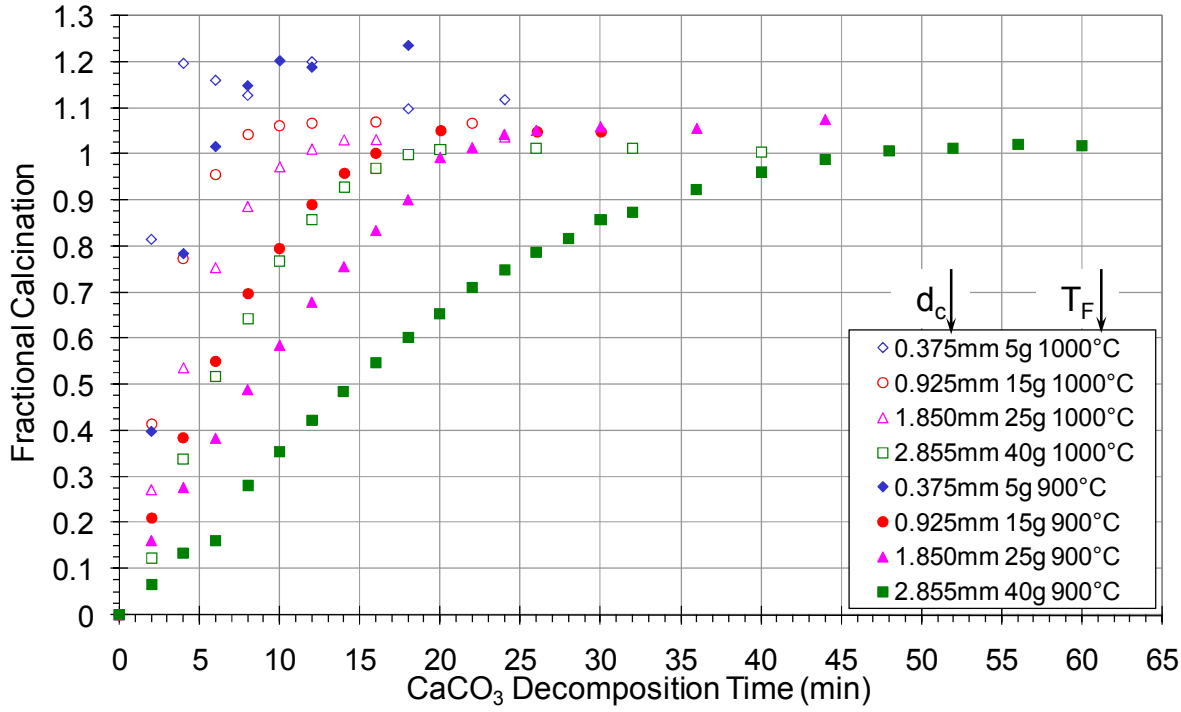

Figure 6-5: Calcination profiles of Penrice marble at T_F = 900°C and T_F = 1000°C conducted on four different particle size ranges spread evenly over an area of 80mm diameter with a bed thickness of 1.5 times the particle diameter in the muffle furnace.

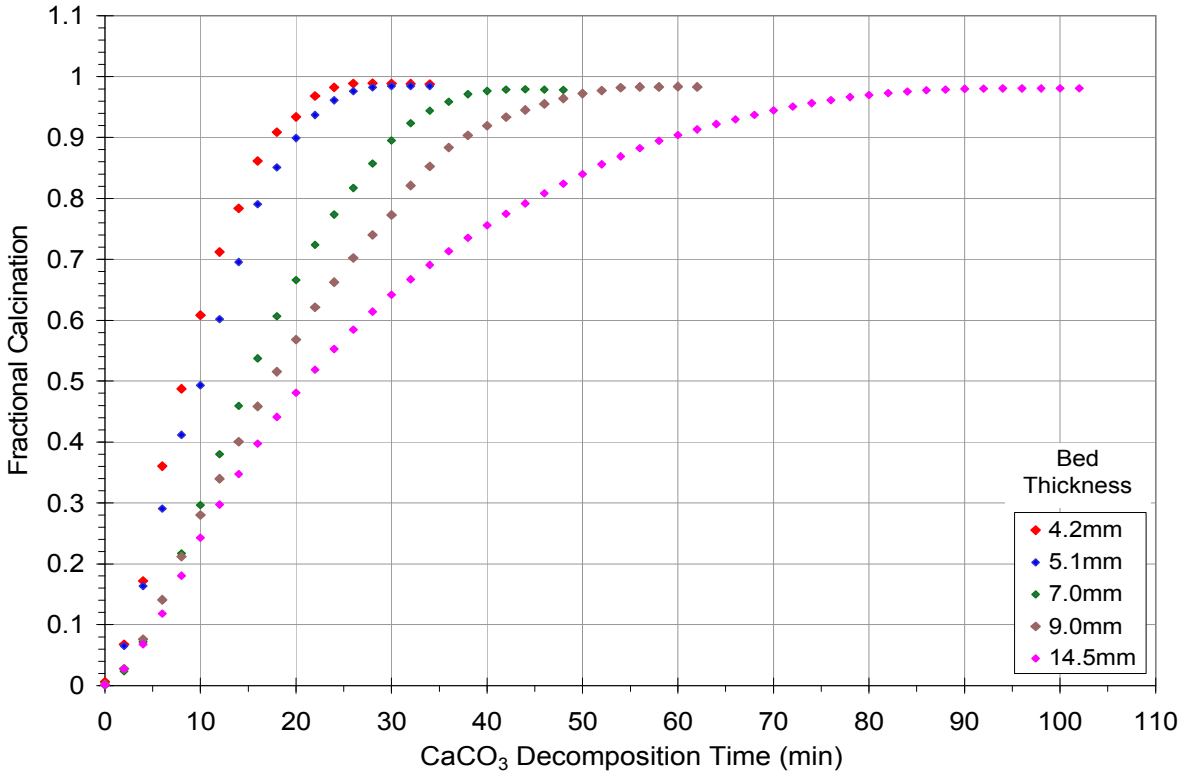

Figure 6-6: Calcination profiles of 100g samples of 3mm nominal diameter Penrice marble spread to form five different bed thicknesses at T_F = 1000°C muffle furnace tests.

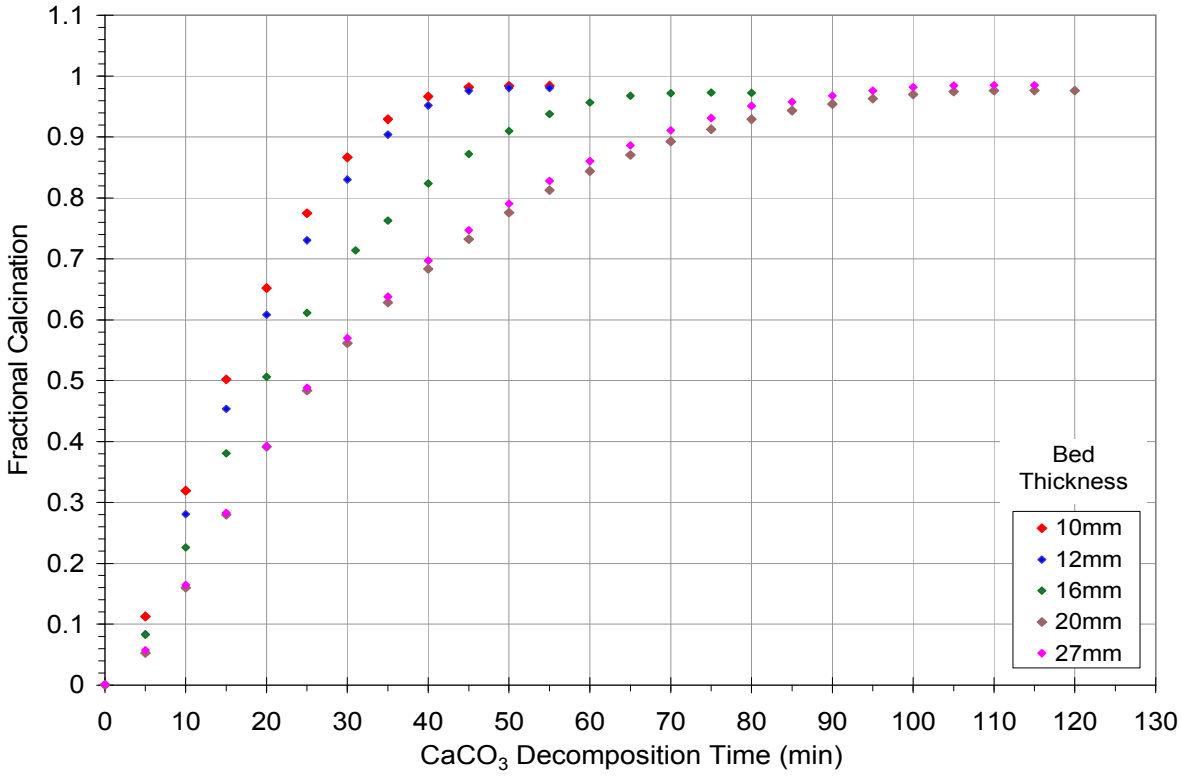

Figure 6-7: Calcination profiles of 200g samples of 10mm nominal diameter Penrice marble spread to form five different bed thicknesses at T_F = 1000°C in the muffle furnace.

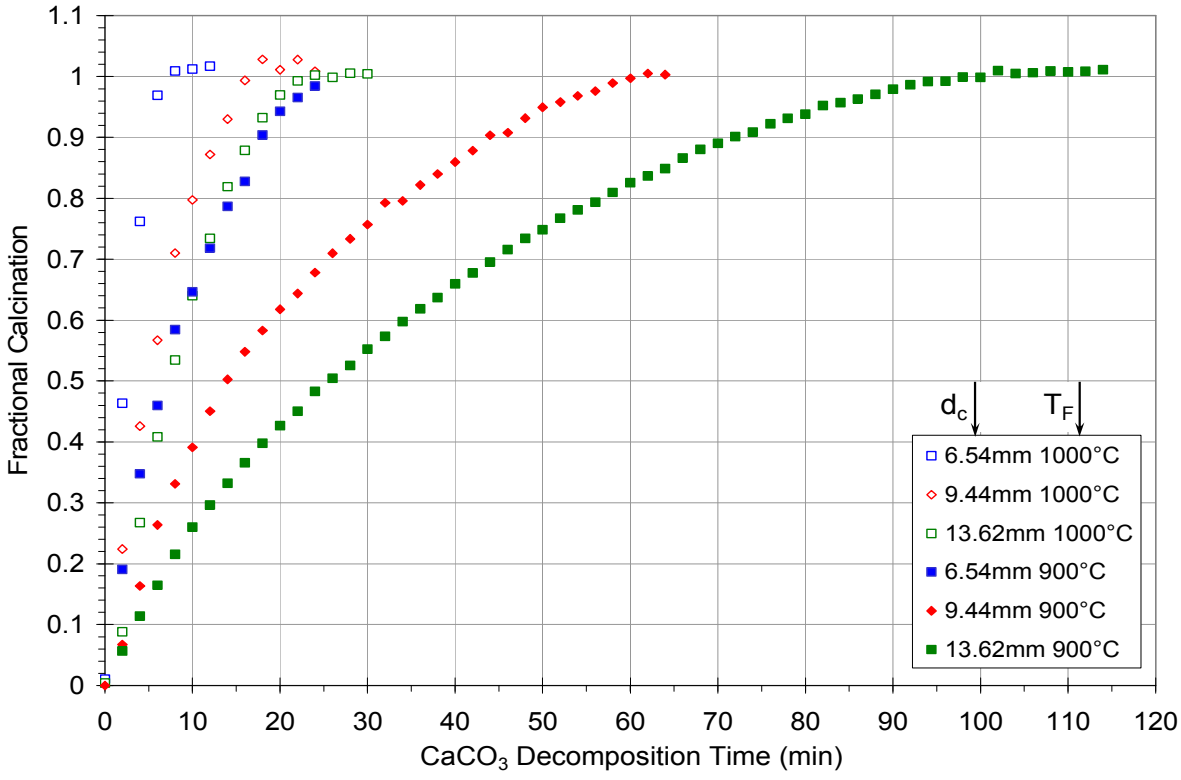

Figure 6-8: Calcination profiles of Penrice Marble at T_F = 900°C and T_F = 1000°C conducted on single marble samples of three different d_c in the muffle furnace.

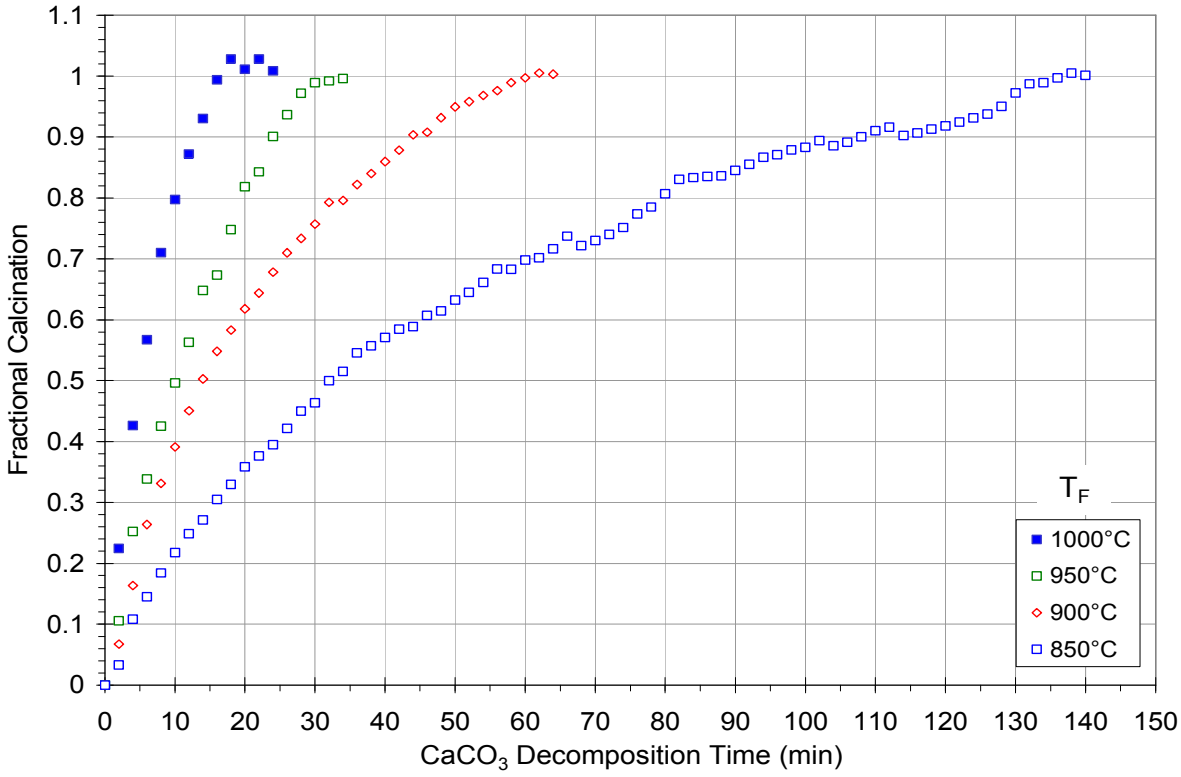

Figure 6-9: Calcination profiles for 1.000g (d_c = 9.44mm) Penrice marble for varying muffle furnace temperatures.

Tables 6-5 to 6-11 show the calculated rates of conversion from $CaCO_3$ to CaO for the calcination experiments. The rate of calcination (dm/dt) has been calculated from the slope of the first 50% of decomposition (i.e. dm/dt = 0.5, denoted by dm/dt_{50}) from the fractional calcination profiles shown above in Figures 6-3 to 6-9. Displayed in Tables 6-10 and 6-11 is the time (in minutes) taken to complete calcination, denoted t_{100}.

Table 6-5: Calcination rates for the 100g crucible muffle furnace experiments.

Marble Nominal Diameter d_C (mm)	**Rate of Calcination for 900°C dm/dt_{50} (g/g.s)**	**Rate of Calcination for 1000°C dm/dt_{50} (g/g.s)**
2.855	0.331	1.053
1.850	0.319	1.040
0.925	0.312	0.905
0.375	0.290	0.804

Table 6-6: Calcination rates for the 40g flat bed muffle furnace experiments.

Marble Nominal Diameter d_C (mm)	**Rate of Calcination for 900°C dm/dt_{50} (g/g.s)**	**Rate of Calcination for 1000°C dm/dt_{50} (g/g.s)**
2.855	2.081	5.18
1.850	2.369	5.13
0.925	2.180	4.92
0.375	1.359	2.81

Table 6-7: Calcination rates for the bed thickness of 1.5 x d_c muffle furnace experiments.

Marble Nominal Diameter d_C (mm)	**Rate of Calcination for 900°C dm/dt_{50} (g/g.s)**	**Rate of Calcination for 1000°C dm/dt_{50} (g/g.s)**
2.855	2.081	5.18
1.850	3.670	8.04
0.925	5.510	11.58
0.375	11.76	24.47

Table 6-8: Calcination rates for 100g samples of d_c = 3mm Penrice marble at T_F = 1000°C in the muffle furnace.

Bed Diameter (mm) D_C	**Measured Bed Thickness (mm) $b_{d,m}$**	**Rate of Calcination for 1000°C dm/dt_{50} (g/g.s)**
80	14.5	1.41
100	9.1	1.71
120	6.7	2.00
140	5.1	2.96
150	4.2	3.61

Table 6-9: Calcination rates for 200g samples of 10mm nominal diameter Penrice marble at T_F = 1000°C in the muffle furnace.

Bed Diameter (mm) D_C	**Measured Bed Thickness (mm) $b_{d,m}$**	**Rate of Calcination for 1000°C dm/dt_{50} (g/g.s)**
80	27	1.14
100	20	1.12
120	16	1.52
140	12	1.82
150	10	2.01

Table 6-10: Calcination rates and time to complete calcination for d_c = 6.54mm, d_c =9.44mm and d_c = 13.62mm marble for muffle furnace temperature of T_F = 900°C and T_F = 1000°C.

Marble Nominal Diameter d_C (mm)	**Rate of Calcination for T_F = 900°C dm/dt_{50} (g/g.s)**	**Time to Complete Calcination t_{100} for T_F = 900°C (minutes)**	**Rate of Calcination for T_F = 1000°C dm/dt_{50} (g/g.s)**	**Time to Complete Calcination t_{100} for T_F = 1000°C (minutes)**
13.62	1.178	24	3.98	10
9.44	2.154	64	5.69	22
6.54	4.404	104	11.27	26

Table 6-11: Calcination rates for d_c = 9.44mm (1.000g) marble for muffle furnace temperatures between T_F = 850°C and T_F = 1000°C.

Furnace Temperature °C	**Rate of Calcination for Decomposition up to dm/dt_{50} (g/g.s)**	**Rate of Calcination for Decomposition up to dm/dt_{75} (g/g.s)**	**Rate of Calcination for Decomposition up to dm/dt_{100} (g/g.s)**	**Time to Complete Calcination t_{100} (minutes)**
850	0.937	0.609	0.437	138
900	2.154	1.513	0.973	62
950	2.976	2.492	1.758	34
1000	5.687	4.795	3.433	18

6.4 Analysis of Results

The factional calcination profiles plot of the 100 gram crucible tests, Figure 6-3, show that the rate of calcination of Angaston marble increases with an increase in furnace temperature for all d_c investigated. Table 6-5 shows that the calcination rate for the 2.855mm diameter marble is approximately 14.2% faster than for the 0.375mm for T_F = 900°C. The calcination rate is 31% faster for the same comparison using T_F = 1000°C. This is indicating that heat and mass transfer within the packed bed of marble is playing a more significant role for the rate controlling step, than chemical kinetics. It is well documented by Satterfield and Feakes (1959) and Silcox *et al*. (1989) that increasing the void area between each particle allows the evolved CO_2 to diffuse through and away from the reaction zone within the bulk sample. Equally, Telfer (1999) reports that the reaction rate slows significantly due to the CO_2 diffusion resistance in closely packed fine grained samples, especially as the decomposition tends to 100%. This highlights the need to investigate the ratio between marble diameter and the depth of the bed, and optimise it for increasing the calcination rate.

The fractional calcination profiles seen in Figure 6-4, for the 40 gram flat bed experiments show that the rate of decomposition of the Angaston marble increase by between 200% to 250% with an increase in furnace temperature for all of the four marble diameters. This range is easily seen in Table 6-6. A comparison in the calcination rate between the d_c = 2.855mm and d_c = 0.375mm shows that the d_c = 2.855mm is approximately 52% faster for T_F = 900°C, and 84% faster for T_F = 1000°C. Table 6-6 also shows that the calcination rates for the d_c = 1.850mm and d_c = 0.925mm are faster than the 2.855mm diameter sample. This illustrates that the bed depth for the 2.855mm stones is shallow enough for the heat and mass transfer effects to no longer be limiting the rate of the reaction. The marble diameter (d_c) to bed thickness (b_d) ratio for this case is approximately 1.5. It should also be noted that at approximately 70% decomposition, the rate for the d_c = 0.925mm particle becomes slower than for the d_c = 2.855mm sized particle. This change-over illustrates the effect of the bed depth (and particle packing) on restricting heat and mass transfer through it.

Table 6-6 also shows that there is a substantial increase in calcination rate (approximately 5.5 times faster) between these experiments and the 100g crucible experiments. This increased calcination rate reduces the residence time required within the furnace to achieve full and complete calcination. The residence time decreases together with the particle bed thickness, as described by Wingate (1985) who states that the thickness of the particle bed influences the manner of heating (direct or indirect) and consequently the residence time and the homogeneity of the produced quicklime.

Figure 6-5 shows the fractional calcination profiles for the experiments where the marble bed thickness (b_d) is 1.5 times the nominal diameter of the marble (d_c). The profiles show that the rate of calcination of Angaston Marble increases (up to 250%) with the increase in furnace temperature for all the four marble diameters investigated. The 10 to 20% overshoot seen in the calcination profiles again show measurement errors which are discussed in detail later in this chapter.

Table 6-7 indicates that the calcination rate for a marble bed thickness of 1.5 times the nominal diameter of the marble increases with increasing marble diameter, with the smallest diameter calcining at the fastest rate. The effects of heat and mass transfer within the bed of marble are no longer playing a significant role in the calcination rate; but there may still be heat and mass transfer effects within each marble particle. It is also seen that there is an increase in calcination rate (approximately 3.4 times faster) between these experiments and the 40g bed experiments. Additionally there is a substantial increase in calcination rate (approximately 14 to 19 times faster) between these experiments and the 100g crucible experiments.

Figure 6-6 shows the fractional calcination profiles for the 100 gram, 3mm nominal diameter marble samples calcined at T_F = 1000°C. The plot shows an increase in calcination time as the bed thickness increases. The accompanying Table 6-8 indicates that the thinly spread marble with a bed thickness of 4.2mm calcines approximately 2.5 times faster than the thicker 14.5mm thick bed. It should be noted that the calcination rate substantially decreases for the thicker marble bed as the conversion of $CaCO_3$ tends towards 100%. For example, there is a 59% decrease in calcination rate for b_d = 4.2mm, where as there is a 121% decrease for b_d = 14.5mm bed. This decrease in calcination rate shows the resistance to heat transfer to the inner most stones and mass transfer of the CO_2 out of the thicker bed.

From Table 6-8 it is possible to derive the following Equation [6.4], showing the relationship between the calcination rate and the bed thickness for the 3mm Penrice marble.

$$\frac{dm}{dt} = 1.17 + \frac{43.54}{(b_d)^2} \quad \text{g/g.s} \qquad [6.4]$$

Equation [6.4] has a coefficient of determination, R^2 of 0.9902 indicating a good fit with the data. The rate Equation [6.4] is shown against the data in Figure 6-11 which also indicates the 95% confidence limits as errors bars of the equation line.

The fractional calcination profiles seen in Figure 6-7 for the 200g, 10mm nominal diameter Penrice marble show similar trends to that described for the 3mm, 100g samples. The plot shows that generally there is an increase in calcination time as the bed thickness increases. The exception is the 27mm thickness bed where a faster calcination time was recorded than for the 20mm thick bed. This can be seen more easily in Table 6-9 where the calcination rate for the 27mm bed is 1.14 g/g.s and the 20mm 1.12 g/g.s. This particular irregularity is thought to have occurred because there was similar impedance to heat transfer to the inner most stones and CO_2 diffusion away from the calcination zone. This similarity occurred because it was very difficult to stack and maintain the 27mm bed thickness for the duration of the experiment. Moving the platform between the muffle furnace and the analytical balance disturbed some of the more precariously placed stones causing them to settle and thus reduce the bed thickness and subsequently increase the beds diameter. The heights of the 20mm and 27mm thick beds appeared very similar, as shown in the profile photos in Figure 6-10 of the two beds taken after each calcination experiment.

Figure 6-10: Photographs taken after calcination showing the heights of the 20mm and 27mm thick beds of the 10mm nominal diameter Penrice marble.

From Table 6-9 to the following Equation [6.5] was derived, showing the relationship between the calcination rate and the bed thickness for the 10mm Penrice marble. It should be noted that this equation has the same form ($y = a + b / x^2$) as that for the 3mm nominal diameter experiments but differing constants of proportionality.

$$\frac{dm}{dt} = 0.979 + \frac{109.33}{(b_d)^2} \quad g/g.s \qquad [6.5]$$

Equation [6.5] has a coefficient of determination, R^2 of 0.9355 indicating a reasonably good fit with the data, though not as good as Equation [6.4]. The rate Equation [6.5] is shown against the data in Figure 6-11 which also indicates the 95% confidence limits as errors bars on the equation line.

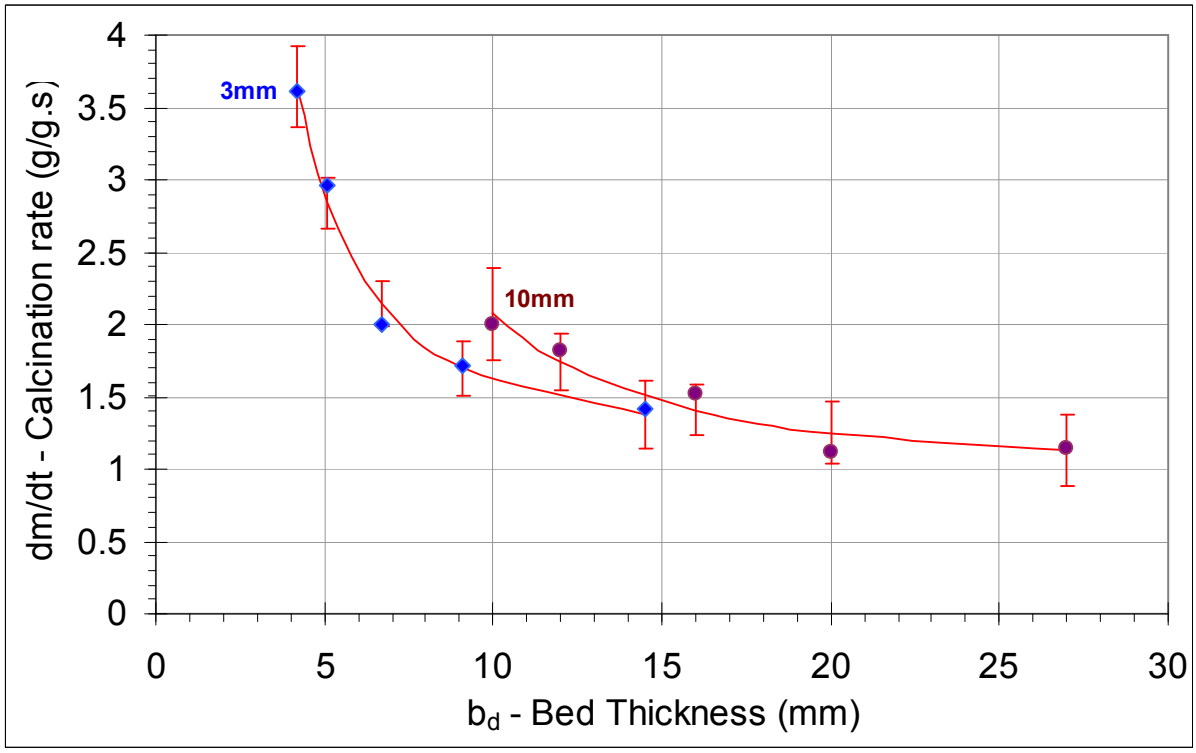

Figure 6-11: Measured calcination rate verses bed thickness for the 3mm and 10mm nominal diameter Penrice marble. Also showing the fit with Equations [6.4] and [6.5] with 95% confidence limits.

Figure 6-8 shows the fractional calcination profiles for single marble samples of three different nominal diameters calcined at T_F = 900°C and T_F = 1000°C. As expected the calcination rate increases with the increase in furnace temperature. For example, the 9.44mm diameter sample calcination rate is 164% faster for T_F = 1000°C than for T_F = 900°C. Again there is some minor overshoot in the calcination profiles, especially for the small particles at the high furnace temperature. The measurement errors are discussed in Section 6.6.

Table 6-10 shows the calcination rates calculated from the slope of the first 50% (dm/dt_{50}) of decomposition for the single marble particles placed within the muffle furnace. The

relationship between particle mass and the rate of decomposition is shown on a log / log axis of Figure 6-12. This plot also displays the relationship between marble sample diameter (and thus particle mass) and calcination rate for the other sized marble samples for both furnace temperatures. The trend in calcination rate with particle diameter, is of interest. The rate of calcination should increase with decreasing particle diameter and thus have an upward slope right to left. The effect of bed thickness causes the upward slope seen in the 100 gram sample experiments. The slope for the 40 gram samples show an initial increase with increasing particle diameter but then levels out and begins a downward slope for the larger diameter particles. This increase and then downward turn indicates that the bed thickness as a function of stone diameter (b_d / d_c), is at a tipping point where the impediment to calcination rate by heat and mass transfer is reducing. This tipping point is at a b_d / d_c value of approximately 2.5. It is therefore recommended that the bed thickness for a solar calcination plant be no thicker than 2.5 times the diameter of the marble.

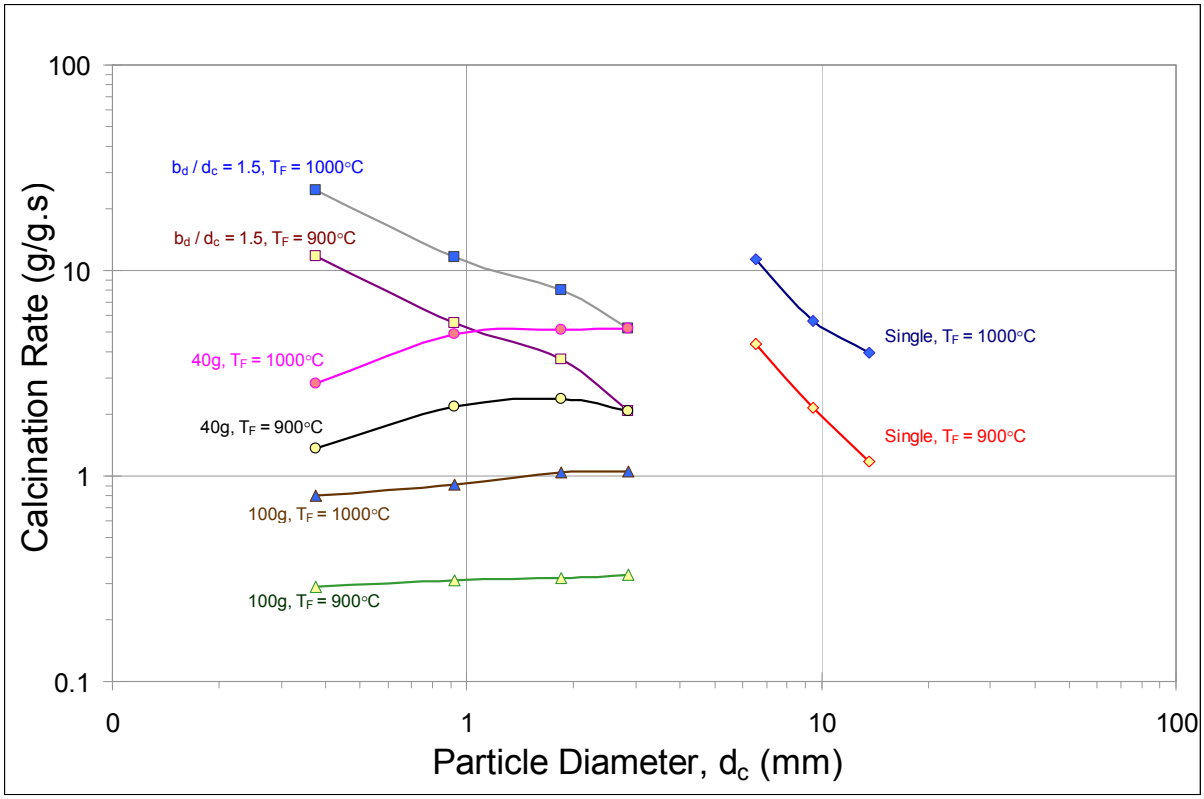

Figure 6-12: Relationship between particle diameter (d_c) and calcination rate for various bed thicknesses and muffle furnace temperatures (T_F).

Figure 6-9 shows the fractional calcination profiles for single 9.44mm nominal diameter (1.000 gram) marble samples calcined at muffle furnace temperatures of 850°C, 900°C, 950°C and 1000°C. The calcination rates for these experiments are shown in Table 6-11, which is graphically displayed in Figure 6-13 below. The plot shows the calcination rates for

the decomposition time (t) from 0 to 50%, t = 0 to 75% and t = 0 to 100%. Using the values from Table 6-11 the following Equation [6.6] was derived, showing the relationship between the calcination rate and furnace temperature for the 9.44mm nominal diameter (1.0 gram) Penrice marble.

$$\ln\left(\frac{dm}{dt}\right) = a + bT^{2.5} \quad \text{g/g.s} \qquad [6.6]$$

Here: T is the furnace temperature,

a = -2.997 and b = 1.495×10^{-7} for t = 0 to 50%,

a = -3.688 and b = 1.688×10^{-7} for t = 0 to 75%,

a = -4.398 and b = 1.782×10^{-7} for t = 0 to 100%.

Equation [6.6] has a minimum coefficient of determination, R^2 of 0.9858 (for t = 0% to 50%), indicating a good fit with the data. Equation [6.6] is displayed against the data in Figure 6-13 which also indicates the 95% confidence limits as errors bars on the equation line.

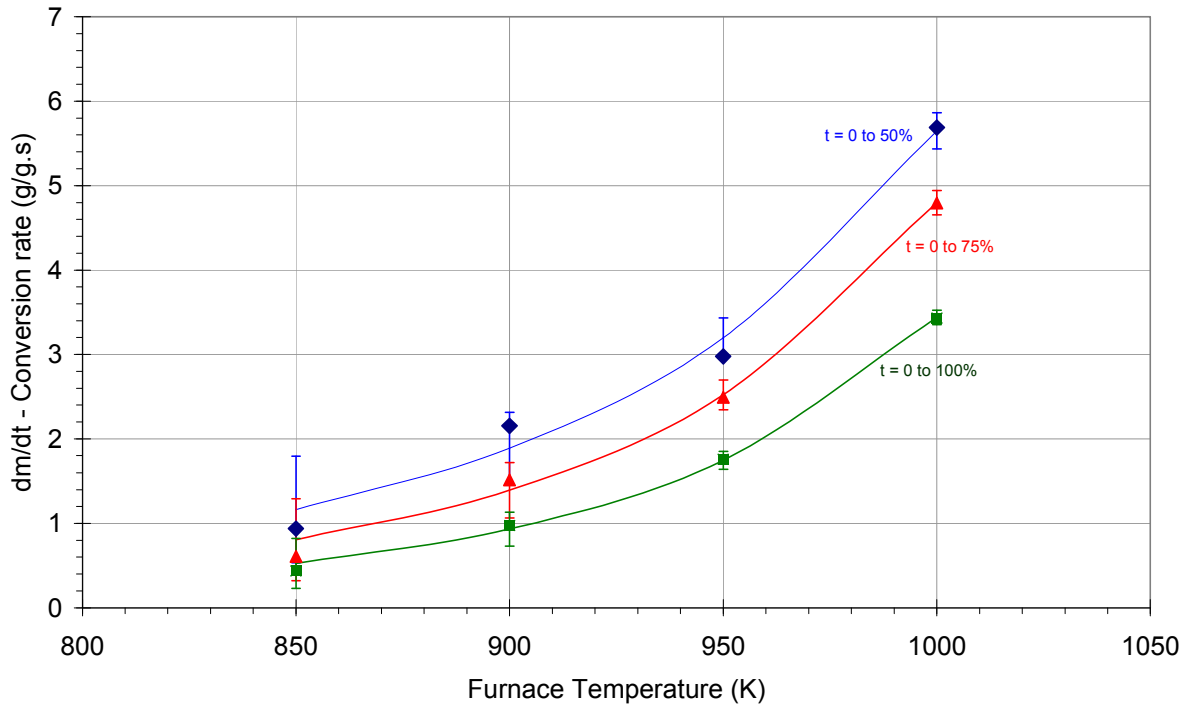

Figure 6-13: Measured calcination rates verses muffle furnace temperature for d_c = 9.44mm Penrice marble. Also showing the fit with Equation [6.6] with 95% confidence limits.

6.5 Conversion Rate and the Arrhenius Equation

The relationship between conversion rate and temperature can be mathematically represented using one form of the Arrhenius equation shown as Equation [6.7]. The Arrhenius equation is a relatively simple formula to characterise the temperature dependence of the rate constant, and therefore, rate of a chemical reaction. It should be remembered that the Arrhenius equation is for chemical kinetics and should be the same, regardless of particle size if the reaction is kinetically controlled.

$$k = Ae^{\left(\frac{-E_a}{RT}\right)} \qquad [6.7]$$

Where:

k is the rate constant for the chemical reaction (sec^{-1}),
A is the pre-exponential factor (sec^{-1}),
E_a is the Arrhenius activation energy (J/mol),
R is the gas constant (8.314 J/ K. mol), and
T refers to temperature (K).

The activation energy, E_a and Arrhenius rate constant, k are calculated from the slope and intercept from linear regression of the Arrhenius plot, respectively.

Figure 6-14 presents the Arrhenius plot for the 100 gram crucible experiments. The rate of calcination (dm/dt) has been deduced from the slope of the first 50% (dm/dt_{50}) of $CaCO_3$ conversion, from the T_F = 900°C and T_F = 1000°C calcination profiles shown in Figure 6-3.

Table 6-12 displays the activation energy, E_a and rate constant, k, which were calculated from the slope and intercept of the Arrhenius plot Figure 6-14, respectively, for each particle size range.

Telfer (1999, Table 7.1) quotes Arrhenius parameters for Angaston limestone which range between E_a = 163 to 195 J/mol and k between 1.10×10^5 and 3.46×10^6 sec^{-1} for 53μm to 355μm size range. The values in Table 6-12 show similar rate constants but substantially lower activation energy values. The difference can be explained because the marble for Telfer's experiments was collected several years before the marble used within these experiments. The marble would therefore be from a different location within the quarry and thus be slightly different in composition.

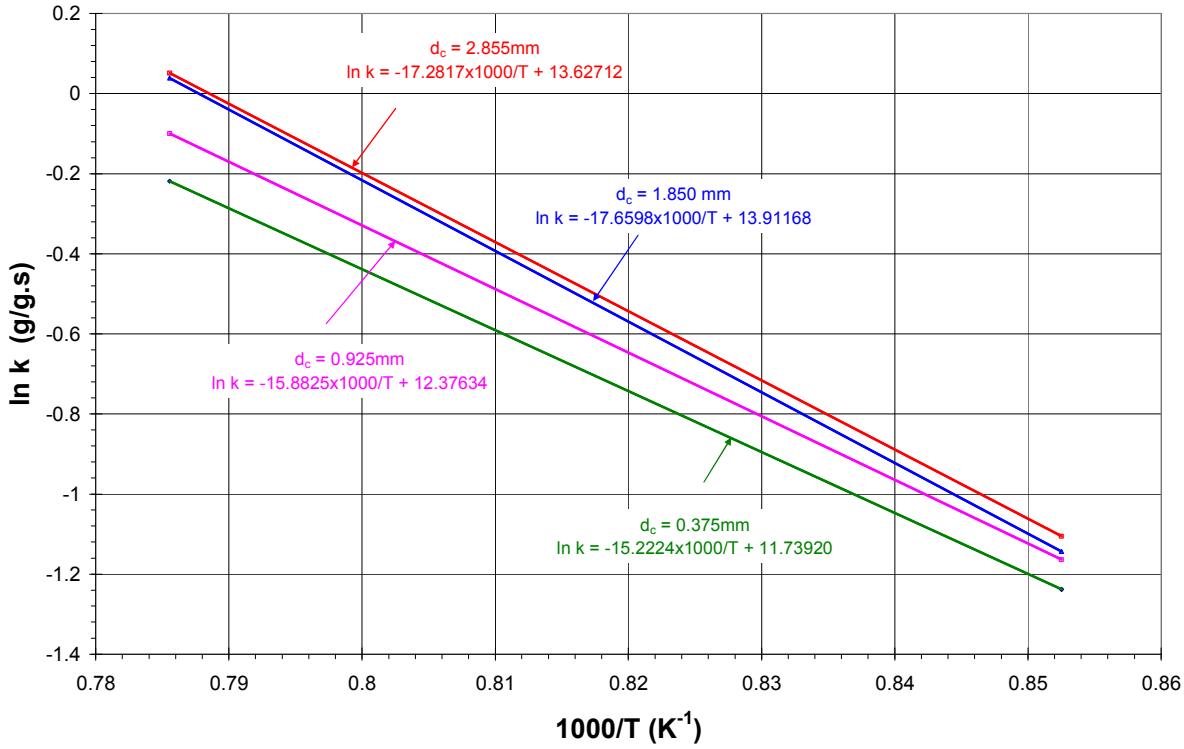

Figure 6-14: Arrhenius plot of the calcination of Penrice marble from the 100 gram crucible experiments for the four different particle size ranges for T_F = 900°C and T_F = 1000°C. Slopes of $CaCO_3$ conversion taken for X=50%.

The data in Table 6-12 suggests that the activation energy required to ensure that a reaction occurs increases, with increasing particle size. The marble samples used within the first three experiments where the same size and exposed to the same furnace temperatures, therefore if the rate of conversion was controlled by chemical kinetics alone, the Arrhenius parameters for all of the different sized marble samples would be the same.

Table 6-12: Arrhenius parameters for the calcination of Penrice Marble for the 100 gram crucible experiments with 900°C < T_F < 1000°C, for chemical conversion dm/dt_{50}.

Arrhenius Parameters			
Marble Nominal Diameter d_C (mm)	**E_a (kJ mol^{-1})**	**E_a (kcal mol^{-1})**	**k (sec^{-1})**
0.375	129	30.8	$1.56x10^5$
0.925	135	32.1	3.01×10^5
1.850	149	35.7	1.40×10^6
2.855	146	35.0	1.08×10^6

Table 6-13 shows the variation in Arrhenius parameters by comparing data from all of the muffle furnace experiments for 900°C < T_F < 1000°C using dm/dt_{50}. These variations in Arrhenius parameters indicate that the calcination rate is not controlled by chemical kinetics but rather through another effect such as heat transfer, or by diffusion of the carbon dioxide through the material.

The 9.44mm nominal diameter (1.000g) multiple furnace temperature experiments show the activation energy (E_a) and rate constant k calculated from the four furnace temperature measurements.

Only single measurements were taken for the 6.54mm and 13.62mm marble samples and therefore a variation comparison is not available. The 100g - 3mm and 200g – 10mm experiments were at a single 1000°C furnace temperature, therefore Arrhenius parameters cannot be calculated.

Table 6-13: Variation in Arrhenius parameters from all muffle furnace calcination experiments using 900°C < T_F < 1000°C and dm/dt_{50}.

Variation in Measured Arrhenius Parameter			
Nominal Particle Size	**E_a (kJ mol^{-1})**	**E_a (kcal mol^{-1})**	**k (sec^{-1})**
0.375 mm	90 to 129	21.5 to 30.8	$1.37x10^4$ to $1.56x10^5$
0.925 mm	92 to135	22.0 to 32.1	6.81×10^4 to $3.00x10^5$
1.850 mm	94 to 149	22.4 to 35.7	3.64×10^4 to $1.40x10^6$
2.855 mm	113 to 146	27.1 to 35.0	2.77×10^5 to 1.08×10^6
6.54 mm (0.333g)	117	27.9	6.88×10^5
9.44 mm (1.000g)	139	33.3	3.03×10^6
13.62 mm (3.000g)	151	36.1	6.33×10^6

It should be noted that the variation in the rate constant, k, and activation energy, E_a, become larger as the chemical conversion increased from dm/dt_{50} to dm/dt_{100}. During the calcination of a particle, a layer of CaO forms which is more porous than the $CaCO_3$ which insulates the core which restricts the transfer of heat to the reaction zone. The pores also trap the CO_2 and thus cause a resistance to the flow of CO_2 diffusing away from the reaction zone. Khinast *et al*. (1996) note that this resistance will be greater as the conversion tends to 100%. The strength of the resistance varies between different shaped particles which can

cause discrepancies in the pre-exponential factor (and rate constant) and activation energy. Telfer *et al*. (2000) discussed how it is common for gas-solid reactions to have differing controlling steps during the stages of the reaction due to the structural changes which are occurring within the solid.

Table 6-13 shows that the activation energies calculated for the Penrice marble ranges between 47% to 11% lower than for the theoretical heat of reaction. This shows the difference in experimental outcome between using idealised equipment (such as a thermogravimetric apparatus) with chemically pure calcium carbonate and an atmospherically open electric muffle furnace with "unprocessed" quarry limestone.

6.6 Error Analysis for the Muffle Furnace Calcination Experiments

An error analysis was conducted to identify possible causes for discrepancies in the muffle furnace calcination measurements. This section assesses measurement accuracy and also recommends methods to improve the precision further.

One of the largest sources of error was the loss of the stone, or parts of the stone due to decrepitation. Penrice Angaston marble is known to decrepitate, and affects manufacture of lime by the Penrice Soda Company in their rotary and vertical shaft kilns. It occurs when an ambient temperature stone is placed into a very hot furnace. Within a period of approximately 40 seconds (depending on stone size) the stone can explode into small pieces, although this does not always occur. Within the muffle furnace experiments presented here, some of the limestone pieces were observed to eject 20cm from the original location. Decrepitation is thought to occur due to different mechanisms including the vaporisation of trapped moisture within the stone, and the variation in heating rate within the stone causing high shear forces along grain boundaries. The exact cause could be investigated within another scientific research project in the future.

The variation in the analytical balance readout during the mass measurements of the experiments was observed to be approximately ± 5 milligrams over the 10 second measurement. The 10 to 20% overshoot seen in some of the calcination profiles are the result of this variation. The overshoot was generally for the small sample masses and for the higher muffle furnace temperatures. This discrepancy was minimised by calculating the arithmetic mean of the measured values. The root mean squared and standard deviation of each data set was used to monitor and then evaluate the dispersion of the collected data.

An average standard deviation of approximately 0.0041 grams was recorded, thus representing a maximum 1.2% error in the mass measurements.

A small variation in the muffle furnace temperature at the location of the marble was recorded. This variation was discussed in section 4.4.1 with the maximum temperature difference being calculated to be approximately 1.04% or 5 degree centigrade at a muffle furnace temperature of 950°C.

During the 10 second mass measurement on the analytical balance, the temperature of the surface of marble sample and refractory board / crucible bowl decreased. This reduction in surface temperature was measured on three occasions: once during the 0.925mm, 100g crucible bowl 900°C experiments, with a temperature reduction of 62°C being measured, once during the 1.850mm, 40g flat bed 1000°C experiments, with a temperature reduction of 77°C being measured, and once during the 0.375mm, bed thickness of 1.5 times marble diameter 1000°C experiments, with a temperature reduction of 92°C being measured. The temperature decrease of the sample was higher for the 1000°C furnace temperatures and also higher for the lower thermal mass samples. It is difficult to directly quantify the effect of this temperature reduction on the calcination rate, but it might be a contributing factor in the discrepancies in the experimental activation energy (E_a).

During the experiments it was observed that there was a 40°C and 55°C reduction in the furnace temperature when the furnace door was opened for removing for mass measurement or replacing the sample back into the furnace, for the 900°C and 1000°C muffle furnace temperatures respectively. After closing the door, the furnace took approximately 30 seconds to regain temperature back to the set point temperature. This temperature loss was the same for all experiments and so represents a scaling effect on the calcination rate. Again it is difficult to directly quantify the effect of this temperature reduction on the calcination rate, but it may be a contributor to the variations in activation energy.

On a few occasions there were experimental timing errors in which the two or five minute measurement intervals were not strictly observed. These occasions were noted and measurement times adjusted accordingly. In general the tolerance in the two minute measurement window was approximately ±10 seconds and the five minute measurement window approximately ±30 seconds. The effect of these discrepancies is considered minor, but note worthy.

The experimental errors reveal the need for better control over the mass measurement system. Removing the samples from the furnace not only cools the sample and furnace but

also causes significant measurement noise due to convective flows around the analytical balance. It is therefore recommended that consideration be made to measure the mass change in situ for future muffle furnace calcination experiments. This may mean fabricating a purpose built muffle furnace to accommodate the mass measurement system.

6.7 Conclusions from the Muffle Furnace Experiments

The aim of these muffle furnace calcination experiments was to quantify the relationships between calcination temperature, particle size and bed depth for small to medium sized Penrice Angaston Marble.

The measurements have shown that the calcination rate of Penrice marble to quicklime increases as the temperature to which it is exposed increases from 900°C to 1000°C. In particular, the rate of calcination for furnace temperatures between 850°C and 1000°C for single 1.000g (9.44mm nominal diameter), Penrice marble particle can be expressed using Equation [6.6], duplicated here:

$$\ln\left(\frac{dm}{dt}\right) = a + bT^{2.5} \quad \text{g/g.s}$$

where, T is the furnace temperature, a = -4.398 and b = 1.782×10^{-7} for a decomposition time between t = 0 to 100%.

The calcination rate for a bed thickness of between 4.5mm to 12mm for 3mm nominal diameter Penrice marble is given by Equation [6.4], replicated below:

$$\frac{\mathrm{dm}}{\mathrm{dt}} = 1.17 + \frac{43.54}{(\mathrm{b_d})^2} \quad \text{g/g.s}$$

where, b_d is the bed thickness.

For 10mm nominal diameter Penrice marble the calcination rate can be expressed using Equation [6.5], reproduced below:

$$\frac{\mathrm{dm}}{\mathrm{dt}} = 0.979 + \frac{109.33}{(\mathrm{b_d})^2} \quad \text{g/g.s}$$

The results have also shown an increase in calcination rate for decreasing particle size, for a marble bed thickness of 2.5 times the nominal thickness of the marble in use. Similarly there

is an increase in calcination rate for decreasing particle size for the calcination of single stones of Penrice marble. Conversely the results show a decrease in the calcination rate for decreasing particle size for bed thickness of more than 2.5 times the nominal thickness of the marble in use. This infers that the calcination rate is affected by the diffusion of CO_2 through a packed bed as well as the transfer of heat to the reaction zone. This implies that the bed thickness should be no thicker than 2.5 times the particles diameter for Penrice marble with a nominal diameter between 0.375mm and 2.855mm.

The results suggest that the solar calcination process should utilise limestone layer no thicker than 2.5 times the nominal diameter of the limestone in use to optimise the exposure of the stone to the direct radiation. This should increase the heat transfer to the lower particle within the bed and allow for unrestricted CO_2 diffusion away from these stones.

These results add significantly to knowledge base in the practical application of limestone beds used for the calcination of limestone. These experiments have quantified the effects of temperature, particle size and bed depth on the rate of calcination. These baseline calcination rates can now be used to evaluate the effects of using radiation as the heating source for the calcination of the same sized Penrice marble samples.

Chapter 7

Calcination Measurements of Penrice Marble Directly Exposed to High Intensity Radiation

7.1 Introduction

These experiments measure the calcination rate of small to medium sized Penrice Angaston marble exposed to radiant flux intensities of approximately 175kW/m^2, 280kW/m^2 and 430kW/m^2. The decomposition rates, the preheating time (t_{cp}) and time to complete calcination (t_{100}) were measured and are used for validation of the calcination modelling presented in Chapter 10. Comparisons are also made between the results from these experiments, the results from the muffle furnace experiments (from Chapter 6) and results from the solar furnace experiments presented in Chapter 8. These experiments quantify the effects on the calcination rate using high intensity concentrated radiation as the sole heating source. The use of radiant energy as the sole heat source for the calcination of Australian limestone has never been reported.

The use of solar thermal radiant energy for the calcination of limestone was discussed in Chapter 2. The evaluation of the four existing solar reactor designs, namely the fluidised bed, the cyclone or falling particle (flash calciner), the rotary kiln and the flat bed furnace, identified that the flat bed furnace has the greatest potential. Calcination experiments by solar energy using a bed of limestone were conducted by Salman and Khraishi (1988) who used a tracking 3 $\times$ 3m heliostat and concentrator parabolic dish to illuminate one side of a 13mm diameter 2mm-high, reagent grade, calcium carbonate or gypsum placed within their flat bed reactor. The measurements were conducted using a variable source of radiant heat flux, so that the intensity varied with time and location within the reaction chamber. No assessment on the influence of bed depth or particle mass is reported.

The calcination of limestone in a bed was investigated by Meier and Cella (2004) using a 75 kW high pressure argon arc solar simulator designed and presented by Hirsch *et al*. (2003) for the supply of radiant energy for the calcination of calcium carbonate. Their 2mm to 3mm diameter $CaCO_3$ particles were arranged to form a mound (prism) 100mm length, 20mm wide and 3.7mm high and placed onto a silicon carbide plate and exposed to “constant power fluxes” for a “controlled interval of time”. No data is reported from varying the radiant flux or the particle size. Confirmation of the calcination rates from their solar bed experiments was determined by using an electric furnace.

The experiments presented within this Chapter use no enclosure (or furnace) surrounding the calcination platform or marble, and therefore can be considered open system experiments. This is distinct from the experiments presented within Chapter 8 which use a furnace enclosure to surround the marble.

The calcination experiments involved measuring the weight loss over time of 6.54mm, 9.44mm and 13.62mm nominal diameter Penrice Angaston marble exposed to radiant heat fluxes of either 175 $\pm$ 10 kW/m^2, 280 $\pm$ 20 kW/m^2 and 430 $\pm$ 30 kW/m^2. The results from these single particle experiments quantify the relationship between stone size, calcination rate and heat flux intensity.

An additional set of qualitative experiments were performed, the details of which can be found in Appendix D. These experiments maintained a constant bed size (diameter) while varying the bed thickness by varying the mass of the sample. Due to the large variation in the radiant heat flux intensity within the beam profile, complete calcination of the bed-sample was not achieved before hard burning of the marble within the region of highest heat flux occurred.

7.2 Experimental Methodology

7.2.1 Experimental Apparatus

The experimental equipment used within these experiments includes the 5 kW xenon short arc lamp, the Cinemeccanica - Milano lamphouse, the aluminium deflection mirror, the calcination platform and the analytical balance. The specifications for this equipment are presented in Chapter 4, Section 4.5.

7.2.2 Single Stone Calcination Experiments

The single stone open system radiation experiments were performed by placing a single marble sample onto the surface of the ceramic fibre refractory board and placing it within the radiation beam. Three series of experiments were conducted, with the heat flux being varied between each. The intensity of the radiation illuminating the platform was varied by changing the distance between the focal point of the beam and the platform, denoted by ‘S’ in this thesis. The distances were S = 100mm, S = 75mm and S = 50mm which provided radiant

heat flux of approximately 175 ± 10 kW/m^2, 280 ± 20 kW/m^2 and 430 ± 30 kW/m^2 respectively.

The mass of the three marble used within these experiments were 0.333g, 1.000g and 3.000g. The nominal diameters of these sized marble particles, as displayed in Table 6.4, were 6.54mm, 9.44mm and 13.62mm respectively.

The xenon lamp and calcination platform were preheated for a minimum 90 minutes prior to placing the ceramic fibre refractory board into the radiation beam. Preheating the lamp and calcination platform ensured that a steady state radiation heat flux condition was established. The stone was then placed onto the preheated refractory board within the radiation beam. Using the digital image heat flux measurement methods described in Chapter 5, images were taken of the marble in the radiation beam, and processed to ascertain the heat flux profile at the measurement platform.

During the decomposition measurements the mass of the calcining marble was automatically measured at 5 second intervals for the duration of the experiments using the GX-600 analytical balance. The mass loss due to calcination of each sample was calculated for each mass measurement using Equation [6.1].

7.2.3 Measurement Accuracy

The repeatability within these measurements and therefore measurement accuracy was tested by repeating four experiments at two different heat fluxes; eight experiments in all. The measurement were conducted using the 6.54mm nominal diameter Penrice marble placed at S =75mm (430 ± 30 kW/m^2) and S = 50mm (280 ± 20 kW/m^2) positions. This sized stone (0.333g), placed at these heat fluxes, were selected because they represent the “worst case” measurement scatter compared to the heavier stone sizes

The scatter was identified as being primarily due to vibration of the analytical balance by the cooling fan for the xenon bulb. This was reduced by isolating the analytical balance platform from the lamphouse frame. Another source of scatter derived from convective air flow past the calcination platform.

The scatter was reduced by using a 5 point moving average scheme. Figure 7-1 shows the fractional calcination verses decomposition time for the four 6.54mm nominal diameter Penrice marble exposed to 280 kW/m^2, and Figure 7-2 the fractional calcination for the 430 kW/m^2 experiments. Recollecting that fractional calcination is the fraction of CO_2 released

during calcination divided by the total combined CO_2 within the sample as shown in Equation [7.1].

$$\text{Fractional calcination} = \frac{m_{CO_2} - m_{CO_2,i}}{m_{CO_2}} \qquad [7.1]$$

Figures [7-1] and [7-2] also show the average preheating time (or sensible heating time) denoted on the figure by t_{cp}, the average time to achieve 50% of calcination which is denoted by t_{50}, the average time to achieve 75% of calcination denoted t_{75}, and the average time to complete calcination denoted by t_{100}. The mass of the sample at t_{50} is denoted by m_{50}, at t_{75} by m_{75} and at t_{100} by m_{100}.

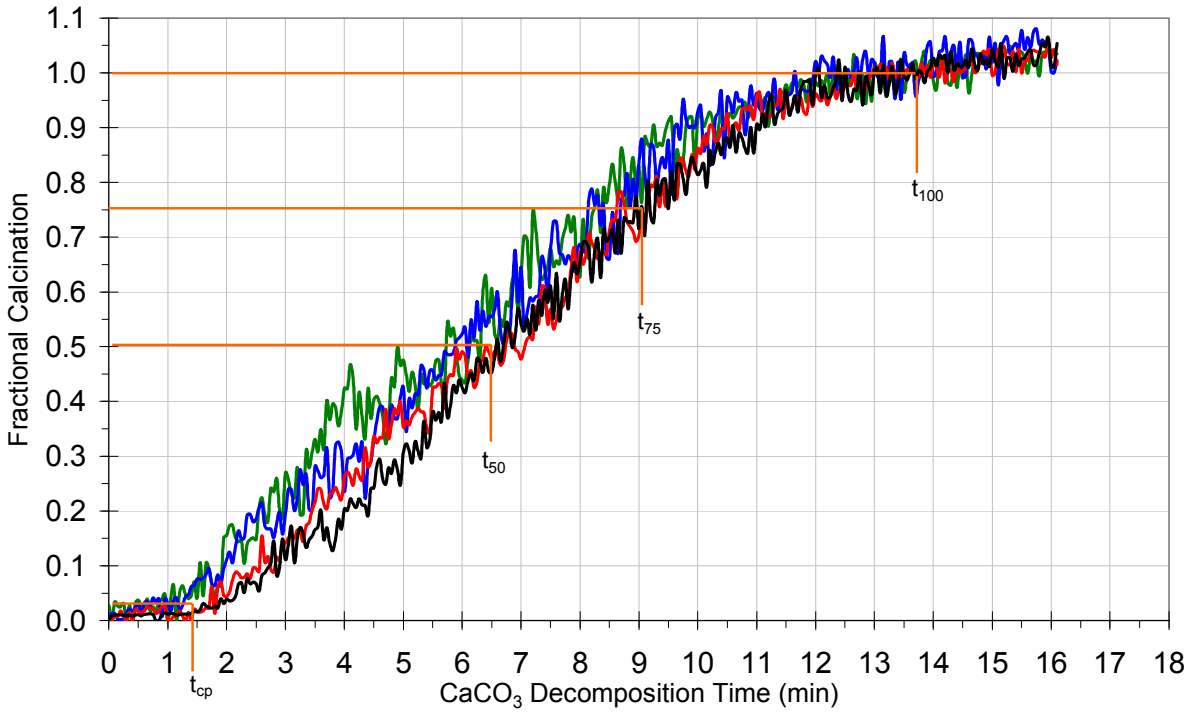

Figure 7-1: Calcination profiles of four single 6.54mm nominal Penrice marble stones exposed to a radiant heat flux of 280±20 kW/m^2 at S = 75mm in the open atmosphere solar calcination system.

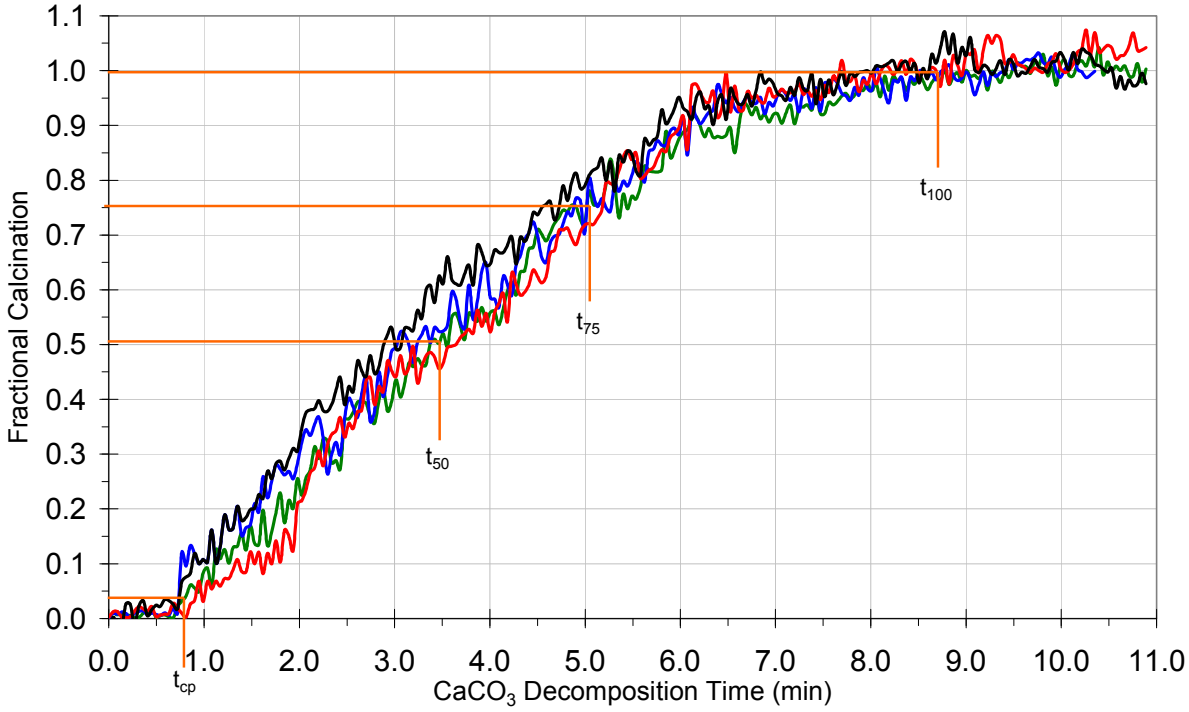

Figure 7-2: Calcination profiles of four single 6.54mm nominal Penrice marble stones exposed to a radiant heat flux of 430±30 kW/m^2 at S = 50mm in the open atmosphere solar calcination system.

Table 7-1 shows the preheating time, rates of calcination and time to complete calcination for the eight 6.54mm single stones calcined at two heat fluxes. The preheating time (t_{cp}) has been calculated as being the time between placing the sample within the radiation beam and the sample reaching a loss of mass equal to 3% of the stones final mass (denoted using m_3).

Three rates of calcination (dm/dt) have been calculated from the slope of the fractional calcination profiles. The three measures of conversion rate by mass loss over time are:

1). 50% of decomposition, i.e. $$dm/dt_{50} = \frac{m_{50} - m_3}{t_{50} - t_{cp}} \qquad [7.2]$$

2). 75% of decomposition, i.e. $$dm/dt_{75} = \frac{m_{75} - m_3}{t_{75} - t_{cp}} \qquad [7.3]$$

3). 100% decomposition i.e. $$dm/dt_{100} = \frac{m_{100} - m_3}{t_{100} - t_{cp}} \qquad [7.4]$$

The mean value and standard deviation as a percentage of the mean value have also been calculated and are displayed in Table 7-1.

It should be noted that the variation (standard deviation) may not entirely be measurement error owing to small variations in the compositional characteristics between each Penrice marble stone.

Table 7-1: Comparison of preheating time, calcination rate and time to complete calcination for d_c = 6.54mm Penrice marble exposed to either 280±20kW/m^2 or 430±30 kW/m^2 for the open atmosphere solar calcination system.

Stone Number	**Preheating time t_{cp} (minutes)**	**Rate of Calcination for dm/dt_{50} (g/g.s)**	**Rate of Calcination for dm/dt_{75} (g/g.s)**	**Rate of Calcination for dm/dt_{100} (g/g.s)**	**Time to Complete Calcination t_{100} (minutes)**
Heat Flux of 280±20 kW/m^2					
1	1.4	5.759	5.780	4.766	12.2
2	1.2	5.272	5.911	4.728	12.7
3	1.4	5.719	5.876	4.920	12.4
4	1.6	5.594	5.889	4.634	12.7
Mean	**1.4**	**5.586**	**5.864**	**4.762**	**12.5**
Standard Deviation (%)	10.35	3.95	0.99	2.50	1.86
Heat Flux of 430±30 kW/m^2					
1	0.81	10.821	10.410	7.230	8.0
2	0.72	11.784	10.684	7.397	8.1
3	0.81	10.519	10.217	7.684	7.8
4	0.77	12.197	10.847	7.378	7.7
Mean	**0.8**	**11.330**	**10.540**	**7.422**	**7.9**
Standard Deviation (%)	5.55	6.98	2.66	2.55	2.00

The mean value, shown in Table 7-1, has been calculated using the data from the four samples. The standard deviation was then calculated which is displayed as the percentage of the mean value. The standard deviation is used to calculate the error bars presented later in the analysis of the calcination results.

7.3 Results

Figures 7-3 to 7-5 show the calcination profiles for the single marble stone samples with nominal diameter of 6.54mm (0.333g), 9.44mm (1.000g) and 13.62mm (3.000g), exposed to a radiant heat flux of either 175kW/m^2, 280kW/m^2 and 430kW/m^2.

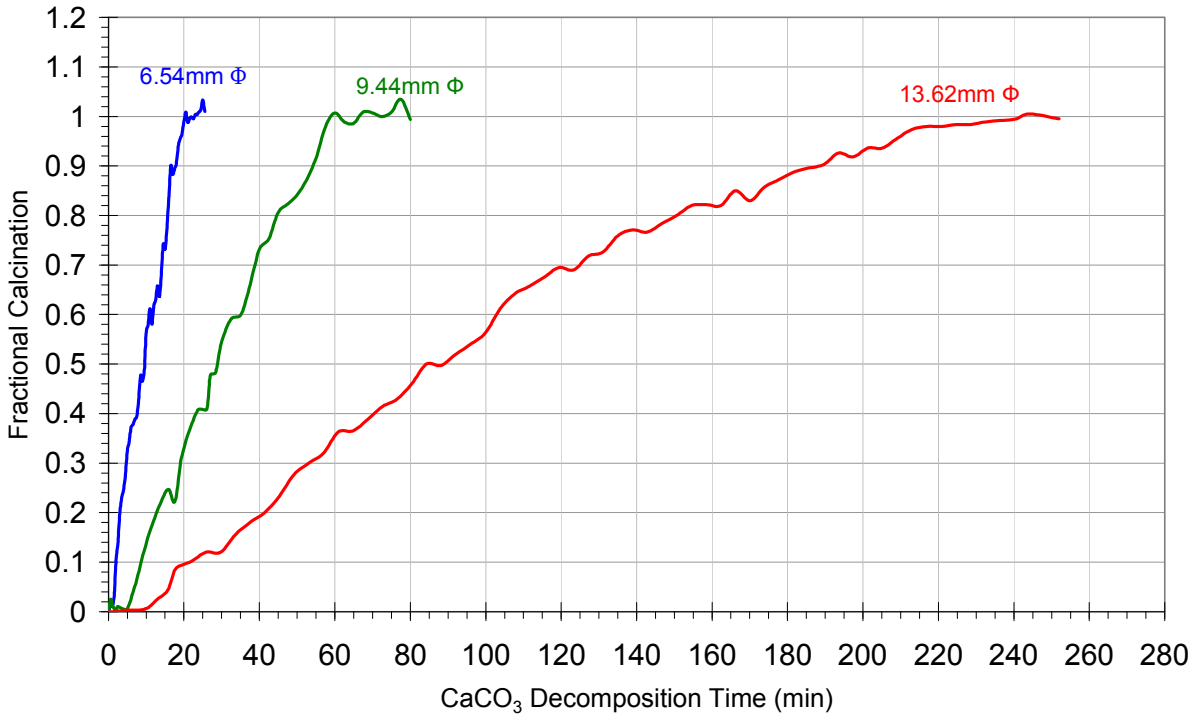

Figure 7-3: Calcination profiles of single Penrice marble stones exposed to a radiant heat flux of 175±10 kW/m^2 in an open atmosphere solar system.

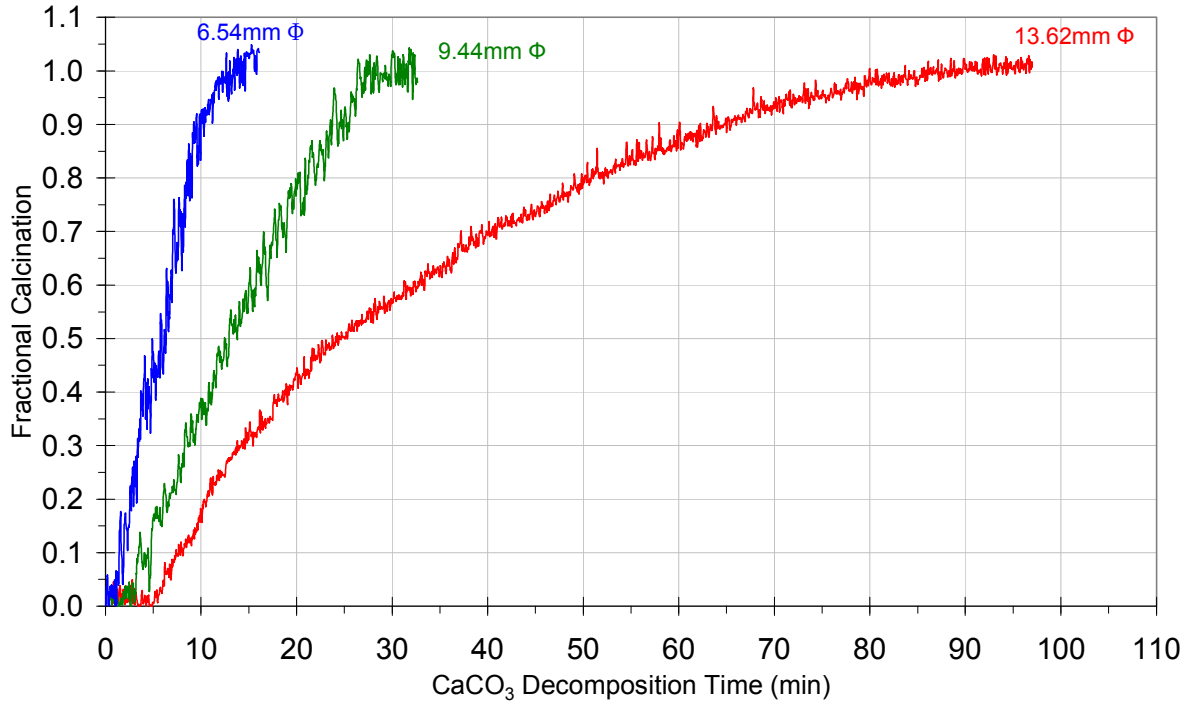

Figure 7-4: Calcination profiles of single Penrice marble stones exposed to a radiant heat flux of 280±20 kW/m^2 in an open atmosphere solar system.

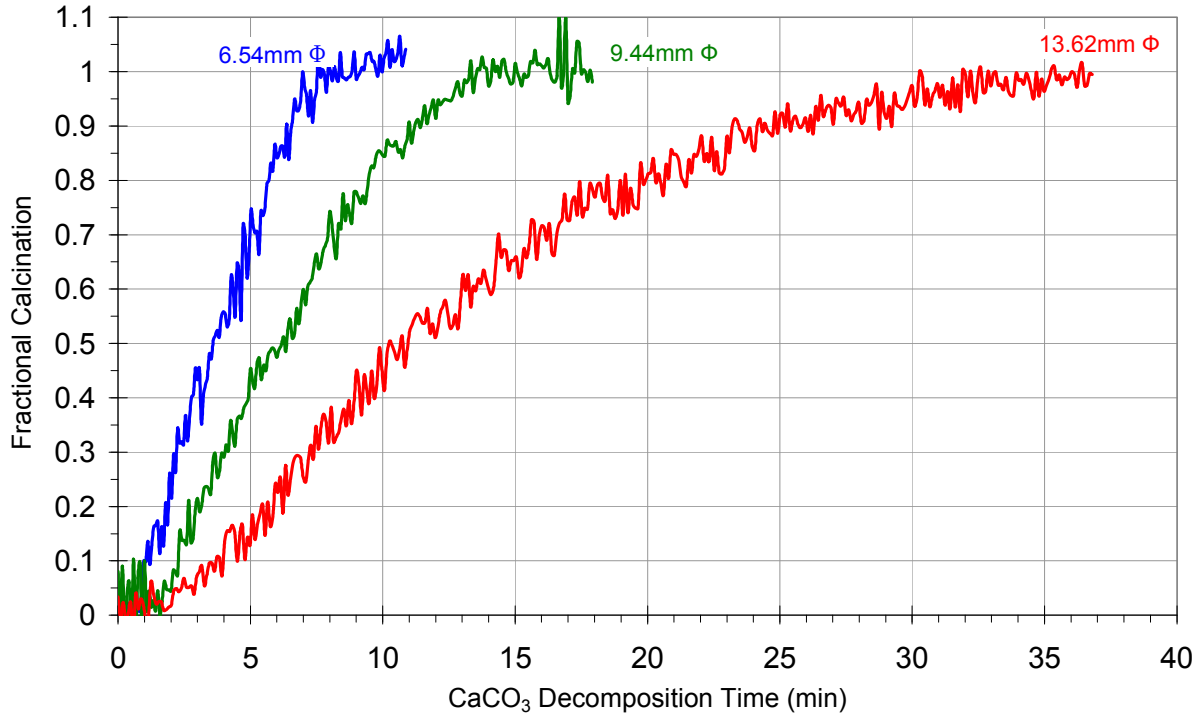

Figure 7-5: Calcination profiles of single Penrice marble stones exposed to a radiant heat flux of 430±30 kW/m^2 in an open atmosphere solar system.

Tables 7-2 to 7-4 show the preheating time, rates of calcination, time to complete calcination and CO_2 release rate for the single marble stone open system calcination experiments. The rate of calcination (dm/dt) has been calculated using the slope of the fractional calcination verse time plots shown in Figures 7-3 to 7-5. Three rates were calculated, the first being the change of mass over time for the first 50% of decomposition, i.e., for dm/dt from 0 to 50% represented by dm/dt_{50}, the change of mass over time for up to 75% of decomposition, i.e. dm/dt from 0 to 75% represented by dm/dt_{75} and the change of mass over time to completion i.e. dm/dt from 0 to 100%, represented by dm/dt_{100}. Also shown in the tables is the time before calcination begins which represents the preheating time, denoted by t_{cp}, and the time over which the conversion takes place, which is the time from the beginning of calcination to final completion, denoted by t_{100}. The release rate for the CO_2, given in mg of CO_2 per second, was calculated using the total mass loss from each sample divided by the time to complete calcination, t_{100}.

Table 7-2: Preheating time, calcination rate and time to complete calcination for single Penrice marble exposed to a radiant heat flux of 175±15kW/m^2 in an open atmosphere solar system.

Marble Nominal Diameter d_C (mm)	**Preheating time t_{cp} (minutes)**	**Rate of Calcination for dm/dt_{50} (g/g.s)**	**Rate of Calcination for dm/dt_{75} (g/g.s)**	**Rate of Calcination for dm/dt_{100} (g/g.s)**	**Time to Complete Calcination t_{100} (minutes)**	**CO_2 release rate $mgCO_2$ / sec**
6.54	2.0	3.088	2.987	2.571	21	0.116
9.44	5.0	1.293	1.195	0.924	65	0.113
13.62	9.8	0.371	0.330	0.245	242	0.091

Table 7-3: Preheating time, calcination rate and time to complete calcination for single Penrice marble exposed to a radiant heat flux of 280±20kW/m^2 in an open atmosphere solar system.

Marble Nominal Diameter d_C (mm)	**Preheating time t_{cp} (minutes)**	**Rate of Calcination for dm/dt_{50} (g/g.s)**	**Rate of Calcination for dm/dt_{75} (g/g.s)**	**Rate of Calcination for dm/dt_{100} (g/g.s)**	**Time to Complete Calcination t_{100} (minutes)**	**CO_2 release rate $mgCO_2$ / sec**
6.54	1.4	5.586	5.864	4.762	12.5	0.196
9.44	2.6	2.672	2.681	2.087	28.3	0.259
13.62	5.4	1.499	1.054	0.675	87	0.253

Table 7-4: Preheating time, calcination rate and time to complete calcination for single Penrice marble exposed to a radiant heat flux of 430±30kW/m^2 in an open atmosphere solar system.

Marble Nominal Diameter d_C (mm)	Preheating time t_{cp} (minutes)	Rate of Calcination for dm/dt_{50} (g/g.s)	Rate of Calcination for dm/dt_{75} (g/g.s)	Rate of Calcination for dm/dt_{100} (g/g.s)	Time to Complete Calcination t_{100} (minutes)	CO_2 release rate $mgCO_2$ / sec
6.54	0.8	11.330	10.540	7.422	7.9	0.310
9.44	1.5	6.274	6.253	4.353	13.4	0.547
13.62	2.0	3.443	2.808	1.688	34.8	0.632

7.4 Analysis of Results

Figure 7-3 shows the calcination profiles for the 6.54mm, 9.44mm and 13.62mm nominal diameter marble exposed to approximately 175 kW/m^2. The plot shows a decrease in calcination time with decreasing stone size. This is also reflected in Table 7-2 which shows the calcination rate for the 6.54mm stone is approximately 730% faster than for the 13.62mm nominal diameter stone for calcination time dm/dt_{50}. A comparison in calcination rates for the three calcination times, dm/dt_{50}, dm/dt_{75} and dm/dt_{100} show that the rate decreases as the conversion proceeds through the stone. This is expected because the stone becomes insulated by the newly formed CaO layer which increases in thickness as the calcination reaction proceeds through the stone. This insulation impedes the transfer of heat to the calcination front which reduces the calcination rate.

Table 7-2 also indicates that the release rates of CO_2 for the stones are approximately the same when exposed to the same heat flux. This is also reflected in Table 7-3. Table 7-4 does not follow the same trend, but instead there is an increase in release rate of CO_2 for increasing stone size. This indicates that there may be a limit to the calcination time for a particular sized stone, which may be due to one of the rate limiting steps: heat transfer, mass transfer or chemical reaction. The analysis of which is not presented here, but is identified as an aspect which can be analysed in the future.

The average release rates and standard deviation for the three heat fluxes are shown in Table 7-5, which shows an increase in release rate for increasing radiant heat flux. This indicates that the reaction rate is dependent on the available energy, and independent of the stone size.

Table 7-5: Average CO_2 release rate for Penrice marble exposed to radiant heat flux of 175±15kW/m^2, 280±20kW/m^2 or 430±30kW/m^2.

	175 kW/m^2	**280 kW/m^2**	**430 kW/m^2**
Average CO_2 Release Rate (mg CO_2 / sec)	0.107	0.236	0.496
Standard Deviation	0.0138	0.0351	0.1672

Figure 7-3 shows overshoot in the fractional calcination for the 6.54mm and 9.44mm nominal diameter fractional calcination profiles. This over shoot indicates measurement error which can be attributed to measurement noise from the analytical balance and also measurement inaccuracy due to the convective air flow around the calcination platform.

Figure 7-4 shows the fractional calcination profiles for the 6.54mm, 9.44mm and 13.62mm nominal diameter marble exposed to a heat flux of approximately 280 kW/m^2. These measurements show that again there is a decrease in calcination time with decreasing stone size. Table 7-3 displays the measured calcination rates from the slope the plots for the calcination times, dm/dt_{50}, dm/dt_{75} and dm/dt_{100}. The calcination rate for the 6.54mm stone is approximately 3.7 times faster than for the 13.62mm nominal diameter stone for calcination time dm/dt_{50}, and increases to over 7 times faster over the entire calcination time, i.e. dm/dt_{100}.

Figure 7-5 shows that there is a decrease in calcination time with decreasing stone size for the 6.54mm, 9.44mm and 13.62mm nominal diameter marble exposed to a heat flux of approximately 430 kW/m^2. Table 7-4 displays the calcination rates which show a similar trend to the 175kW/m^2 and 280kW/m^2 experiments. The calcination rate for the 6.54mm stone is approximately 3.2 times faster than for the 13.62mm nominal diameter stone for calcination time dm/dt_{50}, and increases to 4.4 times faster for the entire calcination time, dm/dt_{100}.

Figure 7-6 shows the decomposition rate (dm/dt_{50}) verses heat flux for the 6.54mm (0.333g), 9.44mm (1.000g) and 13.62mm (3.000g) nominal diameter marble exposed to radiant heat flux of either 175 kW/m^2, 280 kW/m^2 or 430 kW/m^2. The error bars for the calcination rate represent a standard variation of 6.98% of the value, while the error bars for the heat flux represent 15, 20 and 30 kW/m^2 for 175 kW/m^2, 280 kW/m^2 and 430 kW/m^2 respectively.

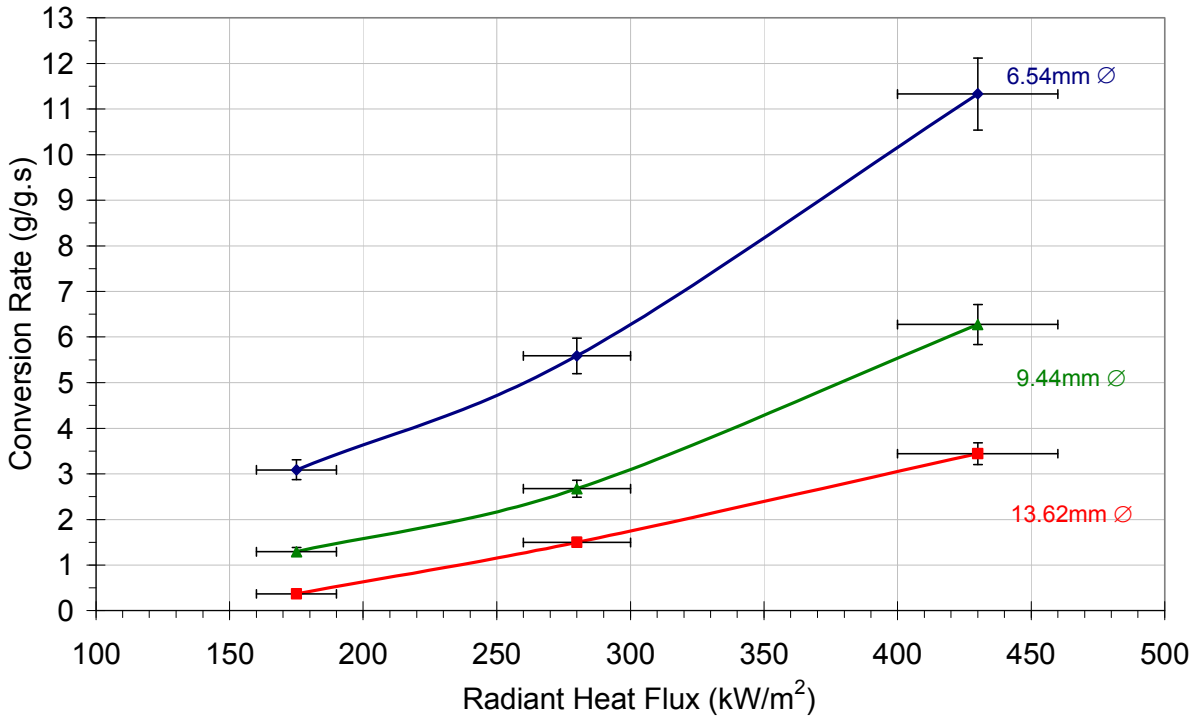

Figure 7-6: Calcination rate (dm/dt_{50}) verses radiant heat flux for d_c = 6.54mm, d_c = 9.44mm and d_c = 13.62mm.

A comparison of the calcination rates shows that the 6.54mm stone calcines approximately 1.8 times faster between 175kW/m^2 and 280kW/m^2 and around 2.0 times faster between 280kW/m^2 and 430kW/m^2. The 9.44mm stone calcines approximately 2.1 times faster between 175kW/m^2 and 280kW/m^2 and around 2.4 times faster between 280kW/m^2 and 430kW/m^2. The calcination rate for the 13.62mm stone increases from 4.0 to 2.3 times between 175kW/m^2 and 280kW/m^2 and between 280kW/m^2 and 430kW/m^2 respectively. These values indicate that if larger sized stones are to be used within an industrial solar furnace then the heat flux should be as high as possible to reduce processing time. Although at these higher heat fluxes (430kW/m^2) visible signs of mild hard burning, or sintering, were present on the surface of the 13.62mm marble stone. Figures 7-7 and 7-8 are photos of before and after calcination, using radiation as the sole heating source. The dark brown area was the surface facing the radiation beam. The hard burning is occurring because the higher temperatures required on the illuminated surface to drive the heat through the newly formed CaO to the calcination zone on the other side of the stone. The newly formed CaO layer acts as an insulator. This explanation is confirmed within Table 7-4 which shows that the calcination rate reduces by up to a half (1/2) between the decomposition times dm/dt_{75} and dm/dt_{100}. Additionally on page 147 of Oates (1998), he explains that exposure to very high temperatures or prolonged exposure to high temperatures causes sintering of the surface of the stone, while dissociation is still in progress.

Figure 7-7: Photo of the 13.62mm nominal diameter stone before calcination.

Figure 7-8: Photo of the 13.62mm nominal diameter stone after calcination at 430 kW/m^2.

Figure 7-9 shows a comparison of preheating times for the three nominal diameter Penrice marble samples exposed to radiant heat flux of either 175 kW/m^2, 280 kW/m^2 or 430 kW/m^2. The plots show that the higher the heat flux, the shorter the preheating time. The errors bars for the preheating time use a standard deviation of 10.35% which is the maximum error displayed in Table 7-1.

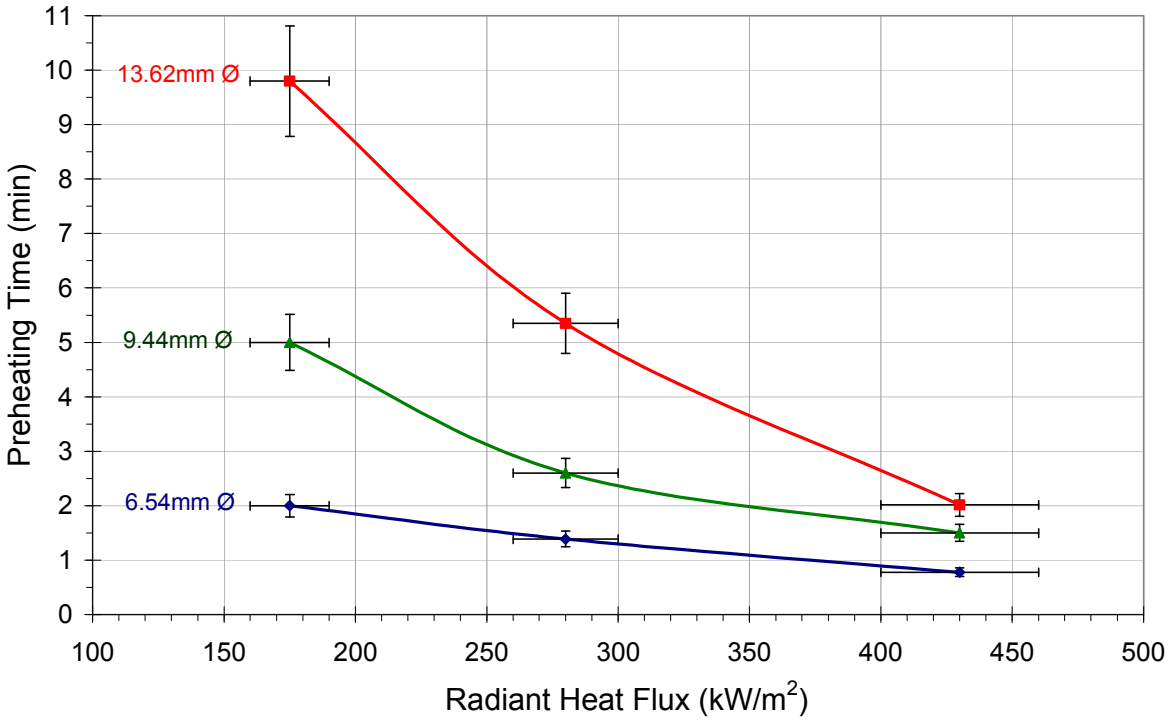

Figure 7-9: Preheat time verses radiant heat flux for d_c = 6.54mm, d_c = 9.44mm, and d_c = 13.62mm calcined at 175±15kW/m^2, 280±20kW/m^2, and 430±30kW/m^2.

The preheating times also increase for increasing stone nominal diameter. This is expected because heat transfer to the stone from the radiant heat flux is through the illuminated surface area of the stone, which is a function of the nominal diameter of the stone. The illuminated surface area was calculated as being the projected area of a sphere with diameter equal to the nominal diameter of each stone. The projected area is calculated using Equation [7.5].

$$A_{\text{Proj}} = \pi\left(\frac{d_C}{2}\right)^2 \qquad [7.5]$$

The calculated illuminated area for each sized stone is shown in Table 10-1. The relationship between the illuminated surface area of the stone and preheat time is shown graphically in Figure 7-10. As shown, the relationship is almost linear indicating the direct relationship between preheat time, heat flux and projected area.

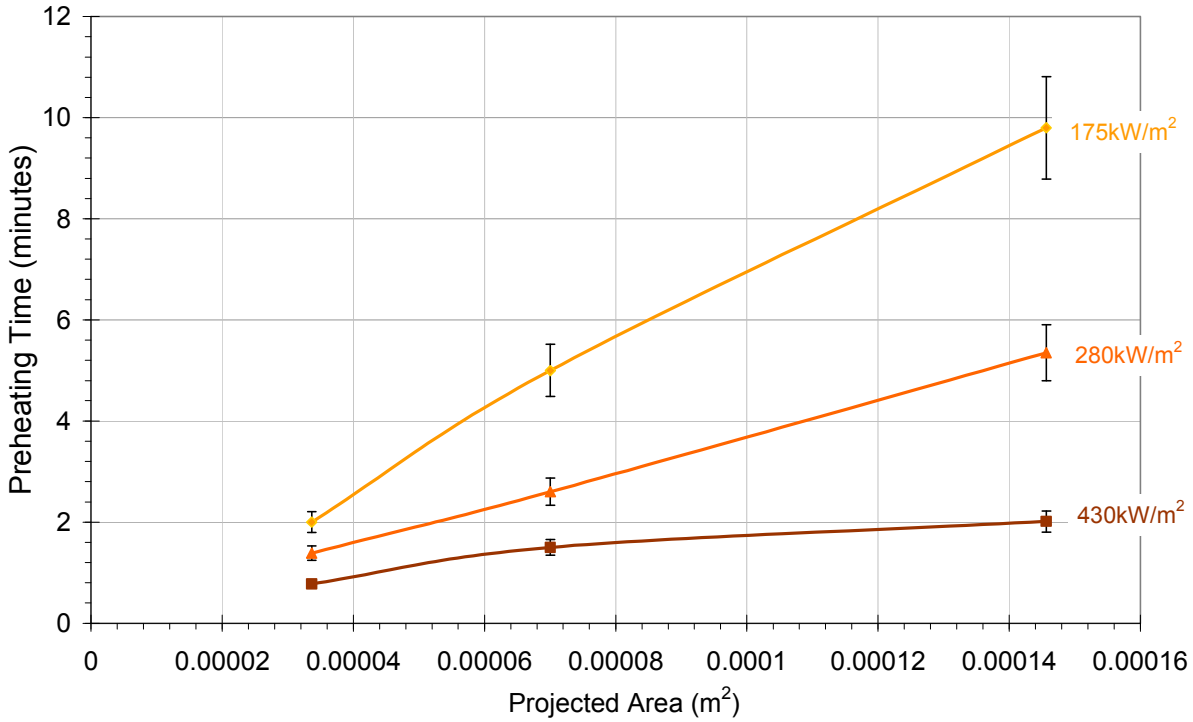

Figure 7-10: Plot showing relationship between the preheat time and projected area, for each stone size exposed to 175±15kW/m^2, 280±20kW/m^2, and 430±30kW/m^2.

Figure 7-11 shows the time to completion against radiant heat flux for the three stone sizes. The calcination time increases with increasing stone size and decreasing radiant heat flux. The 6.54mm stone achieves full calcination between 2.2 to 3.1 times faster than the 9.44mm stone for all heat fluxes. The completion time of the 9.44mm stone between 2.6 to 3.7 times

faster than the 13.62mm stone for all of the heat fluxes. The longest completion time is for the 13.62mm at 175kW/m^2 which completed within approximately 4 hours, which can be considered slow, if compared to a modern rotary kiln processing the same sized material that takes approximately 2.5 hours. Faster conversion rates would be more desirable (economically) for an industrial solar manufacturing plant. It is therefore recommended that the radiant heat flux be greater than 175kW/m^2 to provide calcination rates high enough to achieve full calcination within 4 hours, and conversely radiant heat fluxes less than this should be avoided.

The error bars for the completion time represent the maximum standard deviation of 2.0% of the calcination time which is from column five of Table 7-1.

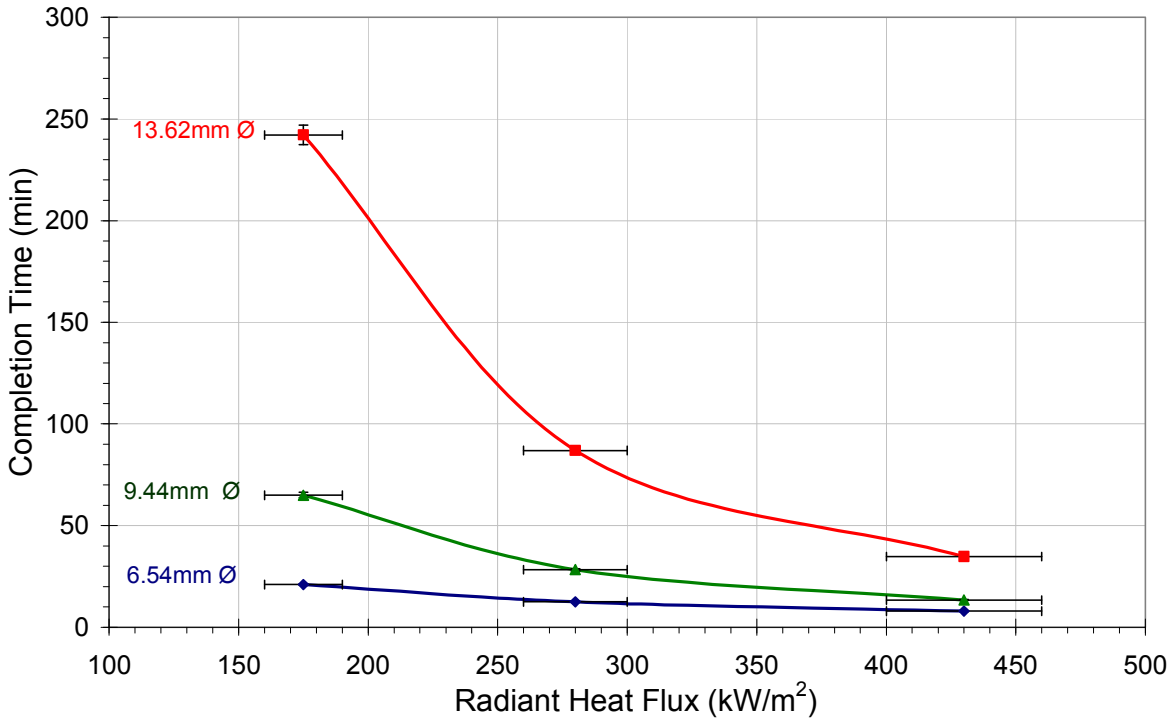

Figure 7-11: Calcination completion time verses radiant heat flux for d_c = 6.54mm, d_c = 9.44mm, and d_c = 13.62mm exposed to 175±15kW/m^2, 280±20kW/m^2, and 430±30kW/m^2 in the open solar system.

7.5 Comparison of Results from Muffle Furnace Calcination and Open System Radiation Calcination Experiments

Figure 7-12 shows a comparison between calcination rates, dm/dt_{50}, for the open system radiation calcination measurements for heat fluxes of 175 kW/m^2, 280 kW/m^2 and 430 kW/m^2 and the muffle furnace calcination experiments conducted at 900°C and 1000°C for Penrice marble with nominal diameter of 6.54mm, 9.44mm and 13.62mm. The calcination rates for

the 430 kw/m^2 and 1000°C are very similar for the smallest stone size and are within 13% of each other for the other two stone sizes. The data for the 900°C muffle furnace experiments lay between the results from the 280 kW/m^2 and 175 kW/m^2 but slightly closer to the 280 kW/m^2 plot. The difference being a maximum of 27% for the smallest sized stone 280 kW/m^2.

It is interesting to note that the 13.62mm marble calcined at 1000°C within the muffle furnace did not experience the same kind of surface burning as was identified when calcining it using radiation at it 430 kW/m^2. This difference is because the stone exposed to the radiation is not being heated uniformly over its entire surface. If the stone was turned (or rotated, like in a rotary kiln) during its exposure to these high heat fluxes it is speculated that it would calcine faster due to the more uniform heating, and also not become surface burnt.

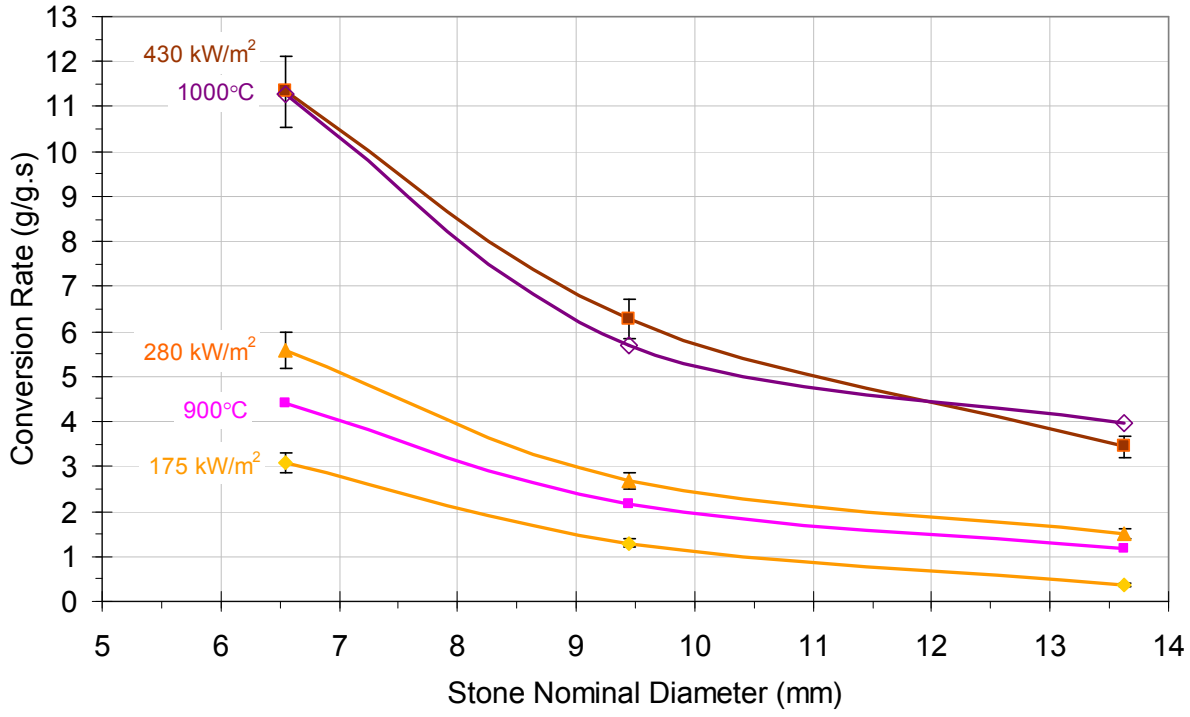

Figure 7-12: Comparison between open solar system and muffle furnace measurements of calcination rate for d_c = 6.54mm, d_c = 9.44mm, and d_c = 13.62mm.

7.6 Conclusions from Open System Radiation Calcination Measurements

These open system calcination experiments using radiation as the sole heat source have shown that the rate of calcination increases with an increase in radiant heat flux and also with a decrease in stone diameter. The decomposition rates, preheating time (t_{cp}) and time to complete calcination (t_{100}) which were measured within these experiments are used for

comparison with values calculated using the modified shrinking core model presented in Chapter 10.

This chapter has identified the following:

- The 13.62mm nominal diameter marble calcined using a heat flux of 430 $\pm$ 30 kW/m^2 showed signs of hard burning on the surface facing the high intensity radiation.
- The 13.62mm nominal diameter marble calcined using a heat flux of 175 $\pm$ 10 kW/m^2 takes approximately 4 hours to complete calcination, which would be considered too long for an industrial solar lime manufacturing plant.
- The preheating time of the stone is directly proportional to the surface area of the stone which is illuminated and intensity of the heat flux to which it is exposed.
- The reaction rate is dependent on the available energy, and to some extent independent of the stone size for heat fluxes less than 430 kW/m^2.

A direct comparison between these open system radiation experiments and the muffle furnace test have shown that the calcination rates for all three stone sizes is similar between the 280 kW/m^2 and 900°C experiments. There is virtually no difference in the calcination rates for the 6.54mm nominal diameter stone when comparing the results from the 430 kW/m^2 radiation experiments and the 1000°C muffle furnace experiments. The results from the other two stone sizes for the same comparison are within 13% of each other.

These measurements significantly add to the knowledge base for the calcination of Penrice Angaston marble. These open system experiments have quantified the effects of radiant heat flux and marble diameter (and mass) on the rate of calcination. These experiments also provide base calcination rates for the calcination of Penrice marble using radiation as the sole heating source. The next Chapter presents experimental results of calcination experiments on single Penrice marble stone placed within a furnace enclosure.

Chapter 8

Calcination of Penrice Marble within an Enclosed Solar Furnace.

8.1 Introduction

These experiments quantify the benefits of using a furnace enclosure when calcining Penrice marble using radiation as the sole heating source. The measurements follow directly from the open system experiments presented in Chapter 7.

The decomposition rates, the preheating time (t_{cp}) and time to complete calcination (t_{100}) were measured for the 6.54mm, 9.44mm and 13.62mm nominal diameter (d_c) single stone samples of Penrice marble placed within the radiation furnace enclosure. Comparisons are made between the results from these experiments, the results from the muffle furnace experiments (from Chapter 6) and results from the open system experiments presented in Chapter 7. Additionally, they were used for validation of the calcination modelling presented in Chapter 10. The heat flux illuminating the stone was measured within each experiment and was used for validation of the furnace modelling which is presented in Chapter 9.

The zero dimensional studies of solar lime furnaces within Chapter 3 identified that the right angled triangular furnace showed the highest efficiency of the different furnace shapes investigated. The modelling indicated that the floor area should be as large as possible to maximise the limestone's exposure to the radiation, while minimising the height of the vertical walls and size of the roof to minimise the unused kiln surface area, therefore reducing the structural heat losses. A small scale solar furnace with a triangular cross section was therefore constructed and used for the Penrice marble calcination experiments within this research.

The use of a triangular shaped furnace is uncommon because of the structural and practical complexities of a flat, sloped roof. A review of literature did reveal two examples of furnaces with large flat sloping roofs, both are used for the heating of steel (Thring, 1962, pg23 and Correia, 2001, pg90). No literature on the use of triangular shaped kilns for lime manufacture or for solar applications was found. These experiments are therefore unique in the use of such a furnace.

8.2 Experimental Methodology

8.2.1 Experimental Apparatus

The experimental equipment used within these experiments includes the 5 kW xenon short arc lamp, the Cinemeccanica - Milano lamphouse, the scaled furnace enclosure, the calcination platform and the analytical balance. The specifications for this equipment are detailed in Chapter 4.

8.2.2 Single Stone Calcination Experiments

The furnace enclosure radiation experiments involved placing a single marble sample onto the ceramic fibre refractory board of the calcination platform, closing the furnace by replacing the rear wall and measuring the weight loss of the stone over time. The xenon lamp, furnace enclosure and calcination platform were preheated for a minimum 90 minutes prior to placing the stone onto the calcination platform within the furnace.

The mass of the marble samples used within the solar furnace was 0.333g, 1.000g, and 3.000g which have nominal diameter (d_c) of 6.54mm, 9.44mm and 13.62mm respectively, as displayed in Table 4-6. Two additional stone sizes were investigated, 2.000g (d_c = 11.90mm) and 5.000g (d_c = 16.15mm). These were conducted to provide additional results for comparison and validation of the calcination modelling.

The calcination platform provided a false floor within the furnace, which could be raised or lowered to place the stone at the desired distances, S, from the focal point. Figure 8-1 is a photo of the inside of the scaled solar furnace showing the calcination platform and the location at which the stone samples were placed. It should be recalled that the radiant heat flux intensity on the marble increases with decreasing distance ‘S’ from the focal point, shown in Figure 5-4. The d_c = 6.54mm, d_c = 9.44mm and d_c = 13.62mm stones were placed at distances, i.e. S = 50mm, S = 75mm and S = 100mm, from the radiation beam’s focal point. These distances are the same as were conducted within the open system experiments. The experiments using d_c = 11.90mm and d_c = 16.15mm stones were placed at S = 70mm and S = 60mm respectively.

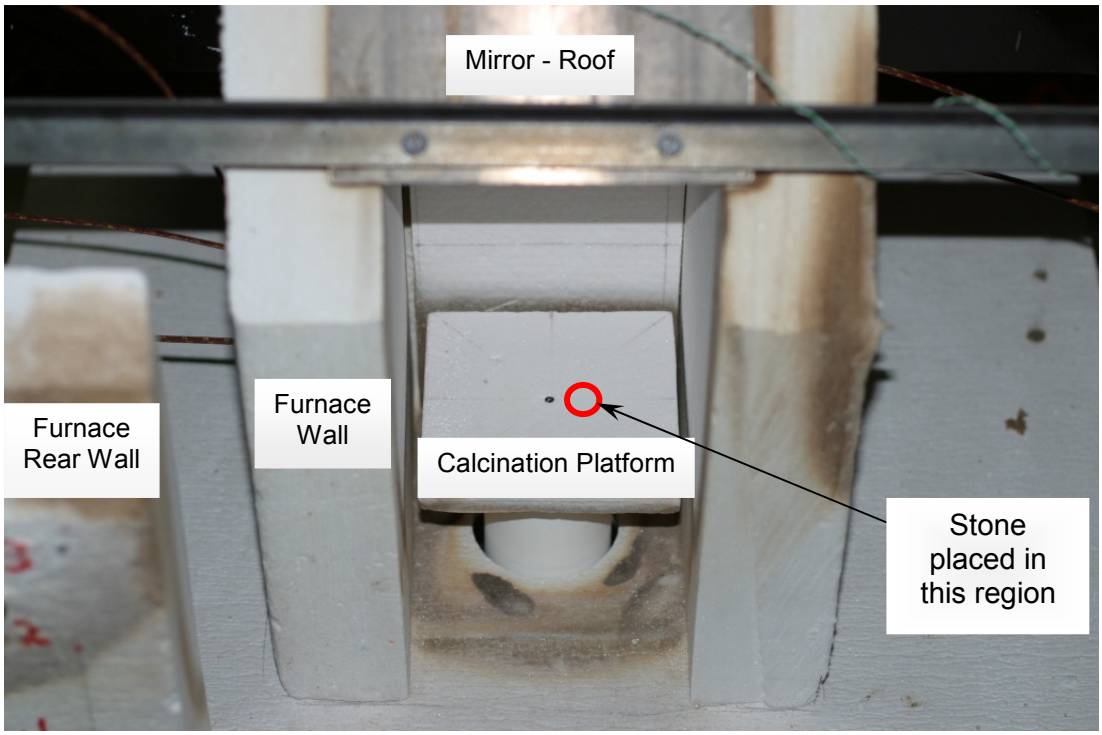

Figure 8-1: Photo of the solar furnace enclosure with the rear wall removed showing the calcination platform on which the marble is placed.

Using the digital image heat flux measurement methods described in Chapter 5, images were taken of the stone immediately after placing it on the preheated platform. Images were also taken of the stone within the hot furnace enclosure immediately after complete calcination. The images were processed and the heat flux to which the stone was exposed, was calculated. It should be noted that the measured heat flux was with the rear wall removed, and thus the measured heat flux on the stone is lower than would be expected with a fully enclosed furnace. Figure 8-2 is the measured heat flux after preheating the solar furnace before placing a stone in location. Images of the 6.54mm, 9.44mm and 13.62mm stone located in the radiation beam at S = 100mm are shown as Figures 8-3 to 8-5 respectively. The latter images show the isorad contours from which the average measured heat flux on each stone was calculated, which is presented in Table 8-1. This average measured heat flux was calculated from the stones projected surface area.

The mass of the calcining marble was measured continually and automatically at 5 second intervals for the duration of the experiment using the GX-600 analytical balance. The mass loss due to calcination of each sample was calculated using Equation [6.1] for each mass measurement.

Table 8-1: Average measured heat flux on the projected surface area of stone at various distance (S) from the focal point.

Distance 'S' from the focal point (mm)	**Average Measured Heat Flux on stone kW/m^2**
100mm	200 ± 15
75mm	300 ± 25
70mm	325 ± 25
60mm	385 ± 25
50mm	450 ± 30

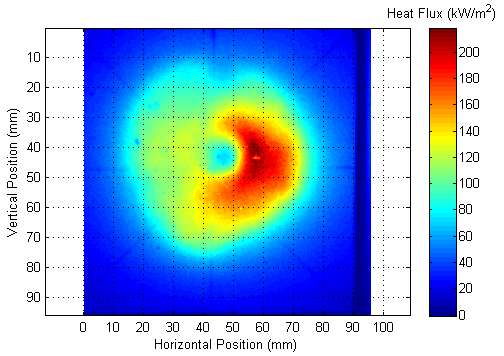

Figure 8-2: Heat flux measurement on the preheated calcination platform prior to marble placement, for S = 100mm.

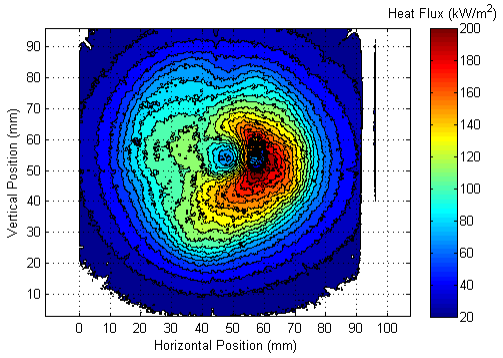

Figure 8-3: Heat flux measurement with isorad contours showing placement of the d_c = 6.54mm (0.333g) Penrice marble within the beam, for S = 100mm.

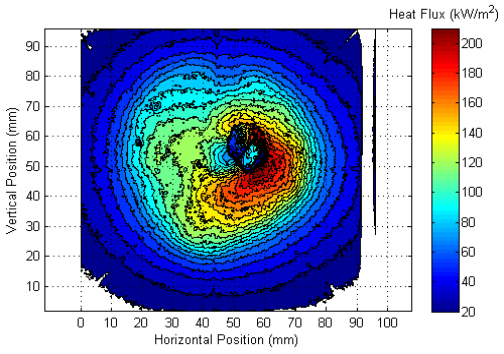

Figure 8-4: Heat flux measurement with isorad contours showing placement of the d_c = 9.44mm (1.000g) Penrice marble within the beam, for S = 100mm.

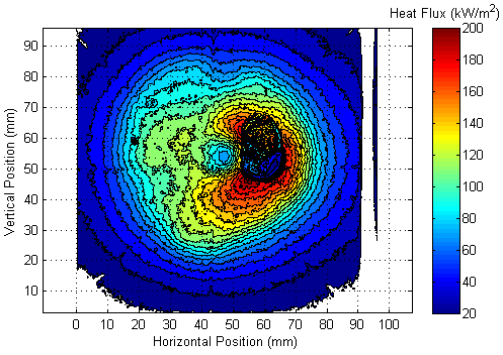

Figure 8-5: Heat flux measurement with isorad contours showing placement of the d_c = 13.62mm (3.000g) Penrice marble within the beam, for S = 100mm.

8.2.3 Measurement Accuracy

The experimental scatter measured within several of the mass loss measurements was assessed within the open furnace experiments as being primarily due to vibration of the analytical balance by the cooling fan for the xenon bulb. This was reduced by isolating the balance from the lamphouse although some noise is still present which can be attributed to convective air flow past the calcination platform. The noise was particularly prevalent for the smaller sized marble, e.g. d_c = 6.54mm stone. To display the data within the results plots, the level of noise was reduced by taking the mean over 5 consecutive measurements.

Repeatability within these measurements was tested by calcining 5 of the d_c = 6.54mm Penrice marble placed at S =75mm and S = 50mm positions. The measurement noise was most prevalent when using this sized stone at these distances. The two sets of fractional calcination verse $CaCO_3$ decomposition time are shown as Figures 8-6 and 8-7. Recalling that fractional calcination is the fraction of CO_2 released during calcination divided by the total CO_2 within the sample, as shown within Equation [7.1].

Table 8-2 shows the preheating time, rates of calcination and time to complete calcination for the ten 6.54mm single stones calcined at the two heat fluxes. The preheating time, denoted by t_{cp}, has been calculated as being the time between placing the sample within the radiation beam and the sample reaching a loss of mass equal to 3% of the stones final mass (i.e. m_3).

Three rates of calcination (dm/dt) have been calculated from the slope of the fractional calcination profiles. The three rates denoted by dm/dt_{50}, dm/dt_{75}, and dm/dt_{100}, are the change of mass over time of the marble sample. These rates are specified within Equations [7.2], [7.3] and [7.3]:

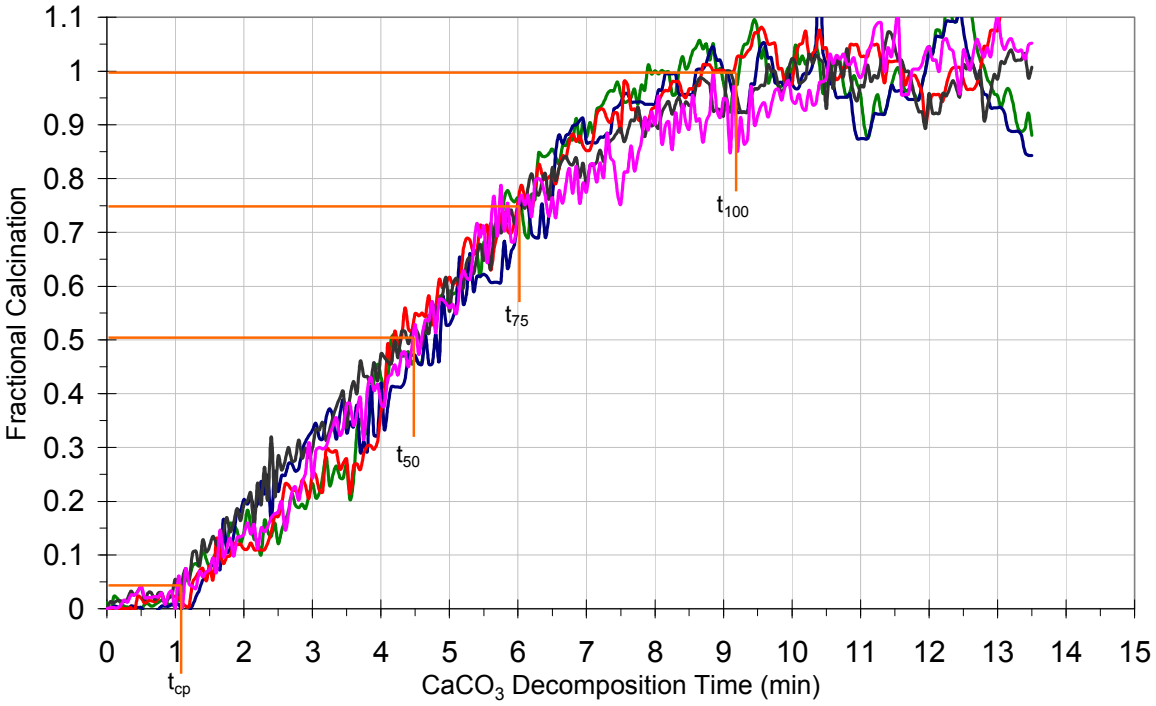

Figure 8-6: Calcination profiles of five single d_c = 6.54mm Penrice marble stones exposed to a radiant heat flux of 300±25 kW/m^2 at S = 75mm in the enclosed solar furnace.

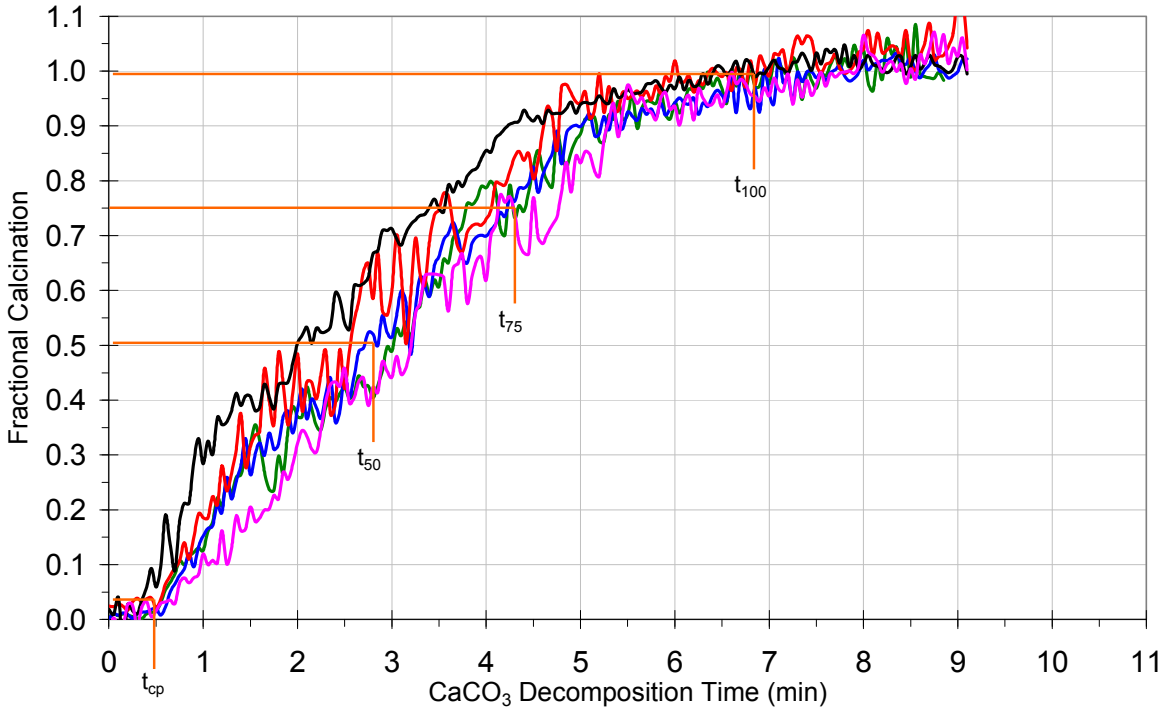

Figure 8-7: Calcination profiles of five single d_c = 6.54mm Penrice marble stones exposed to a radiant heat flux of 450±30 kW/m^2 at S = 50mm in the enclosed solar furnace.

Table 8-2: Comparison of preheating time, calcination rate and time to complete calcination for d_c = 6.54mm Penrice marble exposed to either 300±25kW/m^2 or 450±30 kW/m^2.

Stone Number	Preheating time t_{cp} (minutes)	Rate of Calcination for dm/dt_{50} (g/g.s)	Rate of Calcination for dm/dt_{75} (g/g.s)	Rate of Calcination for dm/dt_{100} (g/g.s)	Time to Complete Calcination t_{100} (minutes)
Radiant Heat Flux of 300±25 kW/m^2					
1	1	9.490	9.476	8.421	8.1
2	1.25	8.517	8.783	7.639	9.0
3	1.2	10.232	9.395	7.518	9.15
4	0.9	8.180	7.839	7.523	8.65
5	1.1	8.674	9.078	6.613	9.9
Mean	**1.1**	**9.019**	**8.914**	**7.543**	**9.0**
Standard Deviation %	14.86	9.22	7.41	8.50	7.40
Radiant Heat Flux of 450±30 kW/m^2					
1	0.25	11.387	12.141	10.137	5.9
2	0.55	13.591	12.071	9.298	6.6
3	0.5	14.459	12.238	10.874	5.5
4	0.3	17.439	13.535	9.753	6.2
5	0.5	10.726	11.322	8.797	6.8
Mean	**0.4**	**13.520**	**12.261**	**9.772**	**6.2**
Standard Deviation %	31.57	19.78	6.52	8.13	8.09

The mean value, shown in Table 8-2, was calculated using the data from the five samples. The standard deviation was then calculated which has been displayed as the percentage of the mean value. The standard deviation is used to calculate the error bars presented later in the analysis of the calcination results.

8.3 Results

Figures 8-8 to 8-10 show the fractional calcination profiles for single marble stone with nominal diameter of 6.54mm, 9.44mm and 13.62mm, placed at 100mm, 75mm, and 50mm from the focal point. Figure 8-11 shows the calcination profile for the 11.90mm nominal diameter (2.000 gram) marble located at S = 70mm from the focal point. Figure 8-12 shows

the calcination profile for the 13.62mm and 16.15mm nominal diameter marble located at S = 60mm from the focal point.

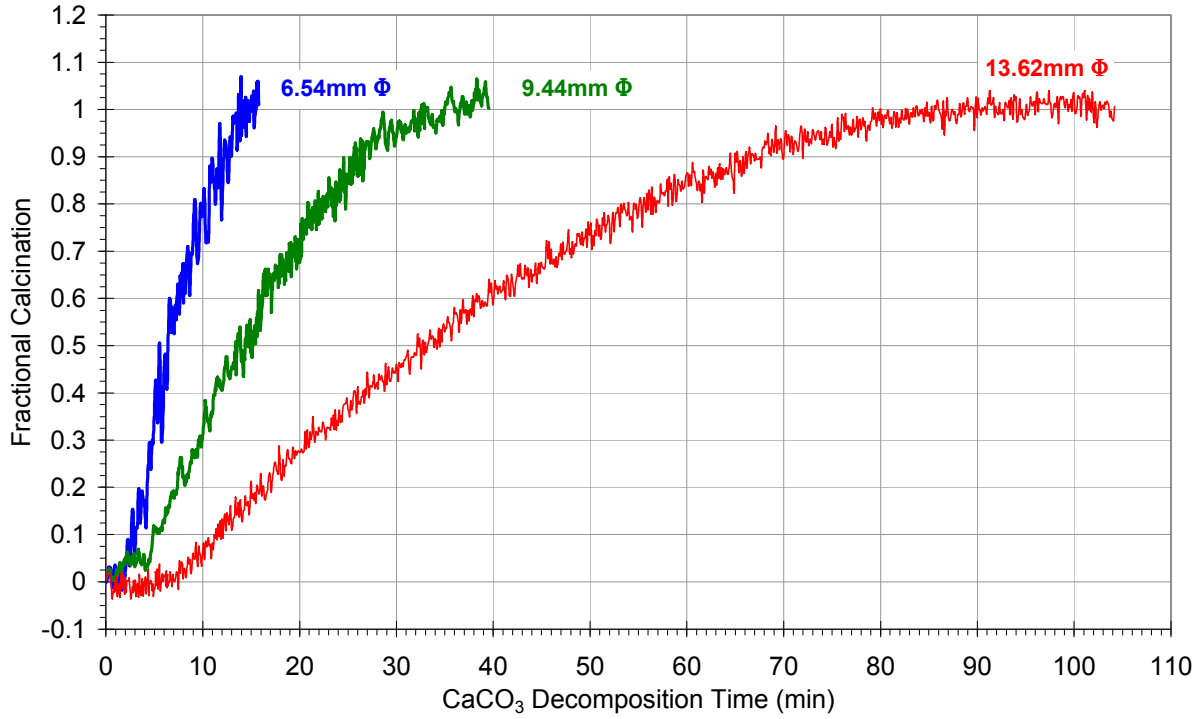

Figure 8-8: Calcination profiles of single Penrice marble stones placed at S = 100mm and exposed to a radiant heat flux of 200±15 kW/m^2 in the enclosed solar furnace.

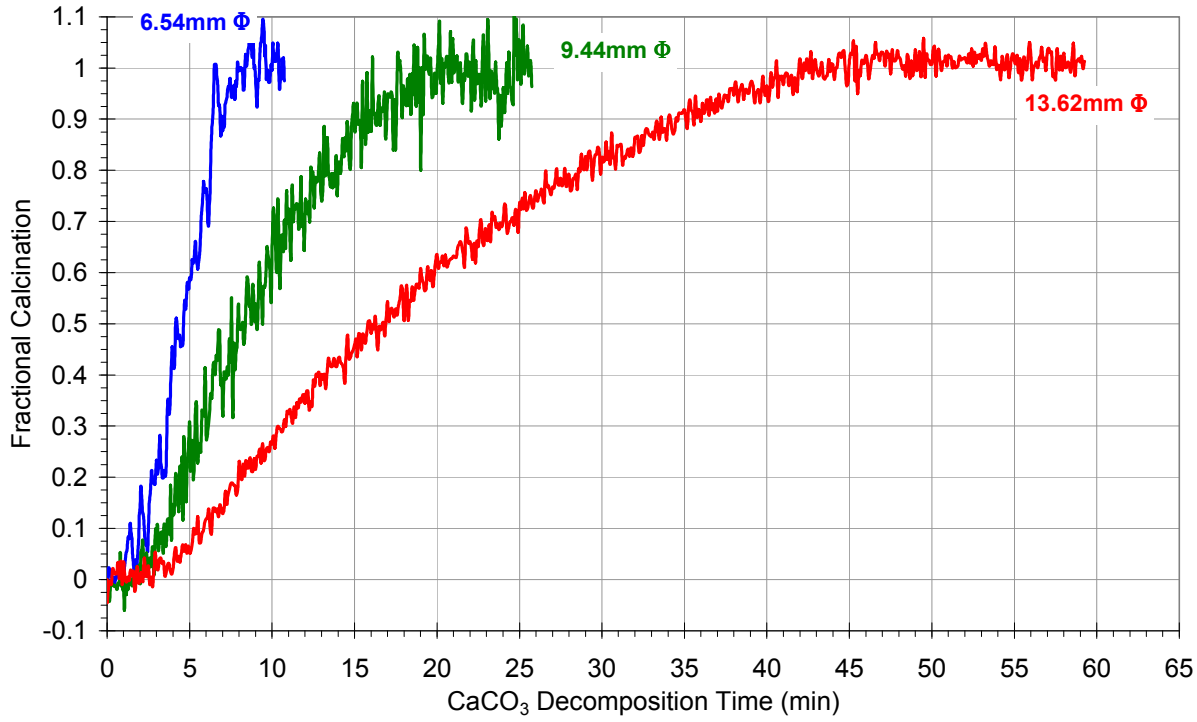

Figure 8-9: Calcination profiles of single Penrice marble stones placed at S = 75mm and exposed to a radiant heat flux of 300±25 kW/m^2 in the enclosed solar furnace.

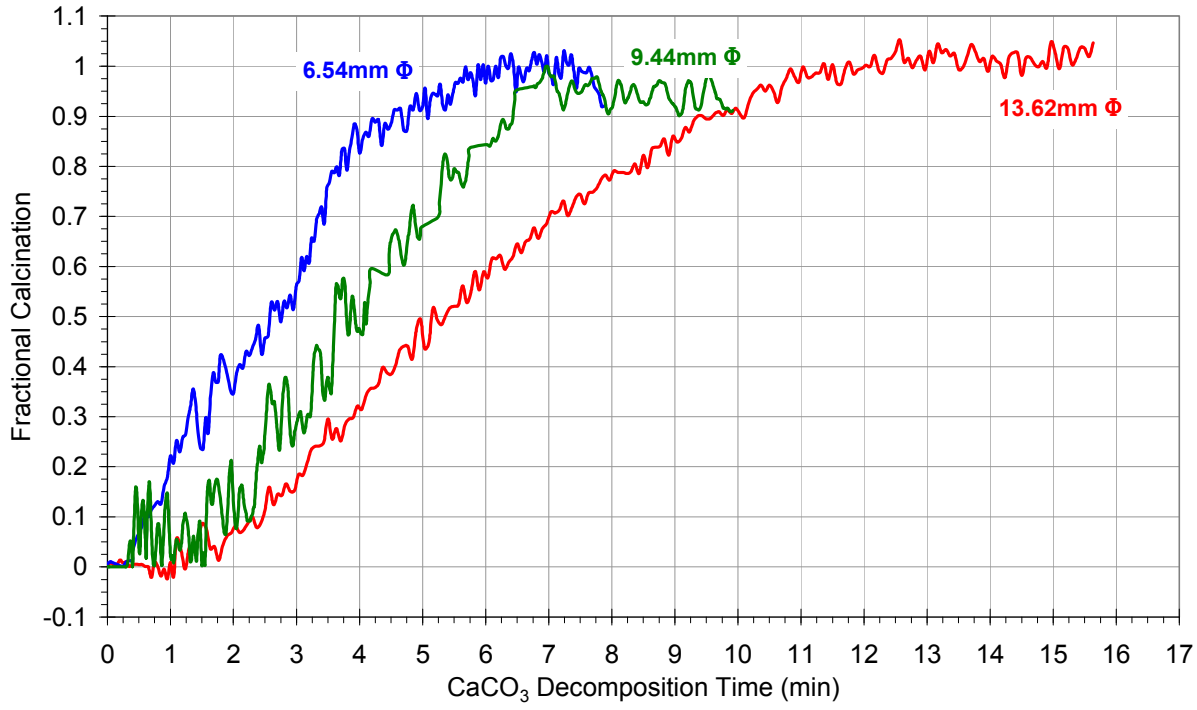

Figure 8-10: Calcination profiles of single Penrice marble stones placed at S = 50mm and exposed to a radiant heat flux of 450±30 kW/m^2 in the enclosed solar furnace.

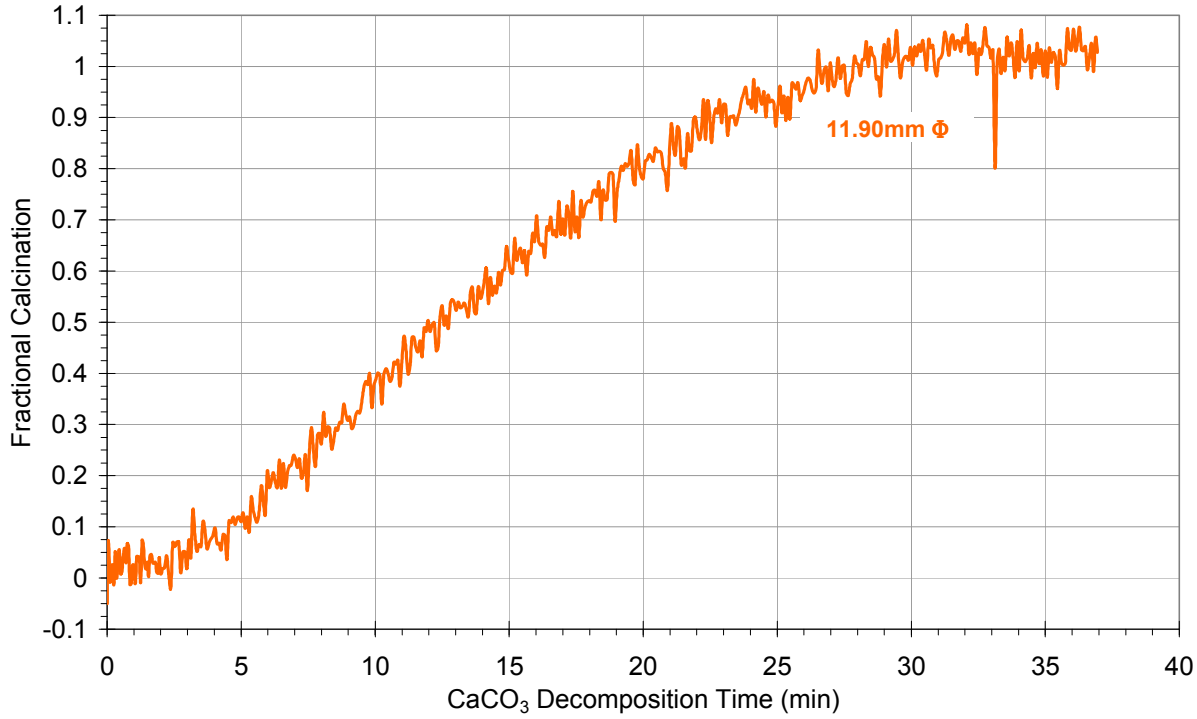

Figure 8-11: Calcination profile for d_c =11.90mm (2.000 gram) single Penrice marble stones placed at S = 70mm and exposed to a radiant heat flux of 325±25 kW/m^2 in the enclosed solar furnace.

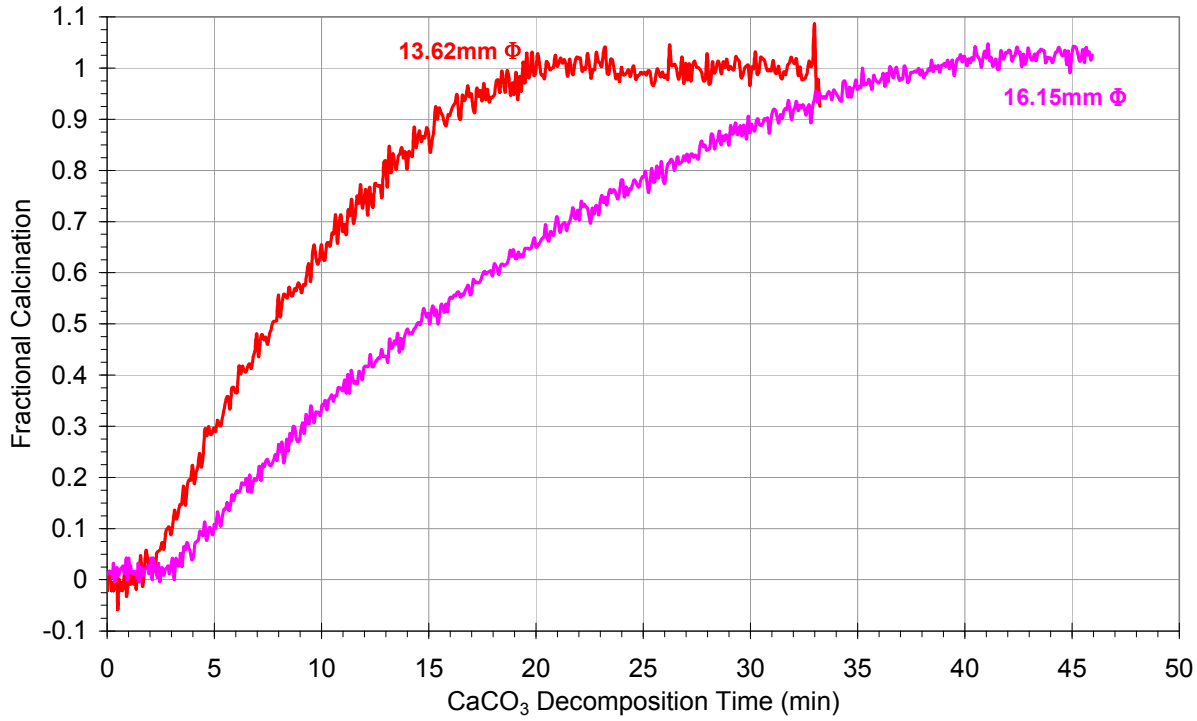

Figure 8-12: Calcination profiles for d_c =13.62mm (3.000 gram) and d_c =16.15mm (5.000 gram) single Penrice marble stones placed at S = 60mm and exposed to a radiant heat flux of 385±25 kW/m^2 in the enclosed solar furnace.

Tables 8-3 to 8-6 show the rate of calcination (dm/dt) calculated from the slope of the calcination profiles shown in Figures 8-8 to 8-12. Three rates are given, the first being the change of mass over time for the first 50% of decomposition, i.e., for dm/dt from 0 to 50% represented by dm/dt_{50}, the change of mass over time for up to 75% of decomposition, i.e. dm/dt from 0 to 75% represented by dm/dt_{75} and the change of mass over time to completion i.e. dm/dt from 0 to 100%, represented by dm/dt_{100}. Also shown are the stones preheating time t_{cp}, which is the time between placing the stone within the radiation and the beginning of calcination, and the time to complete calcination t_{100}, which is the time between the beginning of calcination and reaching an asymptotic completion value.

Table 8-3: Preheating time, calcination rate and time to complete calcination for single Penrice marble exposed to a radiant heat flux of 200±15kW/m^2 in an enclosed solar furnace.

Marble Nominal Diameter d_C (mm)	Preheating time t_{cp} (minutes)	Rate of Calcination for dm/dt_{50} (g/g.s)	Rate of Calcination for dm/dt_{75} (g/g.s)	Rate of Calcination for dm/dt_{100} (g/g.s)	Time to Complete Calcination t_{100} (minutes)	CO_2 release rate $mgCO_2$ / sec
6.54	1.7	6.147	6.033	4.681	13.4	0.183
9.44	3.2	2.460	2.418	1.879	30.7	0.239
13.62	6.9	1.117	1.007	0.711	83.3	0.264

Table 8-4: Preheating time, calcination rate and time to complete calcination for single Penrice marble exposed to a radiant heat flux of 300±25kW/m^2 in an enclosed solar furnace.

Marble Nominal Diameter d_C (mm)	Preheating time t_{cp} (minutes)	Rate of Calcination for dm/dt_{50} (g/g.s)	Rate of Calcination for dm/dt_{75} (g/g.s)	Rate of Calcination for dm/dt_{100} (g/g.s)	Time to Complete Calcination t_{100} (minutes)	CO_2 release rate $mgCO_2$ / sec
6.54	1.1	9.019	8.914	7.543	7.9	0.311
9.44	1.9	4.567	4.011	3.618	16.9	0.433
13.62	2.8	2.113	1.919	1.379	42.8	0.515

Table 8-5: Preheating time, calcination rate and time to complete calcination for single Penrice marble exposed to a radiant heat flux of 450±30kW/m^2 in an enclosed solar furnace.

Marble Nominal Diameter d_C (mm)	Preheating time t_{cp} (minutes)	Rate of Calcination for dm/dt_{50} (g/g.s)	Rate of Calcination for dm/dt_{75} (g/g.s)	Rate of Calcination for dm/dt_{100} (g/g.s)	Time to Complete Calcination t_{100} (minutes)	CO_2 release rate $mgCO_2$ / sec
6.54	0.4	13.520	12.261	9.772	5.6	0.435
9.44	0.65	9.843	9.905	8.290	6.9	1.071
13.62	1.1	6.275	6.316	5.082	11.3	1.941

Table 8-6: Preheating time, calcination rate and time to complete calcination for 11.90mm (2.000g) Penrice marble exposed to a radiant heat flux of 325±25kW/m^2 in an enclosed solar furnace.

Marble Nominal Diameter d_C (mm)	Preheating time t_{cp} (minutes)	Rate of Calcination for dm/dt_{50} (g/g.s)	Rate of Calcination for dm/dt_{75} (g/g.s)	Rate of Calcination for dm/dt_{100} (g/g.s)	Time to Complete Calcination t_{100} (minutes)	CO_2 release rate $mgCO_2$ / sec
11.90	2.0	2.993	2.637	2.228	26.9	0.545

Table 8-7: Preheating time, calcination rate and time to complete calcination for single Penrice marble exposed to a radiant heat flux of 385±25kW/m^2 in an enclosed solar furnace.

Marble Nominal Diameter d_C (mm)	Preheating time t_{cp} (minutes)	Rate of Calcination for dm/dt_{50} (g/g.s)	Rate of Calcination for dm/dt_{75} (g/g.s)	Rate of Calcination for dm/dt_{100} (g/g.s)	Time to Complete Calcination t_{100} (minutes)	CO_2 release rate $mgCO_2$ / sec
13.62	1.4	4.705	4.271	2.711	21.9	1.004
16.15	2.9	2.5362	2.1632	1.6684	35.7	1.027

Table 8-8 shows a summary of the measured temperatures on the internal surface on the furnace walls at the eight permanent thermocouple positions displayed in Figure 4-15. The table shows the values measured when the calcination platform is positioned 100mm, 75mm, 70mm, 60mm and 50mm from the focal point and therefore exposed to radiant heat fluxes of 200±15kW/m^2, 300±25kW/m^2, 325±25kW/m^2, 385±25kW/m^2 and 450±30kW/m^2 respectively. The technique used for these temperature measurements is described in Chapter 4, Section 4.7.1. The full set of measured temperatures for both the internal and external wall surfaces are displayed in Appendix E.

Table 8-8: Summary of measured wall temperatures on the internal surface of the solar furnace at the permanent thermocouple locations presented in Figure 4-15 when the calcination platform is positioned at S = 100mm, S = 75mm, S = 70mm, S = 60mm and S = 50mm from the focal point and therefore exposed to radiant heat fluxes of 200±15kW/m^2, 300±25kW/m^2, 325±25kW/m^2, 385±25kW/m^2 and 450±30kW/m^2 respectively.

Thermocouple Position	Distance (S) between Focal Point and Calcination Platform (mm)				
	100	**75**	**70**	**60**	**50**
2A	407	412	417	428	462
3A	379	388	392	401	417
6A	378	387	385	392	413
3B	381	387	394	403	419
7B	372	382	389	392	414
9B	291	296	298	299	321
2C	410	415	418	432	460
2D	406	413	417	430	467

8.4 Analysis of Results

The three calcination profile plots, Figures 8-8 to 8-10, show the calcination plots for the 6.54mm, 9.44mm and 13.62mm nominal diameter marble located at S = 100mm, S = 75mm and S = 50mm. All three plots show a decrease in calcination time with decreasing stone size, as expected. This is reflected in the completion times displayed within Tables 8-3 to 8-7. Figures 8-11 and 8-12 show the calcinations plots for the 11.90mm (2.000g) and 13.62mm (3.000g) and 16.15mm (5.000g) nominal diameter marble located at S = 70mm, and S = 60mm. The trends for these stones show an increase in calcination time with increasing stone size, which is the same trend as for the smaller sized stones.

A comparison of the completion times for all stone sizes show a decrease in completion time for increasing radiant heat flux, which is displayed graphically in Figure 8-13. Also shown is the decrease in completion time with decreasing stone diameter. The errors bars were calculated for each data point using the standard deviation data presented in Table 8-2.

Comparing the completion times shown in Figure 8-13 indicates that the completion time is a function of the mass of the stone sample, i.e. there is (almost) a tripling of the completion times as the mass of the stone is tripled.

These completion times are good and compare nicely with a modern rotary kiln processing the same sized material. The longest completion time is for the 13.62mm at 200kW/m^2 which completed within approximately 83 minutes.

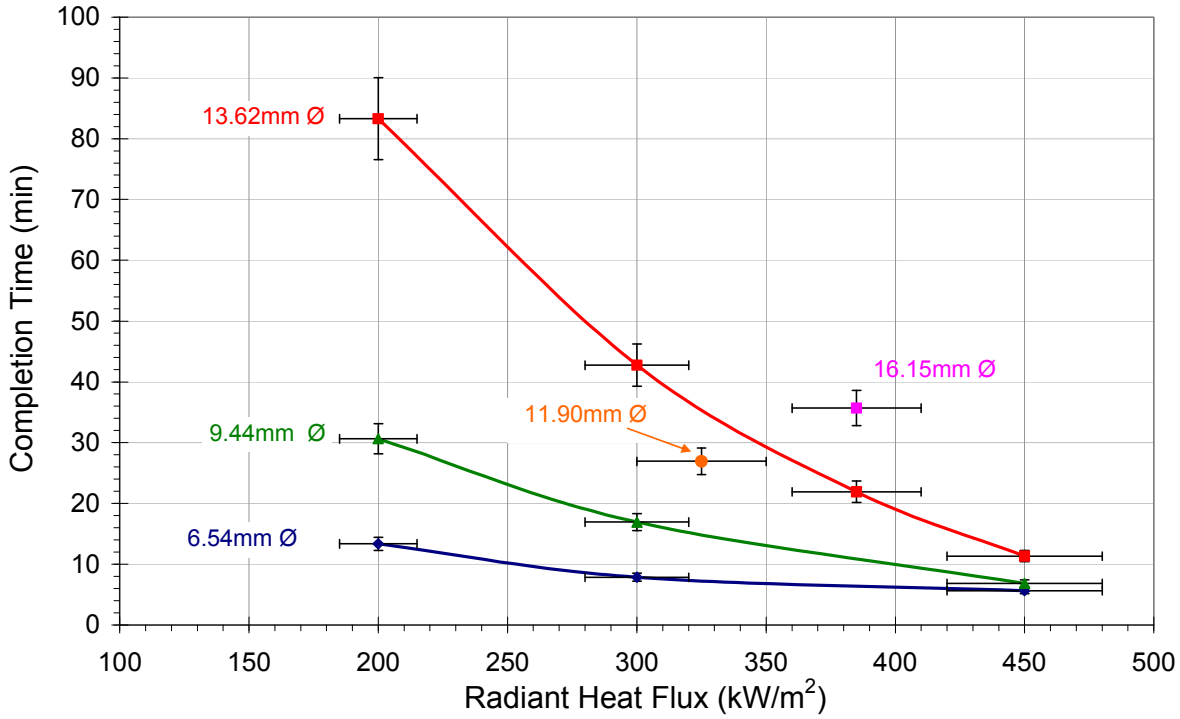

Figure 8-13: Completion time verses radiant heat flux for d_c = 6.54mm, d_c = 9.44mm, d_c = 11.90mm, d_c = 13.62mm and d_c = 16.15mm Penrice marble calcined in the enclosed solar furnace.

Table 8-3 shows a slight increase in the release rates of CO_2 from the three sized stones exposed to the same heat flux. Tables 8-4 and 8-5 a more pronounced increase in release rate of CO_2 for increasing stone size. If the CO_2 release rates were the same, it would indicate that the calcination time for any sized stone could be calculated solely from knowing the heat flux to which it is exposed. Unfortunately the release rate of CO_2 varies between stones because of minor differences in composition of the stone and that the rate of calcination is limited by a combination of heat transfer, mass transfer or chemical reaction.

Tables 8-3 to 8-7 show a decrease in preheating time t_{cp} with decreasing stone size, but for increasing heat flux, which is shown graphically in Figure 8-14.

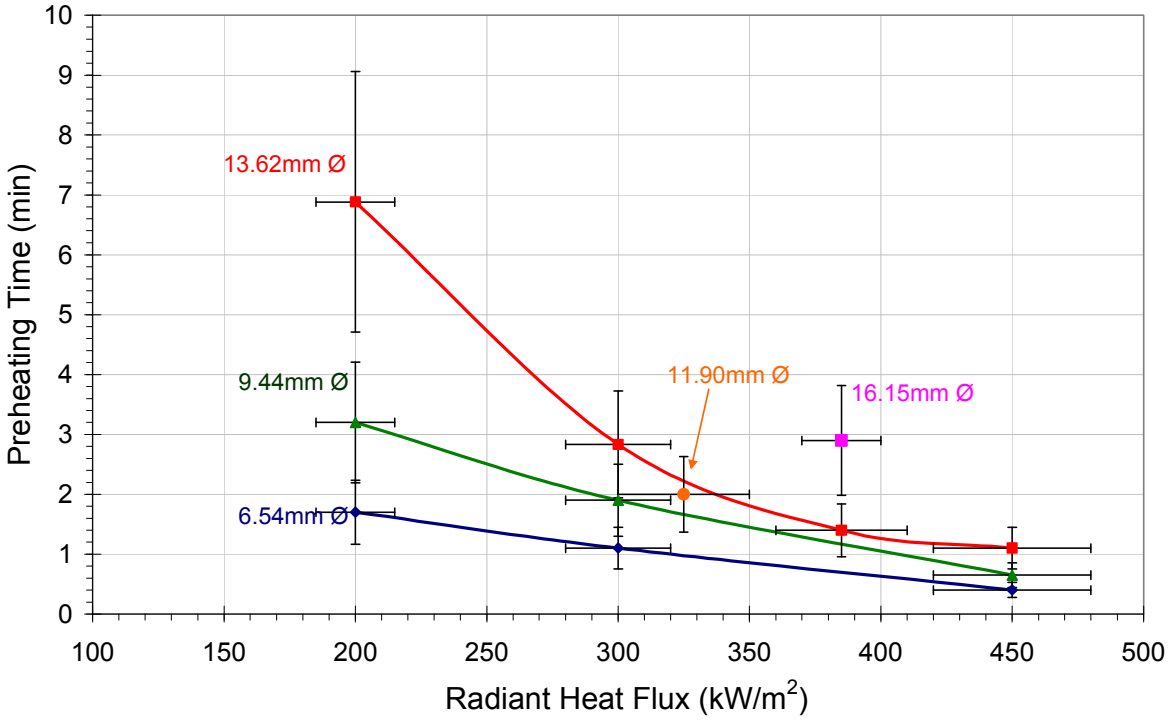

Figure 8-14: Preheat time verses radiant heat flux for d_c = 6.54mm, d_c = 9.44mm, d_c = 11.90mm, d_c = 13.62mm and d_c = 16.15mm Penrice marble in the enclosed solar furnace.

A comparison between preheating time and illuminated surface area for the three heat fluxes 200kW/m^2, 300kW/m^2 and 450kW/m^2 is shown in Figure 8-15. As can be seen, there is a linear relationship between preheating time and the illumination area. This reaffirms the discussion presented in Chapter 7 about the direct linear relationship between preheat time, heat flux and stone illumination area. The illumination area for this case has been calculated using Equation [8.1] which assumes the illuminated area is 2/3 of the total surface area of a sphere with nominal diameter the same as each stone size.

$$A_{\text{illum}} = \frac{8}{3}\pi\left(\frac{d_C}{2}\right)^2 \qquad [8.1]$$

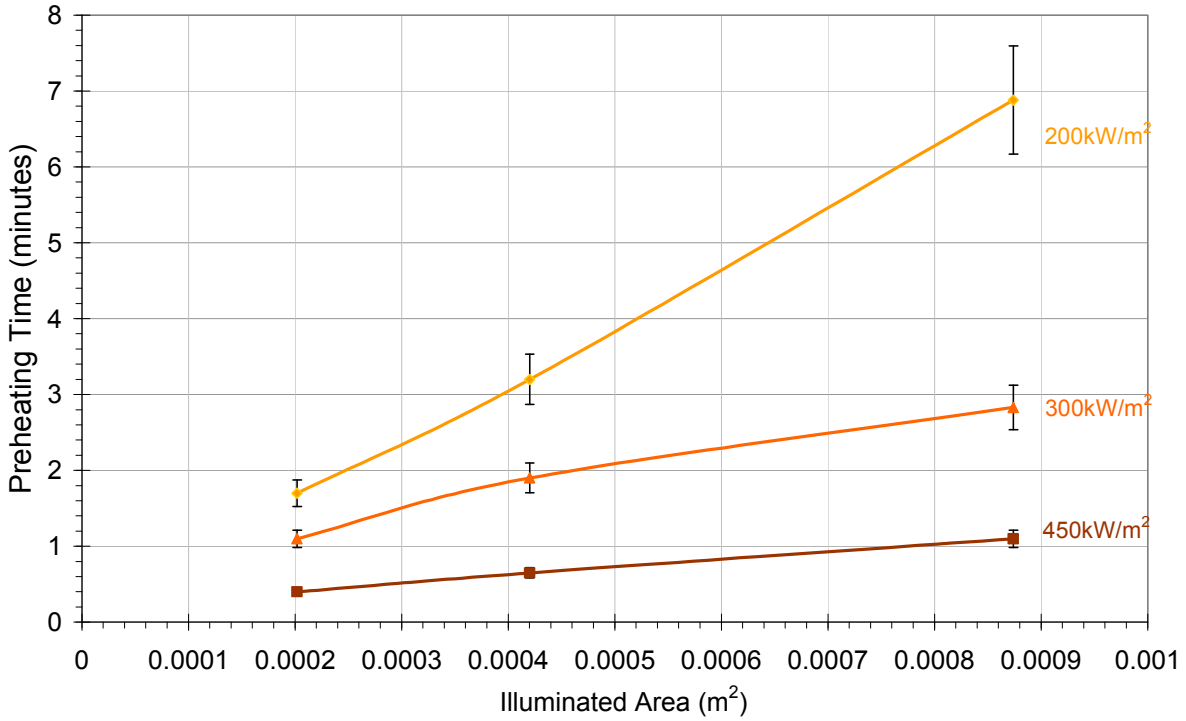

Figure 8-15: Plot showing relationship between the preheat time and illuminated surface area, for each stone size exposed to 200±15kW/m^2,300±25kW/m^2, and 450±30kW/m^2.

A comparison of the calcination rates from Tables 8-3 to 8-7 show an increase in rate for increasing radiant heat flux. The rate also increases for decreasing stone size as displayed graphically in Figure 8-16.

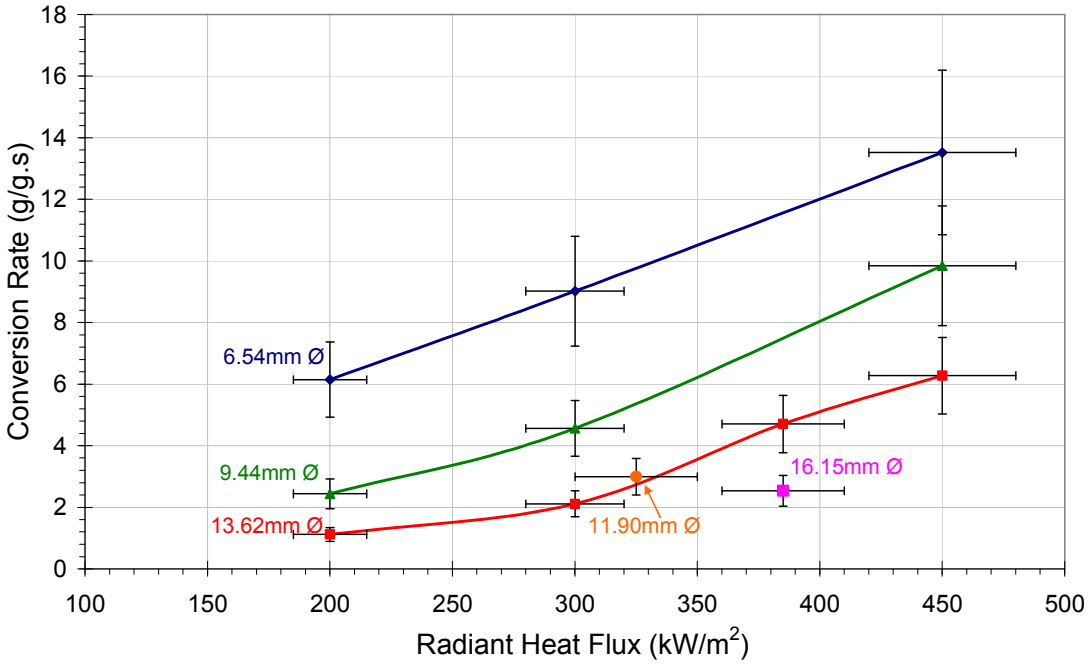

Figure 8-16: Calcination rate (dm/dt_{50}) verses radiant heat flux for d_c = 6.54mm, d_c = 9.44mm, d_c = 11.90mm, d_c = 13.62mm and d_c = 16.15mm Penrice marble calcined within the solar furnace.

Comparing the calcination rates shown in Figure 8-16, the rate for the 6.54mm stone is approximately 185% faster than for the 13.62mm nominal diameter stone for calcination time dm/dt_{50} when exposed to the same heat flux. Comparing the rates for the same stones at higher heat flux levels, shows that the difference decreases as the heat flux increases, e.g. the 6.54mm is only 62% faster than the 13.62mm when exposed to 450kW/m^2.

The 11.90mm nominal diameter stone calcined 325kW/m^2 shown in Figure 8-16 has a rate of conversion at dm/dt_{50} of approximately 3.00 g/g.s which when compared to the other trends is slightly lower than would be expected. Conversely, the conversion rates of the two stones located at 385$\pm$25kW/m^2 are slightly higher than expected. These discrepancies in data can be attributed to the minor variation in delivered radiant heat flux between experimental days and to variations in placement of the stone within the 'zone' of maximum radiant heat flux. Such factors are all incorporated in the error bars displayed in the figure.

An interesting aspect to note is the lack of mild hard burning or sintering on the surface of the 13.62mm stone calcined at a heat flux of 450kW/m^2. This is in contrast to the open system experiments of the same sized stone located at the same distance, S =100mm, from the focal point. The difference is because of two reasons: 1). the time to complete conversion was significantly quicker (83 minutes) compared to 4 hours for the open system and therefore the stone is heated for less time, and 2). the stone is being heated over more of its surface and thus the transfer of heat during the latter stages of calcination has less impedance from the newly formed CaO and therefore the surface temperature is not as high. These findings are important because they signify that the lime quality can be controlled, which is important for practical systems.

Tables 8-3 to 8-7 show that the calcination rates for dm/dt_{50}, dm/dt_{75} and dm/dt_{100} decrease as the decomposition proceeds through the stone for all three stone sizes and heat fluxes. This is expected because heat transfer to the calcination zone is being restricted as the newly formed CaO layer increases in thickness and therefore leads to insulation of the inner core of the stone.

The fractional calcination verses decomposition time plots (Figures 8-8 to 8-12) show slight overshoot in fractional calcination for almost all stone sizes. This overshoot is a measurement error and can be attributed to vibration of the analytical balance and also measurement inaccuracy due to the convective air flow around the calcination platform. Measurement accuracy and precision is discussed in detail within Section 8.2.3.

Table 8-8 shows the increase in measured internal wall temperature for decreasing distance, S, between the calcination platform and the radiation focal point. These relationships are displayed in Figure 8-17 which also shows three distinct temperature bands which correspond to the temperature measurement distances from the calcination platform. These bands indicate that the wall temperature is hotter closer to the calcination platform and decreases towards the top of the furnace as is expected.

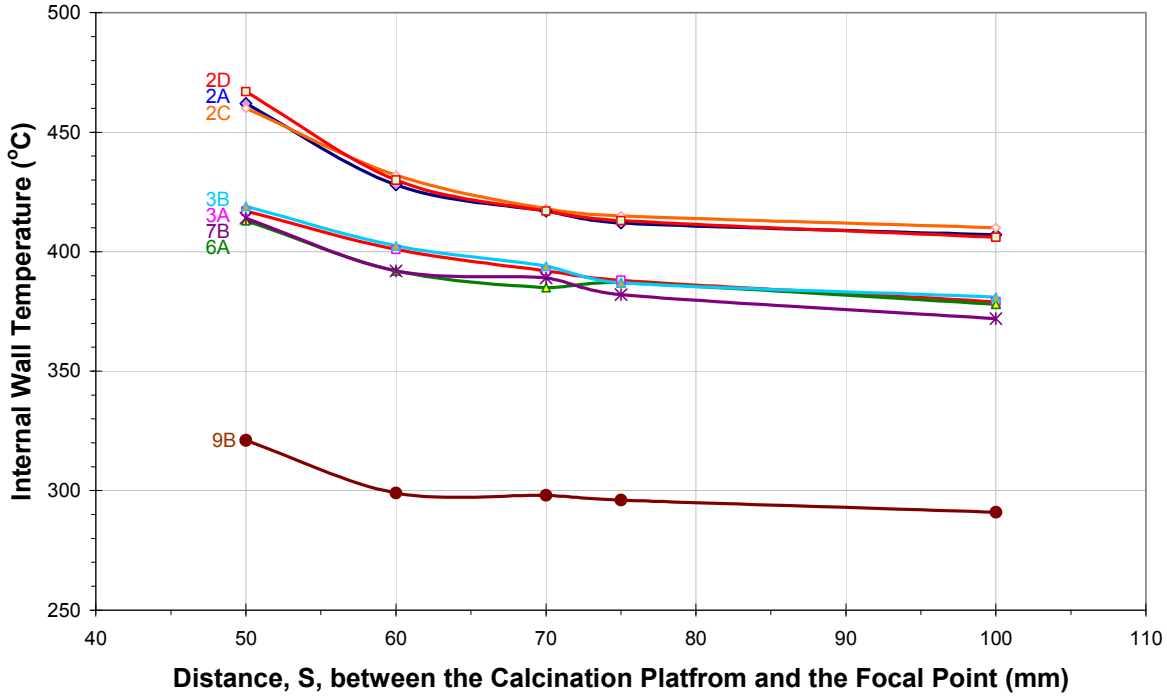

Figure 8-17: Measured wall temperatures on the internal surface of the solar furnace at the thermocouple locations presented in Figure 4-15 when the calcination platform is positioned at S = 100mm, S = 75mm, S = 70mm, S = 60mm and S = 50mm and therefore exposed to radiant heat fluxes of 200±15kW/m^2, 300±25kW/m^2, 325±25kW/m^2, 385±25kW/m^2 and 450±30kW/m^2 respectively.

The measured calcination rates, the preheating time (t_p) and time to complete calcination (t_{100}) are now compared to the measurements from the open system radiation calcination experiments, which were of the same nominal diameter marble located at the same distance, S from the focal point. Comparisons are also made between these results and the muffle furnace results. It should also be remembered that the results are used for validation of the calcination modelling, presented in Chapter 10.

8.5 Comparison of Results from Enclosed Solar Furnace and Open System Calcination Experiments

Figure 8-18 shows a comparison between calcination rates, dm/dt_{50} for the enclosed solar furnace calcination measurements for heat fluxes of 200 kW/m^2, 300 kW/m^2 and 450 kW/m^2, the open system radiation calcination measurements for heat fluxes of 175 kW/m^2, 280 kW/m^2 and 430 kW/m^2 and the muffle furnace calcination experiments conducted at 900°C and 1000°C. The plot shows the calcination rates for Penrice marble with nominal diameter of 6.54mm, 9.44mm and 13.62mm.

The calcination rates for the 450kW/m^2 enclosed solar furnace measurements are the highest of all of the measurements for all stone sizes. The 9.44mm and 13.62mm stone at 450kW/m^2 are the most significant because they show a 57% and 82% increase, respectively, in calcination rate compare to the no furnace / open system. It should be remembered that the stones were placed at the same distance, S, from the focal point for the 430kW/m^2 and 450kW/m^2 measurements. Similarly the same S distance is used for the 280kW/m^2 and 300kW/m^2 measurements and for the 175kW/m^2 and 200kW/m^2 measurements.

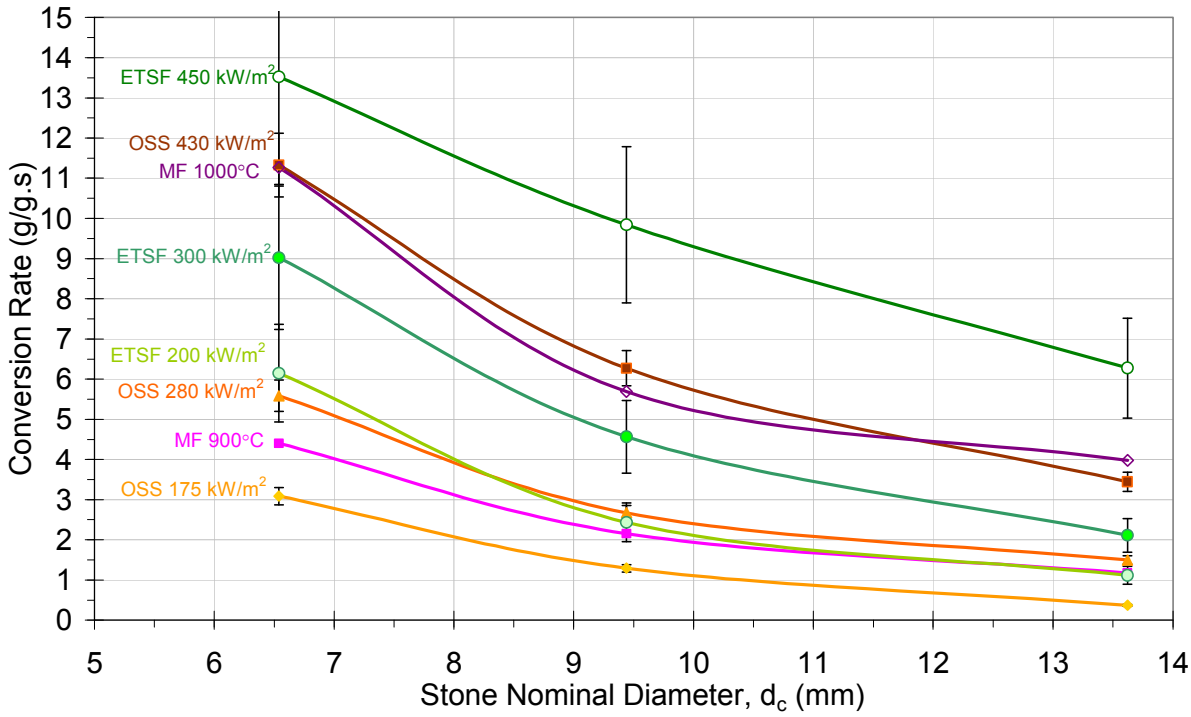

Figure 8-18: Comparison of conversion rates for the Enclosed Triangular Solar Furnace (ETSF) measurements, the Open Solar System (OSS) measurements and the Muffle Furnace (MF) measurements for dc = 6.54mm, dc = 9.44mm and dc = 13.62mm.

The 13.62mm nominal diameter marble calcined within the enclosed solar furnace at 450kW/m^2 and within the muffle furnace at 1000°C did not experience the same kind of surface burning as was identified when calcining it using the open system exposed to 430kW/m^2. This difference is because the walls of the enclosed solar furnace "contains" the radiation which therefore reflects (and emits) more of the radiation back towards the stone from numerous different angles which therefore irradiates more of the surface area of the stone. This more uniform heating allows a greater amount of heat transfer to the calcination front, which in turn increases the rate of calcination. The rate could be increased further by turning (or rotating) the stone. A future evaluation on the trade off between electrical power used to rotate the stone and calcination rate could be made.

A comparison of the calcination times between the enclosed solar furnace (Tables 8-3 to 8-5) and the open system calcination experiments (Tables 7-2 to 7-4), shows the furnace enclosure decreases the calcination time by between 28% and 67%. The 28% decrease was for the smallest stone size exposed to the lowest heat fluxes, while the 67% decrease was for the 13.62mm stone exposed to the highest heat fluxes. In general, the benefits to the calcination times when using the enclosed solar furnace is best for the higher heat fluxes and for the larger stone sizes.

A comparison between the preheating times shows the furnace enclosure decreases the preheating time by between 15% and 45% compared with the open system calcination experiments. The 15% decrease was for the smallest stone size and lowest heat fluxes, and the 45% decrease was for the largest stone size and the highest heat fluxes. The benefits to the preheat time when using the enclosed solar furnace is again best for the higher heat fluxes and for the larger stone sizes.

These two comparisons re-enforce that, within reason, the solar calcination of limestone should use as higher radiant heat flux as possible, and as large a stone size as practical. Although caution to hard burning of the stones surface needs to be monitored and heat flux or stone size reduced to minimise the effects.

8.6 Conclusions from the Enclosed Solar Furnace Calcination Measurements

The enclosed triangular solar furnace calcination experiments using radiation as the sole heat source have shown that calcination rates of the Penrice marble increases with an increase in radiant heat flux and also with a decrease in stone diameter, which is similar to the open system measurements.

This chapter has also identified the following:

- The benefits to the calcination times when using the enclosed solar furnace is best for the higher heat fluxes and for the larger stone sizes, compared to the open system calcination experiments. A 45% improvement in the calcination time for the 13.62mm nominal diameter stone was measured when exposing the stone to the same direct heat flux but enclosing the stone within a triangular shaped enclosed solar furnace.

- The preheating time of the stone is directly proportional to the illuminated surface area of the stone and the intensity of the heat flux to which it is exposed.

The completion times of between 5 and 85 minutes shown in Figure 8-13 are similar to those for a rotary kiln which demonstrates the practicalities of this technology which could practically interchange with the current industrial plants.

These experiments have quantified the effects of radiant heat flux intensity and marble diameter on the rate of calcination. The use of solar radiation as the sole heating source for the calcination of Penrice marble has never been reported. Additionally, neither has the use of an enclosed triangular shaped solar furnace for thermo-chemical reactions. These experiments are therefore unique in the use of such a furnace and add significantly to the knowledge base for the calcination of limestone.

The decomposition rates, preheating time (t_{cp}) and time to complete calcination (t_{100}) which were measured within these experiments are used for comparison with the calcination modelling and validation purposes presented in Chapter 10.

The next Chapter presents a multi-zone two-dimensional zone modelling which is an extension of the zero dimensional modelling presented in Chapter 3. It is used to model the characteristics of the solar source and aluminium deflection mirror as well as the heat flux distribution within the atmospherically-open flat bed furnace system and the triangular shaped enclosed furnace.

Chapter 9

Multi-Zone Two-Dimensional Studies of a Solar Lime Furnace

9.1 Introduction

The zero dimensional zone model presented in Chapter 3 provides a simple modelling technique which is useful for broad assessments and can provide an indication of trends as furnace parameters are altered. A more comprehensive modelling method is now presented to simulate a radiation (solar) source and resulting heat fluxes to which the limestone is exposed. Validation is achieved through comparison with the measured heat fluxes within the Open Solar System (OSS) and the Enclosed Triangular Solar Furnace (ETSF) used in the experimental program.

After an extensive review of modelling techniques, presented in Chapter 2, the multi-zone two-dimensional zone model was selected. This type of radiation modelling is used to simulate the radiation exchange and heat flux distribution within the OSS and ETSF presented in the experimental investigations of Chapters 7 and 8, respectively. More specifically this modelling is used to calculate an appropriate method for simulating the solar source such that the radiant heat flux intensity on the floor (ceramic fibre platform) of the furnace are appropriately modelled.

The first part of this Chapter presents the basic principles of the zone method used. A more comprehensive presentation of these principles can be found in the books by Hottel and Sarofim (1967) or Rhine and Tucker (1991). Additionally, there are meticulous detail, explanations and applications of the zone method within the Theses of Tucker (1990) and Correia (2001).

This Chapter presents the specific input details used for each of the modelling runs followed by the results of each simulation. Comparisons are then made between the furnace models. The results from the radiant heat flux density measurements presented in Chapter 5 are used to validate these two radiation models.

9.2 Principles of the Zone Method

The Zone Method is an energy balance technique which divides the non-isothermal furnace bounding surfaces and furnace atmosphere into a series of isothermal zones, with uniform radiative properties, called surface zones and gas zones. Energy balances are calculated for each zone taking into account the radiation exchange between all other zones in the system, the heat transfer (absorption) to the process material (load) and refractory linings as well as any heat loss through furnace openings.

If the furnace atmosphere is transparent to radiation, then only surface zones are required because the gas zones do not participate. However, if the furnace atmosphere absorbs and emits radiation (for example an atmosphere of CO_2 and/or H_2O which absorb and emit within specific frequency bands), the furnace is divided into both surface and gas zones.

The zones are specified to be small enough so that each zone can be regarded as having uniform temperature and thermal properties, such as absorptivity and emissivity. The emitting zones are considered to have the characteristics of a grey body and therefore emit radiation diffusely, and also with no spectral variation.

The calculation of the radiation exchange requires knowledge of the exchange factors for each of the zone pairs in the furnace. These are calculated in successive stages using the geometry of the furnace and the radiant properties of each of the zones. Three types of exchange factors require calculation; direct exchange areas, total exchange areas and non-grey flux exchange. Each of these radiation exchange calculations are presented on the next few pages in turn.

9.2.1 Direct Exchange Areas

The direct exchange areas between each pair of zones express the effective area of direct radiative exchange between the two zones. The direct exchange areas are the view factor multiplied by the effective area of the emitting zone. For surface zones, the effective area is the surface area of the zone. For gas zones the radiant emission is in 4π steradians and therefore the effective area is the product of the zone absorptivity and the zone volume multiplied by four.

The direct exchange areas are denoted within this thesis by lower case symbols and are designated as being either surface to surface ($s_i s_j$), surface to gas volume ($s_i g_j$), gas volume

to surface ($g_i s_j$), or gas volume to gas volume ($g_i g_j$). The subscripts *i* and *j* denote the emitting and receiving surfaces respectively.

The proportion of radiation leaving body *i* that arrives directly at another body *j* is dependent on the shape and relative position of the two bodies (zone pairs) and is commonly known as the view factor, F_{ij}. The direct exchange area from a surface zone *i* to any other zone *j* is given by $A_i F_{ij}$ where A_i is the surface area of zone *i*. The direct exchange area from gas zone *i* to any other zone *j* is given by $4\ K_i V_i\ F_{ij}$; where V_i is the volume of zone *i* and K_i is the absorptivity of the gas per unit distance usually referred to as the attenuation factor or extinction coefficient.

The attenuation of the gases within the furnace atmosphere is calculated using the fraction of energy transmitted through the gas, known as the transmissivity factor, which is defined by Rhine and Tucker (1991, page 219) as:

$$\tau = \exp(-Kr) \qquad [9.1]$$

Again K is the extinction coefficient of the gas and r is the distance between each zone.

Explicit mathematical formulae for each of the view factors have been reproduced from Chapter 11 of Rhine and Tucker (1991) and are now presented. The direct exchange area between a surface i and surface j is defined by the following multiple integral, Equation [9.2].

$$s_i s_j = A_i F_{ij} = \int_{A_i} \int_{A_j} \frac{\cos\theta_i \cos\theta_j \exp(-Kr)}{\pi\, r^2}\, dA_j\ dA_i \qquad [9.2]$$

The direct exchange between a surface *i* and gas zone *j* is defined by the integral :

$$s_i g_j = A_i F_{ij} = \int_{A_i} \int_{V_j} \frac{K_j \cos\theta_i \exp(-Kr)}{\pi\, r^2}\, dV_j\ dA_i \qquad [9.3]$$

The exchange from a gas zone *i* to a surface zone *j* is given by:

$$g_i s_j = 4K_i V_i F_{ij} = \int_{V_i} \int_{A_j} \frac{K_i \cos\theta_j \exp(-Kr)}{\pi\, r^2}\, dA_j\ dV_i \qquad [9.4]$$

The direct exchange area integral for exchange between two gas zones is given by:

$$g_i g_j = 4K_i V_i F_{ij} = \int_{V_i}\int_{V_j} \frac{K_i K_j \exp(-Kr)}{\pi r^2}\, dV_j\, dV_i \qquad [9.5]$$

Correia, (2001) explains that the analytical evaluation of these multiple integral equations is difficult and tedious to perform for complicated furnace geometries. The method that "probably represents the best numerical method for computing view factors" (Emery *et al*. 1991) is the Monte Carlo method. This calculation method and its application to zone modelling is described in Section 9.2.5.

It should be noted that, for clear gases or grey gases with uniform radiative properties, the direct exchange areas are exclusively a function of the geometric configuration of the enclosure, so a single computation is sufficient.

The symmetry of the integrals provides reciprocity relationships that are used to calculate the conservation of energy equations shown in Equations 9.6 and 9.7. These energy balance equations are for an enclosure comprising ***M*** surface elements and ***L*** volume elements.

$$A_i = \sum_{j=1}^{M} s_i s_j + \sum_{j=1}^{L} s_i g_j \qquad [9.6]$$

$$4K_i V_i = \sum_{j=1}^{M} g_i s_j + \sum_{j=1}^{L} g_i g_j \qquad [9.7]$$

These energy balances are used for checking the accuracy of the exchange factor calculations. They can also allow estimation of some of the exchange areas through arithmetic difference calculation.

9.2.2 Total Exchange Areas

The total exchange area calculations account for the direct and indirect radiant exchange between two surface zones. In furnaces with grey surfaces, the radiation exchange must account for the possibility of multiple reflections and the normal emission of heat flux from the participating surfaces. The total exchange factors are therefore dependent on the reflectivity and emissivity of the surfaces involved. The total radiant flux leaving a surface depicted in Figure 9-1 incorporates the total amount of radiation emitted from a surface zone ($\varepsilon_i E_{bi}$) plus the reflected flux due to the reflectivity (ρ) of the surface. The total exchange areas are denoted by the upper case symbols S_iS_j (surface to surface), S_iG_j (surface to gas volume), G_iS_j (gas volume to surface) and G_iG_j (gas volume to gas volume).

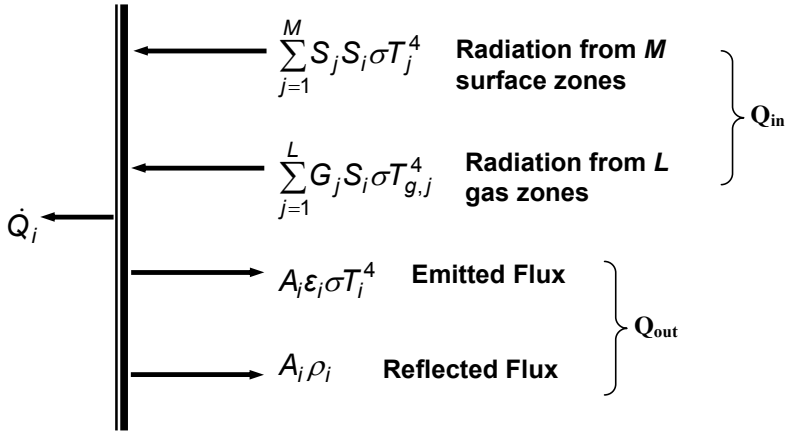

Figure 9-1: Incident, emitted and reflected radiant fluxes at a surface element.

The total radiation leaving a surface zone *i*, which is denoted Q_{out}, is calculated using Equation 9.8

$$Q_{out,i} = \varepsilon_i E_i + \rho_i Q_{in,i} \qquad [9.8]$$

For an enclosure comprising ***M*** surface elements and ***L*** volume elements the radiative energy balance equation for each surface zone *i* is given by:

$$A_i Q_{in,i} = \sum_{j=1}^{M} S_i S_j Q_{out,j} + \sum_{j=1}^{L} S_i G_j E_{g,j} \qquad [9.9]$$

and for each volume zone *i* the radiative energy balance equation is given by Equation 9.10:

$$4K_i V_i Q_{in,i} = \sum_{j=1}^{M} G_i S_j Q_{out,j} + \sum_{j=1}^{L} G_i G_j E_{g,j} \qquad [9.10]$$

In essence the total exchange areas give the effective area of blackbody radiative exchange between two zones. The radiative energy balance equations 9.9 and 9.10 are best expressed and solved using matrices, the specific detail of which are given by Rhine and Tucker (1991) on page 222.

9.2.3 Non-Grey Flux Exchange

The non-grey flux exchange is calculated to account for the radiant energy transfer between gas zones, making allowance for the non-grey, temperature characteristics of the furnace atmosphere. A real (non-grey) gas exhibits a variation in absorption coefficient and

emissivity with both temperature and wavelength. For example, the non-grey gases H_2O and CO_2 emit and absorb radiation within spectral bands centred on the following wavelengths.

Table 9-1: Median wavelength of emitting and absorbing spectral bands for H_2O and CO_2.

NOTE:
This table is included on page 246 of the print copy of the thesis held in the University of Adelaide Library.

Adapted from Rhine and Tucker, (1991, pg 202).

The equations for calculating radiative heat transfer within a furnace are greatly simplified if the grey gas assumption can be retained. Hottel and Cohen (1957) demonstrated that the contribution of a non-grey gas can be represented as a weighted sum of a number of grey gases (N_g) with different absorption coefficients $k_{g,n}$ and temperature independent weighting coefficient $a_{g,n}$ (for a gas) or $a_{s,n}$ (for a surface). If the above assumptions are applied, the total emissivity and absorptivity of a non-grey gas which contains H_2O and CO_2 can be expressed mathematically as:

$$\varepsilon_g = \alpha_g = \sum_{n=1}^{N_g} a_{g,n}\left[1 - \exp\left(-k_{g,n}\left(P_{H_2O} + P_{CO_2}\right)L\right)\right] \qquad [9.11]$$

Where $\sum_{n=1}^{N_g} a_{g,n} = 1$, P is the partial pressure of the gas, and L is the beam length.

Correia (2001) notes that the total emissivity of CO_2 and H_2O, and mixtures of the two gases over a wide range of temperatures and partial pressure path length products, can be accurately expressed by a sum of two or three grey gases plus one clear gas (i.e. with zero absorption coefficient) to account for the non-absorbing regions in the spectrum. Tucker (1990) provides the polynomial for the temperature dependence of the weighting coefficients for the gas and surface used in Equation 9.11:

$$a_{g,n} = b_{1,n} + b_{2,n}T_g \qquad [9.12]$$

$$a_{s,n} = b_{1,n} + b_{2,n}T_s \qquad [9.13]$$

Where T_g is the gas temperature and the correlation coefficients for $k_{g,n}$, $b_{1,n}$ and $b_{2,n}$ are given in Table 9-2.

Table 9-2: Grey gas parameters used in mixed grey gas correlations for CO_2 and H_2O mixtures.

Adapted from Rhine and Tucker (1991, pg 208).

For any given furnace geometry containing gases that are to be approximated using a mixture of grey gases, N_g sets of direct and total exchange areas must be evaluated for all zone pairs prior to evaluating the total radiative energy balance for each zone.

The modelling presented in this chapter uses a steady state system and, as such, the variations in furnace temperature that can occur over time are not considered. This results in constant gas coefficients for CO_2 and H_2O in Equation 9.12. Its extension to a time stepped approach (transient model) is beyond the scope of the present study.

9.2.4 Total Energy Balances

The total energy balance is calculated as being the difference between all the incoming radiant energy and all the leaving radiant energy for each surface zone (M) and volume zone (L) within the furnace. For any particular surface zone *i* the radiant balance for a surface is written as:

$$\dot{Q}_{s,i} = \sum_{j=1}^{M} \left(\overline{S_j S_i}\right) \sigma T_i^4 + \sum_{j=1}^{L} \left(\overline{G_j S_i}\right) \sigma T_i^4 - A_i \varepsilon_i \sigma T_i^4 \qquad [9.14]$$

and for a volume zone:

$$\dot{Q}_{g,i} = \sum_{j=1}^{M} \left(\overline{S_j G_i}\right) \sigma T_i^4 + \sum_{j=1}^{L} \left(\overline{G_j G_i}\right) \sigma T_i^4 - 4 \sum_{n=1}^{N_g} a_{g,n} k_{g,n} p_i V_i \sigma T_i^4 \qquad [9.15]$$

The first summation is over the surface zones and represents the total amount of radiation emitted by any surface zone and absorbed by zone *i*, and the second sum is over the gas zones and represents the total amount of radiation emitted by any gas zone and absorbed by zone *i*. A system of simultaneous non-linear algebraic equations is obtained that must be solved iteratively for the temperatures, and hence heat fluxes, by means of numerical techniques such as the Newton-Raphson method, as is discussed on pages 425-429 of Rhine and Tucker (1991).

The calculation of the energy balances within the zone method is not straightforward due to the difficulties associated with the evaluation of the view factors and exchange areas. Correia (2001) discusses several numerical methods used for the analytical evaluation of the multiple integral equations for complicated geometries. This probability distribution technique is used within the industrial multi-zone two-dimensional zone model named RADEX which is used within the radiation modelling conducted within this research investigation. Details of Radex are discussed in Section 9.3.

9.2.5 Monte Carlo Probability Distribution Technique

The Monte Carlo method is a statistical approach, which for application to thermal radiation, works by simulating the paths of a large number of randomly directed bundles of energy (photons) from a source, through a medium, to the absorbing sink. The radiative behaviour of the system is calculated from the average behaviour of all of the photons.

The Monte Carlo method, as described on page 258 of Rhine and Tucker (1991), is relatively simple to formulate and able to simulate both complex geometry and spatial variation in radiative properties including anisotropic scattering, directional emissivity, and spatial variation in attenuation coefficient. The Monte Carlo method employs random numbers to generate the probability distributions for the direction of emission, scattering, and reflection of photons of radiation from a nominated surface and the final absorption of each photon by the furnace atmosphere. Correia (2001) notes that, because of the statistical nature of this method, the results produced will fluctuate randomly around the exact solution. A large number of photons are therefore desired for each calculation, with the accuracy increasing as the number of photons is increased.

The RADEX zone modelling code uses the Monte Carlo ray tracing technique to provide the temperature independent radiative exchange factors required by the zone model to calculate the direct exchange areas as described in Section 9.2.1. Due to the stochastic nature of the

Monte Carlo method, the exchange factors computed by RADEX do not always achieve total summation rules or the reciprocity principle. Smoothing of the radiation factors is therefore employed using arithmetic averaging of the reciprocal exchange factors and least-squared method for the energy conservation balance.

The exchange factors used to model the geometry of the experimental solar furnace are calculated using 540000 rays in total from all the surfaces. The exchange factors are calculated prior to each zone model simulation and stored within a text file ready for use.

9.3 The RADEX Program

The RADEX modelling code was developed by Professor Duncan Lawson at Coventry University for British Gas to evaluate furnaces and boilers fired by natural gas (or town gas). Prof Lawson further developed the program into a FORTRAN 77 computer code which provides a user interface for furnace geometric and atmospheric inputs. This computer code was developed in two parts: RADEXF, which calculates the various exchange factors (view factors, direct exchange areas and total exchange areas) and RADEX, which calculates the net heat flux out of all the zones from a specified temperature field. The user and system guides for RADEXF (Lawson, 1992) and the RADEX user guide (Lawson, 1993) provide detailed explanation of all subroutines, subordinate routines, and variables and so are not repeated. However a brief explanation of the required inputs is provided below.

After compiling the main program module and subroutine files, the first data input requirement for each calculation 'run' is to specify the general operating conditions and global parameters. This list of variable maximums provides the program with the dimensions of the calculation arrays for each furnace characteristic parameter. The next item required is to specify the number of tracing rays used within the Monte Carlo method to calculate the exchange factors. The geometry of the furnace enclosure is then defined using a Cartesian coordinate system. The program requires the furnace to be symmetric along the *z* axes. The cross sectional shape of a furnace is therefore defined by the *x* and *y* co-ordinates of each corner (or vertex). The program automatically joins consecutive vertices with a straight line. To make the enclosure three dimensional, the furnaces *z* dimension is represented as an extrusion of the cross section outline. The depth of the extrusion (furnace width) and the number of zone slices are then specified. With the external geometry of the furnace defined, a specification of how many, if any, obstacles are present within the enclosure. The input data for the shape (cuboid or cylindrical) and location (*x,y,z*) of each obstacle is required. The zoning of the interior of the furnace enclosure is then conducted by specifying the nodal

points (*x,y*) for the geometric (fine) grid and the heat transfer (coarse) grid. With the geometry defined, and the locations and sizes of all zones specified, the characteristics of each zone must then be defined. The gas absorptivity coefficients use the "sum of grey gases" method and so the concentrations of CO_2 and H_2O need to be specified. The program's interface provides the selection of up to six options ranging from the setting of a uniform absorptivity for the entire enclosure, to specifying the excess air level and carbon concentration for each zone individually. The surface emissivities are then specified using one of four options, ranging from using a uniform emissivity for the entire enclosure, to allocating each surface zone an emissivity. The assumed temperature of the each surface zone and gas zone need to be then specified to allow the calculation of the zone heat fluxes. The calculation run is then started with output text files providing the run details, the exchange areas and the heat flux outputs.

9.4 Calibration of the 2-D Multi-Zone Model

This section describes the formulation and calibration of the multi-zone two dimensional zone model. Calibration of the model is achieved by the calculation of the measured heat flux received by the two heat flux transducers positioned within the radiation beam. The two heat flux transducers were positioned at a distance of 680mm below the centreline of the mirror, corresponding to a distance S_8 = 540mm from the focal point. The median maximum heat flux from these measurements was 16.03 kW/m^2. This heat flux was used as the calibration point to calculate the required temperature of the simulated radiation source to achieve the same heat flux at the same distance within the radiation model. After calibration, a sensitivity analysis is conducted to ascertain the influence of the modelling parameters on the resultant heat flux.

9.4.1 Details of the Modelling Parameters

A representation of the experimental apparatus showing the location of the two heat flux transducers used for the radiation measurements is shown in Figure 9-2. The system components which were used within the calibration model include the radiation source, the silver coated elliptical reflector, the aluminium mirror, the heat sink of the heat flux transducers, and the open atmosphere through which the radiation travels. Figure 9-3 shows the representation of the experimental apparatus and the system components. The 650mm and 680mm distances are the distances measured on the experimental apparatus. The

specifications for the reflectivity, emissivity and temperature for each of the system components are presented in Table 9-3. The temperature of each surface was specified after measuring it within the calcination and heat flux experiments. The emissivity of the heat sink (transducer) and the open atmosphere was set a value of 1.0 so that all of the radiation received is absorbed and not reflected. Due to the low temperature of these two sinks, the emitted radiation is comparatively small and can be neglected.

Table 9-3: Specifications for reflectivity, emissivity and temperature used for model calibration.

	Reflectivity	**Emissivity**	**Temperature**
Aluminium Mirror	0.947	0.053 †	473 K
Silver coated elliptical reflector	0.97 ††	0.03	418 K
Measurement heat sink (heat flux transducer)	0.0	1.0	306 K
Open atmosphere	0.0	1.0	293 K

† Mills (1999)
†† Nostell (2000)

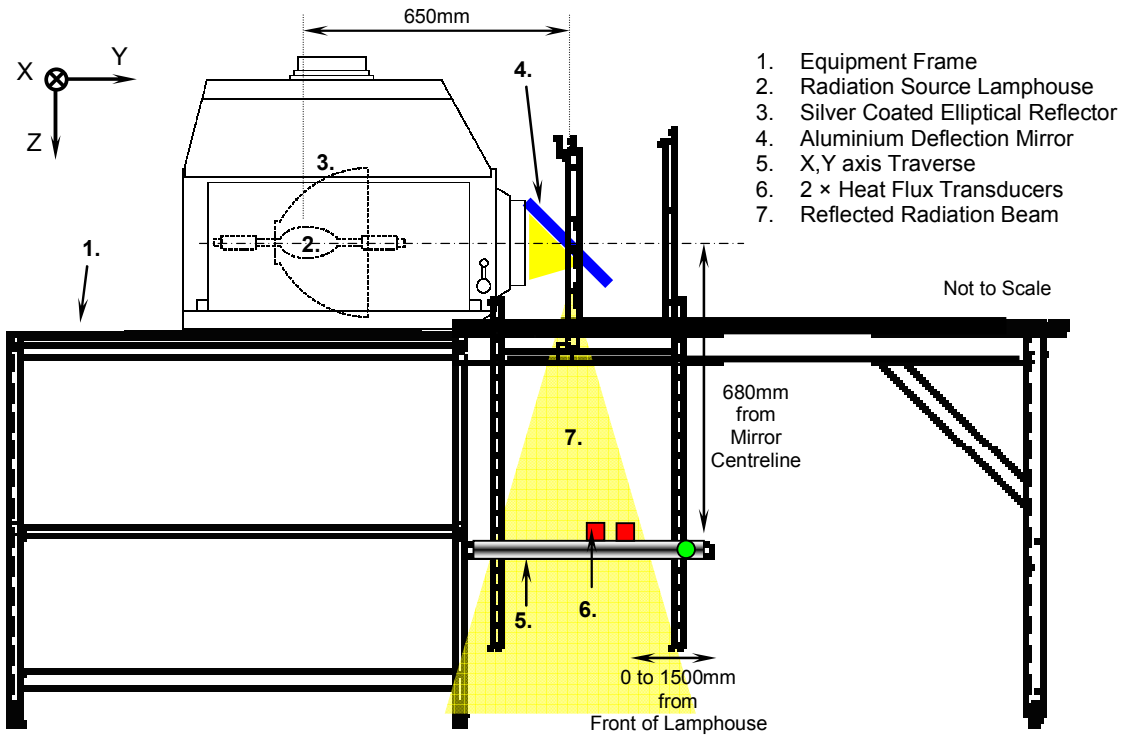

Figure 9-2: Experimental apparatus used for radiation source measurement.

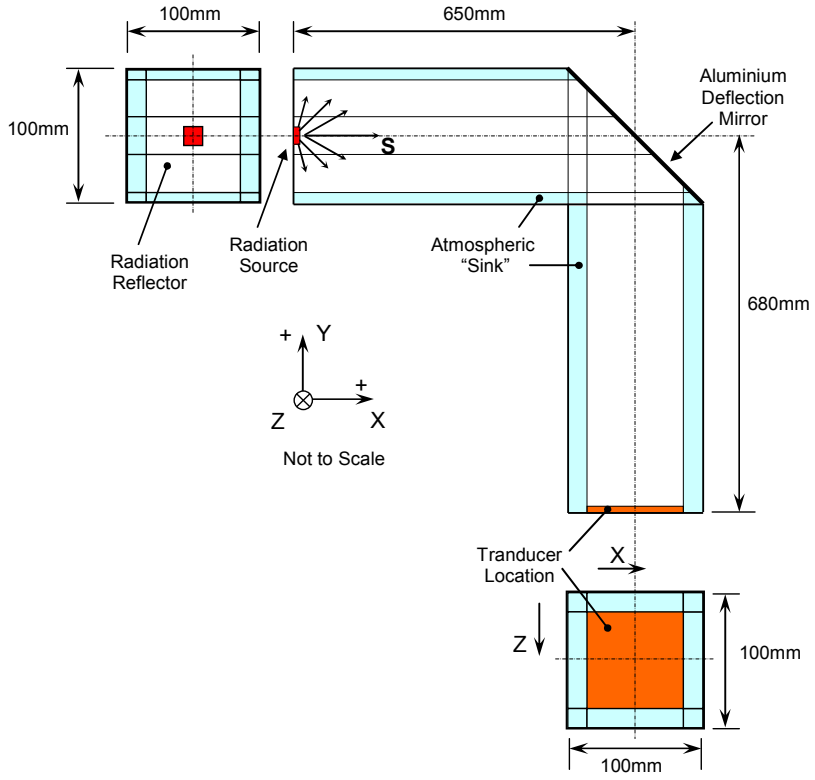

Figure 9-3: Representation of the experimental apparatus used in RADEX for the source temperature calculations.

The main difference between the model and the physical system is that the elliptical reflector behind the radiation source was modelled as a flat surface. This assumption was implemented for two reasons, the first being because curved surfaces can not be modelled in RADEX and secondly, using straight lines to represent the surface was considered to be both time consuming and adding unnecessary complexity at this stage of the investigation. This assumption can be re-evaluated for any future investigations.

Using the flat surface reflector assumption within the model requires that the emission of radiation from the source be substantially more than if an elliptical reflector was modelled. This is because the flat surface reflects the radiation in a hemispherical ($2\pi r^2$) array, the majority of which is lost to the atmosphere. This is in contrast to the elliptical reflector which "collects" and directs the majority of the emitted radiation towards the focal point, after which the radiation beam spreads at a defined conical shape. A very high pseudo-source temperature is therefore required to produce the large output heat flux so that enough radiation reaches the calcination platform (sink). The temperature pf the pseudo-source required to achieve suitable heat fluxes was determined empirically. The methods used to determine the pseudo-source temperature is now presented.

9.4.2 Radiation Pseudo-Source Temperature

Appropriate simulation of the radiation source for the experimental apparatus is desired. The experimental radiation source, which is discussed in depth in Chapter 4, was produced by a high current plasma arc enclosed within a xenon atmosphere. The RADEX program provides the ability to specify the radiation source as a volume zone at a fixed temperature. A volume of 8×10^{-6} m^2 (20mm $\times$ 20mm $\times$ 20mm) was selected for the radiation source because it approximates the volume of the plasma arc between the electrodes within the xenon arc lamp. The source zone was positioned in the middle of the flat surface reflector as is shown in Figure 9-3.

A systematic approach to determine the pseudo-source temperature was then undertaken, which involved changing the temperature of the simulated source and comparing the calculated heat flux at the location of the transducer with the measured heat flux.

Table 9-4 shows the received heat flux at the location of the simulated transducer for variations of radiation source temperature. The source's output heat flux is also shown. These high source temperatures are not physically realistic and arise because the reflector behind the source was modelled as a flat surface which reflects the radiation in an array. The average temperature of the plasma arc within a xenon arc lamp is 6200K (OSRAM, 1996, pg 5).

Table 9-4: Simulated radiation pseudo-source temperature variation and the resulting received heat flux at the transducer measurement location.

Pseudo-Source Temperature (K)	**Source Output Heat Flux (kW/m^2)**	**Calculated Heat Flux at location of Calcination Bed (kW/m^2)**
5000	34,602	0.0679
10000	553,644	2.263
15000	2,802,825	11.77
20000	8,858,310	37.38
25000	21,626,740	91.4

Figure 9-4 shows a plot of the calculated heat flux received at the transducer location verses source temperature, from the data displayed in Table 9-4. A curve fit 5^{th} order polynomial was applied to the plot. To match the measured heat flux of 16.03 kW/m^2, displayed in Table

5-12, the required pseudo-source temperature is 16196K. To achieve this, the calculated output power of the source at this temperature is 7.5 kW, which is 50% higher than the power of the actual 5000W XBO lamp.

The sensitivity of the source temperature to variations in the heat flux transducer measurement tolerance is discussed in the next section.

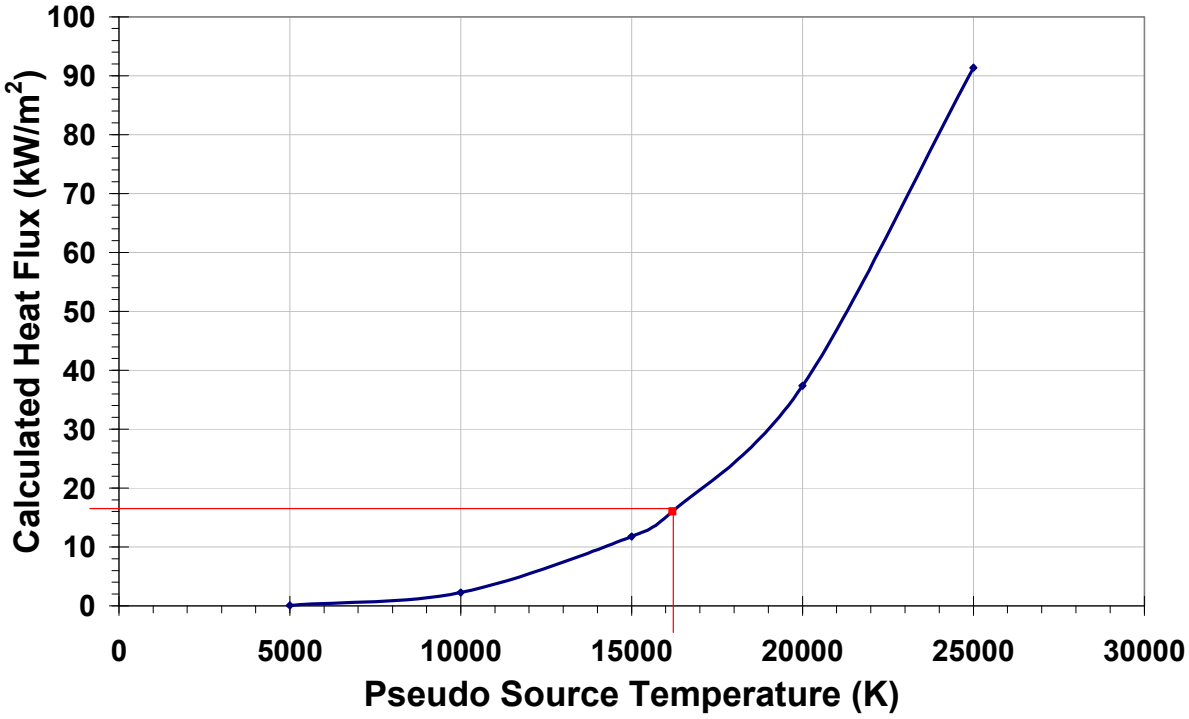

Figure 9-4: Calculated heat flux received at the transducer location for variations in pseudo-source temperature.

9.4.3 Sensitivity Analysis of the Calibration

A sensitivity analysis was conducted to evaluate the influence of the various input values specified for the RADEX model. This includes the variation in tolerance of the heat flux transducer measurement and the values specified for the reflectivity, emissivity and temperature displayed in Table 9-3.

The tolerance of the heat flux transducer measurement was calculated to be ± 4.55% as displayed in Table 5-14. The measured heat flux could therefore vary between 16.76kW/m^2, and 15.30kW/m^2 from the standard value of 16.03kW/m^2. The temperature of the radiation source was therefore varied from 16196K until these measured heat flux values from were obtained. The results are shown in Table 9-5.

The temperature of the aluminium mirror, silver reflector and heat flux transducer were monitored using thermocouples and data logging apparatus, which have an accuracy of approximately ±1%. The temperatures of the aluminium deflection mirror and thermocouple were continually monitored at multiple locations and so that maximum error of these measurements is assumed to be ±2%. The reflector temperature on the other hand, was only monitored periodically in one location towards the outside of the reflector dish due to limited access. The maximum error and uncertainty for the temperature of the reflector is assumed to be ±10% (50°C).

The assumed values for reflectivity of the reflector and mirror are presented in Chapter 4 and were 0.947 from Mills (1999) and 0.97 from Nostell (2000) respectively. These values were varied from the maximum reflectivity value found within literature for highly polished silver (reflector) and aluminium (mirror) to 10% degradation of the reflective surface.

It should be noted that the inputs to the RADEX program include emissivity rather than reflectivity, and so a value of 0.053 was used for the reflector, and a value of 0.03 for the mirror were assumed.

The variations in input parameters for the sensitivity analysis were:

- The measured heat flux was varied by ± 4.55% from the measured reference value of 16.03 kW/m^2.
- The temperature of the flat reflector behind the radiation source was varied by ± 50°C from the measured reference value of 418K.
- The reflectivity of the silver reflector “behind” the radiation source was varied from 0.985 to 0.873, from the reference value of 0.97.
- The temperature of the deflection mirror which was varied by ± 2% from the measured reference value of 473K, i.e. from to 464K to 483K.
- The reflectivity of the deflection mirror was varied from 0.961 to 0.852 from the reference value of 0.947.
- The temperature of the transducer which was varied by ±2% from the measured reference value of 306K, i.e. from to 300K to 312K.

Table 9-5 shows the radiation source temperature required within the RADEX model to achieve the variation in measured heat flux. Also shown is the percentage change from the standard source temperature of 16196K.

Table 9-5: Variation in pseudo-source temperature to achieve the variation in measured heat flux tolerances.

Parameter	Tolerance	Temperature of Radiation Source	Percentage Change
Heat Flux Measured by Transducers (from 16.03 kW/m^2)	16.76 kW/m^2 15.30 kW/m^2	16,376 K 16,009 K	1.11 % 1.15 %

For the following sensitivity analysis tests the source temperature was maintained at a constant value of 16196 K. Table 9-6 shows a comparison of the calculated heat flux received at the simulated transducer location within the RADEX model (S = 650 + 680mm = 1330mm from the source) by varying the input parameters listed above.

Table 9-6: Comparison of calculated heat flux by changing various modelling parameters.

Parameter (reference value)	Extreme Values	Heat Flux Calculated at Transducer Location S = 1330mm (kW/m^2)	Percentage Change From Reference
Temperature of Reflector (ref = 418K)	468 K 368 K	16.03 16.03	0 % 0 %
Reflectivity of Pseudo Reflector (ref = 0.97)	0.985 0.873	16.13 15.37	+0.64 % -4.14 %
Temperature of Mirror (ref = 473K)	483 K 464 K	16.03 16.03	0 % 0 %
Reflectivity of Mirror (ref = 0.947)	0.963 0.852	16.30 14.42	+1.69 % -10.0 %
Temperature of Transducer (ref = 306K)	300 K 312 K	16.11 15.92	+0.5 % -0.7 %

Table 9-6 shows that the calculation is most sensitive to the assumed value of the reflectivity of the mirror with a 10.0% reduction in heat flux predicted at S = 1330mm. The lower the reflectivity, the less radiation is reflected from the surface of the mirror and therefore less heat flux is received at the transducer. The absorbed heat flux increases the mirror's temperature which can be measured and monitored within the physical system. Maintaining a constant mirror temperature will contribute to the accuracy of these simulations.

A decrease in the reflectivity of the reflector "behind" the radiation source reduces the available heat flux transferred to the transducer location (shown in Figure 9-3). The 10% reduction in reflectivity causes only a 4.14% reduction in available heat flux because the pseudo mirror makes only a small contribution to the total heat flux. Modelling the actual reflector would increase the sensitivity of the assumed reflectivity.

The variation in temperature of the reflector and mirror make no contribution to the simulation. This is because of the low emissivity values of the reflective surfaces.

The increase in transducer temperature causes a decrease in the heat flux received at the transducer location. The variation in the transducer temperature indicates the balance between the radiation from the radiation source and the emission of thermal radiation for the transducer itself. The higher the temperature of the transducer the more that it emits thermal radiation and thus the lower the value from the heat flux balance. This becomes relevant when considering the high temperatures of the calcination platform, because the emission of thermal radiation is a function of the surface temperature to the fourth power.

These sensitivity analysis simulations have identified that the reflectivity of the 45° mirror placed within the radiation beam causes the most variation in the heat flux received at the transducers location. To maintain modelling validity, the mirrors temperature was continual measured and the surface repolished twice to maintain a consistent reflectivity.

From Tables 9-5 and 9-6 for the worst case scenario where the source temperature is 16,009K and the reflectivity of the reflector and mirror degrade by 10% and the temperature of the transducer is incorrect by 2%, the error in the calculated heat flux received at the transducer measurement location can be considered to be approximately ±16%. This translates to a tolerance in the calculated heat flux for the reference case of 16.03 ± 2.6 kW/m^2.

9.5 Heat Flux Modelling of the Open Calcination System

The RADEX model is used to mathematically calculate the heat flux at the calcination platform of the atmospherically-open flat bed furnace system. The furnace geometry used within the simulation model is shown in Figure 9-5. The same 650mm distance between the radiation source and centreline of the aluminium mirror was used as in Section 9.4 above. The distance between the centreline of the mirror and the platform on which the marble samples are placed, was varied between 190mm, 215mm, and 240mm, which represents the 50mm, 75mm, and 100mm distances between the platform and the focal point used within the experimental side of this research investigation.

The specifications for reflectivity, emissivity and temperature of the reflector, aluminium mirror and open atmosphere for these simulations are shown in Table 9-3. An increase of 10°C in the temperature of the aluminium mirror was measured as the platform was moved towards the mirror. However this temperature increase made no difference to the heat flux calculation, as discussed in Section 9.4.2. The measured mirror temperature used within each of the simulations is shown in Table 9-7.

The calcination platform heat sink was modelled as a uniformly irradiated flat surface which absorbs all the energy that is provided and therefore has a total hemispherical emissivity of $\varepsilon = 1.0$. This black body assumption was used because it provides the heat flux value to which the marble sample is exposed to when place upon the platform.

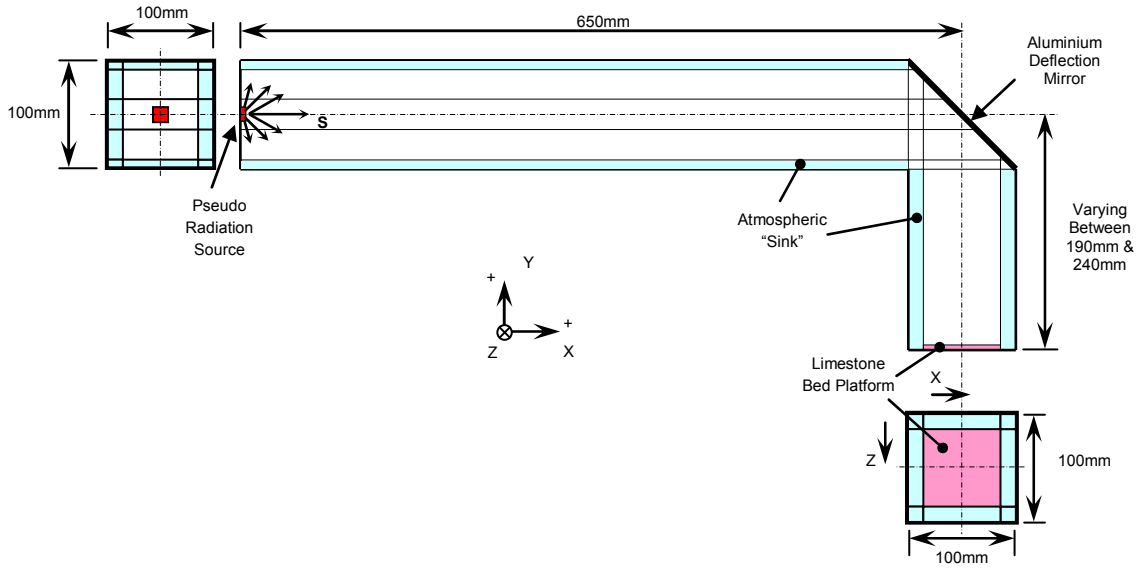

Figure 9-5: Representation of the open solar system (OSS) experimental apparatus used in RADEX.

The heat flux modelling of the atmospherically open calcination system initially used the calculated radiation source temperature of 16196K as the input to the model for calculation of

the heat flux on the surface of the calcination platform. It was found that an input source temperature of 25,400K was required for the model to predict the measured platform temperatures shown in Table 9-7.

The calculated heat flux results for the atmospherically-open flat bed furnace simulation are shown in Table 9-7. It shows that the heat flux increases as the distance from the focal point decreases. This is intuitive because the inverse square law of radiation is being followed. This inverse squared relationship between distance from the focal point (S) and heat flux is best displayed graphically, which can be seen in Figure 9-6.

Table 9-7: Calculated heat flux on the calcination platform for various distances S from the focal point for the open solar system (OSS).

Distance from Centreline of Mirror to Limestone Bed	**Distance 'S' from the focal point**	**Measured Aluminium Mirror Temperature K**	**Measured Platform Temperature K**	**Calculated Heat Flux at distance S kW/m^2**
240mm	100mm	533	1310	180
215mm	75mm	538	1476	293
190mm	50mm	543	1696	457

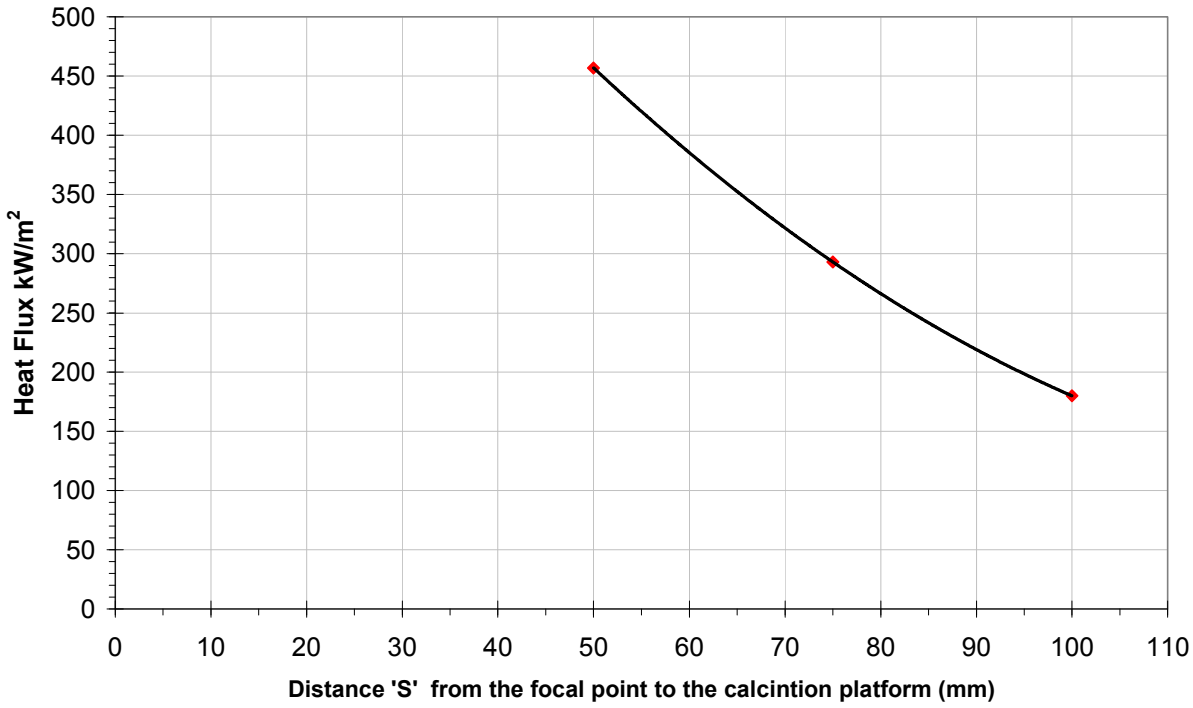

Figure 9-6: Calculated heat flux on the surface of the calcination platform at various distances S, from the focal point for the OSS.

9.5.1 Sensitivity Analysis of the Open System Modelling

A sensitivity analysis was conducted to calculate the effects of various modelling parameter on the resulting heat flux values (displayed within Table 9-7) for the open system simulations. Section 9.4.2 showed that the reflectivity of the mirror caused the most variation to the calculations within the simulations. Degradation of the mirrors surface was therefore monitored in the experimental tests and the surface repolished to maintain a consistent reflectivity. It is estimated that the surface of the aluminium mirror did not degrade to below 0.852 reflectivity, which represents a 10% loss of reflectivity from the reference value of 0.947. Within this sensitivity analysis the variation in the calculated heat flux at the calcination platform is presented in Table 9-8 after changing the reflectivity of the deflection mirror between 0.961 and 0.852.

Similarly, the silver reflector behind the radiation source was routinely cleaned. The reflectivity of the silver surface is estimated to have remained above the 10% loss threshold of 0.873 during the experiments. The change in the calculated heat flux after varying the reflectivity of the reflector from 0.985 to 0.873 is presented in Table 9-8.

The temperature of the calcination platform (heat sink) also caused variation in the heat flux simulations. The variation in temperature across the calcination platform is estimated to be $\pm$1% and the temperature measurement equipment accuracy of $\pm$1%, giving a possible $\pm$2% variation. The variation in the calculated heat flux on the calcination platform, due to a 2% platform temperature measurement discrepancy, is presented in Table 9-8.

The resulting variation in heat flux received by the calcination platform due to the changes in reflectivity and temperature values were calculated for each of the three distances, S, from the focal point. Table 9-8 shows the resulting calculated heat fluxes and the percentage change from the reference heat fluxes of 180 kW/m^2, 293 kW/m^2 and 457 kW/m^2 for distances S = 100mm, S = 75mm and S = 50mm respectively.

Table 9-8 shows that the 10% reduction in the reflectivity of the aluminium mirror causes most percentage change in the calculated heat flux of between 19% and 20%. The lower reflectivity value reduces the amount of reflected radiation from the mirror's surface and therefore less heat flux is received at the calcination platform, as was discussed previously in Section 9.4.2. Increasing the reflectivity of the mirror to 0.963 (1.69% increase) increases the heat flux available at the calcination platform by up to 3.42%.

The 10% reduction in the reflectivity of the silver reflector causes a reduction of up to 15% to the calculated heat flux. It can also be seen within Table 9-8 that an increase in the

reflectivity increases the available heat flux by up to 2.34%. It is interesting to note that less heat flux is 'lost' from the system for the shorter distance from the calcination platform than from the longer distance, e.g. from 10.1% for 50mm up to 15.1% for 100mm. This is probably because less radiation is loss due to scattering from the beam.

Table 9-8: Comparison of calculated heat flux at the simulated calcination platform, after changing various modelling parameters in the OSS model.

Distance 'S' from the focal point	Parameter (reference value)	Extreme Values	Calculated Heat Flux Received at Platform kW/m^2	Percentage Change from Reference
100mm	Reflectivity of Reflector (ref = 0.97)	0.985 0.873	184.2 152.8	2.34% -15.1%
	Reflectivity of Mirror (ref = 0.947)	0.963 0.852	185.9 145.3	3.25% -19.3%
	Platform Temperature (ref = 1310 K)	1336 1284	166.1 193.1	- 7.71% 7.26%
75mm	Reflectivity of Reflector (ref = 0.97)	0.985 0.873	298.1 260.0	1.74% -11.3%
	Reflectivity of Mirror (from 0.947)	0.963 0.852	302.5 236.7	3.24% -19.2%
	Platform Temperature (from 1476 K)	1506 1446	270.3 314.4	-7.75% 7.30%
50mm	Reflectivity of Reflector (from 0.97)	0.985 0.873	464.1 410.9	1.56% -10.1%
	Reflectivity of Mirror (from 0.947)	0.963 0.852	472.6 364.2	3.42% -20.3%
	Platform Temperature (from 1696 K)	1730 1662	418.0 493.7	-8.53% 8.03%

Increasing the platform temperature by 2% resulted in a decrease of up to 8.53% in the heat flux received at the platform. Similarly a decrease of platform temperature by 2% increased the heat flux by up to 8.03%. This inverse temperature relationship is caused by the

temperature difference between the source and the platform, which is used to calculate the radiative heat transfer between the two bodies.

Using the data from Table 9-8, the worst case scenarios for the calculated heat fluxes for the three distances from the focal point are presented in Table 9-9. The positive tolerance has been calculated using the scenario where the reflectivity of the reflector and mirror are at a maximum and the measured temperature of the platform is incorrect by 2%. The negative tolerance has been calculated where the mirror and reflector has degraded by 10% and the measured temperature is 2% higher.

The error bars obtained from these worst case assumptions are large, but have been included to maintain consistency of analysis. They are considered to be quite conservative, since considerable effort was made to minimise them by regular and routine maintenance (polishing) of the surface of the mirror and elliptical reflector.

Table 9-9: Variation in error for the calculated heat flux received at the surface of the calcination platform.

Distance 'S' from the focal point (mm)	**Calculated heat flux from modelling kW/m^2**	**Tolerance %**	**Tolerance kW/m^2**
100	180	+ 12.9 – 42.2	+ 23 – 76
75	293	+ 12.3 – 38.2	+ 36 – 112
50	457	+ 13.0 – 38.9	+ 60 – 178

9.5.2 Comparison of Calculated and Measured Heat Flux for the Open System

A comparison is made between the open system measurements made in Chapter 5 and displayed in Table 5-16 and the results from the open system heat flux modelling calculated within this Chapter.

Table 9-10: Comparison of calculated and measured heat flux on the calcination platform for the OSS.

Distance 'S' from the focal point (mm)	**Calculated heat flux from modelling kW/m^2**		**Measured heat flux kW/m^2**
100	180	+ 23 – 76	175 ± 10
75	293	+ 36 – 112	280 ± 20
50	457	+ 60 – 178	430 ± 30

The calculated and measured values coincide well, with similar uncertainties for each system. This is shown graphically in Figure 9-7.

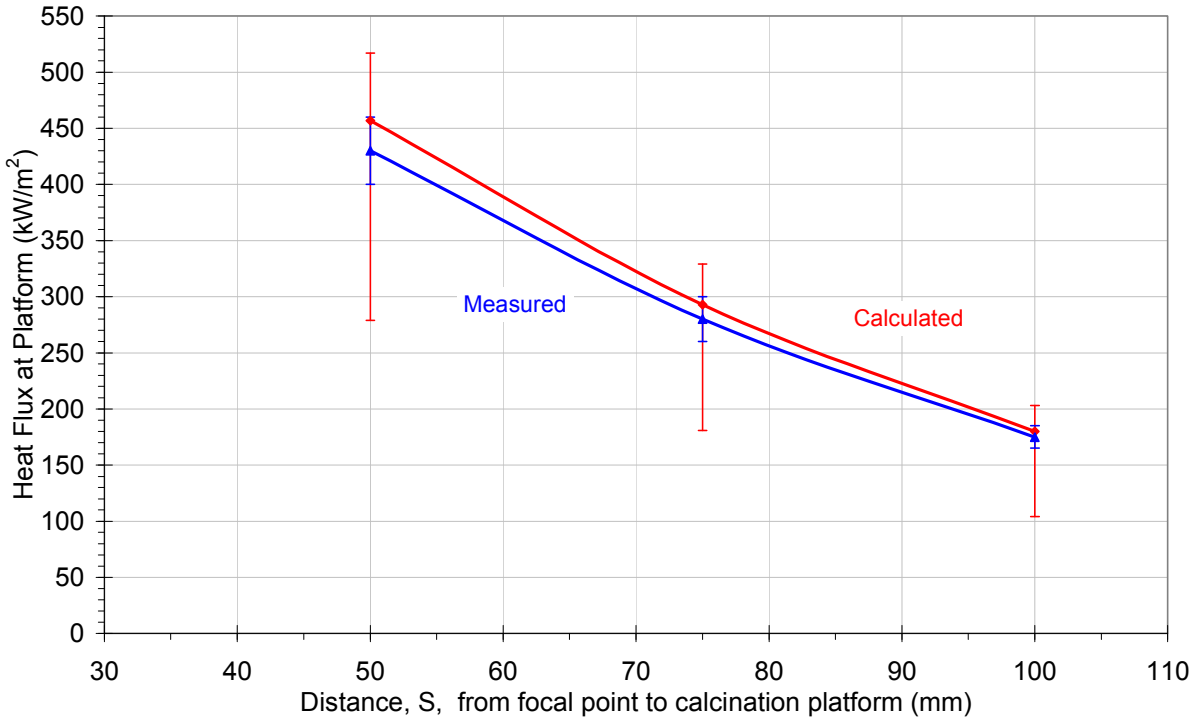

Figure 9-7: Comparison of modelling results and measured heat flux at the calcination platform for the OSS.

A second order polynomial line, Equation [9.16], was produced for the calculated data which provides continuous data for the calculated heat fluxes at distances (S) between 100mm and 50mm which were not simulated.

$$\text{Heat flux, } q = 0.0408 \times S^2 - 23.084 \times S + 3370.1 \quad (\text{kW/m}^2) \qquad [9.16]$$

This calculated representation of the available radiant heat flux is used within the open system calcination modelling presented in Chapter 10.

9.6 Heat Flux Predictions for the Enclosed Triangular Solar Furnace

The methodology used for the heat flux calculations for the enclosed triangular solar furnace (ETSF) follow closely to those of the atmospherically open limestone bed case. The same furnace geometry was used, with the same S = 650mm distance between the radiation source and the aluminium mirror remaining. The distance between the centre line of the aluminium mirror and the calcination platform was varied in three increments to distances of 190mm, 215mm and 240mm. These distances correspond to the measurement distances, S, used within the solar furnace experiments of Chapter 8 and displayed in Table 8-1. Figure 9-8 shows the RADEX representation of the enclosed triangular solar furnace.

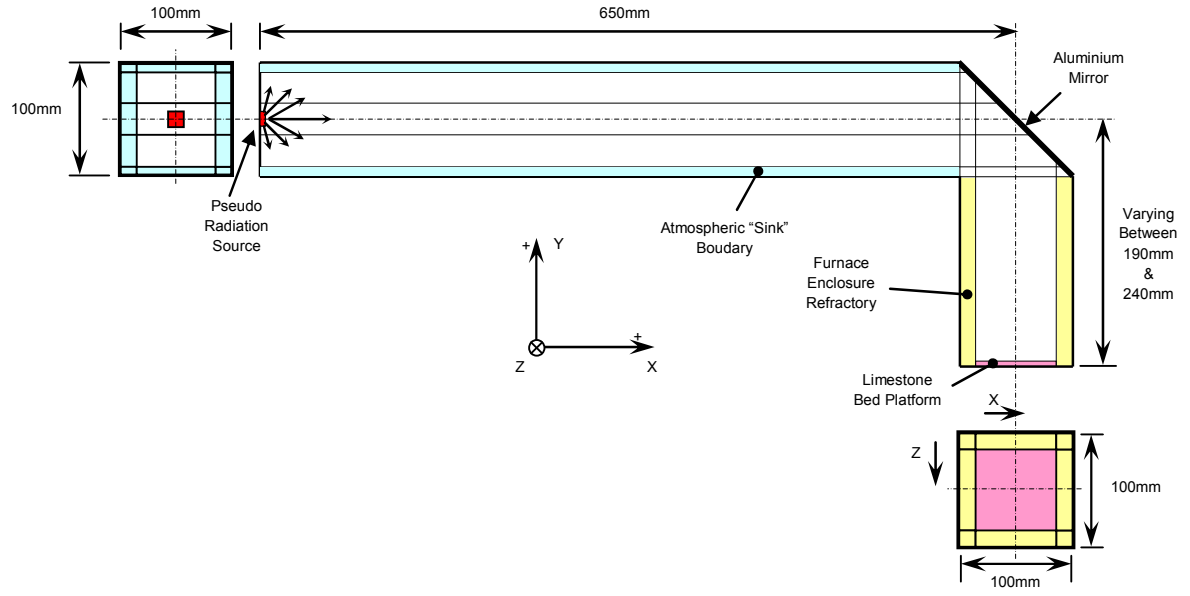

Figure 9-8: Representation of the Enclosed Triangular Solar Furnace (ETSF) experimental apparatus used in RADEX. Note the furnace enclosure refractory above the platform.

The emissivity of the furnace refractory, shown in yellow in Figure 9-8, was set to 0.9. This value was chosen because it is the specified emissivity of the commercially available ceramic fibre refractory used in the experimental apparatus. The emissivity of the atmospheric sink was set to 1.0, the aluminium mirror at 0.053, the reflector behind the radiation source 0.03 and the calcination platform modelled as a uniformly irradiated flat surface which has a total hemispherical emissivity of 1.0.

The temperatures of the aluminium mirror and limestone bed platform were measured during the experiments and used as the input to the RADEX heat flux model. It should be noted that the measured temperatures of the aluminium mirror were approximately 100°C higher for the ETSF than for the OSS. An increase in calcination platform temperatures was also measured, as is shown in Table 9-11.

The open system radiation source temperature of 25,400K was used for these ETSF simulations so that the benefits of using this shaped enclosure for a thermochemical solar reactor can be quantified. The heat fluxes calculated with the RADEX simulation are shown in Table 9-11.

Table 9-11: Calculated heat flux on the calcination platform for S = 100, S = 75 and S = 50 for the ETSF.

Distance from Centreline of Mirror to Limestone Bed mm	**Distance 'S' from the focal point mm**	**Measured Aluminium Mirror Temperature K**	**Measured Platform Temperature K**	**Calculated Heat Flux kW/m^2**
240	100	633	1444	221
215	75	638	1577	327
190	50	658	1735	482

The relationship between calculated heat flux and distance from the focal point, S, is displayed graphically in Figure 9-9.

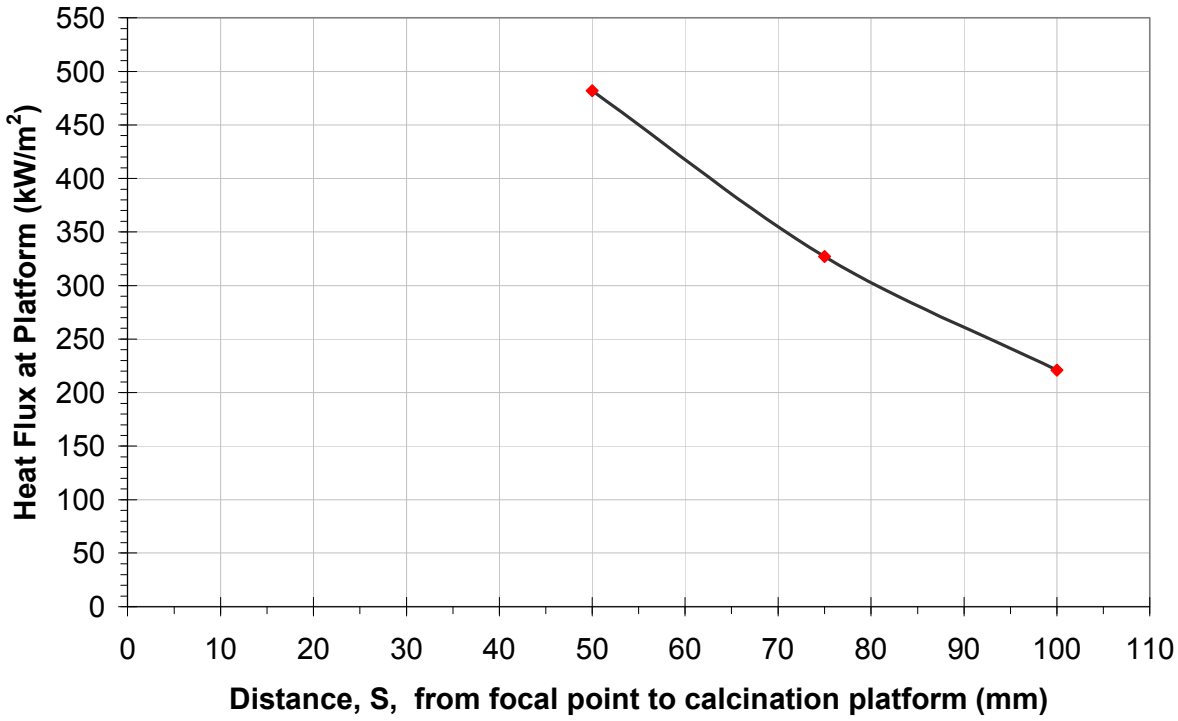

Figure 9-9: Calculated heat flux on the surface of the calcination platform at various distances S, from the focal point for the ETSF.

9.6.1 Sensitivity Analysis for the Enclosed Triangular Solar Furnace Modelling

This sensitivity analysis followed the same procedure as employed for the open system simulations. The reflectivity of the silver reflector "behind" the radiation source and of the aluminium mirror was varied from a maximum of 0.985 and 0.963 respectively to 10% degradation. The temperature of the calcination platform was varied by ± 2%, which accounts for measurement and data collection error.

Table 9-12 shows the resulting calculated heat flux received at the calcination platform. Also shown is the percentage change from the 'reference' heat flux parameters.

Table 9-12: Comparison of calculated heat flux at the simulated calcination platform, after changing various modelling parameters in the ETSF model.

Distance 'S' from the focal point	Parameter	Variation	Calculated Heat Flux Received at Platform kW/m^2	Percentage Change
100mm	Reflectivity of Reflector (from 0.97)	0.985 0.873	225.7 190.7	2.12% -13.72
	Reflectivity of Mirror (from 0.947)	0.963 0.852	227.4 182.9	2.91% -17.2%
	Platform Temperature (from 1444 K)	1473 1415	203.3 238	-7.99% 7.54%
75mm	Reflectivity of Reflector (from 0.97)	0.985 0.873	332.3 282.1	1.63% -10.6%
	Reflectivity of Mirror (from 0.947)	0.963 0.852	336.9 268.27	3.03% -17.9%
	Platform Temperature (from 1577 K)	1609 1545	301.7 350.8	-7.74% 7.29%
50mm	Reflectivity of Reflector (from 0.97)	0.985 0.873	488.8 437.9	1.42% -9.16%
	Reflectivity of Mirror (from 0.947)	0.963 0.852	496.9 393.6	3.09% -18.3%
	Platform Temperature (from 1735 K)	1770 1700	441.6 520.0	-8.38% 7.88%

Table 9-12 shows the same trends as for the open system sensitivity analysis presented in Section 9.5.1. The increase in reflectivity of both the reflector and mirror cause an increase in available heat flux at the calcination platform. Likewise, a decrease in reflectivity causes a decrease in heat flux. The 10% decrease in reflectivity of the mirror causes the highest heat flux loss of up to 18.3%. The same 10% reduction for the reflector causes a maximum 13.72% loss.

Increasing the platform temperature by 2% resulted in a decrease of up to 8.38% in the heat flux received at the platform. Similarly a decrease of platform temperature by 2% increased

the available heat flux by up to 7.88%. The inverse temperature relationship is caused by the temperature difference between the source and the platform, which is used to calculate the radiative heat transfer between the two bodies.

The worst case scenarios for the calculated heat fluxes for the ETSF, for the three distances from the focal point are presented in Table 9-13. The positive tolerance has been calculated using the scenario where the reflectivity of the reflector and mirror are at a maximum and the measured temperature of the platform is incorrect by 2%. The negative tolerance has been calculated where the mirror and reflector has degraded by 10% and the measured temperature is 2% higher.

Table 9-13: Variation in error for the calculated heat flux received at the surface of the calcination platform in the ETSF model.

Distance 'S' from the focal point (mm)	**Calculated Heat Flux at Platform located at distance S kW/m^2**	**Tolerance %**	**Tolerance kW/m^2**
100	221	+ 12.6 – 39.0	+ 27 – 86
75	327	+ 11.95 – 36.3	+ 39 – 119
50	482	+ 12.4 – 35.9	+ 60 – 173

9.6.2 Comparison of Calculated and Measured Heat Flux for the Enclosed Triangular Solar Furnace

A comparison is made between the calculated heat flux at the calcination platform from the RADEX simulation and the heat flux measured using the digital imagery techniques discussed in Chapter 5.

Table 9-14: Comparison of calculated and measured heat flux on the calcination platform for the ETSF.

Distance 'S' from the focal point (mm)	**Calculated heat flux from modelling kW/m^2**		**Measured heat flux kW/m^2**	**Difference %**
100	221	+ 27 – 86	200 ± 15	10.5
75	327	+ 39 – 119	300 ± 25	9
50	482	+ 60 – 173	450 ± 30	7.1

The calculated and measured values coincide reasonably well, with all of the uncertainty values (error bar values) overlapping. The calculated values are 7 to 10.5% higher than the measured values which is consistent with the measurements being taken with the rear wall removed. Removing the furnace wall would lower the measured heat flux because of escape of radiation through the large gap. This comparison is displayed graphically in Figure 9-10.

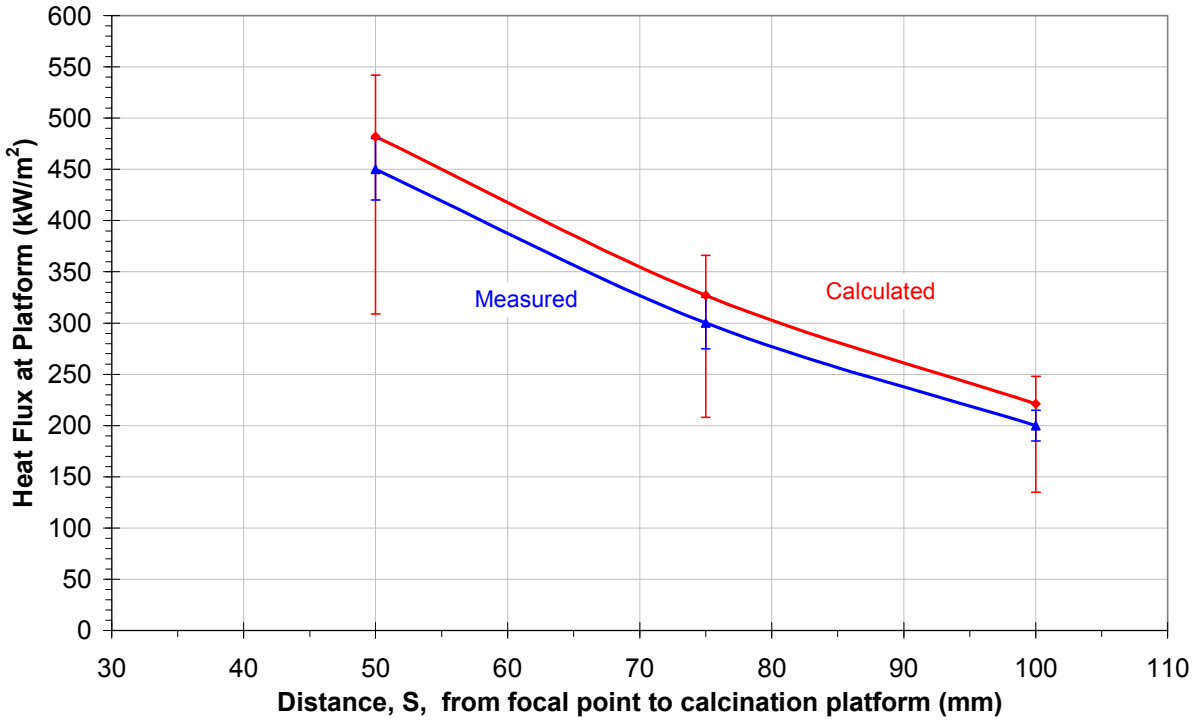

Figure 9-10: Comparison of calculated and measured heat flux on the calcination platform for the ETSF.

A second order polynomial line, Equation [9.17] for the calculated heat flux was fitted to the data as follows. This estimation can therefore provide heat fluxes for other distances (S) between 100mm and 50mm which were not modelled.

$$\text{Heat flux, } q = 0.040 \times S^2 - 11.18 \times S + 939.6 \ (\text{kW/m}^2) \qquad [9.17]$$

9.6.3 Comparison of Calculated Heat Flux between the Enclosed Triangular Furnace and the Open System

Figure 9-11 compares the calculated heat flux for the open system displayed in Table 9-10 with that for the ETSF. This shows that the heat flux on the calcination platform decreases with distance from the mirror, as expected. A comparison of the calculated values show a maximum 20% improvement in heat flux levels at the calcination platform by using this triangular cross sectional enclosure.

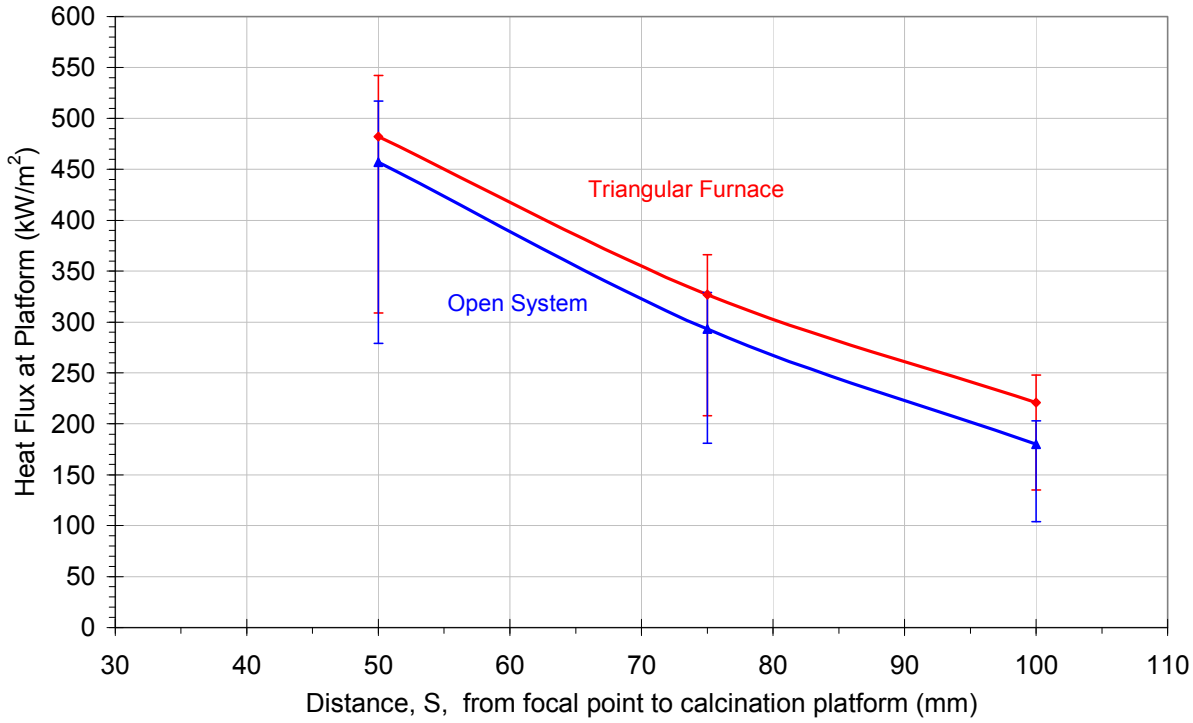

Figure 9-11: Comparison of calculated heat flux on the calcination platform for the ETSF and OSS for various distances S from the focal point.

9.7 Conclusions from the Multi-zone Modelling

This multi-zone two dimensional modelling has provided a method to simulate a solar radiation source and then predict the radiant heat flux on the base platform of an atmospherically-open flat bed furnace system and an ETSF. These furnaces represent the

systems used within the calcination experiments used within this research investigation. The zone method for radiation calculation was used to calculate the intensity of radiant heat flux on the floor (base platform) of each furnace, where the Penrice marble samples were positioned and thus the heat flux to which the marble is receiving was mathematical calculated.

Calibration of the calculated heat fluxes using the RADEX model was achieved by comparing the results to the measured heat fluxes from the heat flux density measurements of Chapter 5 and the measurements within the experiments of Chapter 7 and 8.

To match the measured heat flux of 16.03 kW/m^2 the pseudo-source temperature needed to be approximately 16196K. A source temperature of 25,400K was required for the OSS model and for the ETSF model. The sensitivity analysis for the calibration showed that using the maximum tolerance in measurement parameters within the model provided a $\pm$ 16% variation in the calculated heat flux. For the open and enclosed furnace models the sensitivity analysis showed a maximum variation of 42.2% and 39%, respectively, in the calculated heat flux at the calcination platform for a constant simulated solar source. The accuracy of these relatively simplified multi-zone models may be improved by finer zoning of the furnace walls. Due to time constraints, a sensitivity analysis to assess the effects of increasing the number of zones was not considered.

The results from the heat flux simulations show an increase in the heat flux on the calcination platform as the distance between the platform and focal point decreases. This was observed for both the OSS and ETSF.

The modelling shows a 20% increase in heat flux can be obtained at the location of the calcination platform if a ceramic fibre refractory triangular shaped enclosure is used. This finding is specific to the application, but shows an ability of the modelling method for other solar applications. The scalability of this modelling provides a significant base from which real sized furnaces and sun source modelling can progress. If such a model was to be used on a practical furnace, finer zoning on the furnace walls would be required due to the significant variation in temperature over the surface.

The calculated radiant heat flux values are used to evaluate the rate of calcination for various sized limestone particles within the mathematical calcination model presented in Chapter 10.

Chapter 10

Modelling the Calcination of Limestone

10.1 Introduction

There are several ways to mathematically represent gas-solid reactions depending on the rate controlling step. The three mathematical models discussed within Chapter 2 that are most commonly used are:

- the shrinking core reaction model,
- the uniform conversion model (homogeneous model), and
- the grain model.

The shrinking core model was selected because investigators such as Conley (1939), Satterfield and Feakes (1959), Ingraham and Marier (1963), Hills (1968), and Dennis and Hayhurst (1987) showed that the decomposition of limestone occurred at a distinctive boundary between the CaO and $CaCO_3$, which moved at a constant rate towards the middle of the particle. This is backed up by observations of Furnas (1931), who displayed cross sections of 25mm to 85mm diameter samples of partially calcined limestone that showed a distinctive narrow zone of calcination. To this author's best knowledge, to date, all mathematical modelling studies of the rate of calcination of limestone assume the stone is uniformly heated over its surface. Using solar radiant energy as the heat supply, the stone is not uniformly heated over the entire surface by the radiation, but from only one side. Salman and Khraishi (1988) observed that the calcination was not completed on the "dark side" of the sample and thus they did not obtain complete conversion for any of their experiments.

The standard shrinking core model equation developed by Hills (1968), assumes the core is concentric about the centre of the sample. This may not be the most appropriate approach for representing the current solar calcination process. Two alternative calcination models are therefore assessed; the standard shrinking core model using a concentric core and a shrinking core model where the core is offset to the lower side of the sample. A representation of these two models is shown graphically in Figure 2-5.

The mathematical calcination model developed here uses an energy balance approach to calculate the heat absorbed by the marble sample from the radiation source. The energy balance model then calculates the heat transferred between the participating mediums

around the marble sample to obtain the resultant energy available to heat and then calcine the sample.

The rate of temperature rise of the stone is calculated depending on the available resultant energy. The heating time, t_{cp}, is then calculated using the time taken for the stone's temperature to rise from ambient until the stone reaches the 1173K calcination temperature. The calcination time is then calculated by determining the conductive heat transfer across the newly formed lime layer to the reaction interface. The transfer of heat to the reaction interface depends on the difference in temperature between the reaction interface and the surface temperature. Three surface temperature scenarios have been investigated to determine which approach best accounts for the single sided heating.

The difference in the calcination model between the Open Solar System (OSS) and the Enclosed Triangular Solar Furnace (ETSF) is an increase of radiation received by the stone when enclosed. This increase in received radiation was measured (see Chapter 5) and modelled (see Chapter 9) and these are used as inputs to the present model.

The theoretical results from the energy balance calcination model are compared with the experimental measurements from the open system radiation calcination experiments and the enclosed triangular solar furnace calcination experiments.

The modelling was first conducted within a Microsoft Excel spreadsheet but then transferred into a MATLAB file format for ease of conducting the multiple calculations. The plots therefore appear slightly different from the Excel plots shown within other Chapters of this Thesis.

10.2 Model Overview

An energy balance approach is used to calculate the energy available for heating the stone and then available for the endothermic calcination reaction. The balance accounts for heating of the marble sample, by both the direct and indirect radiation from the radiation source, as well as radiative, convective and conductive energy exchange between the marble sample and the platform on which the sample is placed. Heat losses from the marble sample are assumed to be via radiation to the surrounding environment and natural convection to the surrounding atmosphere. The system domain is defined as the surface of the single marble sample which is resting upon the calcination platform, as shown in Figure 10-1.

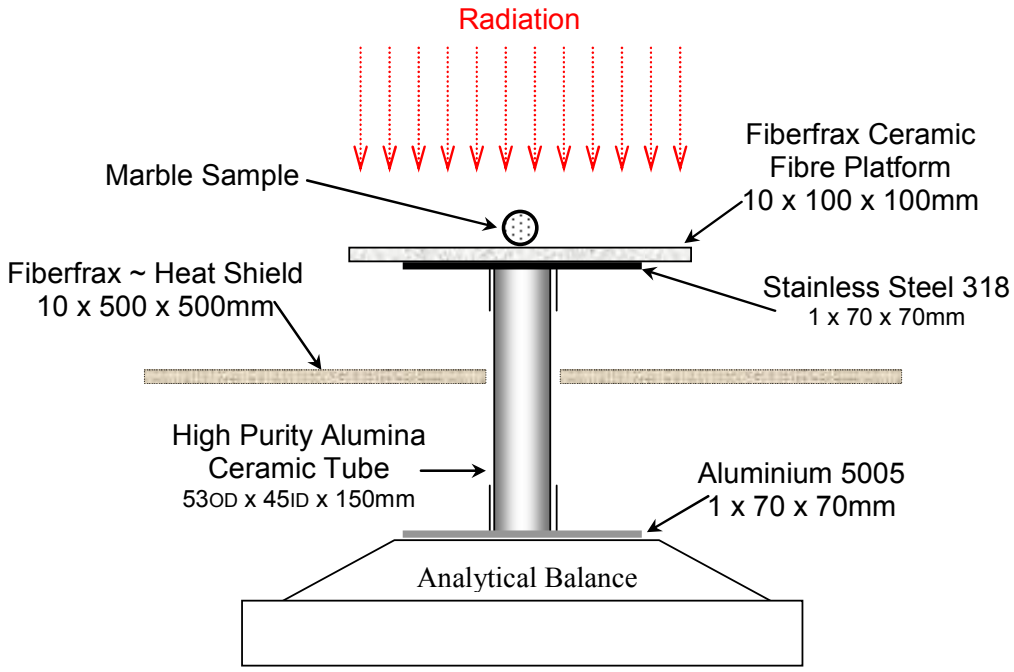

Figure 10-1: Representation of the marble sample on the platform irradiated by radiation.

The energy available, after accounting for heat losses, is first used to heat the marble sample from ambient to a temperature of 873K. Calcination begins on the surface of the marble sample at a temperature of around 873K as shown in Figure 2-2. The characteristics of the surface of the marble therefore change, causing a change in the energy balance which affects the rate of further heating. The marble is further heated to a temperature of 1173K at this new rate. During heating, 873K to 1173K, it is assumed that no further calcination progression occurs. Boynton (1980, pg 161), explains that, for the reaction to penetrate into the interior of the stone particle, attainment of temperatures considerably higher than the dissociation temperature (1173K) is necessary on the surface of the particle. This is mainly due to the extremely low thermal conductively of the newly formed lime layer. The calcination mathematical model presented here uses the conductive heat transfer equation to calculate the temperature differential between the surface and the interfacial reaction location. The two versions of the shrinking core model are then used to calculate the rate of calcination as the front moves through the marble sample.

The calculations for the calcination model were divided into two main sections:

1. Heating of the marble sample by the high intensity radiation and by the heated platform.
2. The calcination of the marble sample including the heat exchange between the marble sample, the heated platform and the surrounding environment.

The first section of the model uses an energy balance to evaluate the energy available for heating the stone. The measured mass of each stone size is used to calculate the volume and total surface area, which are used to calculate the projected area directly illuminated by the high intensity radiation. Solar absorptivity, and reflectivity values for white marble are then used to calculate the energy absorbed by the particle. The absorbed energy includes the radiant energy received from the heated platform by calculating the view factor relationship. This energy is divided into being either absorbed or reflected using values for low temperature radiation. The energy transfers via natural convective flows around the heated platform and conduction from the platform, add a small percentage of total heat available to the stone. The energy balance equates the total energy absorbed by the particle and balances it with the energy losses; such as the infrared radiation emitted from the particle as its temperature increases. The energy balance therefore calculates the amount of heat energy available for heating the stone. The heating rate is calculated using the specific heat values for limestone that are available of page 20 of Oates (1998).

The second section of the model calculates the calcination rate of the marble samples. The calculation includes an energy balance to account for the heat exchange between the marble sample, the heated platform and the surrounding environment. The energy balance calculates the amount of heat energy available for the calcination reaction. The calcination rates for the three nominal diameter marble samples used within the experiments are modelled using the two versions of the shrinking core model.

10.3 Assumptions Used in the Modelling

The following assumptions are used in the calcination model.

1) There is uniform, steady state heat flux irradiating the marble sample and the base platform from the radiation point source. It is assumed that the direct irradiation illuminates the projected area of the marble sample.

2) Uniform characteristic properties throughout the marble sample.

3) Fixed and uniform geometry of marble sample that does not change during the calcination process.

4) The calcination reaction begins on the surface of the particle at 873K, but the reaction front does not proceed into the stone until a surface temperature of 1173K has been achieved.

5) The average Nusselt number for the natural convective heat transfer from the platform to the surrounding air is calculated using *'a heated horizontal plate facing up'* and the natural convective heat transfer from the marble sample is calculated assuming '*an object which is spherical in shape*' both described by Mills (1999, pages 327 – 329).

6) There is conductive heat transfer between the stone and the calcination platform through the contact area between the two.

7) The radiative exchange from the marble sample to the surrounding environment is assumed to be from an area equivalent to 85% of the total surface area of the marble sample.

8) The effectiveness of the all heat transfer is 100%.

9) Heat loss from the escaping evolved CO_2 from the calcination reaction, is considered small compared to the radiative, convective and conductive heat transfers and is therefore neglected.

10) There is no accumulation of CO_2 within the newly formed pores in the CaO, and thus the calcination reaction front temperature does not increase as the front propagates through the limestone particle.

11) All temperatures and physical characteristics of the surrounds remain constant, e.g. furnace wall temperatures and dimensions, ambient temperatures, platform characteristics.

12) Possible sintering of the outer surface of the limestone particle is neglected at the higher heat fluxes. Sintering generally increases calcination time by impeding heat transfer from the surface to the calcination reaction zone within the particle.

10.4 Mass, Volume and Surface Area of the Marble Samples

These calcination calculations are based on the three different sized Penrice marble samples which have mass 0.333g, 1.000g and 3.000g. The mass tolerance for all three experimental marble samples was $\pm$ 0.005 grams.

The number of moles of $CaCO_3$ for each sized marble was calculated using a molecular weight of 100.09 g/mol. Table 10-1 shows this calculation and also the results from the remaining mass, volume and surface area equations.

The volume (m^3) of each marble sample was calculated by dividing the mass of the marble by the density, 2720 kg/m^3, as provided by Oates (1998, pg 18).

$$V_{CaCO_3} = \frac{m_{CaCO_3}(kg)}{\rho_{CaCO_3}(kg/m^3)} \qquad [10.1]$$

Using this volume calculation, the surface area of each sized marble particles are calculated using Equation [10.2]. This surface area (SA_{CaCO_3}) equation uses the median surface area between a sphere, a cylinder (assuming that the diameter and length were equal), and a cube, to account for its granular shape.

$$SA_{CaCO_3} = \frac{4\pi\left(3V_{CaCO_3}/4\pi\right)^{2/3} + \left(6\pi\left(V_{CaCO_3}/2\pi\right)^{2/3}\right) + \left(6\times\left(V_{CaCO_3}\right)^{2/3}\right)}{3} \qquad [10.2]$$

The characteristic diameter of each marble sample size was then calculated by first computing the volume of an equivalent sphere (V_{eq}) which has a surface area as calculated in equation [10.2] and then calculating the diameter of that spherical shape. The equations that describe these are shown in Equations [10.3] and [10.4].

$$V_{eq} = \left(\frac{SA_{CaCO_3}}{4\pi}\right)^{3/2} \times \frac{4\pi}{3} \qquad [10.3]$$

$$d_C = 2\times\left(\frac{3V_{eq}}{4\pi}\right)^{1/3} \qquad [10.4]$$

The area illuminated directly by the high intensity radiation was calculated as being the projected area of the spherical shape as calculated using Equation [10.5].

$$A_{Proj} = \pi\left(\frac{d_C}{2}\right)^2 \qquad [10.5]$$

The results from the mass, volume and surface area calculations for the three sizes of marble sample are shown in Table 10-1.

Table 10-1: Calculated number of moles, volume, total surface area, characteristic diameter and projected area of the Penrice marble samples.

Mass of Sample	**Number of Moles of $CaCO_3$ (n)**	**Volume of Sample** V_{CaCO_3}	**Total Surface Area** SA_{CaCO_3}	**Characteristic Diameter** d_C	**Projected Area** A_{Proj}
gram	mol	m^3	m^2	mm	m^2
0.333	0.00333	1.224×10^{-7}	1.346×10^{-4}	6.54	3.36×10^{-5}
1.000	0.00999	3.676×10^{-7}	2.801×10^{-4}	9.44	7.00×10^{-5}
3.000	0.02997	1.103×10^{-6}	5.826×10^{-4}	13.62	1.46×10^{-4}

Having specified the physical characteristics of each stone, the energy balance is now addressed.

10.5 The Energy Balance

Using the conservation of energy, a theoretical transient temperature energy balance has been calculated on each marble sample. The first law of thermodynamics is the conservation of energy, which in a closed system can be presented using Equation [10.6].

$$Q - W = \Delta U \qquad [10.6]$$

Here: Q is the heat supplied into the system,

W is the work done by the system,

ΔU is the change in internal energy.

Applying the conservation of energy to the irradiation of the marble, Equation [10.6] transforms to:

$$q_{in} = \frac{\partial U}{\partial t} + \left(\frac{\partial q_x}{\partial x} + \frac{\partial q_y}{\partial y} + \frac{\partial q_z}{\partial z} \right) \qquad [10.7]$$

Here: q_{in} is the heat flux supplied to the system,

U is the internal (chemical) energy,

t is time,

q is the heat flux vector field, in either the x, y or z direction

Equation [10.7] can be stated more simply as:

$$q_{in} = \frac{\partial U}{\partial t} + div \cdot q \qquad [10.8]$$

Equation [10.8] describes the heat supplied into the system to equal the change in internal chemically energy over time used for the reaction, plus the sum of all the heat fluxes, conduction convection and radiation occurring within the system. Figure 10-2 displays the heat flux exchanges between the radiation source, the marble sample and the platform on which it sits. The 'positive heat in' to the system of interest sign convention has been used.

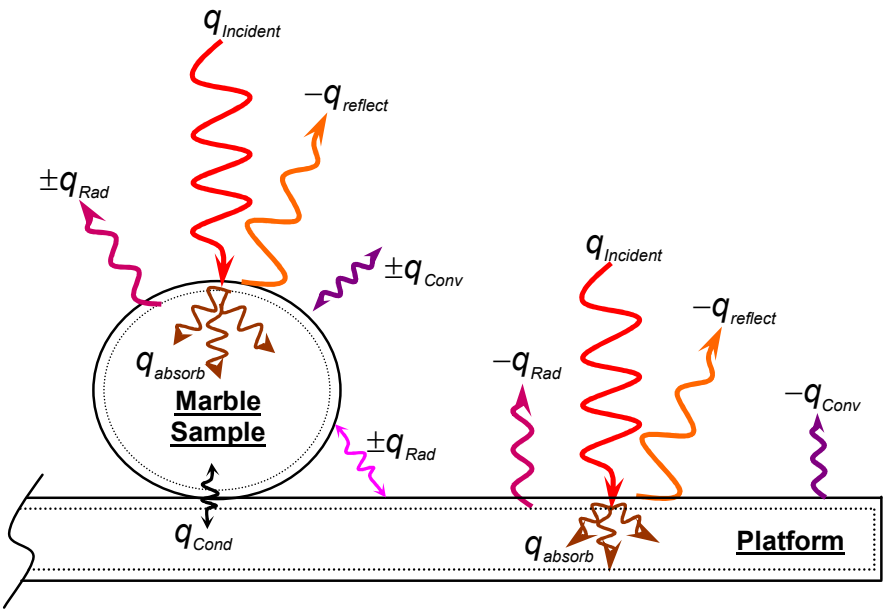

Figure 10-2: Heat flux exchange between the radiation source, the marble sample and the calcination platform.

The energy balance on the surface of the marble sample can be written as:

$$q_{absorb} = q_{Incident} - q_{reflect} + q_{conduction} + q_{convection} + q_{radiation} \qquad [10.9]$$

The source radiation $q_{Incident}$, is assumed to be uniform in intensity and is either reflected from the surface or absorbed into it. Opaque solid bodies do not transmit thermal radiation, therefore the transmissivity component of the source radiation is zero. The reflected heat flux is assumed to be lost to the surrounding environment and takes no further part in the calculations. The conductive component $q_{conduction}$, is the energy transfer between the marble sample and the platform. The convective component $q_{convection}$, consists of two components: 1) the energy transfer between the platform and the boundary layer air and 2) the energy transfer between the boundary layer air and the marble sample. The radiative component, $q_{radiation}$, also consists of two components: 1) the energy transfer between the platform and the marble sample and 2) the energy transfer between marble sample and the surrounding

environment. The resulting heat energy absorbed by the marble sample is assumed to be available for first heating the marble and then for the calcination reaction.

The equations used to calculate each component of Equation [10.9] are displayed in the following four equations [10.10] to [10.13]. Additionally each component is discussed in depth in the following Sections of this chapter.

$$q_{reflect} = (1-\alpha)\, q_{Incident} \qquad [10.10]$$

$$q_{radiation} = \varepsilon\, A\sigma(T^4_{Surface} - T^4_{Surround}) \qquad [10.11]$$

$$q_{convection} = h_C A(T_{Surface} - T_{Air}) \qquad [10.12]$$

$$q_{conduction} = h_i A\left(T_{Platform} - T_{Limestone}\right) \qquad [10.13]$$

Here:

α is the absorptivity of the marble sample, either $CaCO_3$ or CaO, or platform.

ε is the emissivity of the marble sample, either $CaCO_3$ or CaO, or platform.

A is the surface area over which the heat transfer is taking place.

σ is the Stefan-Boltzmann constant 5.6697×10^{-8} W/m^2.K^4.

$T_{Surface}$ is the surface temperature of the marble sample or platform.

$T_{Surround}$ is the temperature of surrounding surfaces.

T_{Air} is the temperature of the surrounding air.

$T_{Limestone}$ is the surface temperature of the marble sample.

h_C is the natural convective heat transfer coefficient.

h_i is the interfacial conductance.

The intensity of the heat flux ($q_{Incident}$) irradiating the marble sample and platform was measured during the experiments and for ease of calculation is assumed to be uniform over the entire surfaces. The temperature of the platform was also measured and again for ease of calculation, is assumed to be uniform over the entire surfaces. The temperature of the platform was measured to increase as the intensity of the heat flux on it increased, as shown in Tables 9-7 and 9-11.

10.5.1 Reflectivity, Absorptivity and Emissivity

Both the marble sample and platform are opaque, therefore the fraction of incident radiation reflected from the surfaces are calculated using the absorptivity Equation [10.14].

$$\rho = 1 - \alpha \qquad [10.14]$$

Where: ρ is the reflectivity of the surface, and

α is the absorptivity.

Radiation absorptivity is the process by which the energy of a photon is absorbed by a surface. The absorptivity of real surfaces depend on the wavelength of the incident radiation and the temperature of the body which is being irradiated, as described by Mills (1999, pg 572). Gubareff *et al*. (1960) discuss how the solar absorptance values can not be obtained from emittance data, because emittance data for solid materials exists only for temperatures far below that of the sun. The absorption of solar radiation by the marble sample and platform is modelled as a function of the illuminating radiation, as opposed to the emissivity which is a function of its temperature.

The spectrum of the xenon arc radiation source used in the present experiments is close to that of the solar spectrum. About half of the available energy within the solar spectrum lies in the visible bands of the electromagnetic spectrum and the other half in the near-infrared bands. The radiation spectrum to which the marble sample is illuminated can be represented as a blackbody with a temperature of 5,960 K.

The measurement of the emissivity and absorptivity of the Penrice marble (limestone) used in the experiments was not available and therefore literature based values are used. A valuable source of solar absorptivity data for marble / limestone is a survey of thermal radiation properties conducted by Gubareff *et al*. (1960). It should be noted that the solar absorptivity values listed in Table 10-2 are from the “building materials” section of Gubareff’s book.

Table 10-2: Solar absorptivity for marble and limestone.

Material	Solar Absorptivity
Marble	
White	0.44
Ground, unpolished	0.465
Cleavage	0.592
Limestone	
Anston	0.60
Bath	0.53
Clipsham	0.46
Indiana	0.571
Ketton	0.42
Portland	0.36
Steetley	0.33

The types of limestone and marble listed in Table 10-2 encompass a range of calcium carbonate materials that have been formed by different deposition processes. This accounts for the variations in absorptivity values. The “Summary of Operations - Penrice Mine” provides a description of the deposition processes for the material used in the experiments. It states: " deposit of fine to medium grained marble which originated from an early Cambrian (Normanville and Kanmantoo Groups) marine transgression dominated by carbonate sedimentation (i.e. limestone). This limestone was subsequently metamorphosed (i.e. Temperature and pressure) to marble and subjected to folding and faulting". The limestone most comparable to the Angaston deposit is the one from Bath. Jenkins (2008) describes the bath limestone as being a marble or travertine, i.e. a metamorphosed or hot spring precipitation limestone. The solar absorptivity value for Bath limestone (0.53) provides a useful first approximation.

An additional consideration in the selection of an appropriate value is the way the rock breaks apart when crushed to provide the appropriate sizes. The crushing process breaks the rock along its cleavage lines producing the small sized stones. These smaller stones were used in the experiments. The solar absorptivity value for cleavage white marble (0.592) provides a second useful estimate.

Because of the similarity in the two values it was decided to use the average between the two, so that a value of 0.561 was assumed to be the solar absorptivity of the Penrice Angaston marble.

The absorptivity of the marble to the low temperature infrared radiation from the platform has a different value to that for the broad spectrum solar radiation. A monochromatic (total) absorptance value of 0.93 has been calculated using Planck's Law and fractional functions for spectral absorption coefficients for calcite ($CaCO_3$) given in Table 326 of Gubareff *et al*. (1960). Coblentz (1913) provides a diffuse reflecting power value of 0.064 at a wavelength of 4.4μm (Wien's displacement law temperature of 660K) for white marble; $CaCO_3$, ground, unpolished. Using the grey surface assumption this reflectivity value equates to an absorptivity of 0.936. Holman (1968) quotes a value of 0.95 at room temperature. An absorptivity value of 0.933 has thus been selected for the absorption of radiation by the Penrice marble of the radiation from the heated platform.

The calcination reaction begins on the surface of the limestone at 873K as stated within the assumptions. There is therefore a period of heating, 873K to 1173K, where the surface characteristics have changed from that of marble to calcium oxide (lime) product. The absorptivity and emissivity values of the surface are therefore different during this heating period. The thickness of the CaO layer is assumed to be only a few nanometres thick and does not change the weight of the stone.

Several options for the value of solar absorptivity of lime (CaO) are shown in Table 10-3. A solar absorptivity value of 0.445 was selected, which represents the average value of Table 10-3.

Table 10-3: Solar absorptivity of lime.

Source: Gubareff *et al*. (1960)

The absorptivity of the lime surface to the low temperature infrared radiation from the platform was selected again from Gubareff *et al*. (1960) who provide a total absorptivity of

0.27 for pure CaO with grain size 3-5 microns at a temperature 850°C (rising to 0.275 at 1275°C).

Emissivity is the ratio of energy radiated by the particle to that by a blackbody at the same temperature, as described in most heat transfer books. Literature on the emissivity value for limestone (white marble) varies considerably between numerous authors, due to variations in the type and characteristics of the limestone investigated. A monochromatic emissivity value as low as 0.2 was used by Hills (1968) while higher values between 0.92 – 0.95 are quoted by Gubareff *et al*. (1960), Mills (1999) and Siegal and Howell (2001). Emissivity values used by Lipinski and Steinfeld (2004) were sourced from Touloukian (1972). The total hemispherical emissivity values are defined for two distinct band-widths separated at a specific wavelength:

$$\text{Emissivity of } CaCO_3 = \quad 0.19 \text{ for } \lambda \leq 2400\text{nm}$$

$$\text{and} \quad = \quad 0.81 \text{ for } \lambda > 2400\text{nm}$$

Nangia *et al*. (1988) developed Equation 10.15 for Linwood limestone which provides the normal total emittance as a function of temperature over the range 711K and 1228K.

$$\varepsilon_{CaCO3} = 0.821 - 1.25 \times 10^{-4} \times T \qquad [10.15]$$

An extrapolation of Equation [10.15] was performed to include temperatures down to 298 K assuming the same linearity. The emissivity of Penrice marble during the initial heating up period is therefore calculated to range between 0.784 (at 298K) and 0.712 (at 873K).

After the marble sample reaches 873K, the surface of the stone changes from $CaCO_3$ to CaO. The emissivity of the surface therefore changes due to the change in surface characteristics of the stone. Unfortunately the measurement of the emissivity of the resulting quicklime was not available and therefore a calculation based upon theoretical values is used. Table 10-4 shows the emissivity values for calcium carbonate and lime reported in the literature.

Table 10-4: Emissivity of lime.

Material	Emissivity
CaO	0.78 † Calculated from reflectivity
	0.41 for $\lambda \leq 2400$nm 0.59 for $\lambda > 2400$nm ††
Lime clay	0.43 † At 1645 K
Lime mortar	0.90 to 0.92 † 310K to 533K
Dolomite lime	0.41 †

Source: † Gubareff *et al*. (1960)
†† Lipinski and Steinfeld (2004)

The values from Lipinski and Steinfeld (2004) were selected for two reasons; firstly CaO has a known composition as opposed to the lime mortar or clay which could also contain additional compounds, and secondly the values could be scaled with temperature in accordance with Wien's displacement law. The resulting linear expression, Equation [10.16], relates the normal total emittance to temperatures between 298K and 2400K.

$$\varepsilon_{CaO} = 0.615 - 8.89 \times 10^{-5} \times T \quad [10.16]$$

Table 10-5 shows the reflectivity values for the reflection of the direct solar irradiation, and the infrared radiation, from the surface of the marble sample during the heating and calcination stages. These reflectivity values were calculated using Equation [10.14] and the selected absorptivity values.

Table 10-5: Reflectivity from the surface of the marble for solar and infrared radiation.

ρ_{CaCO3_Solar}	0.439
ρ_{CaCO3_IR}	0.067
ρ_{CaO_Solar}	0.54
ρ_{CaO_IR}	0.73

The platform was assumed to be a grey surface and isothermal at a constant irradiation intensity. The technical data sheet provided by the manufacturer states the emissivity of the surface of the FiberFrax Duraboard platform to be 0.9. Using the grey body assumption the values of reflectivity and absorptivity are therefore 0.1 and 0.9 respectively.

10.5.2 Radiant Heat Transfer between the Sample and the Platform

The net radiant heat exchange between an arbitrary surface 1 and arbitrary surface 2 is calculated using:

$$\dot{Q}_{1-2} = E_{b1} A_1 F_{1-2} - E_{b2} A_2 F_{2-1} \qquad [10.17]$$

Where: E_b is the total emissive power of each surface (σT^4),
A_1 and A_2 are the areas of object 1 and 2 respectively,
F_{1-2} and F_{2-1} are the view factors.

The view factor between the stone sample and the platform was calculated assuming that the stone can be modelled as a sphere and the square platform modelled as a disc. The view factor that most closely represents this situation is a *sphere to coaxial disc* provided by Howell (2007) which is shown graphically as Figure 10-3. The view factor equation is shown as Equation [10.18]. The distance (a) between the sphere (A_1) and the platform (A_2) is assumed to be half of the characteristic diameter (i.e. radius) of the marble sample. The radius (r) of the flat disc is assumed to be half the length of the experimental platform equalling 50mm.

NOTE:
This figure is included on page 286 of the print copy of the thesis held in the University of Adelaide Library.

Adapted from Howell (2007)

Figure 10-3: Representation of the view factor: sphere to coaxial disk in a parallel plane.

$$F_{1-2} = \frac{1}{2}\left[1 - \frac{1}{\left(1+\left(\frac{r}{a}\right)^{1/2}\right)}\right] \qquad [10.18]$$

Table 10-6 shows the view factor calculations from Equation [10.18] for the three stone sizes.

Table 10-6: View factors for stone to platform radiation exchange.

Penrice Marble Nominal Diameter, d_c	**6.54mm**	**9.44mm**	**13.62mm**
View Factor F_{1-2}	0.4673	0.4530	0.4325

These calculated values are in line with a view factor value of 0.5 stated by Mills (1999), for a sphere near a large plane area.

The view factor between the platform and the stone was calculated using a *rectangle to coaxial disk in a parallel plane* representation shown graphical as Figure 10-4, with associated equation [10.18] provided by Howell (2007). The distance (D) between the disc (A_2) and the platform (A_1) is assumed to be the radius of the marble sample. The surface area of the flat disc facing the platform is calculated as the projected area of the marble sample. The size of the platform (B x L) is assumed to be the breadth and length of the experimental platform which was 100mm. The maximum error for this equation is quoted as being ± 12.59%.

NOTE:
This figure is included on page 287 of the print copy of the thesis held in the University of Adelaide Library.

Adapted from Howell (2007)

Figure 10-4: Representation of the view factor: rectangle to coaxial disk in a parallel plane.

The view factor of the platform to the stone is given as:

$$F_{1-2} = \frac{3.2718\left(1 + D^{1.6491}\right)^{0.2834}}{\left[D^{1.5138} + \left(BL\right)^{0.495}\right]^{2.0417}} \qquad [10.19]$$

Table 10-7 shows the view factor calculations from Equation [10.19] for the three stone sizes.

Table 10-7: View factors for platform to stone radiation exchange.

Penrice Marble Nominal Diameter, d_c	**6.54mm**	**9.44mm**	**13.62mm**
View Factor F_{1-2}	0.00370	0.00755	0.0152

The net radiant heat exchange between the platform and the stone is then calculated using Equation [10.17]. It should be noted that if the temperature of the stone is greater than the platform, then negative values are calculated which represent the loss of heat from the sample which is in line with the 'positive heat in' sign convention discussed previously.

10.5.3 Convective Heat Transfer

Convective heat transfer occurs between the hot platform and marble sample due to the heating of the boundary layer air above the platform. The air is considered to flow concentrically over the top surface of the platform towards the centre where the marble sample is located. The air temperature increases from ambient at the edge of the platform to a maximum at the centre of the platform. The air temperature is also hotter closer to the surface of the platform and decreases with distance from the platform. This boundary layer of air is assumed laminar, and uniform in thickness over the entire plates surface.

The thickness (δ) of the boundary layer was calculated using an equation from Kozanoglu and Lopez (2007) presented here as Equation [10.20]:

$$\delta = 0.0014 Ra_L^{0.24} \qquad [10.20]$$

This equation therefore requires the calculation of the Rayleigh number ($\mathbf{Ra_L}$), which is shown as Equation [10.23]. The Rayleigh number is a function of the Prandtl and Grashof numbers, the temperature of the boundary layer air and the characteristic length of the platform. The Prandtl, Grashof and Rayleigh numbers for the heated platform are given by:

$$\mathrm{Pr} = \frac{C_p \mu}{k} = \frac{\nu}{\alpha} \qquad [10.21]$$

$$Gr_L = \frac{g\beta \Delta T L^3}{\nu^2} \qquad [10.22]$$

$$Ra_L = Gr_L \times \mathrm{Pr} = \frac{g\beta \Delta T L^3}{\nu\alpha} \qquad [10.23]$$

where: ***g*** is gravitational acceleration, m/s^2

β is the thermal expansion coefficient. For an ideal gas $\beta = \frac{1}{T_m}$

T_m is the mean temperature, K

Pr is the Prandtl number = 0.6989 for air at ambient temperatures,

ν is the kinematic viscosity of air at a mean temperature m^2/s

α is the thermal diffusivity of air at a mean temperature, m^2/s

L is the characteristic length of the platform.

An iterative approach was used to calculate the boundary layer air temperatures shown in Table 10-8. These temperatures account for the temperature of the calcination platform (1310K to 1735K), the temperature of the ambient air (298K), and the increasing temperature of the sample (ambient to 1173K).

The boundary layer thickness (Equation [10.20]) was then calculated, and is displayed in Table 10-8.

The heat transfer from the platform to the boundary layer air is calculated using:

$$q_{conv,plat} = h_c A \left(T_{Platform} - T_{Air}\right) \qquad [10.24]$$

The convective heat transfer coefficient for the platform is then calculated using:

$$h_c = \left(\frac{k}{L}\right) Nu_L \qquad [10.25]$$

The average Nusselt number for an isothermal horizontal surface, 0.1m x 0.1m surrounded by air is given within Radziemska and Lewandowski (2005):

$$\overline{Nu}_L = 1.216\, Ra_L^{1/5} \quad \text{for } 10^4 < Ra_L < 10^7 \qquad [10.26]$$

The heat transfer between the heated air and the marble sample was then calculated using:

$$q_{conv,sample} = h_c A \left(T_{Air} - T_{Sample}\right) \qquad [10.27]$$

Where the heat transfer coefficient for the marble sample is calculated similarly to Equation [10.25] with the average Nusselt number being for '*an object which is spherical in shape*' described by Mills (1999) to be:

$$\overline{Nu}_D = 2 + 0.43 Ra_D^{1/4} \qquad [10.28]$$

It should be noted that these heat transfer equations assume a heat transfer effectiveness of 100%. Additionally, the surface area over which the convective heat transfer takes place is assumed to be three quarters (75%) of the total surface area of the marble sample. This surface area was selected after consideration of the upward flow pattern over the sample, and it also accounts for uncertainty in the uniformity of the air temperature.

The average characteristic specifications for the air around the heated platform used within this model is displayed within Appendix F which were calculated using the computer program by Youn *et al*. (1995).

Table 10-8: Calculated air temperature of the natural convection boundary layer using the measured platform temperatures.

Heat Flux (kW/m^2)	**Platform Temperature (K)**	**Calculated Air Temperature Above Platform (K)**	**Boundary Layer Thickness δ (mm)**
Open System			
175	1310	802	40.97
280	1476	885	38.87
430	1696	995	35.45
Triangular Furnace			
200	1444	870	38.40
300	1577	936	36.98
450	1735	1015	34.97

10.5.4 Conductive Heat Transfer

Conductive heat transfer occurs between the marble sample and the platform as the sample rests upon the surface of the platform. The conductive heat transfer is calculated using Equation [10.29] :

$$q_{conduction} = h_i A\left(T_{Platform} - T_{CaCO_3}\right) \qquad [10.29]$$

Here: h_i is the interfacial conductance (W/m^2.K)

A is the contact area (m^2)

T is the temperatures of the platform and marble sample (K)

Data for the contact resistances for the interfacial conductance (h_i), for the solid to solid interface is sparse and unreliable, as stated by Mills (1999). A value of 1750 W/m^2.K was selected from the range 500 – 3000 W/m^2.K given for ceramic to ceramic interfaces, Mills (1999) Table 2.1.

The contact area (A) was calculated by dividing the gravitational force (N) on the stone sample by the specified deformation compressive strength of 0.36×10^6 N/m^2 for the FiberFrax Ceramic Fiber Duraboard platform. Figure 10-5 shows a representation of the assumed spherical marble sample placed upon the platform and the contact area being calculate which is shown in Table 10-9.

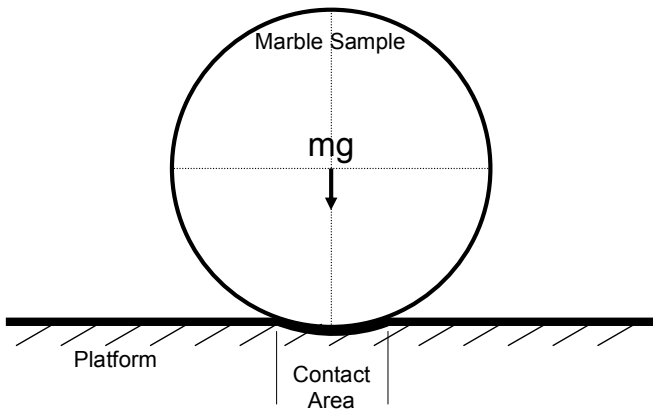

Figure 10-5: Representation of the contact area between the marble sample and the platform.

Table 10-9: Calculated contact area between the marble sample and the platform.

Stone size	**6.54mm**	**9.44mm**	**13.62mm**
	0.333 g	**1.000 g**	**3.000 g**
Contact area between sample and platform mm^2	9.07×10^{-3}	2.78×10^{-2}	8.17×10^{-2}

The present model assumes, the temperature of the platform to be constant and uniform for a specified illumination heat flux intensity. The platform's temperature ($T_{Platform}$) was measured during the experiments as discussed in Section 5.3 and presented in Table 10-8. The measured temperatures were plotted against the measured heat flux and a second order polynomial curve-fit produced for each of the OSS experiments and the ETSF experiments.

Equation [10.30] equates the platform temperature ($T_{Platform}$) to the heat flux on the platform ($q_{Incident}$) for the open system ($_{OS}$), while Equation [10.31] equates the platform temperature to the heat flux on the platform for the triangular solar furnace ($_{TSF}$).

$$T_{Platform,\,OS} = -1.58 \times 10^{-9} \times q_{Incident}^{\,2} + 2.45 \times 10^{-3} \times q_{Incident} + 926 \quad [10.30]$$

$$T_{Platform,\,TSF} = -1.19 \times 10^{-9} \times q_{Incident}^{\,2} + 1.94 \times 10^{-3} \times q_{Incident} + 1104 \quad [10.31]$$

For example a $q_{Incident}$ value of 200kW/m^2 equates to a calcination platform temperature of 1352K for the open system and 1444K for the furnace enclosure.

10.6 Time to Heat the Marble to the Calcination Temperature

The components of heat transfer in Equation [10.9] are presented first, after which the calculated time to raise the temperature of the three marble samples to 900°C (1173 K) is presented.

The first and most dominant heating source is the radiant power received, reflected and absorbed from the direct illumination from the radiation source. The distribution of the calculated values for the three different sized marble samples is shown in Table 10-10. The displayed results are the same for both the OSS and the ETSF for a $q_{Incident}$ heat flux value of 200 kW/m^2.

Table 10-10: Energy distribution of 200kW/m^2 direct radiation received by the three marble sample sizes.

Radiation heat flux	200,000 W/m^2		
Nominal diameter d_c	6.54mm	9.44mm	13.62mm
Direct radiation received	6.72 W	14.0 W	29.1 W
Surface $CaCO_3$ (298K to 873K)			
Radiation reflected from sample	3.58 W	7.46 W	15.5 W
Radiation absorbed by sample	3.14 W	6.54 W	13.6 W
Surface CaO (873K to 1173K)			
Radiation reflected from sample	3.63 W	7.56 W	15.7 W
Radiation absorbed by sample	3.09 W	6.44 W	13.4 W

Table 10-10 shows the similarity in the energy reflected and absorbed from the direct radiation between when the $CaCO_3$ or CaO surface of the sample. Also shown is the increase in energy absorbed with the increase in sample size, which is due to the increase in illuminated surface area of the sample. This increase is shown graphically in Figure 10-6 which displays the linear relationship between the radiant heat flux from the source (X axis) and the energy absorbed into each of the three samples (Y axis) for both the ETSF and OSS. The energy absorbed for the ETSF is an average 12.8% higher than for the OSS. A comparison of the three sample sizes shows an increase in received heat because of the increase in illuminated surface area of the sample.

The next heating source for the marble sample is the infrared radiation from the platform. Equation [10.19] is used to calculate the radiative heat transfer between the platform and stone, with the view factors displayed in Table 10-6 used for each of the stones sizes. Equations [10.30] and [10.31] are used to represent the platform temperatures shown in Table 10-8 for each radiant heat flux within the OSS and ETSF systems. The platform temperature remains at steady state for each variation in illuminating radiant heat flux.

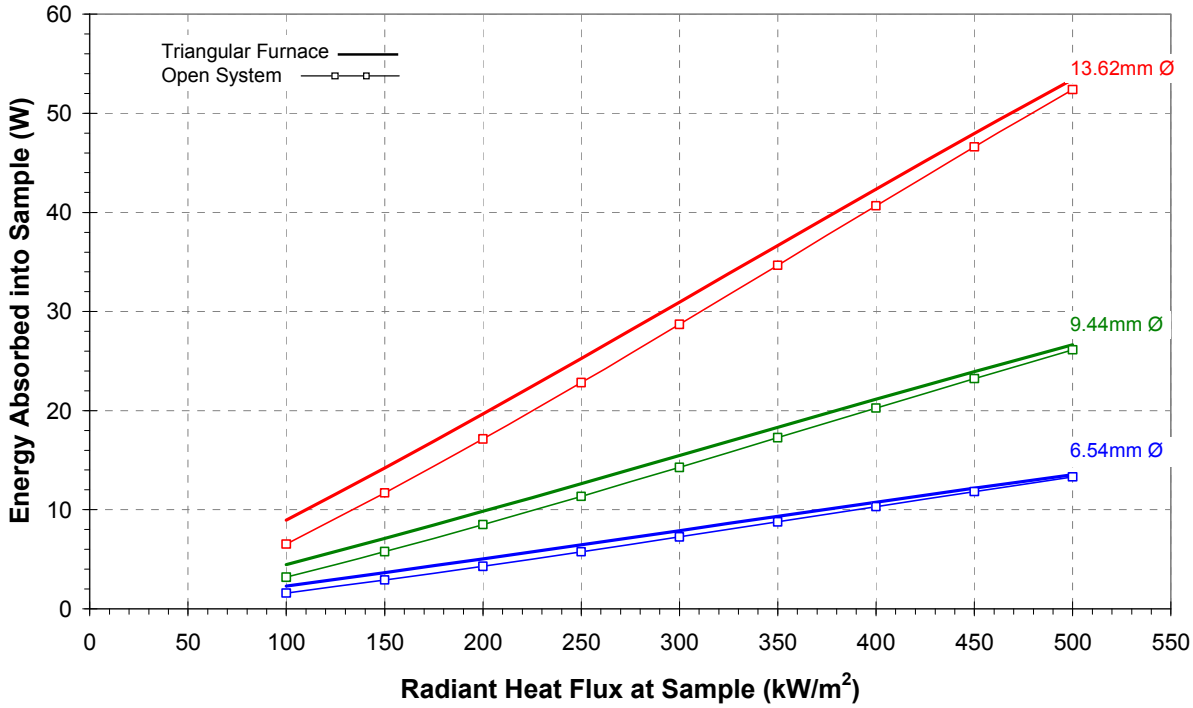

Figure 10-6: Plot showing the calculated energy absorbed by the sample as a function of heat flux from the radiation source received by the three marble samples for the enclosed triangular solar furnace (solid line) and the open solar system (broken line).

Figures 10-7 and 10-8 show the calculated radiant heat transfer between the hot calcination platform and the 1.000g (9.44mm nominal diameter) marble sample as a function of marble temperature, for the OSS and ETSF. A typical value for heat flux ($q_{Incident}$) of 200 kW/m^2 has again been used which produces a steady state platform temperature of 1352K for the OSS and 1444K for the ETSF.

The plots show a reduction in heat transfer from the platform as the sample temperature increases. Also seen is that 93% of the heat received from the platform is absorbed by the stone until the surface of the stone changes from $CaCO_3$ to CaO at a temperature of 873K. After this sample temperature the absorptivity reduces to 27% of the received heat and the reflectivity increases from 7% to 73%. There is therefore less energy available from the heated platform after the sample temperature increases beyond 873K.

Comparing the two plots, the furnace enclosure provides up to 30% more radiation than the open system over the entire sample temperature range. The radiative heat transfer between the platform and the sample in the furnace enclosure is higher because the platform temperature is higher. Similar plots where produced for the 6.54mm and 13.62mm marble samples for both the OSS and ETSF. These plots are presented in Appendix G.

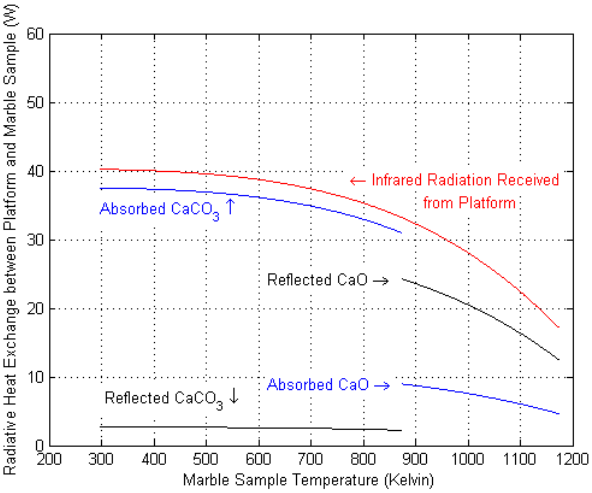

Figure 10-7: Calculated radiative heat transfer between the platform and the 9.44mm (1.00g) marble sample for a fixed direct heat flux of 200kW/m^2 in the Open Solar System (OSS).

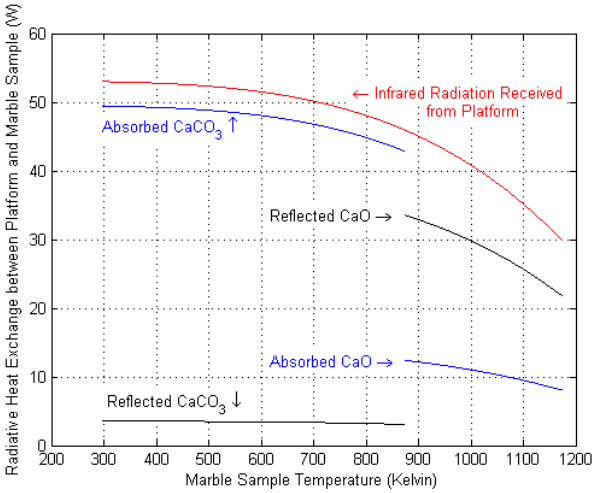

Figure 10-8: Calculated radiative heat transfer between the platform and the 9.44mm (1.00g) marble sample for a fixed direct heat flux of 200kW/m^2 in the Enclosed Triangular Solar Furnace (ETSF).

The conductive heat transfer component of Equation [10.9] between the hot platform and the marble sample is addressed next. Equation [10.29] is used to calculate the conductive heat transfer between the platform and stone, with the contact areas displayed in Table 10-9 used for each of the stones sizes. The steady state platform temperature for each variation in illuminating radiant heat flux was represented using Equations [10.30] and [10.31].

The results for the conductive heat transfer between the hot platform and the three nominal diameter marble samples as a function of marble temperature, for the OSS and ETSF are shown in Figures 10-9 and 10-10. Again a typical value for heat flux ($q_{Incident}$) of 200 kW/m^2 has been used for the displayed plots.

The plots show a decrease in heat transfer from the platform as the sample temperature increases. Also shown is an increase in heat transfer for an increase in stone size. This relationship follows the increase in contact surface area (Table 10-9) between the platform and each stone size.

Comparing the two plots, the ETSF provides approximately 32% more heat transfer from the platform than the OSS when the sample temperature is 298K, and up to 74% more heat when the sample temperature is 1173K.

As would be expected the heat transfer via conduction between the hot platform and the marble sample is relatively small, approximately 0.25%, compared to the other forms of heat transfer. This is because the contact area between the platform and the marble sample is quite small. Figures 10-9 and 10-10 show the calculated conductive heat transfer between

the platform and the three marble samples for a fixed direct heat flux of 200kW/m^2 for the OSS and ETSF respectively. Similar trends in the conductive heat transfer results were found for other incident heat fluxes ($q_{Incident}$).

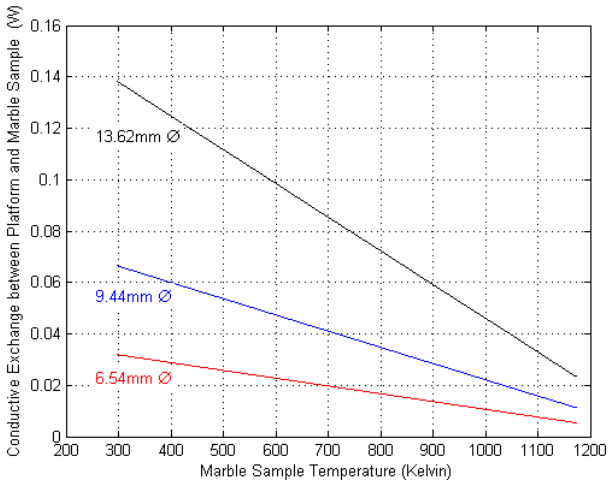

Figure 10-9: Calculated conductive heat transfer between the platform and the three marble samples for a fixed direct heat flux of 200kW/m^2 in the OSS.

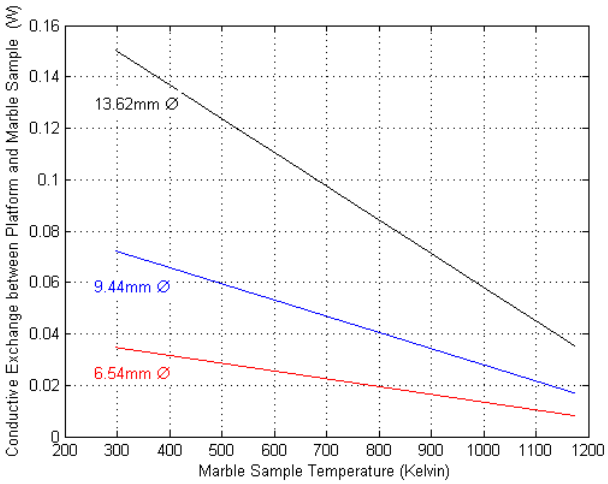

Figure 10-10: Calculated conductive heat transfer between the platform and the three marble samples for a fixed direct heat flux of 200kW/m^2 in the ETSF.

The convective heat transfer component of Equation [10.9] between the air (boundary layer) surrounding the heated platform and the marble sample is now presented. Equation [10.24] is used to calculate the heat transfer between the hot platform and the boundary layer air and Equation [10.27] is used to calculate the heat transfer between boundary layer air and the marble sample.

The results from the calculations of convective heat transfer between the boundary layer air surrounding the platform and the three marble samples is shown in Figures 10-11 and 10-12, that are for the OSS and ETSF respectively. Again a typical value for heat flux ($q_{Incident}$) of 200 kW/m^2 has been used for the displayed plots.

The plots show a decrease in heat transfer from the platform as the sample temperature increases.

At a sample temperature of 823K for the OSS calculations and 870K for the ETSF calculations the heat transfer changes from positive to negative. This indicates that the heat transfer has changed from going *from* the surrounding air to the stone to going *from* the stone to the surrounding air. This is in line with the 'positive heat in' sign convention discussed previously in this chapter.

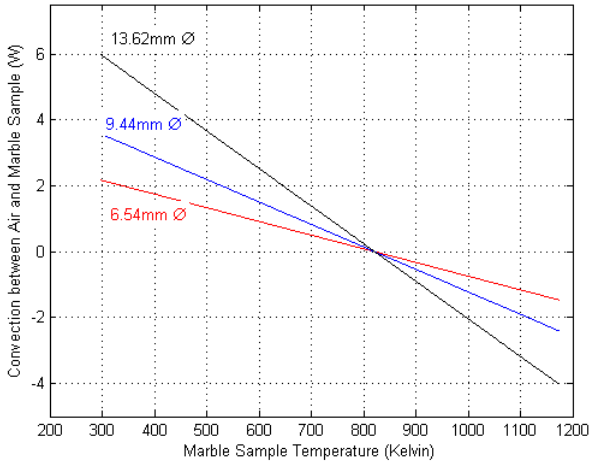

Figure 10-11: Calculated convective heat transfer between the boundary layer air and the three marble samples for a fixed direct heat flux of 200kW/m^2 in the OSS.

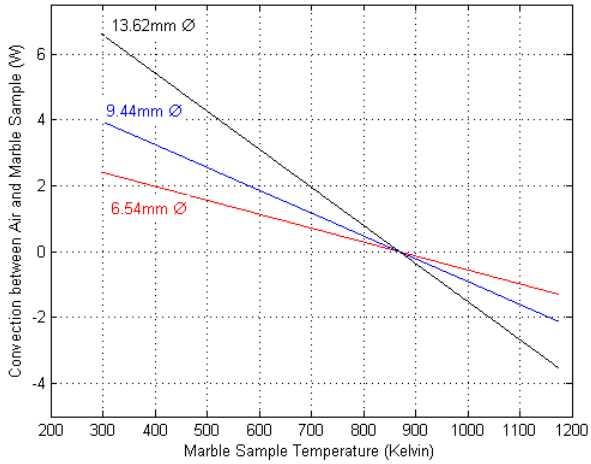

Figure 10-12: Calculated convective heat transfer between the boundary layer air and the three marble samples for a fixed direct heat flux of 200kW/m^2 in the ETSF.

The radiative heat loss component of Equation [10.9] between the marble stone and surrounding atmosphere is calculated using Equation [10.11]. The radiative heat loss calculation uses the temperature of the marble sample as it rises from ambient, 298K to the calcination temperature, 1173K. The surrounding atmosphere for the OSS is considered to be 298K, which is different from the ETSF which has heated walls at the measured temperatures displayed in Table 8-8. The average, maximum, minimum and standard deviation of these measured wall temperatures was calculated for each distance between the platform and the focal point, and are displayed in Table 10-11.

Table 10-11: Average, maximum, minimum and standard deviation of the measured wall temperatures for the furnace enclosure for variations in distance S between the calcination platform and focal point.

Distance (S) between Calcination Platform and Focal Point (mm)	**100**	**75**	**70**	**60**	**50**
Average (K)	651	658	662	670	695
Maximum Temperature (K)	683	688	691	705	740
Minimum Temperature (K)	564	569	571	572	594
Standard Deviation	38.29	38.47	39.17	43.05	46.98
Standard Deviation %	10.1	10.0	10.1	10.8	11.1

The results from the calculations of radiative heat transfer between the three marble samples and the surroundings are shown in Figures 10-13 and 10-14, which are for the OSS and ETSF respectively. Again a typical value for heat flux ($q_{Incident}$) of 200 kW/m^2 has been used for illustration purposes which produce an average furnace wall temperature of 651K.

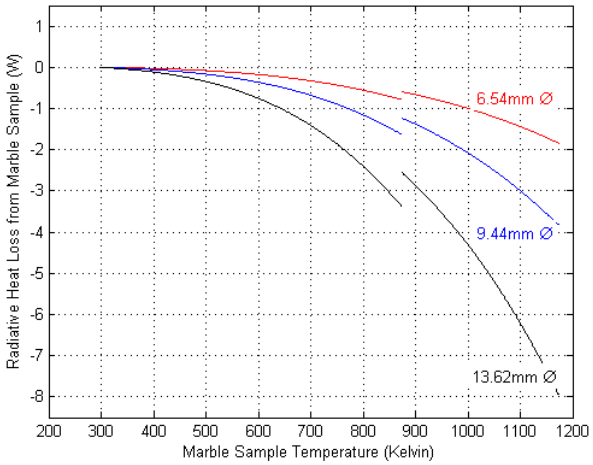

Figure 10-13: Calculated radiative heat transfer between the three marble samples and the surrounding atmosphere for a fixed direct heat flux of 200kW/m^2 in the OSS.

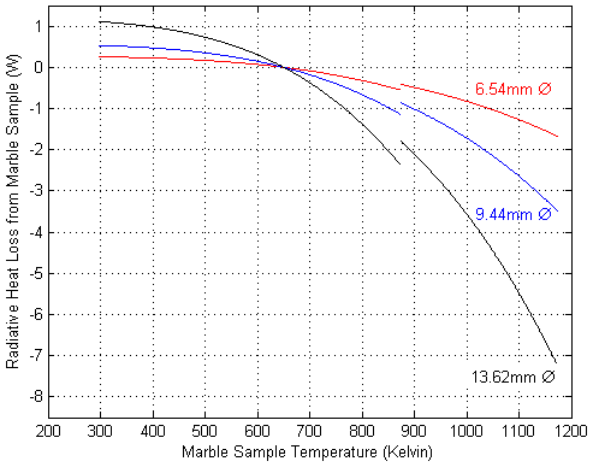

Figure 10-14: Calculated radiative heat transfer between the three marble samples and the surrounding atmosphere for a fixed direct heat flux of 200kW/m^2 in the ETSF.

Figures 10-13 and 10-14 show the calculated radiative heat loss from the three marble samples to its surroundings. As expected, the heat loss from the sample increases as the sample temperature increases, and is directly proportional to the surface area of the emitting particle, i.e. to the square of the diameter. It should be noted that the negative values shown in both Figures represent the loss of heat from the sample which is in line with the 'positive heat in' sign convention discussed previously.

The samples in the ETSF initially gains heat from the furnace walls until the wall and sample temperatures reach equilibrium (651K), after which the temperature of the samples continues to rise resulting in the heat flow to go from the samples to the furnace walls. In the OSS, the samples and surroundings are initially at the same temperature and thus there is no heat flow between the samples and the surroundings.

The components for the energy balance, Equation [10.9], have now been specified. The energy balance calculation on the surface of the marble can now be solved. This calculation provides the heat energy available for heating the stone and then available for the calcination reaction. Figures 10-15 and 10-16 show the energy available for heating the stone as the

marble sample temperature rises. Again for illustrative purposes, the displayed plots are for a typical $q_{Incident}$ heat flux of 200 kW/m^2.

The time to heat each of the three marble sizes from ambient to 1173K, can now be calculated. This calculation is a pseudo steady-state approximation using an iterative approach. The heating time, t_{cp}, was calculated by dividing the sensible heat (kJ) for limestone by the heat (J/s) available for heating the sample for each increment of temperature rise. The sensible heat was calculated by multiplying the average specific heat of limestone by the mass of the sample (kg), for each Kelvin of marble temperature.

The values for specific heat for limestone at temperatures between 298K and 1173K was provided by Oates (1998), Table 3.1. A plot of the data was made, with a polynomial trend line being produced which is shown as Equation [10.33] below:

$$Cp\ (CaCO_3) = 5.96\times10^{-10} \times T^3 - 1.58\times10^{-6} \times T^2 + 1.89\times10^{-3} \times T + 0.394 \qquad [10.33]$$

Table 10-12 displays the calculated heating times to heat each marble sample to a temperature of 1173K when exposed to heat fluxes between 100 kW/m^2 and 500 kW/m^2. A graphical presentation of these values is displayed in Figure 10-17.

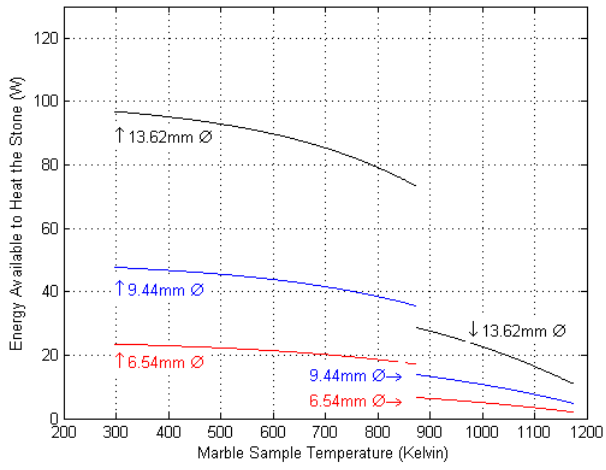

Figure 10-15: Calculated energy available for heating the three marble samples for a fixed direct heat flux of 200kW/m^2 in the OSS.

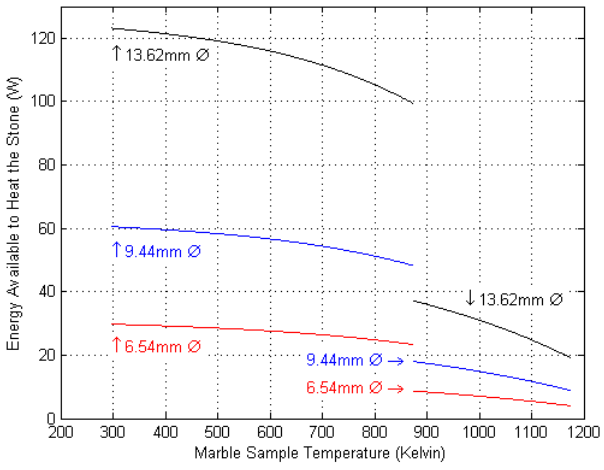

Figure 10-16: Calculated energy available for heating the three marble samples for a fixed direct heat flux of 200kW/m^2 in the ETSF.

Table 10-12: Calculated time (in seconds) to heat the marble samples from 298K to 1173K using heat fluxes between 100kW/m^2 and 500kW/m^2 in the OSS or ETSF.

	Calculated Heating time (seconds)					
	6.54mm (0.333g)		9.44mm (1.000g)		13.62mm (3.000g)	
Radiant heat flux kW/m^2	Open System	**Furnace Enclosure**	Open System	**Furnace Enclosure**	Open System	**Furnace Enclosure**
100	252	**184**	281	**215**	342	**265**
150	142	**100**	167	**123**	197	**158**
200	75	**58**	95	**75**	126	**104**
250	53	**43**	67	**57**	92	**80**
300	39	**33**	51	**46**	73	**65**
350	31	**27**	42	**38**	60	**55**
400	25	**23**	35	**33**	51	**48**
450	22	**20**	30	**29**	44	**42**
500	17	**17**	26	**25**	38	**37**

Table 10-12 shows a decrease of up to 45% in heating time for a marble sample placed in the ETSF rather than the OSS and exposed to the same source radiant heat flux. There is a greater difference between the heating times for the lower heat fluxes than for the higher heat fluxes, where the difference is only approximately 3% for the latter. These differences are best seen in Figure 10-17 where at 500kW/m^2 the heating times plateau to an almost constant value for each stone size.

A direct comparison between these calculated heating time results, and the measured heating time results are shown in Section 10.8.

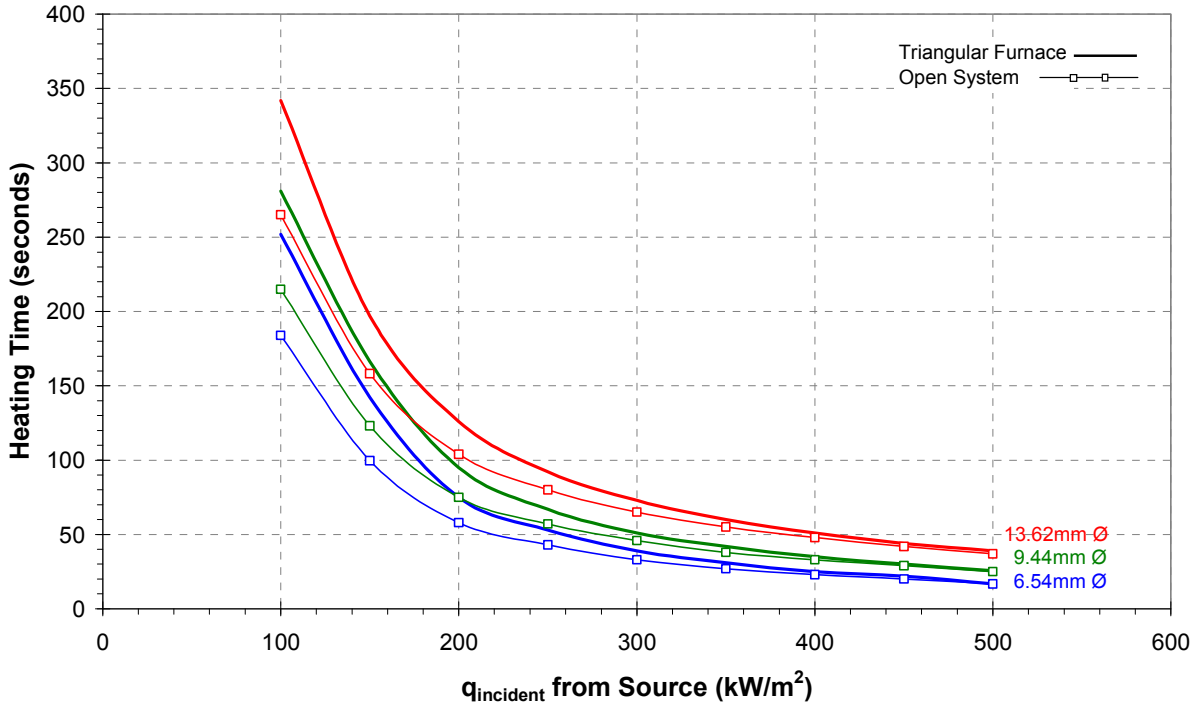

Figure 10-17: Plot showing the time to heat the marble samples to 1173K when exposed to heat fluxes between 100kW/m^2 and 600kW/m^2.

10.7 Calculation of Calcination Time

Calcination begins on the surface of the marble sample at a temperature of around 873K as shown in Figure 2-2. The newly formed calcium oxide layer insulates the particle and impedes further calcination until the marble's temperature reaches 1173K. The calcination reaction front then moves from the surface of the stone, into the sample at a rate depending on the heat supplied to it[8]. To drive the reaction front into the marble sample, a temperature differential between the surface and the reaction zone is required.

This section presents three temperature differential scenarios to determine which approach best represents the experimental results. Additionally, this section presents a comparison between the calculated calcination times when using the standard concentric shrinking core model and the eccentric shrinking core model.

In should be noted that these calculations assume the CO_2 partial pressure at the reaction zone is negligible. Chapter 2, Section 2.3 discusses the exponential relationship between

[8] Chapter 2, Section 2.3.5 discusses the three major mechanisms controlling the reaction rate: heat transfer, mass transfer and chemical reaction. The calculations of calcination time presented in this Chapter assume heat transfer controls the propagation of the reaction into the sample.

temperature and CO_2 partial pressure at the reaction zone, and concluded that the partial pressure plays only a minor role in the rate of calcination at the high furnace (platform) temperatures (which were measured).

10.7.1 Energy Available for Calcination

The net energy available for the calcination reaction is a function of the incident heat flux ($q_{Incident}$) and the heat exchanges between the stone sample and the surrounding surfaces and atmosphere. For a constant incident heat flux the surface temperature of the sample increases as it is heated. This causes a variation in radiant heat loss from the sample which varies the net energy available for the calcination reaction. A balance therefore exists between heat loss and the transfer of heat to the calcination zone. At equilibrium, the net heat flux exchange between the marble sample and its surroundings equal zero.

As the temperature of the surface of the marble sample increase, radiative heat losses begin to outweigh the incoming energy and therefore the energy balance, Equation [10.9] equates to zero. Figure 10-18 shows the net energy available for calcination of the three marble sample as the sample temperature increases for a constant $q_{Incident}$ = 175kW/m^2 for the OSS. For higher incident heat fluxes, the net energy available increases and thus higher marble sample temperatures are reached before the energy available for calcination reaches zero. Table 10-13 shows the calculated maximum sample temperatures for these higher incident heat fluxes.

Most of the calculated maximum temperatures displayed in Table 10-13 are higher than the measured platform temperature. This is expected because the surface colour of the lime is slightly darker (light grey) than the surface of the platform (white) and therefore the equilibrium surface temperature should be slightly higher. Conversely, calculated maximum temperatures lower than the platform temperature can be attributed to errors associated with the calculation assumptions discussed in Section 10.3.

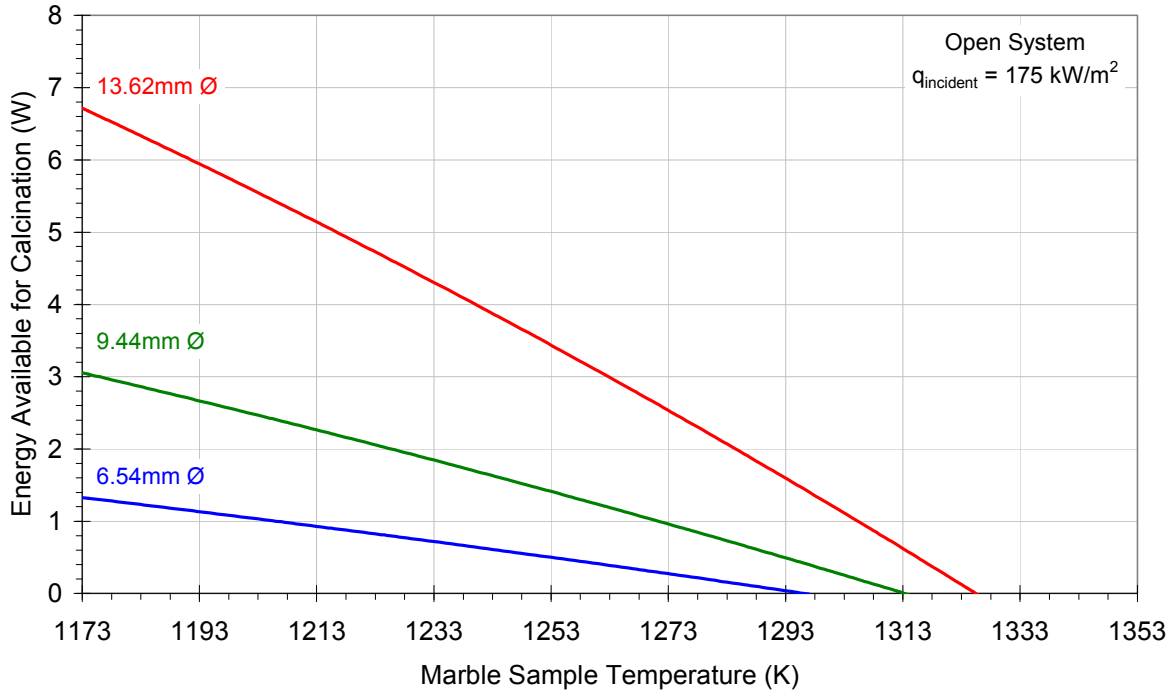

Figure 10-18: Plot showing the calculated net energy available for calcination as the temperature of the marble sample increases for an incident radiant heat flux of 175kW/m^2 for the OSS.

Table 10-13: Calculated maximum temperature of the marble samples when exposed to various incident heat fluxes in the OSS and ETSF.

$q_{Incident}$ heat flux kW/m^2	Measured Platform Temperature K	Calculated Maximum Marble Surface Temperatures K		
		6.54mm ∅	9.44mm ∅	13.62mm ∅
Open Solar System (OSS)				
175	1310	1296	1313	1325
280	1476	1491	1507	1517
430	1696	1716	1730	1739
Enclosed Triangular Solar Furnace (ETSF)				
200	1444	1406	1421	1432
300	1577	1569	1583	1593
450	1735	1757	1770	1779

10.7.2 Stone Surface Temperatures

The calcination reaction front moves from the surface of the stone into the sample at a rate depending on the heat supplied to it. To drive the reaction front into the marble sample, a temperature differential between the surface and the reaction zone is required. Three

temperature differential scenarios are investigated to determine which approach best represents the experimental results.

The reaction front is assumed to progress into the marble sample at a temperature of 1173K. The first surface temperature scenario (TS.1) uses a fixed surface temperature of 1223K. The surface temperature is assumed to be the same for all three stones sizes which does not change with $q_{Incident}$. The TS.1 follows the measurements of Conley (1939) who measured the calcination rate of cylindrical samples 38mm (1½") in diameter and ranging from 51mm to 76mm (2" to 3") in length, exposed to furnace temperatures between 915°C and 1135°C. After heating the sample, Conley measured a surface temperature which remained constant and was equal to the furnace temperature. The differential temperature between the surface and the centre of the sample was also measured with a difference of about 50 ± 5°C being measured, until calcination was complete.

For a constant temperature differential the energy transferred between the surface and the reaction zone needs to increase as the distance between surface and the calcination front increases. Similarly, for a constant energy transfer, the temperature differential needs to increase for increasing distance. In the TS.1 calculations for a constant 1223K surface temperature, the temperature differential begins small and increases to a maximum of 50K e.g. a minimum 1173K at the calcination zone. This limit causes a reduction in the energy transferred between the surface and the reaction zone towards the end of calcination.

Table 10-14 displays the marble surface temperature for TS.1 for the various $q_{Incident}$ on the calcination platform for both the OSS and ETSF. The temperature profile of the stone during calcination for TS.1 is displayed graphically as the red line in Figure 10-20. It should be noted that the surface temperature of the 6.54mm nominal diameter sample exposed to 175kW/m^2 in the OSS does not reach 1223K, instead a maximum temperature of 1219K is being used which has a corresponding 'net available energy' of 0.043 W.

The second temperature scenario (TS.2) uses a surface temperature 1% lower than the maximum sample temperature where the energy balance equals zero. One percent represents the tolerance of a temperature measurement system as was discussed in Chapter 9, Section 9.5.1. Table 10-14 displays the surface temperatures of the marbles for TS.2 for the various $q_{Incident}$ on the calcination platform for the OSS and ETSF. These comparatively high surface temperatures result in a relatively low net energy transferred to the calcination reaction zone. A minimum reaction zone temperature of 1173K has again been used. The surface temperature profile of calcination time against marble sample temperature for TS.2 is displayed graphically as the green line in Figure 10-20.

Table 10-14: Proposed surface temperatures for the three sizes of Penrice marble.

$q_{Incident}$ heat flux kW/m^2	Measured Platform Temperature K	TS.1 Marble Surface Temperature K	TS.2 Marble Surface Temperature K		
			6.54mm ∅	9.44mm ∅	13.62mm ∅
Open Solar System (OSS)					
175	1310	1223	1284	1301	1313
280	1476	1223	1477	1493	1503
430	1696	1223	1700	1714	1723
Enclosed Triangular Solar Furnace (ETSF)					
200	1444	1223	1393	1408	1419
300	1577	1223	1554	1568	1578
450	1735	1223	1740	1753	1762

The third temperature scenario (TS.3) uses a varying, but increasing, surface temperature which follows the measurements (and calculations) of Mallen (1956) and Satterfield and Feakes (1959). Both investigators measured the temperature of the centre of the samples and in most cases, on (or near) the surface of the stone.

Mallen (1956) measured the temperatures 3.175mm (1/8") outside and inside the marble samples which had diameters between 19mm and 51mm (3/4" and 2"). He measured an initial rapid temperature increase inside the sample followed by an almost constant temperature once the sample achieved a temperature 100°C below that of the *Globar* electric furnace. The sample temperature then rose by 2.8°C per minute until the calcination reaction reached 65% and the sample temperature had reached 50°C below the furnace temperature. The rate of temperature rise then reduced further to 0.55°C/min, until calcination was complete. A reproduction of the temperature profiles and mass loss measurements for a 44.5mm (1¾") diameter stone calcined at 1100°C is shown as Figure 10-19.

In Section 4:2:2 of his thesis, Mallen also calculated the interfacial temperatures during the progression of the calcination front through the stone. The derived values (and subsequent plots) indicate the interfacial temperature remains approximately 50 ± 5°C lower than the surface temperature until calcination completes. A plot of interfacial temperatures presented by Mallen for the 1¾" sphere is reproduced in Figure 10--19.

A similar furnace / surface temperature relationship was found by Satterfield and Feakes (1959) in their heat transfer and chemical kinetics analysis. The surface temperature was calculated to rise to approximately 100°C below the furnace temperature at the initial stages and then increase linearly at a rate of approximately 0.56°C/min until calcination was complete.

Figure 10-19: Temperature / time and fractional calcination / time curves for a 44.45mm (1 ¾ inch) cube of marble calcined at 1100°C. Adapted from Mallen (1956), Figs 31 and 35.

The surface temperature profile used for the TS.3 calculations in this thesis follows that of Mallen (1956), where the surface of the marble sample rises due to sensible heat to a temperature 100°C below that of the measured platform temperature (shown in Table 10-14). The surface temperature then rises by 50°C over the time it takes for calcination to go from 40% to 65%. The surface temperature then increases by another 50°C over the time it takes for calcination to go from 65% to completion (t_{100}). The temperature profile for the marble surface temperature for TS.3 is displayed graphically as the blue line in Figure 10-20 which is for a $q_{incident}$ of 200kW/m^2.

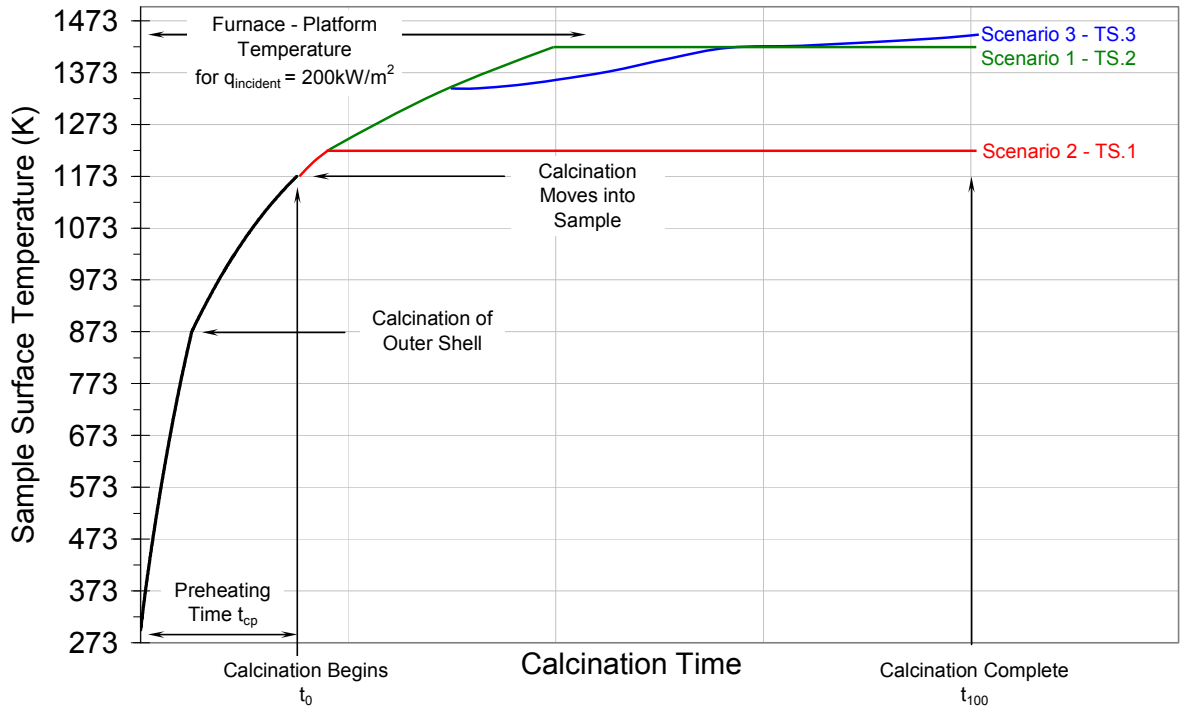

Figure 10-20: Representation of the calcination time against sample surface temperature for the three surface temperature scenarios for $q_{incident}$ = 200kW/m^2.

Figure 10-20 shows that additional surface heating of the limestone sample is required for each of the three temperature scenarios before the calcination reaction zone progresses into the sample. The energy balance, Equation [10.9] is used to calculate the addition heating time above 1173K and Table 10-15 displays these calculated values each of the three stone sizes, exposed to each $q_{incident}$ heat flux for the OSS or in the ETSF, for each of the three surface temperature scenarios. These additional surface heating times are calculated using a CaO 'shell' thickness of 1mm covering the stones surface. It should be noted that these calculated additional surface heating times use idealised assumptions which represent a conservative approach which, as will be presented later in this chapter, accounts for less than 1% of the total calcination time.

Scenarios one and two assume a constant surface temperature until calcination is complete. Scenario three assumes an increasing surface temperature which reaches the platform temperature at the completion of calcination (T_{100}). The surface heating times displayed in Table 10-15 for TS3 represent heating the surface up to the platform temperature displayed in Table 10-14 for each $q_{incident}$ of interest.

Table 10-15: Calculated additional heating time (in seconds) to heat the three marble samples from 1173K to the proposed surface temperature for the three surface temperature scenarios for all the $q_{incident}$ of interest in the OSS and ETSF.

	Calculated Additional Surface Heating time (seconds)								
	6.54mm (0.333g)			9.44mm (1.000g)			13.62mm (3.000g)		
$q_{Incident}$ heat flux kW/m^2	Scenario #			Scenario #			Scenario #		
	1	2	3	1	2	3	1	2	3
Open Solar System (OSS)									
175	1.1	2.0	3.3	2.3	4.3	7.2	4.1	7.6	13.1
280	0.6	3.5	4.3	1.1	7.1	8.9	1.9	12.4	15.9
430	0.4	4.3	4.8	0.7	8.6	9.9	1.1	15.2	17.7
Enclosed Triangular Solar Furnace (ETSF)									
200	0.8	4.0	5.1	1.6	8.6	11.3	2.7	15.4	20.6
300	0.5	4.4	5.2	1.0	9.0	10.8	1.6	16.0	19.4
450	0.3	4.4	4.9	0.6	8.8	10.0	1.0	15.5	17.9

10.7.3 Shrinking Core Calculation and Results

This shrinking core calculation uses a standard steady state conduction equation as given on pages 162 to 164 of Mills (1999), and displayed as Equation [10.34] here. The conduction equation is used to calculate the rate of heat transfer between the surface and reaction zone so that the rate of calcination of the sample, dm/dt, can then be calculated. Dennis and Hayhurst (1987) used a similar heat transfer estimation for their intra-particle temperature gradients between the reaction interface and the outer surface of the particle. Their equation was also used by Hills (1968) for calcination rate calculations. He showed that there was negligible error if all of the heat transferred to the reaction front is assumed to be absorbed by the reaction.

Equation [10.34] calculates the rate of heat transfer to the calcination front (interfacial zone) as the radius of the $CaCO_3$ core shrinks within the particle. The energy balance presented in this chapter accounts for each of the heat transfers to and from the sample. The shrinking core calculation therefore reduces to the calculation of the energy conducted from the surface, through the newly formed CaO layer, to the reaction interface as the core shrinks.

The standard shrinking core model equation developed by Hills (1968), assumes the core is concentric to the centre of the sample. This may not be the most appropriate approach for representing the current solar calcination process. Two calcination models are therefore investigated; 1). the standard shrinking core model using a concentric core and 2). a shrinking core model where the core is offset to the lower side of the sample, as displayed graphically in Figure 2-5. The shape factor, S in Equation [10.34] is therefore different between the concentric and eccentric shrinking core calculation.

A review of literature for an eccentric spheres shape factor equation found that it did not currently exist. The eccentric spheres equation used in these shrinking core calculations was therefore adapted from the shape factor for eccentric cylinders and by setting the cylinder length of the pipe to the diameter of the sphere.

$$q_{Cal} = k_{CaO} S \left(T_{Surf} - T_{\text{Reaction}} \right) \qquad [10.34]$$

Where: q_{Cal} is the calculated heat flow through the CaO (W).

k_{CaO} is the thermal conductivity of the quicklime 0.628 to 0.837 W/m.K (average 0.7325). Referenced from Oates (1998), Boynton (1980) and Schwarzkopf (1974).

S is the shape factor (m),

where for concentric spheres, $S = \dfrac{4\pi}{1/r_i - 1/r_o}$, and

for eccentric spheres, $S = \dfrac{4\pi r_o}{\cosh^{-1}\left(\dfrac{r_o^2 + r_i^2 - e^2}{2 r_i r_o} \right)}$

r_o is the initial characteristic radius of the marble sample,

r_i is the characteristic radius of the reaction front within the marble sample,

e is the distance between the centres of the two eccentric spheres.

The shape factor value (S) is a function of the calcination front radius, r_i which changes as the calcination front proceeds into the sample. The shrinking core calculation was therefore divided into twenty equal radial divisions with twenty values of Equation [10.34] being calculated iteratively.

The rate of heat transfer to the calcination front, q_{Cal}, calculated in Equation [10.34] is equated to the rate of calcination of the sample, dm/dt, using Equation [10.36] :

$$q_{Cal} = -\Delta E_{cal}\left(\frac{dm}{dt}\right) \qquad [10.36]$$

Where ΔE_{Cal} is 168752 J/mol; the enthalpy of calcination of Penrice marble according to Mallen (1956, pg 8-9), and dm/dt is represented by Equation [10.37] for shrinking-core kinetics :

$$\left(\frac{dm}{dt}\right) = -\frac{d}{dt}\left\{\frac{4\pi r_c^3}{3V_{CaCO_3}}\right\} = -\frac{4\pi r_c^3\left(r_i/r_o\right)^2}{V_{CaCO_3}}\frac{d\left(r_i/r_o\right)}{dt} \qquad [10.37]$$

The 'calcination time' was calculated by multiplying the enthalpy of calcination, E_{Cal}, by the mass (kg) of the marble sample and then dividing by the heat energy (W) transferred to the calcination front.

The calcination process was assumed to be complete when :

$$\frac{\text{radius of the calcination front}}{\text{initial radius of limestone particle}} = \frac{r_i}{r_o} = 0.05.$$

Table 10-16 displays the calculated calcination times for the concentric shrinking core model, while Table 10-17 displays the calculated results for the eccentric shrinking core model.

The calcination time is defined as being the time between the sample reaching the maximum preheated temperature and the completion of the calcination reaction, $r_i / r_o = 0.05$.

Table 10-16: Time (in minutes) to complete calcination of the three nominal diameter Penrice marble for the three sample surface temperature scenarios for the OSS and ETSF assuming a concentric shrinking core model.

	Calculated Calcination Times using a **Concentric** Shape Factor (Minutes)								
	6.54mm (0.333g)			9.44mm (1.000g)			13.62mm (3.000g)		
$q_{Incident}$ heat flux kW/m^2	Scenario #			Scenario #			Scenario #		
	1	2	3	1	2	3	1	2	3
Open Solar System (OSS)									
175	12	64	16	14	91	44	19	136	117
280	2.8	39	8.9	4.2	53	21	6.4	81	58
430	1.5	25	5.8	2.5	36	12	4.3	53	23
Enclosed Triangular Solar Furnace (ETSF)									
200	4.3	49	15	6.1	64	37	8.8	106	95
300	2.1	33	8.0	3.3	48	22	5.3	70	49
450	1.4	22	5.6	2.4	34	9.7	4.1	46	16

Table 10-17: Time (in minutes) to complete calcination of the three nominal diameter Penrice marble for the three sample surface temperature scenarios for the OSS and ETSF assuming an eccentric shrinking core model.

	Calculated Calcination Times using an **Eccentric** Shape Factor (Minutes)								
	6.54mm (0.333g)			9.44mm (1.000g)			13.62mm (3.000g)		
$q_{Incident}$ heat flux kW/m^2	Scenario #			Scenario #			Scenario #		
	1	2	3	1	2	3	1	2	3
Open Solar System (OSS)									
175	12	65	17	18	91	46	29	136	120
280	3.1	40	9.4	11	53	22	22	81	65
430	2.3	25	6.3	9.9	36	13	21	53	27
Enclosed Triangular Solar Furnace (ETSF)									
200	4.3	49	17	12	64	41	23	106	98
300	2.6	33	8.7	11	49	24	21	70	51
450	2.2	22	5.9	9.9	34	10	20	46	18

10.7.4 Analysis of Calculated Shrinking Core Results

The calculated values for both the concentric and eccentric shrinking core models follow the same trends measured in the experiments, where the calcination time increases with increasing stone size and for decreasing radiant heat flux. A direct comparison with the measured results is shown in Section 10.8 following.

The main difference between the concentric (Table 10-16) and eccentric (Table 10-17) shrinking core models is the increased calculated values for the eccentric shrinking core calculations for temperature scenarios 1 and 3 (TS.1 and TS.3). For TS.1 the eccentric model calcination times are between 0% and 393% longer than for the concentric model. For TS.3 the eccentric model is between 2.8% and 14.3% longer. The differences between the two models increases as the stone size increases and as the incident heat flux increases. These differences show the increase in conduction distance which occurs between the surface and the reaction zone for the eccentric shrinking core model when using a constant surface temperature.

The second temperature scenario (TS.2) shows maximum differences of 0.3% in calcination times between the concentric and eccentric shrinking core models, but due to the number of significant figures shown, these differences are not apparent between Tables 10-16 and 10-17.

Comparing the surface temperature scenarios, TS.1 shows the shortest calculated calcination times and TS.2 the longest. The calculated values for TS.3 are between the TS.1 and TS.3 values. The higher surface temperatures for TS.2 decrease the available energy which can transfer to the reaction front and thus an increase in calcination time is calculated. Conversely the low surface temperature for TS.1 retains more energy for the reaction and thus a faster calcination time is realised.

10.8 Comparisons with the Experimental Results

The preheating time (t_{cp}) and time to complete calcination (t_{100}) were calculated for the three nominal diameter Penrice marble using three surface temperature scenarios and two different shrinking core models. These theoretical calculations are compared to the values measured during the open system radiation calcination experiments and the triangular solar furnace calcination experiments, as presented in Chapters 7 and 8.

10.8.1 Comparison of Measured and Calculated Calcination Times for the Open Solar System

Comparisons are made between the measurements from the single stone open solar system experiments conducted at 175±15kW/m^2, 280±20kW/m^2, and 430±30kW/m^2 and results from the theoretical modelling calculations. Table 10-18 compares the preheating times and calcination times for the 6.54mm (0.333g), 9.44mm (1.000g), and 13.62mm (3.000g) Penrice marble.

Table 10-18: Comparison of calculated (using eccentric model) and measured preheating times and calcination times for d_c = 6.54mm, d_c = 9.44mm and d_c = 13.62mm Penrice marble exposed to 175kW/m^2, 280kW/m^2 and 430kW/m^2 in the OSS.

Marble Nominal Diameter d_C (mm)	**Measured Preheating Time t_{cp} (Minutes)**	**Calculated Preheating Time t_{cp} (Minutes)**	**Measured Calcination Time t_{100} (Minutes)**	**Calculated Calcination Time using the Eccentric Model t_{100} (Minutes)**		
				TS.1	**TS.2**	**TS.3**
175±15kW/m^2						
6.54	2.0 ± 0.2	0.9	21 ± 0.5	12	65	17
9.44	5.0 ± 0.5	1.3	65 ± 1.3	18	91	46
13.62	9.8 ± 1.0	1.8	242 ± 5	29	136	120
280±20kW/m^2						
6.54	1.4 ± 0.1	0.5	12.5 ± 0.3	3.1	40	9.4
9.44	2.6 ± 0.3	0.8	28 ± 0.6	11	53	22
13.62	5.4 ± 0.6	1.1	87 ± 1.7	22	81	65
430±30kW/m^2						
6.54	0.8 ± 0.1	0.33	7.9 ± 0.2	2.3	25	6.3
9.44	1.5 ± 0.2	0.5	13.4 ± 0.3	9.9	36	13
13.62	2.0 ± 0.2	0.7	34.8 ± 0.7	21	53	27

Comparing the preheating times, Table 10-18 shows that the calculated preheating times are lower than the measured preheating times. The difference between the calculated and measured values is less for the higher heat fluxes than for the lower heat fluxes. This under estimation occurs because the calculation model assumes ideal heat transfer to the surface of the stone, and equal and instantaneous conductive heat transfer within the stone. The

calculations also assume the marble sample is uniform in geometry and molecular composition.

The measured preheating times increase by a factor of approximately 2 between each stone size, when exposed the same heat flux. This corresponds to the increase in exposed surface area between the stone sizes. The calculated values do not follow the same trend and only increase by a factor of approximately 0.7 between each stone size, which corresponds to the increase in radius between stone sizes. The measured preheating times are therefore following a squared correlation, where the calculated are following a linear correlation. The exact cause and analysis of this variation in trend will be investigated in future work.

Comparing the measured and calculated calcination times displayed in Table 10-18: TS.1 under-calculates the calcination times, while TS.2 mostly over-calculates the calcination times. That leaves TS.3 which fits between TS.1 and TS.2 and shows some ‘reasonable’ correlations with the measured values. The calculated values for TS.3 under-calculate the measured calcination times by between 7% and 102%. The term "reasonable" is of course subjective, but has been used here to describe values that exhibit the same trends as the measured data and agrees within 50% for the majority of the cases.

For the 6.54mm nominal diameter stone, the calculated values for TS.3 under-calculate the measured calcination times by between 20% and 43%. The calcination time values for the 9.44mm stone compare reasonably well with an under-estimation of between 8% and 44%. A comparison of the calcination times for the 13.62mm stone shows that the values for the 280 kW/m^2 and 430 kW/m^2 heat fluxes are 31% and 35% respectively, but for the 175 kW/m^2 heat flux the calculated value is 102% lower (approximately half) than the measured.

This mismatch between the trends of the measured and calculated calcination times becomes more apparent when the data is displayed graphically, as shown in Figure 10-21. It can be said that the shrinking core calculation model represents the measured data reasonably well, for the shorter calcination times and higher heat fluxes.

The error bars on the calcination times and radiant heat fluxes were calculated using the standard deviation from the possible maximum errors which could occur in the calcination model. These errors are from parameter variation errors which are discussed in the sensitivity analysis of Section 10.9.

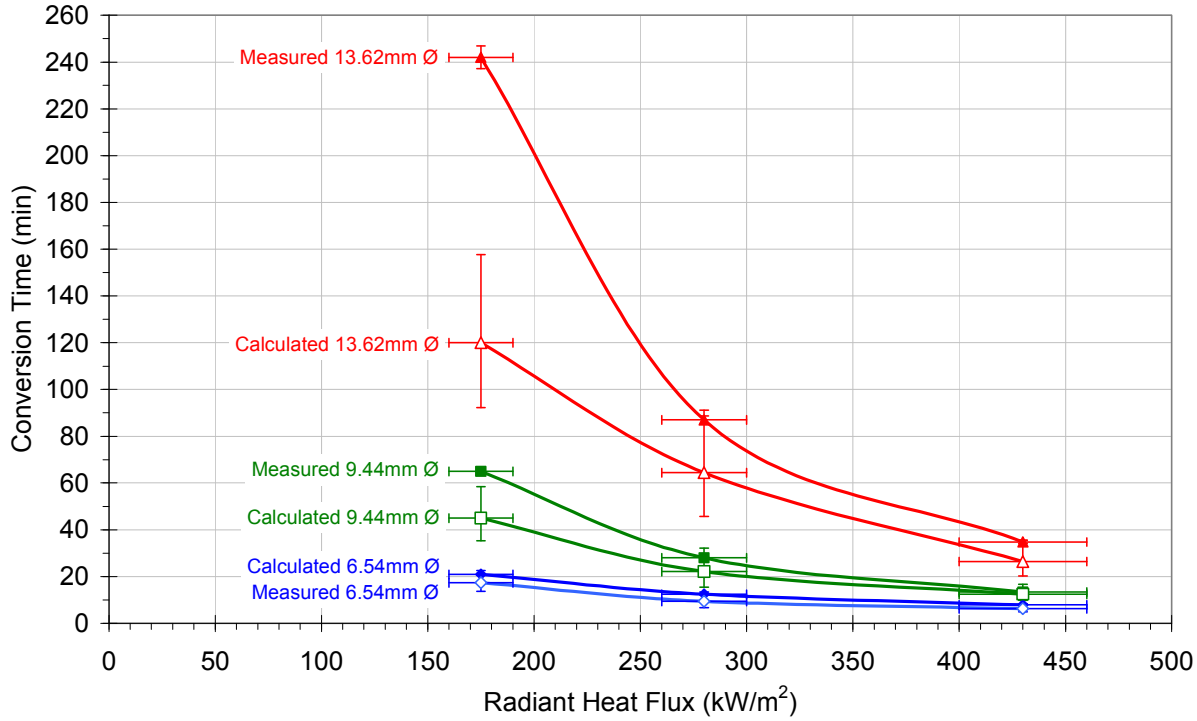

Figure 10-21: Comparison of calculated and measured calcination times for the d_c = 6.54mm, d_c = 9.44mm and d_c = 13.62mm Penrice marble exposed to radiant heat fluxes of 175kW/m^2, 280kW/m^2 and 430kW/m^2 in an OSS.

10.8.2 Comparison of Measured and Calculated Calcination Times for the Enclosed Triangular Solar Furnace

Comparisons are made between the measurements from the enclosed triangular solar furnace experiments conducted at 200±15kW/m^2, 300±25kW/m^2, and 450±30kW/m^2 and results from the theoretical shrinking eccentric core model calculations. Table 10-19 shows the preheating times and calcination times for the 6.54mm (0.333g), 9.44mm (1.000g), and 13.62mm (3.000g) sized Penrice marble.

Comparing the preheating times displayed in Table 10-19 shows that the calculated preheating times are slightly lower than the measured preheating times. The calculated values for the 430kW/m^2 heat fluxes represent the measured values more closely than for the 175kW/m^2 heat fluxes. Similar to the OSS comparison, the measured preheating times are following a squared correlation (surface area), where as the calculated preheating times are following a linear correlation (radius), within a particular heat flux band. It should be noted though, that there is a closer match between measured and calculated values, than for the OSS. This under estimation occurs because the calculation model assumes ideal heat transfer to the surface of the stone, and equal and instantaneous conductive heat transfer

within the stone. The calculations also assume the marble sample is uniform in geometry and molecular composition.

Table 10-19: Comparison of calculated (using eccentric model) and measured preheating times and calcination times for d_c = 6.54mm, d_c = 9.44mm and d_c = 13.62mm Penrice marble exposed to 200kW/m^2, 300kW/m^2 and 450kW/m^2 in the ETSF.

Marble Nominal Diameter d_C (mm)	**Measured Preheating Time t_{cp} (Minutes)**	**Calculated Preheating Time t_{cp} (Minutes)**	**Measured Calcination Time t_{100} (Minutes)**	**Calculated Calcination Time using the Eccentric Model t_{100} (Minutes)**		
				TS.1	**TS.2**	**TS.3**
200±15kW/m^2						
6.54	1.7 ± 0.2	0.7	13.4 ± 1.1	4.3	49	17
9.44	3.2 ± 0.3	1.0	30.7 ± 2.5	12	64	41
13.62	6.9 ± 0.7	1.5	83.3 ± 6.7	23	106	98
300±20kW/m^2						
6.54	1.1 ± 0.1	0.5	7.9 ± 0.7	2.6	33	8.7
9.44	1.9 ± 0.2	0.7	16.9 ± 1.4	11	48	24
13.62	2.8 ± 0.3	1.0	42.8 ± 3.5	21	70	51
450±30kW/m^2						
6.54	0.4 ± 0.04	0.32	5.6 ± 0.5	2.2	22	5.9
9.44	0.65 ± 0.1	0.5	6.9 ± 0.6	9.9	34	10
13.62	1.1 ± 0.1	0.7	11.3 ± 0.9	20	46	18

Comparing the measured and calculated calcination times displayed in Table 10-19 shows that TS.1 under-calculates the calcination times, while TS.2 mostly over-calculates the calcination times. Again TS.3 fits between TS.1 and TS.2 and shows some ‘reasonable’ correlations with the measured values. The calculated values for TS.3 over-calculate the measured calcination times by between 5% and 34%. Again it should be remembered that the term reasonable is subjective, but has been used here to describe values which follow the same trends displayed in the measured data and in the majority does not exceed the value by approximately 50%.

Comparing values calculated using temperature scenario 3 (TS.3) and the measured calcination times, for the 6.54mm nominal diameter stone, the calculated values for TS.3

over-calculate the measured calcination times by between 5.5% and 18.5%. The calcination time values for the 9.44mm stone compare reasonably well, with an over-calculation of between 25% and 34%. A comparison of the calcination times for the 13.62mm stone shows that the calculated values are between 15% and 34% lower than the measured values.

These comparisons between the measured and calculated calcination times becomes more apparent when the data is displayed graphically, as shown in Figure 10-22. It can be said that this eccentric shrinking core calculation model represents the measured data reasonably well.

It should be noted that the comparisons in measured and calculated values are closer for the ETSF (5.5% to 34%) than for the OSS (7.6% to 102%). Table 10.19 also shows that the calculated times for the ETSF over-calculate the calcination times, where as the calculated times for the OSS under-calculated it.

The displayed error bars on the calcination times and radiant heat fluxes were calculated using the standard deviation from the possible maximum errors which could occur within the calcination model. These errors are from parameter variation errors which are discussed in the sensitivity analysis in Section 10.9.

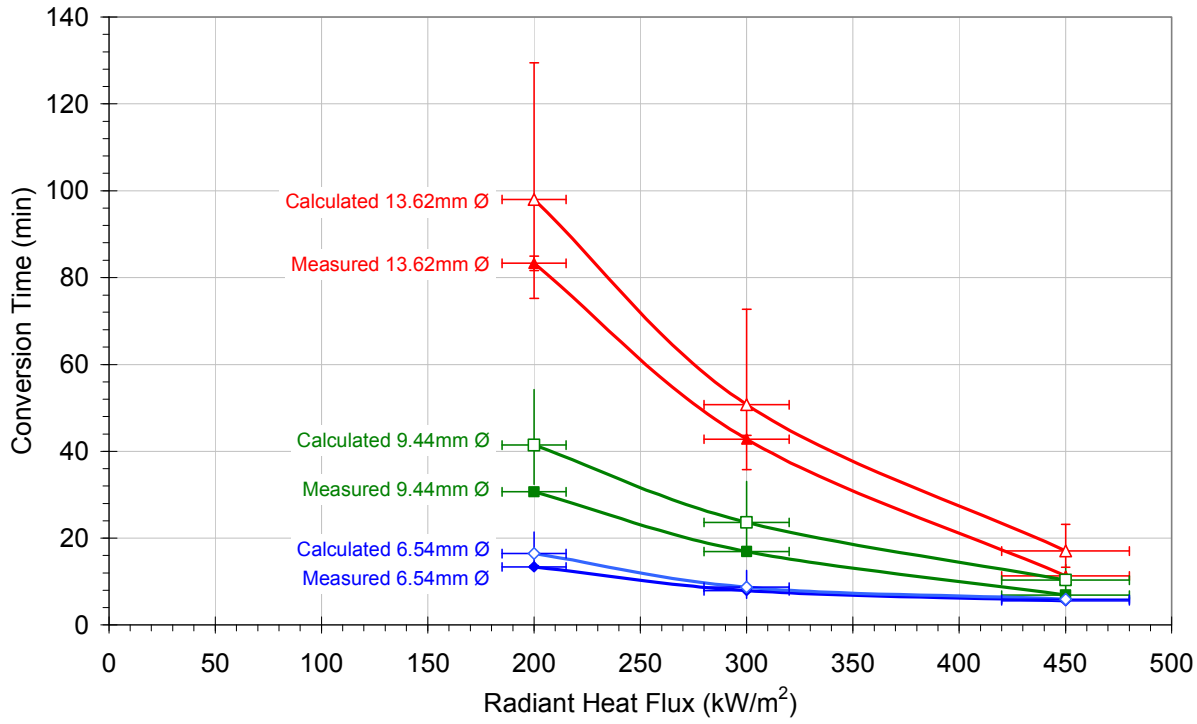

Figure 10-22: Comparison of calculated and measured completion times for the d_c = 6.54mm, d_c = 9.44mm and d_c =13.62mm Penrice marble exposed to radiant heat fluxes of 200kW/m^2, 300kW/m^2 and 450kW/m^2 in an ETSF.

10.9 Sensitivity Analysis of the Calcination Model

A sensitivity analysis was conducted to evaluate the influence of various parameters used within the calcination model.

Comparing Table 10-18 and Table 10-19 the calcination time represents approximately 98% of the total calcination time, compared to the preheating time. This sensitivity analysis concentrates on the modelling parameters which affect the calcination time only. The parameters were varied by percentages and values which encapsulate the range of possible values found in literature, as was discussed in previous sections of this chapter.

The smallest and largest nominal diameter stone sizes are displayed in this sensitivity analysis because the values for the 9.44mm stone lay proportionally between the two. Similarly, only the highest and lowest radiant heat fluxes are used for the evaluation here. This provides eight 'standard' cases which are displayed within this evaluation.

The parameters which were varied within this sensitivity analysis are:

- The emissivity of the CaO surface, ε_{CaO}, which was varied from the average value of 0.511 to the maximum and minimum values shown in Table 10-4 i.e. from 0.92 to 0.41.

- The solar absorptivity of the CaO, α_{CaO}, which was varied between the maximum, 0.50, and minimum, 0.41 values found in literature and shown in Table 10-3 from the average value of 0.445 (at 1173K).

- The thermal conductivity of the quicklime, $\boldsymbol{k_{CaO}}$ (from equation [10.34]) which was varied by $\pm$ 15% from the standard value of 0.7325 W/m.K; i.e. 0.623 W/m.K to 0.842 W/m.K which encompasses the minimum and maximum values shown in Section 10.7.3.

- The irradiant heat flux was varied by $\pm$ 12% from the measured heat values for the OSS and ETSF. The 12% value was selected because it represents the maximum uncertainty in the heat flux measurements, as displayed in Table 5-17.

The scenarios above are displayed in the following four Tables. The negative percentage change value indicates a shorter calcination time than 'standard' and positive value longer calculated calcination time.

Table 10-20: Changes in the calculated calcination time for variation of emissivity of CaO for d_c = 6.54mm and d_c = 13.62mm Penrice marble in the OSS and ETSF.

Parameter Changed		**Stone Nominal Diameter d_c (mm)**	**Heat Flux kW/m^2**	**Calculated Calcination Time (minutes)**	**Percentage Change %**
Change of Emissivity of CaO ε_{CaO} **(from 0.511)**	**Open Solar System (OSS)**				
	0.92	6.54	175	20.10	15.56
			430	7.45	18.79
		13.62	175	136.17	13.53
			430	30.54	15.39
	0.41	6.54	175	16.27	-6.48
			430	5.84	-6.99
		13.62	175	113.82	-5.11
			430	24.92	-5.85
	Enclosure Triangular Solar Furnace (ETSF)				
	0.91	6.54	200	19.05	15.84
			450	7.05	18.88
		13.62	200	111.31	13.53
			450	19.80	16.14
	0.41	6.54	200	15.33	-6.78
			450	5.50	-7.22
		13.62	200	92.68	-5.47
			450	16.04	-5.92

Table 10-21: Changes in the calculated calcination time for variation of absorptivity of CaO for d_c = 6.54mm and d_c = 13.62mm Penrice marble in the OSS and ETSF.

Parameter Changed		**Stone Nominal Diameter d_c (mm)**	**Heat Flux kW/m^2**	**Calculated Calcination time (minutes)**	**Percentage Change %**
Change of Absorptivity of CaO α_{CaO} **(from 0.46)**	**Open Solar System (OSS)**				
	0.5	6.54	175	16.56	-4.81
			430	5.97	-4.88
		13.62	175	114.79	-4.29
			430	25.29	-4.45
	0.41	6.54	175	18.22	4.77
			430	6.57	4.75
		13.62	175	125.13	4.33
			430	27.60	4.27
	Enclosure Triangular Solar Furnace (ETSF)				
	0.5	6.54	200	15.64	-4.85
			450	5.64	-4.86
		13.62	200	93.88	-4.25
			450	16.33	-4.23
	0.41	6.54	200	17.25	4.88
			450	6.21	4.85
		13.62	200	102.32	4.36
			450	17.79	4.31

Table 10-22: Changes in the calculated calcination time for variation of thermal conductivity of the CaO layer on the d_c = 6.54mm and d_c = 13.62mm Penrice marble in the OSS and ETSF.

Parameter Changed		Stone Nominal Diameter d_c (mm)	Heat Flux kW/m^2	Calculated Calcination Time (minutes)	Percentage Change %
Change of Thermal Conductivity of CaO k_{CaO} (from 0.7325 W/m.K)	**Open Solar System (OSS)**				
	0.842	6.54	175	17.01	-2.22%
			430	6.13	-2.22%
		13.62	175	115.35	-3.83%
			430	25.45	-3.83%
	0.623	6.54	175	17.95	3.17%
			430	6.47	3.17%
		13.62	175	126.77	5.69%
			430	27.97	5.69%
	Enclosure Triangular Solar Furnace (ETSF)				
	0.842	6.54	200	16.08	-2.22%
			450	5.80	-2.22%
		13.62	200	94.29	-3.83%
			450	16.40	-3.83%
	0.623	6.54	200	16.96	3.17%
			450	6.12	3.17%
		13.62	200	103.63	5.69%
			450	18.02	5.69%

Table 10-23: Comparison of calculated calcination time by varying the illuminating radiant heat flux for both d_c = 6.54mm and d_c = 13.62mm Penrice marble in the OSS and ETSF.

Stone Nominal Diameter d_c (mm)	Standard Heat Flux kW/m^2	Change of Available Heat Flux kW/m^2	Calculated Calcination Time (minutes)	Percentage Change %
Open Solar System (OSS)				
6.54	175	154	18.46	6.12
		196	16.11	-7.35
	430	378.4	6.72	7.13
		481.6	5.82	-7.28
13.62	175	154	129.42	7.90
		196	108.21	-9.78
	430	378.4	28.90	9.19
		481.6	24.07	-9.08
Enclosure Triangular Solar Furnace (ETSF)				
6.54	200	176	17.49	6.36
		224	15.40	-7.23
	450	396	6.36	7.38
		504	5.50	-6.36
13.62	200	176	106.38	8.50
		224	90.19	-9.75
	450	396	18.66	9.44
		504	15.39	-8.02

Table 10-20 shows a decrease in calculated calcination time for decreasing value of CaO emissivity for both the 6.54mm and 13.62mm nominal diameter stone sizes. This is as expected because the higher emissivity, the higher the radiant heat loss from the stone and thus less energy is available for the calcination reaction. It is interesting to note that varying the emissivity value causes a larger change in the calculated calcination time for the smaller 6.54mm stone than for the larger stone. This is because the energy loss from the smaller stone represents a greater proportion of the total heat balance, and thus less energy is available to be transferred to the calcination reaction.

Table 10-21 shows a decrease in calculated calcination time for increasing value of CaO absorptivity for both the 6.54mm and 13.62mm nominal diameter stone sizes. Again, this is expected because the higher the value of absorptivity, the more energy that is available

within the stone and thus the more energy that makes it to the calcination reaction. Varying the absorptivity value causes approximately the same percentage change in the calculated calcination times for both the 6.54mm and 13.62mm nominal diameter stones. Additionally, varying the absorptivity value by equal amounts from the standard value, causes the same percentage difference in calcination time.

Table 10-22 indicates a decrease in calculated calcination time for increasing value of thermal conductivity of the CaO layer for both the 6.54mm and 13.62mm nominal diameter stone sizes. A low value of thermal conductivity impedes the transfer of the heat to the calcination interfacial zone and therefore reduces the available heat for the reaction, which causes the increase in calcination time.

The percentage change in calculated calcination time for the smaller stone is a little over half the value of the larger 13.62mm nominal diameter stone. This is because thermal conductivity is a function of material thickness and thus the larger stone size can have a thicker CaO layer than the smaller stone. Table 10-22 also shows that the thermal conductivity coefficient is not a function of the radiant heat flux indicated by the same percentage change values for the low and high illuminating radiant heat fluxes.

Table 10-23 shows a decrease in calculated calcination time when increasing the available radiant heat flux. This trend is supported by the experimental results of Chapter 6, 7 and 8 which showed a faster calcination time for higher furnace temperatures and higher radiant heat fluxes. The 12% variation in available heat flux caused a slightly larger percentage change for the larger sized stone than for the smaller one. This implies that the available heat flux has a greater affect on the larger stone than for the smaller one. This may be due to the larger surface area of the stone which collects proportionally more of the radiant heat than the smaller surface.

This sensitivity analysis has shown a range of possible variations in the parameters used for calculation of the calcination times for the calcination of Penrice marble. Comparing the tables 10-20 to 10-23, shows that the value of emissivity and the available heat flux cause the greatest influence to the calculation of the calcination calcination times. With precise measurement of the emissivity of the marble and also of the radiant heat flux, this mathematical modelling of the calcination of Penrice marble could become significantly more accurate.

Using a summation of the maximum and minimum variation in calculated calcination times displayed in the percentage change data of Tables 10-20 to 10-23, the ‘worst case’ scenario from the ‘standard’ cases is presented in Table 10-24. This table also includes the maximum

calculated variation for the 9.44mm nominal diameter stone. Note that the negative values indicate a reduction in calcination time.

Table 10-24: Maximum variation in calculated calcination time for d_c = 6.54mm, d_c = 9.44mm and d_c = 13.62mm Penrice marble in the OSS and ETSF.

Stone Nominal Diameter d_c (mm)	Standard Heat Flux kW/m^2	Calculated Calcination time (minutes)	Maximum Percentage Change %
Open Solar System (OSS)			
6.54	175	17.39	29.63
			-20.86
	430	6.27	33.84
			-20.24
9.44	175	44.99	30.11
			-21.44
	430	12.45	34.05
			-21.15
13.62	175	119.94	31.44
			-23.02
	430	26.47	34.53
			-23.20
Enclosure Triangular Solar Furnace (ETSF)			
6.54	200	16.44	30.25
			-21.09
	450	5.93	34.29
			-20.66
9.44	200	41.44	30.81
			-21.77
	450	10.34	34.80
			-21.19
13.62	200	98.05	32.08
			-23.31
	450	17.05	35.58
			-22.00

The maximum and minimum tolerances were then calculated for the calcination times presented in Tables 10-18 and 10-19 for the three stone sizes exposed to heat fluxes for both the OSS and the ETSF.

Table 10-25: Calculated calcination times with maximum and minimum tolerances for d_c = 6.54mm, d_c = 9.44mm and d_c = 13.62mm Penrice marble using the heat fluxes from the OSS and ETSF investigations.

Radiant heat flux kW/m^2	**Calculated Calcination Times with Tolerances Minutes**					
	6.54mm (0.333g)		**9.44mm (1.000g)**		**13.62mm (3.000g)**	
Open Solar System (OSS)						
175	17.4	+5.2 - 3.6	45	+14 - 9.6	120	+38 - 28
280	9.4	+4.0 - 2.6	22	+10 - 6.7	65	+27 - 19
430	6.3	+2.1 - 1.3	12.4	+4.2 - 2.6	27	+9.1 - 6.1
Enclosure Triangular Solar Furnace (ETSF)						
200	16.4	+5.0 - 3.5	41	+13 - 9.0	98	+32 - 23
300	8.7	+3.9 - 2.6	24	+9.4 - 6.2	51	+22 - 15
450	5.9	+2.0 - 1.2	10.3	+3.6 - 2.2	17.1	+6.1 - 3.8

These calcination times and tolerances are displayed graphically in Figure 10-23 along with the error bars for the uncertainty in the calculation of the radiant heat flux.

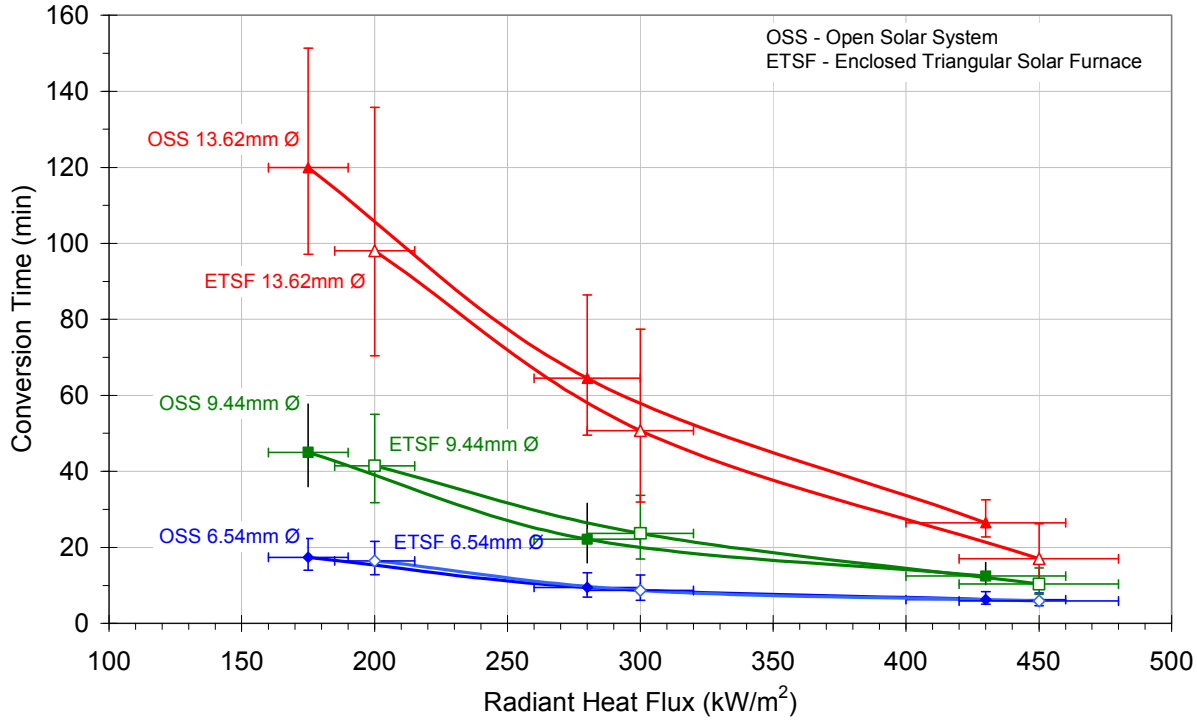

Figure 10-23: Comparison of calculated calcination times with error bars for the three nominal diameter Penrice for the OSS and the ETSF.

10.10 Calcination Rate Calculation

Three rates of decomposition (dm/dt - change of mass over time) have been calculated using the slope of the curve obtained using the calcination times calculated using modified shrinking core model with variable surface temperature (TS.3). Three rates are calculated, 1). The change of mass over time for the first 50% of decomposition, i.e., for dm/dt from 0 to 50% represented by t_{50}, 2). the change of mass over time for up to 75% of decomposition, i.e. dm/dt from 0 to 75% represented by t_{75} and 3). the change of mass over time to completion i.e. dm/dt from 0 to 100%, represented by t_{100}. The three rates were calculated using equations [7.2], [7.3] and [7.4].

A generalised curve for the calcination of the Penrice marble is displayed as Figure 10-24 which shows fractional calcination verses normalised calcination time.

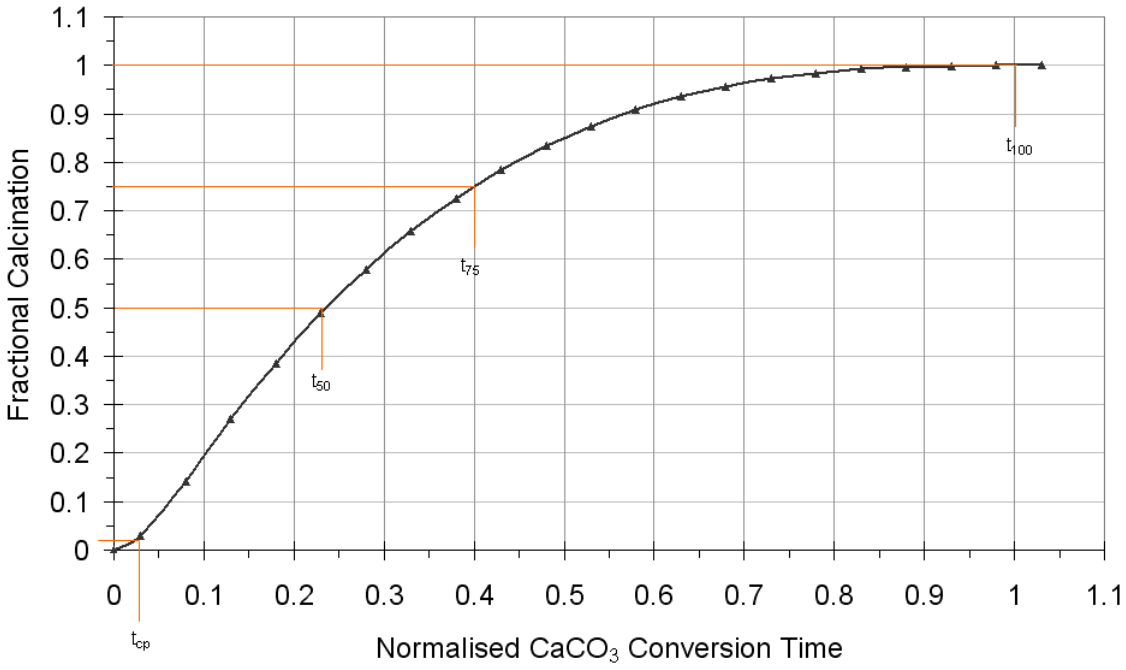

Figure 10-24: Calculated fractional calcination verses normalised calcination time using the modified shrinking core mathematical model.

A direct comparison between the calculated calcination rates of Table 10-26 and the measured rates for the open solar system, Tables 7-2 to 7-4, and triangular solar furnace measured rates, Tables 8-3 to 8-5 was made. The calculated values for the open solar system were higher than the measured values by between 187% and 9%. This largest difference was for the 13.62mm stone size at the 175kW/m^2 radiant heat flux and for the t_{50} and t_{75} fractional calcination values. The 9% difference was for the 430 kW/m^2 heat flux, the 9.44mm stone size and for the t_{100} fractional calcination. The t_{100} rate values for all three heat fluxes were consistently better than the other two fractional calcination values. There is no consistent pattern when comparing the rates between each stone size.

The calculated values for the ETSF compared better than the OSS. The difference between the calculated and measure varied between 62% and -32%. The negative sign indicating that the calculated rate values are lower than the measured values. Comparing rates within each stone size the calculations represent the measurements best for the t_{100} fractional calcination values. Additionally, the rate values compare better for the 200kW/m^2 heat flux than the 450kW/m^2. A comparison between stone sizes indicates that the rate of calcination calculated for the 13.62mm stone size represents the measurement the best. The calculated values, on average, are only 15% different than the measured values.

Table 10-26: Calculated rates of calcination for d_c = 6.54mm, d_c = 9.44mm, and d_c = 13.62mm Penrice marble exposed to the heat fluxes from the OSS and ETSF investigations.

Radiant heat flux kW/m^2	Percentage of Decomposition	Calculated Rate of Calcination dm/dt g/g.s		
		6.54mm (0.333g)	9.44mm (1.000g)	13.62mm (3.000g)
Open Solar System (OSS)				
175	t_{50}	7.298	2.822	1.058
	t_{75}	6.522	2.522	0.946
	t_{100}	3.393	1.312	0.492
280	t_{50}	13.456	5.725	1.969
	t_{75}	12.025	5.116	1.760
	t_{100}	6.256	2.662	0.915
430	t_{50}	20.233	10.197	4.796
	t_{75}	18.082	9.113	4.286
	t_{100}	9.406	4.741	2.230
Enclosure Triangular Solar Furnace (ETSF)				
200	t_{50}	7.720	3.063	1.295
	t_{75}	6.899	2.738	1.157
	t_{100}	3.589	1.424	0.602
300	t_{50}	14.610	5.366	2.502
	t_{75}	13.057	4.795	2.236
	t_{100}	6.792	2.495	1.163
450	t_{50}	21.416	12.278	7.445
	t_{75}	19.139	10.972	6.653
	t_{100}	9.956	5.708	3.461

10.11 Validation of the Calcination Modelling

The calcination model presented in this chapter is used to calculate the preheating times, calcination times and calcination rates for three additional Penrice marble samples which were previously calcined (the results of which are presented in Chapter 8). These stones were a 2.000 gram (11.90mm nominal diameter) Penrice marble exposed to a radiant heat flux of 325kW/m^2, a 3.000 gram (13.62mm nominal diameter) and a 5.000 gram (16.15mm nominal diameter) marble sample both exposed to 385 kW/m^2.

Table 10.27 shows the preliminary specifications for each for these three additional "validation" marble samples.

Table 10-27: Measured heat fluxes and platform temperatures used for the calculation of calcination times for d_c = 11.90mm, d_c = 13.62mm and d_c = 16.15mm Penrice marble.

Measured Marble Mass (grams)	**Calculated Nominal Diameter d_C (mm)**	**Measured Radiation Heat Flux (kW/m^2)**	**Measured Platform Temperature (K)**
2.000 ± 0.005	11.90	325 ± 25	1609
3.000 ± 0.005	13.62	385 ± 25	1674
5.000 ± 0.005	16.15	385 ± 25	1674

The calculated preheating and calcination times are compared in Table 10-28 to the measured results from Tables 8-6 and 8-7.

Table 10-28: Comparison of calculated and measured preheating and calcination times for d_c = 11.90mm, d_c = 13.62mm and d_c = 16.15mm Penrice marble exposed to 325kW/m^2 and 385kW/m^2.

Calculated Nominal Diameter d_C (mm)	**Calculated Power Received (W)**	**Calculated Preheating Time t_{cp} (minutes)**	**Measured Preheating Time t_{cp} (minutes)**	**Calculated Calcination Time t_{cp} (minutes)**		**Measured Calcination Time t_{cp} (minutes)**
11.90	36.1	1.0	2.0 ± 0.2	36.6	+14 - 9.6	26.9 ± 2.2
13.62	56.1	0.88	1.4 ± 0.1	26.2	+13 - 8.5	21.9 ± 1.8
16.15	78.8	1.1	2.9 ± 0.3	33.5	+19 - 12	35.7 ± 2.9

The calculated calcination times compare quite well with the measured values with the difference between the 16.15mm values being less than 7%. The difference between the calculated and measured calcination times for the 11.90mm and 13.62mm diameter stone is 19.4% and 21.3% respectively.

Comparing the preheating times, again the calculations could be considered ‘reasonable’ (considering the assumptions) with a maximum difference of 67% being between the maximum (+0.3) measured preheating time for the 16.15mm stone and the calculated time. A minimum difference of 27% was achieved between the calculated and measured preheating times for the 13.62mm stone.

The calculated calcination times and preheating times for these “validation” scenarios compare favourably, considering the bounding assumptions. With further refinement in the future, this calcination model could be improved to reduce this divergence.

10.12 Conclusions from the Calcination Modelling

This chapter presented a heat balance based theoretical mathematical model to simulate the calcination of three different sized Penrice marble exposed to radiant heat fluxes between 175kW/m^2 and 450kW/m^2 within an open solar calcination system and a triangular shaped solar calcination furnace enclosure.

An energy balance calculation was used on the surface of each marble stone to determine the portion of energy available for heating the stone to 1173K and higher. Using energy exchanges between the marble and its surroundings, the energy balance is then used to calculate the energy available for transfer to the calcination reaction interface. During the calcination stage of the sample, three surface temperature scenarios were considered within the mathematical model. These scenarios were required because conductive heat transfer through the stone, from the surface to the calcination reaction zone, was identified as being a parameter which caused the largest variation in calculated calcination time. The first surface temperature scenario (TS.1) uses a fixed surface temperature of 1223K. TS.1 under estimated the measured calcination times. The second temperature scenario (TS.2) uses a surface temperature 1% lower than the maximum sample temperature where the energy balance equals zero. TS.2 over-estimated the calcination time. The third temperature scenario (TS.3) uses a varying, but increasing, surface temperature. TS.3 provided a reasonable representation of the measured calcination times and was selected for further calculations. These theoretical calculations were then compared to the measured values.

The preheating time was calculated by dividing the documented sensible heat (kJ) for limestone by the heat (J/s) available for heating the marble sample. The modified version of the shrinking core model was then used to calculate the calcination times for the marble stones, after which the calcination rates were calculated. The difference between the

shrinking core model developed in this study and previous model approaches is that the uncalcined core is offset from the centre of the stone. This modification was required because of the non uniform heating of the stone by the illuminating radiant heat flux. This eccentric shrinking core model provided an improvement of up to 14.3% over the standard model, but only when a non-uniform, non-steady state surface temperature was assumed on the surface of the stone during calcination. Additionally, the eccentric shrinking core model produced a better match to the measurements for the small nominal diameter stone of d_c = 6.54mm at the lowest heat fluxes, and for the d_c = 13.62mm at the highest heat fluxes.

The comparison between the measured and calculated heating times show that the calculated values underestimate the measured times by between 50% and 83% for the OSS and between 9% and 80% for the ETSF. It was also shown that the measured preheating times are a function of the surface area of the exposed stone (squared relationship), where as the calculated times are a function of the radius of the stone (linear relationship).

The comparison between the measured and calculated calcination times show that the calculated values coincide reasonably well. The calculated calcination times for the 6.54mm nominal diameter stone over-calculate the measured calcination times by between 5.5% and 18.5%. The calculated times for the 9.44mm stone are between 25% and 34% of the measured values, and for the 13.62mm stone the calculated times are between 15% and 34% of the measured values.

The modelling results indicate that the calculated values for the triangular solar furnace enclosure compared better to the measured data than for the open solar system. The calculated calcination times for the ETSF over-estimated the measured calcination times, where as the OSS under-estimates it.

Validation of the calcination model presented within this chapter has been achieved through the reasonably close representation of the values obtained within the experimental measurements conducted within this research. Improvements to the current model are recommended as future work, so that a more precise and detailed modelling package can be developed.

The conclusions from this research investigation and future work recommendations are presented in the next Chapter.

Chapter 11

Conclusions

The objective of this research investigation was to answer fundamental questions regarding the effectiveness of using concentrated solar energy as the sole heating source for the thermo-chemical decomposition of Penrice, Angaston marble. The conclusions from these investigations are now presented, followed by recommendations for future work to further develop and improve the current research.

11.1 Zero Dimensional Studies of a Solar Lime Furnace

The mathematical heat and mass balance model developed to simulate the flow of heat and mass through both conventional and solar energy lime manufacturing processes revealed the following. The thermal efficiency of a solar energy supplied lime manufacture system compares favourably with the best fossil fuelled system. The solar energy consumption was calculated to be approximately 4560 MJ/tonne of CaO. A good heat recovery system as well as a comprehensive preheating system is recommended to minimise the energy losses from the system. A relatively concentrated and homogeneous CO_2 gas stream can be collect and sequestered as desired, by bypassing the preheating air around the solar calcination chamber.

The Hottel zero dimensional zonal model was used to evaluate the energy efficiency of various solar furnace shapes. For a kiln with a 4m equivalent diameter (cross-sectional area of 12.57m^2), the cross sectional shape with the highest efficiency was the right angled triangle. The modelling indicated that the floor area of the triangular kiln should be as large as possible to maximise exposure of the limestone to the solar radiation. Maximising the available limestone bed surface area can be achieved by either increasing kiln length or increasing the kiln width. Lower heat losses from the furnace structure were achieved by increasing the kiln width and minimising the surface area of any unused sections of the furnace, such as the vertical wall and the roof area. Additionally, openings which allow the flow of the process material should be minimised to improve the thermal efficiency of the furnace.

11.2 Multi-Zone Two Dimensional Studies of a Solar Lime Furnace

The findings from the multi-zone two-dimensional zone radiation modelling package used to model the radiation source and the resulting radiation exchange and heat flux distribution within the Open Solar System (OSS) and Enclosed Triangular Solar Furnace (ETSF) are as follows.

A pseudo-source temperature of approximately 16196K is need to match the measured heat flux of 16.03 kW/m^2. The sensitivity analysis for this calibration showed that using the maximum tolerance in measurement parameters provided a $\pm$ 16% variation in the calculated heat flux. A source temperature of 25,400K was required for the OSS model and for the ETSF model. For the open and enclosed furnace models the sensitivity analysis showed a maximum variation of 42.2% and 39%, respectively, in the calculated heat flux at the calcination platform for a constant simulated solar source.

Using these uncertainty values, the calculated heat flux values at the calcination platform coincide quite well with the measured values for both the OSS and ETSF.

The modelling also indicates that using the ETSF increases the heat flux at the location of the calcination platform by as much as 20% compared to the OSS.

11.3 Muffle Furnace Calcination Experiments

The muffle furnace calcination experiments quantified the relationships between furnace temperature, particle size and bed depth for 3mm to 13mm nominal diameter Penrice marble. As expected, the measurements showed that the calcination rate of Penrice marble increases as the temperature of the furnace increases. The calcination rate for 1.000g (d_c = 9.44mm) Penrice marble when exposed to furnace temperatures between 850°C and 1000°C can be expressed using:

$$\ln\left(\frac{dm}{dt}\right) = a + bT^{2.5} \quad \text{g/g.s} \qquad [11.1]$$

where, T is the furnace temperature, a = -4.398 and b = 1.782×10^{-7} for a calcination time between t = 0 to 100%.

The calcination rate for 3mm nominal diameter Penrice marble, spread to form a bed with thickness of between 4.5mm to 12mm is given by:

$$\frac{dm}{dt} = 1.17 + \frac{43.54}{(b_d)^2} \quad g/g.s \qquad [11.2]$$

where, b_d is the bed thickness.

For 10mm nominal diameter Penrice marble the calcination rate can be expressed using:

$$\frac{dm}{dt} = 0.979 + \frac{109.33}{(b_d)^2} \quad g/g.s \qquad [11.3]$$

The results also show that there was an increase in calcination rate for decreasing particle size, for a marble bed thickness of up to 2.5 times the nominal thickness of the marble. A bed thickness larger than this reduced the calcination rate, which infers that the calcination rate is affected by the diffusion of CO_2 through a packed bed as well as the transfer of heat to the reaction zone. The bed thickness should therefore be no thicker than 2.5 times the particles diameter for Penrice marble with nominal diameter between 0.375mm and 2.855mm.

The muffle furnace experiments were also used to quantify the calcination rates and completion times for single stones of Penrice marble, as displayed in Table 11-1. As expected, the calcination rates increase for decreasing particle size, and for increasing furnace temperature.

Table 11-1: Calcination rates and completion times for single stone marble in a muffle furnace at either T_F = 900°C or T_F = 1000°C.

Marble Nominal Diameter d_C (mm)	**Rate of Calcination for 900°C dm/dt_{50} (g/g.s)**	**Time to Complete Calcination t_{100} for TF = 900°C (minutes)**	**Rate of Calcination for 1000°C dm/dt_{50} (g/g.s)**	**Time to Complete Calcination t_{100} for TF = 1000°C (minutes)**
13.62	1.178	24	3.98	10
9.44	2.154	64	5.69	22
6.54	4.404	104	11.27	26

11.4 Open System Calcination Experiments

The findings of the open solar system calcination experiments show that the rate of calcination increase with an increase in radiant heat flux and also with a decrease in stone diameter. In particular the experiments identified the following:

- The 6.54mm stone calcines in approximately 21 minutes when exposed to a solar radiant heat flux of 175kW/m^2. It calcines 1.8 times faster when exposed to 280kW/m^2 compared to 175kW/m^2 and around 2.0 times faster when exposed to 430kW/m^2 compared to 280kW/m^2.

- The 9.44mm stone calcines in approximately 65 minutes when exposed to a solar radiant heat flux of 175kW/m^2. It calcines 2.1 times faster for the 280kW/m^2 than for the 175kW/m^2 and around 2.4 times faster for 430kW/m^2 than 280kW/m^2.

- The 13.62mm nominal diameter marble calcined using a heat flux of 175 $\pm$ 10 kW/m^2 takes approximately 4 hours to complete calcination, which would be considered too long for an industrial solar lime manufacturing plant. The calcination rate for the 13.62mm stone increased from 4.0 to 2.3 times between 175kW/m^2 and 280kW/m^2 and between 280kW/m^2 and 430kW/m^2 respectively.

- The 13.62mm nominal diameter marble calcined using a heat flux of 430 $\pm$ 30 kW/m^2 showed signs of hard burning on the surface facing the high intensity radiation.

- The preheating time of the stone is directly proportional to the illuminated surface area of the stone and inversely proportional to the intensity of the radiant heat flux to which it is exposed.

A direct comparison between these open system radiation experiments and the muffle furnace test have shown that the calcination rates for all three stone sizes is similar between the 280kW/m^2 and 900°C experiments. There is virtually no difference in the calcination rates for the 6.54mm nominal diameter stone when comparing the results from the 430kW/m^2 radiation experiments and the 1000°C muffle furnace experiments. The results from the other two stone sizes for the same comparison are within 13% of each other.

11.5 Enclosed Solar Furnace Calcination Experiments

The results of this experimental investigation show that there is a decrease in calcination time with decreasing stone size and increasing heat flux, as expected. The relationship between completion times and stone size appear directly proportional with a tripling of completion time with tripling of stone size. The CO_2 release rate increases with increasing stone size and increasing heat flux, but are not directly proportional to each other.

The calcination rate for the 6.54mm stone is approximately 185% faster than for the 13.62mm nominal diameter stone (at dm/dt_{50}) when exposed to the same heat flux. This difference decreases as the heat flux increases, e.g. the 6.54mm is only 62% faster than the 13.62mm when exposed to 450kW/m^2.

The enclosed solar furnace experiments shows that an increase in calcination rate of up to 45% can be achieved by using a triangular shaped furnace enclosure compared to the open system calcination results. It was also shown that increased calcination rates were measured as the radiant heat flux increases. Additionally there was higher calcination rates for the larger stone sizes than the smaller ones owing to the increase in stone surface area exposed to the reflected and emitted heat flux from the heated furnace walls.

These measurements show that the preheating time of the stone is directly proportional to the surface area of the stone and inversely proportional to the intensity of the radiant heat flux to which it is exposed. This relationship is similar to that found for the open system experiments.

The completion times shown in Table 8-13 are typical of those found for a rotary kiln which demonstrates the practicalities of this technology which could practically interchange with the current industrial plants. The scale up issues associated with previous reported works (rotary kiln, fluidised bed, or falling particle) are not present with a travelling grate solar furnace design.

11.6 Modelling the Calcination of Limestone

A heat transfer mathematical model was developed which uses an energy balance approach to calculate the preheating and calcination time for single Penrice marble stones exposed to radiant heat flux. The heating time was calculated by dividing the sensible heat (kJ) for limestone by the heat (J/s) available for heating the marble sample. After heating the stone, the available energy is assumed to be available for the calcination reaction.

The calcination conversion time was calculated by considering the conductive heat transfer from the surface of the stone through the CaO layer to the calcination front on the outside of the $CaCO_3$ core. This constitutes a modified version of the shrinking core model. The main difference is that the core is considered to shrink eccentric to the centre of the sample. This modification better represents the non uniform heating of the stone by the radiant heat flux.

The comparison between the measured and calculated heating times show that the calculated values underestimate the measured times by between 50% and 83% for the OSS and between 9% and 80% for the ETSF. It was also shown that the measured preheating times are a function of the surface area of the exposed stone (squared relationship), where as the calculated times are a function of the radius of the stone (linear relationship).

The comparison between the measured and calculated calcination times using the eccentric shrinking core model show that the calculated values coincide reasonably well. The calculated calcination times for the 6.54mm nominal diameter stone over-calculate the measured calcination times by between 5.5% and 18.5%. The calculated times for the 9.44mm stone are between 25% and 34% of the measured values, and for the 13.62mm stone the calculated times are between 15% and 34% of the measured values.

The modelling results indicate that the calculated values for the ETSF compared better to the measured data than for the OSS. The calculated calcination times for the ETSF over-estimated the measured calcination times, where as the OSS under-estimates it.

11.7 Recommendations for Further Work

11.7.1 Process Modelling

The present work has established a process efficiency model to evaluate various system configurations. Improvements in modelling the heat and mass transfer within the chambers of the proposed solar lime manufacturing plant would provide a better representation of the system. Future evaluation modelling should focus on the recovery of heat from the cooling product and preheating of the incoming limestone feed.

Coupled to this proposed process model is the evaluation of the system through an embodiment design. This needs to include improvements in technical specification, the development of an economic criterion, include an overall layout design and preliminary form design.

11.7.2 Solar Furnace Design and Radiation Modelling

The current multi-zone two-dimensional zone model represents the reflector behind the radiation source as a flat sheet. A true representation of the elliptical reflector would produce a more realistic and consistent source temperature and thus better representation of the

lamphouse solar simulator. An alternative approach would be to place the radiation source at a distance from the deflection mirror such that the radiation reaching it was a parallel beam.

11.7.3 Mathematical Calcination Model

The present mathematical calcination model uses the equation for eccentric cylinders for the eccentric spheres, by setting the length of the cylinder to be the nominal diameter of the marble stone being simulated. This assumption was used after extensive review and discussion with Howell (2009) regarding the calculation of a shape factor for eccentric spheres. The calculation of a shape factor for eccentric spheres would improve the modelling.

11.7.4 Experimental Investigations into the Calcination of Limestone using Solar Radiation

The present investigation measured the heat up time and calcination rates for small to medium sized Penrice marble using solar radiant energy as the sole heating source. During the experimental investigation it was identified that the calcination time was affected by the shape of the stone sample being decomposed. It was recognised that the thinner stones calcined quicker than the more rounded stones. It is recommended that further investigations be carried out to correlate stone shape with calcination rate for variations in heat flux intensity.

The solar calcination experiments would be further enhanced by measuring temperatures within the sample during calcination. Mallen (1956) used imbedded thermocouples to measure temperatures near the surface and at the centre of various shaped Penrice marble samples during thermo-gravimetric convection experiments. Similar temperature measurements within the stone should be considered when using solar radiation, but also include an intermediate location so that the interfacial zone temperature can be measured. A comparison between single-sided heating and uniform heating of the stone will quantify the benefits of turning the sample during calcination and also provide a basis for evaluation of the electrical energy consumed to turning the stone. The influence of turning rate could also be evaluated.

Measurements in the solar calcination experiments revealed that there is an increase in release rate of CO_2 (g / sec) with increasing stone size when exposed to the same heat flux. Numerous repetitive experiments are recommended to confirm and identify the cause of this finding. These experiments would help identify if there is variations in the rate limiting step for different stone sizes or for different radiant heat flux intensities.

Solar calcination experiments using different types of limestone would help establish a data base for comparison and also identify the effects of different contaminants (and colours) found in the various limestone.

11.7.5 The Road to Industrial Solar Lime Manufacture

The objective of this project is to develop the fundamental components required for the efficient and cost- effective integration of solar energy into industrial lime manufacture. The research presented in this thesis forms part of a technical feasibility study. A flat bed reactor was chosen because it offered the best potential for scale-up from laboratory scale to a typical scale lime kiln of 100-500 tonne/day production. It has been experimentally demonstrated that a flat bed type of reactor could be used for the solar thermal decomposition of various small to medium sized limestone. The next step is to complete a conceptual design and then detailed design for a pilot scale demonstration plant. The focus of the demonstration plant would be to assess:

- the development of the optical system and procedures to optimise delivery of the concentrated radiation into the reactor,
- analyse the effects of bed mixing including optimisation of stone turning rates,
- further analyse and develop optimal reactor designs to improve thermal efficiency,
- the design and development control systems for both the solar energy delivery as well as for process control,
- the development of improved real time measurement tools,
- providing real data for further modelling.
- conduct a preliminary economic assessment and assess the market potential for a stand alone or integration of solar limestone heating systems into existing industrial manufacturing sites, and
- assess and address scale up issues.

An assessment can then be conducted to evaluate the potential for an on-site proof of concept pilot scale facility. This facility will incorporate all of the features which were tested

and improved on the laboratory scale demonstration plant. Additionally, this pilot scale facility can be used to design and test heat recovery systems as well as evaluate various preheating systems. The final stage is to develop a full-scale facility.

A significant factor to the future development of solar lime manufacturing is the price put on carbon. The carbon price is an administrative approach imposing a cost on the emission of greenhouse gases such as CO_2 which cause global warming. Imhof (1997) conducted a preliminary economic assessment of a large scale solar cement production plant and concluded that it was not currently competitive with a conventional fossil fuel (or wood) burning system. Imhof (2000) estimated that a carbon price of $50 US/tonne CO_2 is required achieve comparable production costs.

Appendix A

Specifications and results from a preliminary heat and mass balance evaluation for lime burning processes. Specifications and combustion data for the fossil fuels sourced from Borman and Ragland (1998), Johnson and Auth (1951), The Institute of Fuel (1963) and Rose and Cooper (1977).

Table A-1: Enthalpy analysis for four fuels and two solar energy furnaces **NR ~ Not Required**

	General Purpose Coal (902)	Coke	Heavy Fuel Oil	Methane	Solar with Full Limestone Preheating	Solar with No Limestone Preheating	Solar with Partial Limestone Preheat
Calorific Value (kJ/kg)	22600	32780	44200	55536	NR	NR	NR
Air / Fuel Ratio	7.85	11.53	13.5	17.2	NR	NR	NR
Fuel Consumption (MJ/tonne CaO)	3531	3438	3168	3364	3197	4044	3197
Fuel Consumption (MWh/Tonne)	0.98	0.955	0.880	0.93	0.888	1.123	0.888
Quantity of Fuel (kg/tonne CaO)	156	105	72	61	NR	NR	NR
Specific Heat (Cp) of Fuel at 295K	1.300	0.722	0.859	2.217	NR	NR	NR
Specific Heat (Cp) of Fuel at 1173K	1.300	1.491	1.153	4.859	NR	NR	NR
Combustion Air Mass (kg/tonne CaO)	1226	1209	968	1042	1063	Zero	886
Combustion Air Preheat Temperature (K)	929	938	1099	1042	1027	NR	1173
Specific Heat (Cp) of Air at 295K	1.005	1.005	1.005	1.005	1.005	NR	1.005
Specific Heat (Cp) of Air at 1173K	1.174	1.174	1.174	1.174	1.174	NR	1.174
Exhaust Gas Mass (kg/tonne CaO)	2168	2100	1825	1888	1849	786	1672
Specific Heat (Cp) of Exhaust Gas at 295K	1.839	2.428	3.295	1.113	0.937	0.846	0.930
Specific Heat (Cp) of Exhaust Gas at 1173K	2.110	2.785	3.780	1.369	1.215	1.270	1.219
Limestone Mass (kg)	1786	1786	1786	1786	1786	1786	1786
Limestone Temperature after Preheating (K)	1173	1173	1173	1173	1173	662	1088
Specific Heat (Cp) of Limestone at 295K	0.828	0.828	0.828	0.828	0.828	0.828	0.828
Specific Heat (Cp) of Limestone at 1173K	1.401	1.401	1.401	1.401	1.401	1.401	1.401
Quicklime Quantity (kg)	1000	1000	1000	1000	1000	1000	1000
Quicklime Outlet Temperature (K)	1173	1173	1173	1173	1173	1173	1173
Specific Heat (Cp) of Quicklime at 295K	0.762	0.762	0.762	0.762	0.762	0.762	0.762
Specific Heat (Cp) of Quicklime at 1173K	1.169	1.169	1.169	1.169	1.169	1.169	1.169

Appendix B

Derivation of the zero-dimensional Hottel model equations.

The net heat exchange from the hot gases to the sink is given by:

$$Q = (GS_1)_R \sigma (T_g^4 - T_1^4) \qquad \text{[B-1]}$$

where the total exchange area between gas and sink in radiative equilibrium is given by:

$$(GS_1)_R = \frac{A_T}{\left(\frac{1}{\varepsilon_{fuel}}\right) + \left(\frac{1}{C_S \varepsilon_1}\right) - 1} \qquad \text{[B-2]}$$

The energy balance of the system can be written as:

$$\frac{(H_f - Q)}{H_f} = \frac{T_g - \Delta - T_0}{T_{af} - T_0} \qquad \text{[B-3]}$$

Where: The rate of enthalpy obtained from the fuel gases and air inputs is:

$$H_{fuel} = \dot{m}_{fuel} HHV + \dot{m}_{sa} C_p \Delta T + \dot{m}_{pa} C_p \Delta T \qquad \text{[B-4]}$$

The calculation of the adiabatic flame temperature is achieved using:

$$T_{AF} = \frac{\sum \Delta H_{reac} - \sum \Delta H_c}{\sum \dot{m} \times Cp} + T_0 \qquad \text{[B-5]}$$

Combing Equation B-1 and Equation B-3 gives,

$$\frac{Q}{\sigma (GS_1)_R} + T_1^4 = T_{af}^4 \left[1 + \left(\frac{\Delta}{T_{af}} \right) - \frac{Q(T_{af} - T_0)}{H_f T_{af}} \right]^4 \qquad \text{[B-6]}$$

Dimensionless Groups:

The simplification of the energy balance, as given in Equation B-4, is carried out by incorporating the following dimensionless groups (Equations B-7, B-8, B-9 & B-10).

$$Q' = Q\frac{\left(T_{af} - T_0\right)}{H_f T_{af}} \qquad \text{[B-7]}$$

$$D' = \frac{H_f}{\sigma\left(GS_1\right)_R T_{af}^3\left(T_{af} - T_0\right)} \qquad \text{[B-8]}$$

$$\tau = \frac{T_1}{T_{af}} \qquad \text{[B-9]}$$

$$\Delta' = \frac{\Delta}{T_{af}} \qquad \text{[B-10]}$$

Incorporating the dimensionless groups into Equation B-6 yields Equation B-11.

$$Q'D' + \tau^4 = \left(1 - \Delta' - Q'\right)^4 \qquad \text{[B-11]}$$

The relationship between Q' and Δ' is given in Equation B-12, and combining this with Equation B-11 gives the original version of Hottel's 0-D Model, Equation B-13.

$$\Delta' = \left(1 - \frac{1}{d'}\right)Q' \qquad \text{[B-12]}$$

$$Q'D' + \tau^4 = \left(1 - \frac{Q'}{d'}\right)^4 \qquad \text{[B-13]}$$

The value of d' can be assumed to be 4/3 provided 0.02 < D'< 1.0 (Hottel approximation)

Adding in convective and radiative heat losses through the shell or heat losses through ends gives Equation B-14, The effective exchange area is given below in Equation B-15 was developed from Equation B-3 to account for the losses from the openings fraction.

$$Q = (GS_1)_R\sigma(T_g^4 - T_1^4) + UA_R\left(T_g - T_o\right) + (GS_o)_R\sigma(T_g^4 - T_o^4) \qquad \text{[B-14]}$$

$$(GS_O)_R = \frac{A_T}{\left(\frac{1}{\varepsilon_{fuel}} + \frac{1}{C_O \varepsilon_{fuel}}\right) - 1} \qquad \text{[B-15]}$$

The openings fraction is defined as the ratio of the total surface are of the openings to the total surface area of the kiln.

The following additional dimensionless groups were required to enable the simplification of the energy balance.

$$\tau_o = \frac{T_o}{T_{af}} \qquad \text{[B-16]}$$

$$L_R' = \frac{UA_R}{\sigma (GS_1)_R T_{af}^3} \qquad \text{[B-17]}$$

$$L_o' = \frac{(GS_o)_R}{(GS_1)_R} \qquad \text{[B-18]}$$

The temperature of the combustion gases is eliminated by combining Equation B-4 and Equation B-14 and the dimensionless groups are incorporated to get the final Hottel Model equation,

$$Q'D' = \left(1 - \frac{Q'}{d'}\right)^4 - \tau^4 + L_R'\left[\left(1 - \frac{Q'}{d'}\right) - \tau_o\right] + L_o'\left[\left(1 - \frac{Q'}{d'}\right)^4 - \tau_o^4\right] \qquad \text{B-19}$$

Appendix C

Initial conditions of the zero-dimension Hottel zone model

Kiln Plant Parameters

Plant operational hours per day ~ 24hrs,

Percentage of $CaCO_3$ in the Feed ~ 100%,

Ratio of CO_2 to $CaCO_3$ evolved (product) in kiln ~ 44%,

Problem Parameters

Stefan-Boltzmann Constant = 5.670×10^{-8} W/m^2.K^4

Ambient Air Temperature = 288 K

Primary Air Temperature = 305 K

Secondary Air Temperature = 973 K

Specific heat of Air at 288K = 0.240566 kcal/kg.K = 1.0072 J/kg.K

Specific heat of Air at 305K = 0.24004 kcal/kg.K = 1.007 J/kg.K

Specific heat of Air at 1073K = 0.272407 kcal/kg.K = 1.1405 J/kg.K

Specific heat of Combustion Flue Gases at 2700K = 0.38 kcal/kg.K

Specific heat of Combustion Flue Gases at 1100K = 0.3 kcal/kg.K

Kiln Parameters

Heat Loss Through Kiln Structure = 3.65 kcal/h.m^2.K = 0.0042 W/m^2.K

Kiln Wall Thickness = 0.15 m

Inside Convective Heat Trans Coefficient = 1.81×10^{-3} kcal/s.m^2.K

Outside Convective Heat Trans Coefficient = 2.31×10^{-3} kcal/s.m^2.K

Thermal Conductivity of Wall = 4.00×10^{-3} kcal/s.m.K

Fuel Parameters

Mass flowrate of Fuel (pulverised Coal) = 1.44 kg/s

Mass flowrate of Primary Air = 1.73 kg/s

Mass flowrate of Secondary Air = 10.77 kg/s

Nett Calorific Value of Fuel = 7270 kcal/kg

Combustion Parameters

Stoichiometric Air/Fuel Ratio kg/kg = (primary air + secondary air)/ fuel

Excess Air = 0.05 (%/100)

Temperatures

Material Temperature before entering Kiln = 298 K

Material Temperature on Exit of Kiln = 1173 K

Average Material Temperature of Material in Kiln (AvTemp) = (1173+298)/2 (K)

Charge Material Parameters

Heat of Calcination of lime per kg = 718 kcal/kg

Specific Heat

Specific heat of Lime = $0.238845896627\times(-2.9075000\times10^{-18}\times(\text{AvTemp})^6 + 1.4115689\times10^{-14}\times(\text{AvTemp})^5 - 2.8378867\times10^{-11}\times(\text{AvTemp})^4 + 3.0469569\times10^{-8}\times(\text{AvTemp})^3 - 1.8648961\times10^{-5}\times(\text{AvTemp})^2 + 6.8124355*10^{-3}\times(\text{AvTemp}) - 0.15251766)$ kcal/kg.K

Other Data Parameters

Furnace Gas Emissivity = 0.9

Limestone Emissivity = 0.41 Source: Lipinski and Steinfeld (2004)

Lime Emissivity = 0.41 Source: Lipinski and Steinfeld (2004)]

Hottel Approximation ~ d = 4/3

d is the dimensionless constant in the relation $\Delta' = \left(1 - \frac{1}{d}\right)Q'$ (Hottel 1974)

Appendix D

Calcination Measurements of Penrice Marble Directly Exposed to High Intensity Radiation

This Appendix presents the results from the first set of experiments conducted using radiation as the sole heating source. The first set of open system radiation experiments were similar to the constant diameter bed experiments conducted within the muffle furnace. These experiments maintained a constant bed size (diameter) while varying the bed thickness, by varying the mass of the sample. Unfortunately, due to the large variation in the radiant heat flux intensity within the radiation beam and the diameter of the beam itself, complete calcination of the bed-sample was not achieved before hard burning of the marble within the region of highest heat flux occurred.

The purpose of these experiments were to measure the calcination rate of a bed of Penrice Angaston marble of various stone size exposed to an average radiant heat flux of 115 kW/m^2.

D.1 Constant Bed Diameter Calcination Experiments

Samples of either: 0.375mm, 0.925mm, 1.850mm and 2.855mm nominal diameter Angaston marble samples were spread evenly over the top surface of a flat ceramic fibre refractory board (150mm square and 10mm thick). The marble bed was constrained to fit within a circle 80mm in diameter which resulted in various bed depths for the four nominal diameter marbles. Two bed thicknesses for each nominal diameter marble were used. The first set of experiments resulted in bed thickness of around 45mm, produced by placing 40 gram samples of each of the marble sizes (Table D-1). The second set of experiments used bed thickness's which were 1.5 times the marble's nominal diameter (Table D-2).

Similar to the muffle furnace experiments, the 40 gram sample resulted in differing bed depths for each of the four nominal diameter marble. The depth of each bed was directly measured using Vernier calipers, the results of which can be seen in Table D-1. Also shown is the non-dimensional marble bed depth as a function of the nominal stone diameter, (b_d / d_c), which is the measured bed depth divided by the marble particle nominal diameter.

Table D-1: Bed depth for the 40g marble samples placed to form an 80mm diameter bed exposed to the radiation beam.

Marble Nominal Diameter (mm) d_C	**Measured Bed Depth (mm) (± 0.1mm)** $b_{d,m}$	**Bed Depth as Function of Nominal Diameter** $\frac{b_{d,m}}{d_C}$
0.375	4.4	11.7
0.925	4.6	4.97
1.850	4.9	2.65
2.855	4.2	1.47

Figures D-1 and D-2 are photographs of two of the 40 gram marble samples placed on the refractory board before being placed into the radiation beam. Figures D-5 and D-6 are photographs of the same two marble samples after calcination.

The depth of the marble bed was then adjusted to form beds with thicknesses 1.5 times the nominal diameter of the stone. The mass of each of the four diameter marble samples was adjusted to obtain the 1.5 nominal diameter bed depths. The bed thickness was directly measured using Vernier calipers, as well as being calculated using the bulk density of 1425 kg/m^3 (2:1 size ratio) which is provided by Oates (1998) on page 19. The bulk density can be defined as the mass of many particles of the material divided by the total volume they occupy, where the total volume includes particle volume, inter-particle void volume and internal pore volume. The calculated bed depth was used to provide a guide to obtaining the b_d / d_c = 1.5. Table D-2 shows the nominal marble diameter, the total mass of each sample, the measured and calculated bed depths and the measured bed depth as a function of the nominal marble diameter.

Figure D-1: Photo of d_c = 2.855mm marble spread over refractory board to form 80mm diameter circle, before calcination.

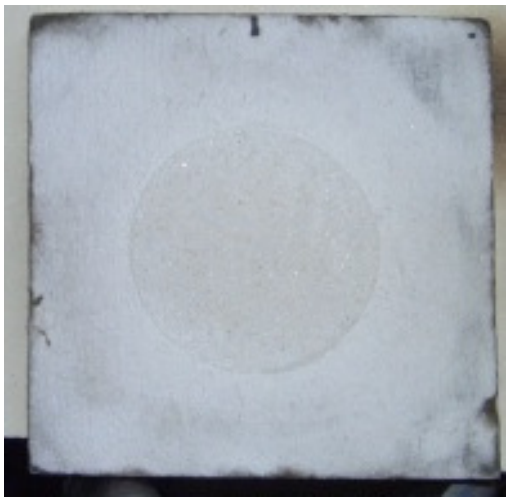

Figure D-2: Photo of d_c = 0.375mm marble spread over refractory board to form 80mm diameter circle, before calcination.

Table D-2: Mass and measured bed depth of samples to obtain a bed thickness of 1.5 times the particle diameter

Marble Nominal Diameter (mm) d_C	**Total Mass of Sample (gram)** m_s	**Measured Bed Depth (mm) (± 0.1)** $b_{d,m}$	**Calculated Bed Depth (mm)** $b_{d,c}$	**Bed Depth as Function of Nominal Diameter** $\frac{b_{d,m}}{d_C}$
0.375	5	0.5	0.56	1.6
0.925	15	1.5	1.38	1.51
1.850	25	2.6	2.77	1.51
2.855	40	4.3	4.28	1.54

The xenon lamp and calcination platform were preheated for a minimum of 90 minutes prior to placing the ceramic fibre refractory board into the radiation beam. Preheating the lamp and calcination platform ensured that a steady state radiation heat flux condition was established. After loading and measuring the depth of the marble, the refractory board (with marble bed) was placed within the radiation at a location S = 100mm from the focal point of the radiation beam. The S = 100mm distance was chosen after several failed attempts at calcining the Penrice marble at larger distances from the focal point. The calcination time was substantially longer (> 4hrs) than would be desirable for an industrial solar calcination furnace using these size stones. The 100mm distance provided a compromise between rate calcination and hard burning of the stone at the zone of maximum heat flux within the beam.

Using the digital image heat flux measurement methods described in Chapter 5, the average heat flux illuminating the bed of marble was calculated to be 115kW/m^2, and the maximum was 175kW/m^2. The diameter of the illumination spot on the refractory board was measured to be approximately 58mm. Unfortunately this distance means that the entire 80mm diameter of marble bed is not illuminated by the radiation beam. To achieve full coverage of the bed, the calcination bed would need to be placed at 150mm from the focal point, but as described above, this did not provide an adequate calcination rate. With the platform placed at S = 100mm the illuminated area represents approximately 52.5% of the total bed area. The calcination measurements were therefore scaled to represent the actual area illuminated. Most of the calcination experiments were unfortunately cut short due to significant hard burning of the marble within the region of maximum heat flux while other areas of the bed remained only partly calcined (or even uncalcined). A qualitative approach to analyse these results was therefore taken.

During the calcination measurements the mass of the calcining marble was automatically measured at 5 second intervals, for the duration of the experiments using the GX-600 analytical balance. The mass loss due to calcination of each sample was calculated using Equation [6.1], which was subsequently multiplied by the ratio of bed area divided by illuminated area.

D.2. Results Plots and Tables

Figures D-3 and D-4 show the calcination profiles for the constant bed diameter calcination experiments for Penrice marble with nominal diameter between 0.375mm and 2.855mm, exposed to the same radiant heat flux.

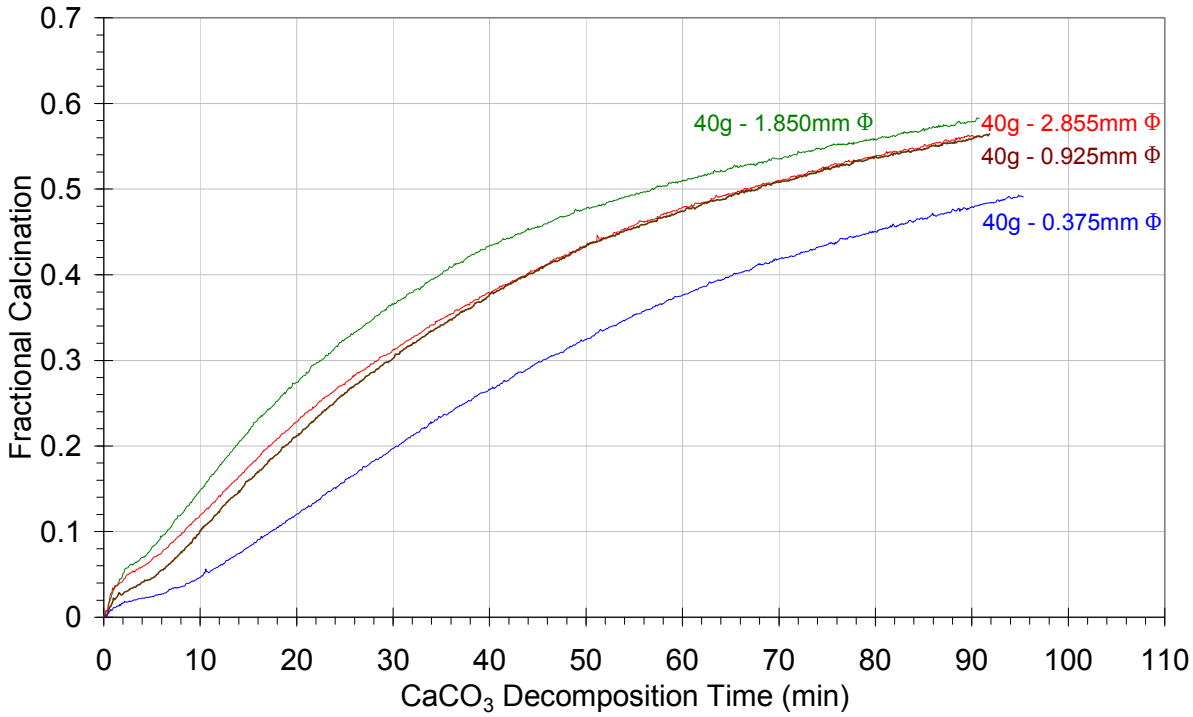

Figure D-3: Calcination profiles of 40 gram samples of four different sized Penrice marble exposed to radiation with an average heat flux of approximately 115 kW/m^2.

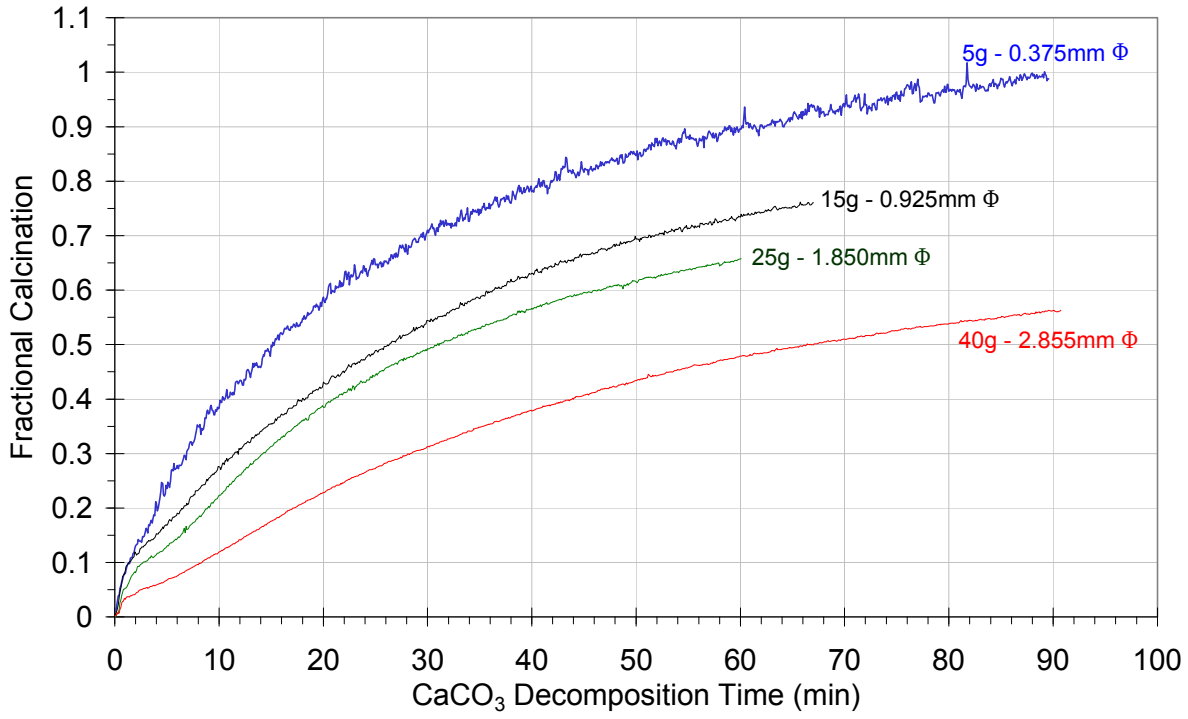

FigureD-4: Calcination profiles of four different sized Penrice marble spread to form a bed 1.5 times the marble's nominal diameter, and exposed radiation with an average heat flux of approximately 115 kW/m^2.

Tables D-3 and D-4 show the calculated rates of calcination for the open system bed calcination experiments. The rate of calcination (dm/dt) has been calculated using the slope

of the fractional calcination profiles shown in Figures D-3 to D-4. Due to incomplete calcination, the only calcination rate available for comparison is dm/dt_{50}, which is the change of mass over time for the first 50% of decomposition, i.e., for dm/dt from 0 to 50%. The preheating time is not applicable within these experiments for three reasons:

1). Because of the small size of the stones, there was instantaneous loss of mass from some stones within the region of highest heat flux, and

2). The non-uniformity of the radiation intensity meant that some the of stone was being preheated even after other stone had achieved completion, and

3). The diameter of the radiation beam compared to the diameter of the bed meant that some stone would never become preheated.

The time from the beginning of calcination to final completion is also not stated because none of the samples achieved complete calcination.

Table D-3: Calcination rates for the 40 gram flat bed experiments exposed to an average 115kW/m^2.

Marble Nominal Diameter d_C (mm)	**Rate of Calcination for dm/dt_{50} (g/g.s)**
0.375	0.309
0.925	0.442
1.850	0.525
2.855	0.448

Table D-4: Calcination rates for the bed thickness of 1.5 x d_c exposed to an average 115kW/m^2.

Marble Nominal Diameter d_C (mm)	**Rate of Calcination for dm/dt_{50} (g/g.s)**
0.375	1.984
0.925	1.137
1.850	0.976
2.855	0.448

D.3 Analysis of Results

The two calcination profile plots, Figure D-3 and D-4 for the constant diameter marble bed experiments show incomplete conversion of the $CaCO_3$ to CaO for all but one stone size. As mentioned previously, the experiments were suspended prematurely because the marble in the region of highest heat flux was becoming visibly hard burnt. Figure D-5 and D-6 show the 2.855mm and 0.375mm nominal diameter marble bed after the calcination experiment, with the prominent hard burning area highlighted in the figures.

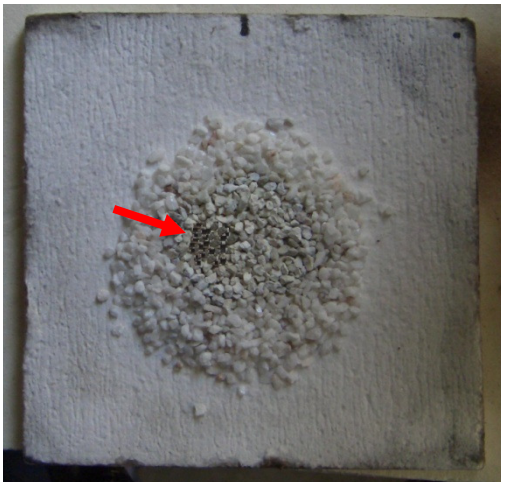

Figure D-5: Photo of d_c = 2.855mm diameter marble spread over refractory board to form 80mm Ø circle, after calcination.

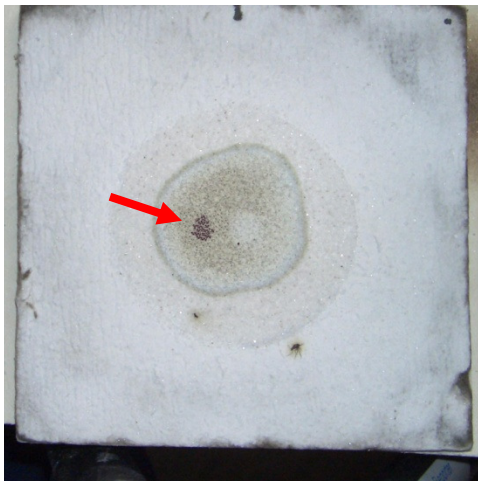

Figure D-6: Photo of d_c = 0.375mm diameter marble spread over refractory board to form 80mm Ø circle, after calcination.

The calcination profile plot, Figure D-3, for the 40 gram constant diameter marble bed measurements, show that the smallest nominal diameter (0.375mm) marble calcines the slowest, with the 1.85mm stone being the quickest. Apart from the 2.855mm stone, the calcination rate increases with increasing stone size. This relationship was also seen in the 40g - 900°C muffle furnace experiments (Figure 6.4) where heat and mass transfer within the packed bed of marble plays a more significant role for the rate controlling step, than chemical kinetics. The void spacing between the each stone within the sample is not sufficiently large enough for convective heat flows to occur, and thus conductive heat transfer is the main form of heat transfer. Conductive heat transfer through $CaCO_3$ (and the newly formed CaO) is very slow because of the low heat transfer coefficient.

A comparison of the calcination rates shown in Table D-3, indicate that the 1.850mm nominal diameter stone is approximately 70% faster than for the 0.375mm. The calcination rates for the 2.855mm and 0.925mm stone are approximately the same.

Figure D-4 shows the calcination profiles for the radiation calcination experiments where the marble bed thickness is 1.5 times the nominal diameter of the marble. The profiles show that the rate of conversion of Penrice marble increases with the decrease in stone diameter. The effects of heat and mass transfer within the bed of marble are therefore no longer playing a significant role in the calcination rate. The associated Table D-4 confirms the increase in calcination rate with decreasing marble diameter, with the 0.375mm diameter calcining at approximately 1.97 g/g.s. A comparison in calcination rate values shows that there is an increase in calcination rate for all but one stone size between these experiments and the 40g bed experiments; for example the 0.375mm stone has a calcination rate 6.42 times faster.

The trend in these experiments indicates that spreading out the stone, increases its exposure to the radiation and allows for the release of the evolved CO_2 and thus increases the calcination rate.

D.4 Comparison of Muffle Furnace Calcination with Open System Radiation Bed Calcination Experimental

This section directly compares the calcination rates between the open system radiation calcination experiments and the muffle furnace. A comparison of the calcination rates for the 40 gram constant bed experiments show that using an average radiant heat of approximately 115kW.m^2 is on average 4.6 times slower than using a muffle furnace at 900°C, and 10.4 times slower than using a muffle furnace at 1000°C. Similar comparison results are obtained for the 1.5 times marble diameter bed experiments where the calcination rate is 4.7 times slower and 10.6 times slower for the average radiant heat flux at approximately 115kW/m^2 when compared to 900°C and 1000°C respectively.

D.5 Conclusions from Open System Radiation Bed Calcination Measurements

This open air calcination experiments of Penrice marble using radiation as the sole heat source have shown that the rate of calcination increases with an increase in radiant heat flux and also with a decrease in stone diameter. It was shown that the thickness of the marble bed can significantly affect the rate of calcination. It is recommended that a bed of marble no thicker than 1.5 times the stones nominal diameter be used, so that heat transfer to each stone and the free release of the evolved CO_2 can occur.

Appendix E

Table E-1: Measured wall temperatures on the internal surface of the solar furnace at the thermocouple locations presented in Figure 4-15 for various calcination platform distances 'S' from the focal point and the associated radiant heat fluxes.

Thermocouple Position	Distance between the Calcination Platform and Focal Point (mm)				
	100 200±15kW/m^2	**75** 300±25kW/m^2	**70** 325±25kW/m^2	**60** 385±25kW/m^2	**50** 450±30kW/m^2
1A	411	419	421	360	348
2A	407	412	417	428	462
3A	379	388	392	401	417
4A	413	417	422	358	342
5A	412	418	424	350	341
6A	378	387	385	392	413
7A	376	384	388	394	412
8A	328	333	338	345	356
9A	292	295	300	305	318
1B	413	421	426	358	348
2B	409	418	423	436	459
3B	381	387	394	403	419
4B	411	419	424	356	344
5B	410	421	427	352	345
6B	377	386	387	395	410
7B	372	382	389	392	414
8B	327	337	339	342	362
9B	291	296	298	299	321
1C	408	417	422	362	345
2C	410	415	418	432	460
3C	371	379	386	393	411
1D	410	418	425	358	347
2D	406	413	417	430	467
3D	408	417	422	353	343
4D	412	418	421	361	342

Table E-2: Measured wall temperatures on the external surface of the triangular solar furnace at the thermocouple locations presented in Figure 4-15 when the calcination platform is positioned at S = 100mm from the focal point and therefore exposed to a radiant heat flux of 200±15kW/m^2.

Thermocouple Position	Furnace Wall Left (A) Deg C	Furnace Wall Rear (B) Deg C	Furnace Wall Right (C) Deg C	Furnace Wall Front (D) Deg C
1	58.0	50.3	49.0	51.0
2	54.2	56.8	56.0	-
3	55.7	59.5	54.3	49.4
4	45.0	47.4	-	49.4
5	45.8	46.3	-	-
6	47.8	52.1	-	-
7	48.5	53.5	-	-
8	-	54.2	-	-
9	-	48.0	-	-

Appendix F

The average characteristic specifications for the convective heat transfer between the hot calcination platform and the ambient air. These values were calculated using the computer program by Youn *et al*. (1995).

Table F-1: Average characteristic specifications for air surrounding the heated platform.

Source Heat Flux (kW/m^2)	**175**	**200**	**280**	**300**	**325**	**385**	**430**	**450**
Platform Temperature (K)	1310	1444	1476	1577	1609	1674	1696	1735
Resulting Air Temperature (K)	**802**	**870**	**885**	**936**	**952**	**984**	**995**	**1015**
Air Density (kg/m^3)	0.4396	0.4058	0.3984	0.3770	0.3707	0.3584	0.3545	0.3477
Dynamic Viscosity (kg/m.s)	3.60×10^{-5}	3.79×10^{-5}	3.84×10^{-5}	3.98×10^{-5}	4.03×10^{-5}	4.11×10^{-5}	4.14×10^{-5}	4.20×10^{-5}
Kinematic Viscosity (m^2/s)	8.19×10^{-5}	9.35×10^{-5}	9.64×10^{-5}	1.06×10^{-5}	1.09×10^{-4}	1.15×10^{-4}	1.17×10^{-4}	1.21×10^{-4}
Thermal Conductivity (W/m.K)	5.61×10^{-2}	5.99×10^{-2}	6.08×10^{-2}	6.37×10^{-2}	6.46×10^{-2}	6.64×10^{-2}	6.70×10^{-2}	6.81×10^{-2}
Prandtl Number	0.7001	0.7008	0.7008	0.7007	0.7005	0.7002	0.7	0.6998
Volume Expansion Coefficient (K^{-1})	1.24×10^{-3}	1.15×10^{-3}	1.13×10^{-3}	1.07×10^{-3}	1.05×10^{-3}	1.01×10^{-3}	1.00×10^{-3}	9.84×10^{-4}
Grashof Number	1.84×10^{6}	1.48×10^{6}	1.40×10^{6}	1.20×10^{6}	1.14×10^{6}	1.04×10^{6}	1.01×10^{6}	9.52×10^{6}
Rayleigh Number	1.29×10^{6}	1.03×10^{6}	9.83×10^{5}	8.40×10^{5}	8.01×10^{5}	7.27×10^{5}	7.04×10^{5}	6.66×10^{5}
Average Nusselt Number	18.19	17.22	17.00	16.35	16.15	15.77	15.94	15.43
Average Heat Transfer Coefficient, hc ($W/m^2.K$)	10.21	10.32	10.34	10.41	10.43	10.47	10.49	10.51

Appendix G

Plots of radiative heat transfer between the hot platform and the 6.54mm nominal diameter (0.333 gram) and 13.62mm nominal diameter (3.000 gram) marble samples.

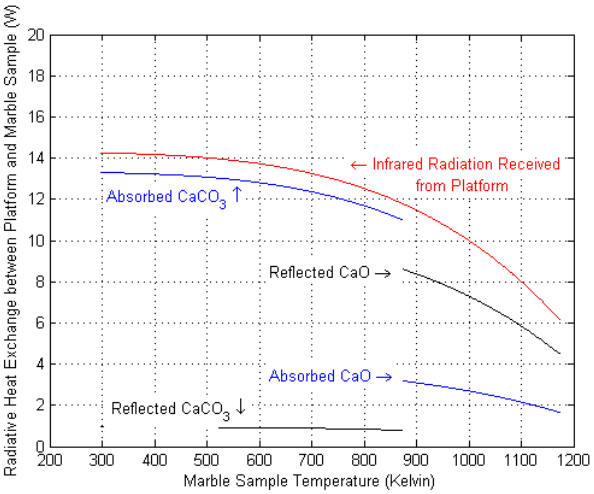

Figure G.1: Calculated radiative heat transfer between the platform and the d_c = 6.54mm (0.333g) marble sample for a fixed direct heat flux of 200kW/m^2 in the OSS.

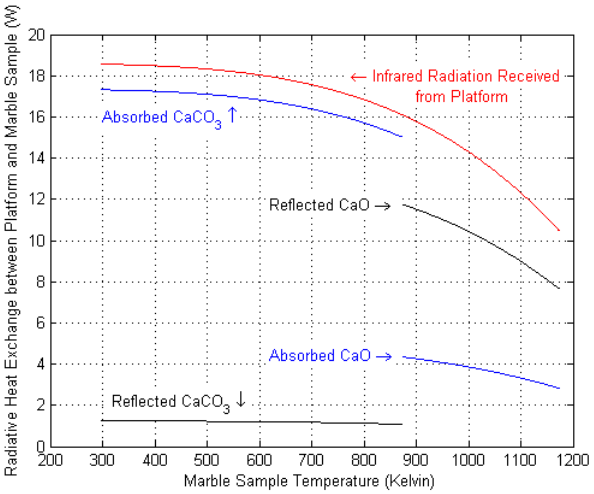

Figure G.2: Calculated radiative heat transfer between the platform and the d_c= 6.54mm (0.333g) marble sample for a fixed direct heat flux of 200kW/m^2 in the ETSF.

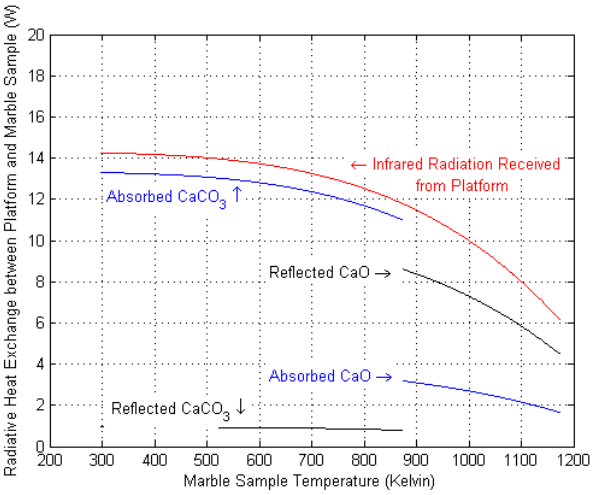

Figure G.3: Calculated radiative heat transfer between the platform and the d_c = 13.62mm (3.000g) marble sample for a fixed direct heat flux of 200kW/m^2 in the OSS.

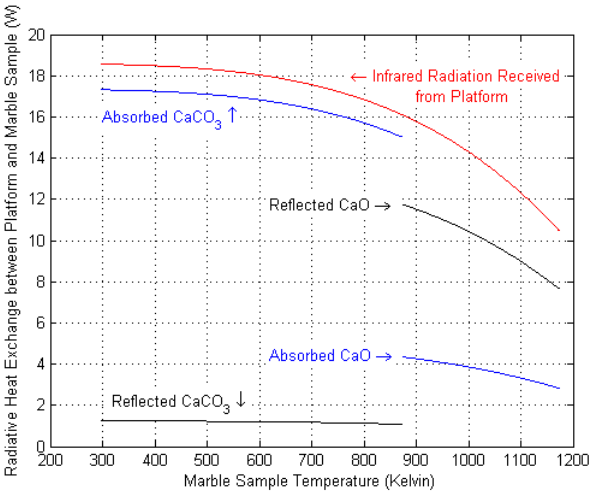

Figure G.4: Calculated radiative heat transfer between the platform and the d_c = 13.62mm (3.000g) marble sample for a fixed direct heat flux of 200kW/m^2 in the ETSF.

Bibliography

American Society for Testing and Materials (2003). Terrestrial Reference Spectra for Photovoltaic Performance Evaluation.

Ar, I. and Dogu, G. (2001). "Calcination kinetics of high purity limestones." Chemical Engineering Journal 83(2): 131-137.

Australian Standard, AS 4489.5.1-1997: Test methods for limes and limestones - Chemical composition - Quicklime and hydrated lime

Augenbraun, H., Matthews, E. and Sarma, D. (1999). "The greenhouse effect, greenhouse gases, and global warming." Institute on Climate and Planets, NASA.

Australian Greenhouse Office (2001). Implementation planning for mandatory targets for the uptake of renewable energy in power supplies final report, Final report of the Renewables Target Working Group, Australian Greenhouse Office. 2002.

Australian Greenhouse Office (A.G.O.) (2006). National Greenhouse Gas Inventory 2004. T. A. G. Office.

Badie, J. M., Bonet, C., Faure, M., Flamant, G., Foro, R. and Hernandez, D. (1980). "Decarbonation of calcite and phosphate rock in solar chemical reactors." Chemical Engineering Science 35(1/2): 413-420.

Baird, C. (1997). Environmental chemistry, W.H. Freeman and Company.

Bartl, J. and Baranek, M. (2004). "Emissivity of aluminium and its importance for radiometric measurement." Measurement of Physical Quantities 4(3): 31 - 36.

Baumeister, T., Avallone, E. A. and Marks, L. S. (1996). Marks' standard handbook for mechanical engineers. New York, McGraw-Hill.

Bennett, R. H. (1997). Lime still makes the best mortar. Long Barn, Morestead, Winchester, Hampshire, United Kingdom, The Lime Centre. 2004.

Bonaldi, E., Cella, G. M., Lipinski, W., Palumbo, R., Steinfeld, A., Wuillemin, D. and Meier, A. (2002). CO_2 mitigation in the lime industry: replacing fossil fuels with concentrated solar energy. 10th International Lime Association Congress, Washington D.C., USA.

Borgwardt, R. H. (1985). "Calcination kinetics and surface area of dispersed limestone particles." American Institute of Chemical Engineers (AIChE journal) 31(1): 103-111.

Borjesson, P. I. I. (1996). "Energy analysis of biomass production and transportation." Biomass and Bioenergy 11(4): 305-318.

Borman, G. L. and K. W. Ragland (1998). Combustion engineering. Singapore, WCB McGraw-Hill.

Boynton, R. S. (1966). Chemistry and technology of lime and limestone, John Wiley & Sons.

Boynton, R. S. (1980). Chemistry and technology of lime and limestone, Edition 2, John Wiley & Sons

Brohez, S., Delvosalle, C. and Marlair, G. (2004). "A two-thermocouples probe for radiation corrections of measured temperatures in compartment fires." Fire Safety Journal 39(5): 399-411.

Brown, M. E., Maciejewski, M., Vyazovkin, S., Nomen, R., Sempere, J., Burnham, A., Opfermann, J., Strey, R., Anderson, H. L. and Kemmler, A. (2000). "Computational aspects of kinetic analysis.; Part A: The ICTAC kinetics project-data, methods and results." Thermochimica Acta 355(1-2): 125-143.

British Standard, BS410-1986, British Standard for Test Sieves; Technical Requirements and Testing.

Cinemeccanica - Milano (1990). Zenith X 6500 H - Service and owners manual.

Coblentz, W. W. (1913). "The diffuse reflecting power of various substances." U.S.A. Bureau of Standards 9(2): 283 - 325.

Conley, J. E. (1939). Calcination conditions for limestone, dolomite and magnesite. American Institute of Mining and Metallurgical Engineers -- Meeting, Feb 1939, New York, NY, United States, American Institute of Mining and Metallurgical Engineers.

Correia, S. A. C. (2001). Development of improved mathematical models for the design and control of gas-fired furnaces, University of Glamorgan/Prifysgol Morgannwg: Degree of Doctor of Philosophy.

Correia, S. A. C., Ward, J. and Sousa, J. L. V. A. (2000a). Application of multi-zone two-dimensional thermal radiation models for control of a metal reheating furnace under transient conditions. 3rd European Thermal Sciences Conference, Edizioni ETS, Pisa.

Correia, S. A. C., Ward, J. and Sousa, J. L. V. A. (2000b). "Numerical prediction of the transient operation of a gas-fired reheating furnace." Combustion, Fire and Computational Modeling of Industrial Combustion Systems 23: 87-94.

Criado, J. M., Gonzalez, M., Malek, J. and Ortega, A. (1995). "The effect of the CO_2 pressure on the thermal decomposition kinetics of calcium carbonate." Thermochimica Acta 254: 121 - 127.

De la Fuente, D., Otero-Huerta, E. and Morcillo, M. (2007). "Studies of long-term weathering of aluminium in the atmosphere." Corrosion Science 49(7): 3134-3148.

Dennis, J. S. and Hayhurst, A. N. (1987). "Effect of CO_2 on the kinetics and extent of calcination of limestone and dolomite particles in fluidised beds." Chemical Engineering Science 42(10): 2361 - 2372.

Dimitriadis, T. (2002). Solar Simulators – “Lamp Efficiency” and “Spectral emissions from solar simulators”. R. Craig. Email, NEVTECH SYSTEMS INC. Gardnerville, Nevada, U.S.A.

Diver, R. B. (1987). "Receiver/reactor concepts for thermochemical transport of solar energy." Journal of Solar Energy Engineering, Transactions of the ASME 109(3): 199-204.

Dobner, S., Sterns, L., Graff, R. A. and Squires, A. M. (1977). "Cyclic calcination and recarbonation of calcined dolomite." Industrial & Engineering Chemistry, Process Design and Development 16(4): 479-486.

Dorman, W. D. (1979). "High Temperature heat requirements for burning lime." Rock Products 82(10): 66-69.

Emery, A. F., Johansson, O., Lobo, M. and Abrous, A. (1991). "Comparative study of methods for computing the diffuse radiation viewfactors for complex structures." Journal of Heat Transfer, Transactions ASME 113(2): 413-422.

Energy Information Administration (E.I.A.) (1998). What does the Kyoto Protocol mean to U.S. energy markets and the U.S. economy? Washington, National Energy Information Center: pp 23.

Energy Information Administration (E.I.A.) (2006). Total carbon dioxide emissions from the consumption of petroleum, natural gas, coal, and the flaring of natural gas, by region with selected countries and world total, 1991-2004, National Energy Information Center. 2006.

Flamant, G., Hernandez, D., Bonet, C. and Traverse, J. P. (1979). "Experimental aspects of the thermochemical conversion of solar energy; decarbonation of $CaCO_3$." Solar Energy 24(4): 385-395.

Foundation for Alternative Energy (1998). Renewable energy, Chapter 2; Solar energy, Environmental Organisation of Slovak. 2002.

Francis, H. L. (1998). Definitions of common lime terminology, E - lime cement gypsum. 2002.

Fraser, B. (2004). Understanding digital raw capture. Digital camera raw file support, Adobe Systems Incorporated.

Freas, R. C. (1990). Lime. Encyclopedia of Materials Science and Engineering. Oxford, UK, Pergamon Press. 2: 1038-1042.

Furnas, C. C. (1931). "Rate of calcination of limestone." Industrial and Engineering Chemistry 23(5): 534-538.

Gallagher, P. K. and Johnson, J., D. W. (1973). "The effects of sample size and heating rate on the kinetics of the thermal decomposition of $CaCO_3$." Thermochimica Acta 6(1): 67-83.

Global Energy Concepts (1995). Renewable energy assessment plan, State of Hawaii, Department of Business, Economic Development & Tourism. 2002.

Graetz, A. (2000). Penrice Mine - Summary of Operations. Angaston, Penrice Soda Products Pty Ltd.

Gubareff, G. G., Janssen, J. E. and Torborg, R. H. (1960). Thermal radiation properties survey - A review of literature. Minneapolis, Honeywell Research Laboratories.

Gutschick, K. A., (1995). Edited Book: Lime and limestone. Kirk-other Encyclopedia of Chemical Technology, John Wiley & Sons, Inc.

Hall, D. O. and J. I. Scrase (1998). "Will biomass be the environmentally friendly fuel of the future?" Biomass and Bioenergy 15(4-5): 357-367.

Hancock, F. (2002). Modeling the calcination of limestone within a solar furnace. Honours research project. Chemical Engineering, University of Adelaide.

Herzog, H. (2002). Carbon Sequestration via Mineral Carbonation: Overview and Assessment, MIT Laboratory for Energy and the Environment: 11.

Hesse, P. (2002). Energy efficiency and renewable technologies. R. Craig. Adelaide, Energy Efficiency and Renewable Energy Clearinghouse.

Hills, A. W. D. (1968). "The mechanism of the thermal decomposition of calcium carbonate." Chemical Engineering Science 23: 297 - 320.

Hirsch, D., von Zedtwitz, P., Osinga, T., Kinamore, J. and Steinfeld, A. (2003). "A new 75 kW high-flux solar simulator for high-temperature thermal and thermochemical research." Journal of Solar Energy Engineering-Transactions of the Asme 125(1): 117-120.

Holman, J. P. (1968). Heat transfer, McGraw - Hill.

Hottel, H. C. (1974). First estimates of industrial furnace performance - the one-gas-zone model reexamined. Heat Transfer in Flames. N. H. Afgan and J. M. Beer. Washington, John Wiley & Sons: Chapter 1: 5 - 28.

Hottel, H. C. and Sarofim, A. F. (1967). Radiative Transfer. New York, McGraw-Hill.

Hottel, H. C. and Cohen, E. S. (1957). "Radiant heat exchange in a gas-filled enclosure: Allowance for nonuniformity of gas temperature." A.I.Ch.E Journal 4(1): 3 -14.

Hottel, H. C. and Sarofim, A. F. (1967). Radiative Transfer. New York, McGraw-Hill.

Howell, J. R. (2007). A catalogue of radiation heat transfer configuration factors. Austin, University of Texas.

Howell, J. R. (2009). Shape factors for eccentric spheres: Private email communication with R. Craig.

Hyperlight (2007). Image:HLR-OSRAM-3KW-B.jpg. Wikipedia. 2007: An 3 KW Xenon Short-Arc Lamp used in medium size movie theatre projectors.

Imhof, A. (1991). "The cyclone reactor - An atmospheric open solar reactor." Solar Energy Materials 24(1 - 4): 733-741.

Imhof, A. (1997). "Decomposition of limestone in a solar reactor." Renewable Energy 10(2-3, 12 September 1996): 239 - 246.

Imhof, A. (2000). "Solar cement plants - an interesting challenge for business and science." ZKG International 53(8): 448 - 456.

Ingraham, T. R. and Marier, P. (1963). "Kinetic studies on the thermal decomposition of calcium carbonate." The Canadian Journal Of Chemical Engineering: 170 - 173.

International Energy Agency (I.E.A.) (2000). Capturing and Storing Carbon Dioxide. World Energy Outlook - 2000.

IPCC (1995). Climate change 1995: The science of climate change. J. T. Houghton, L. G. Meira Filho, B. A. Callander, N. Harris, A. Kattenberg and K.Maskell, Cambridge University Press, UK: 572.

IPCC (1996). Revised 1996 IPCC guidelines for national greenhouse gas inventories. Paris, France., IPCC/OECD/IEA: Volume 1: The reporting instructions; Volume 2: The workbook; Volume 3: The reference manual.

IPCC (2000). Emission scenarios: Summary for policymakers:. A special report of the Intergovernmental Panel on Climate Change; Working group 3, Cambridge University Press, UK: 27.

IPCC (2001a). Impacts, adaptation & vulnerability: Technical summary: Climate change 2001. A report of working group 2 of the Intergovernmental Panel on Climate Change, Cambridge University Press, UK: 56.

IPCC (2001b). The scientific basis: Technical summary: Climate change 2001. J. T. Houghton, Y. Ding, D.J. Griggs, M. Noguer, P. J. van der Linden and D. Xiaosu: A report of working group 1 of the Intergovernmental Panel on Climate Change, Cambridge University Press, UK: 63.

IPCC (2005). Special Report on Carbon Dioxide Capture and Storage – report of working group 3. Bert Metz, Ogunlade Davidson, Heleen de Coninck, Manuela Loos and Leo Meyer, Cambridge University Press, UK: 443.

Jenkins, B. G. (1990). "Comparative assessment of the thermal performance of calcining technologies in the minerals processing industries." CHEMECA '90, Australasian Chemical Engineering Conference Part 2 (of 2): 1078-1086.

Jenkins, B. G. (1999). Well-stirred furnace heat transfer program, O-D Hottel model. Buckinghamshire.

Jenkins, B. G. (2002). An assessment of design methods for high temperature process furnaces. 2002 Australian Symposium on Combustion and The Seventh Australian Flame Days, Adelaide University, The Australian Flame Research Committee Inc.

Jenkins, B. G. (2008). Private communication: Absortivity and emissivity of limestone. R. Craig. Adelaide, Australia.

Johnson, A. J. and G. H. Auth (1951). Fuels and combustion handbook. New York, Toronto, London, McGraw-Hill Book Company.

Khinast, J., Krammer, G. F., Brunner, C. and Staudinger, G. (1996). "Decomposition of limestone: the influence of CO_2 and particle size on the reaction rate." Chemical Engineering Science 51(4): 623- 634.

Khraisha, Y. H. and Dugwell, D. R. (1989). "Thermal decomposition of limestone in a suspension reactor." Chemical Engineering Research & Design 67(1): 52-57.

Kozanoglu, B. and Lopez, J. (2007). "Thermal boundary layer and the characteristic length on natural convection over a horizontal plate." Heat and Mass Transfer/Waerme- und Stoffuebertragung 43(4): 333-339.

Lawson, D. A. (1992). RADEXF : User and system guides, Coventry University, School of Mathematical & Information Sciences.

Laurendeau, N. M. (1978). "Heterogeneous kinetics of coal char gasification and combustion." Progress in Energy and Combustion Science 4(4): 221-270.

Ledley, T. S., Sundquist, E. T., Schwartz, S. E., Hall, D. K., Fellows, J. D. and Killeen, T. L. (1999). "Climate change and greenhouse gases." Eos, Transactions, American Geophysical Union, Electronic Supplement 80(39): 453.

Linguistic Demographer (2006). Image of rotary cement kiln, Wikipedia. 2007.

Lipinski, W. and Steinfeld, A. (2004). "Heterogeneous thermochemical decomposition under direct irradiation." International Journal of Heat and Mass Transfer 47(8-9): 1907-1916.

Liu, B. Y. H. and R. C. Jordan (1960). "The interrelationship and characteristic distribution of direct, diffuse and total solar radiation." Solar Energy 4(3): 1-19.

Mallen, A. L. (1956). Calcination of Penrice limestone. Faculty of Engineering. Adelaide, University of Adelaide: Thesis submitted for the Degree of Master of Engineering, 218.

Marland, G., Boden, T. and Andres, B. (2006). Global CO_2 emissions from fossil-fuel burning, cement manufacture, and gas flaring: 1751-2003. Tennessee, Carbon Dioxide Information Analysis Center: Oak Ridge National Laboratory.

Martin, G. (1932). Chemical engineering and thermodynamics applied to the cement rotary kiln, Crosby Lockwood and Son.

Mason, K., Hill, N. and Ruskulis, O. (1999). The small-scale vertical shaft lime kiln : A practical guide to design, construction and operation, Intermediate Technology Publications.

Medina, M. G., Bond, G. M. and Stringer, J. (2001). "An overview of carbon sequestration." Interface(Spring): 26 - 30.

Medtherm Corporation (2003). 64 series Heat Flux Transducers for the direct measruements of heat transfer rates: Bulletin 118.

Meier, A. (1999). "A predictive CFD model for a falling particle receiver/reactor exposed to concentrated sunlight." Chemical Engineering Science 54(13 & 14): 2899 - 2905.

Meier, A. and Cella, G. M. (2004). Solar Production of Lime. Villigen PSI, Paul Scherrer Institute (PSI): 133.

Meier, A., Bonaldi, E., Cella, G. M., Lipinski, W., Wuillemin, D. and Palumbo, R. (2002). Design and experimental investigation of a horizontal rotary reactor for the solar thermal production of lime. 11th SolarPACES International Symposium on Concentrated Solar Power and Chemical Energy Technologies, Zurich, Switzerland.

Miller, M. M. (2000). Minerals yearbook: volume I - metals and minerals: lime, U.S. Geological Survey: 16.

Mills, A. F. (1999). Heat transfer, Prentice-Hall Inc.

Milne, C. R., Silcox, G. D., Pershing, D. W. and Kirchgessner, D. A. (1990). "Calcination and sintering models for application to high-temperature, short-time sulfation of calcium-based sorbents." Industrial & Engineering Chemistry Research 29(2): 139-149.

Moropoulou, A., Bakolas, A. and Aggelakopoulou, E. (2001). "The effects of limestone characteristics and calcination temperature to the reactivity of the quicklime." Cement and Concrete Research 31(4): 633-639.

Mullinger, P. (2002). Calcination kinetics of limestone. Private communication. Adelaide: Project Meeting with A/Prof G.Nathan.

Mullinger, P. (2007). Thermal efficiencies of process kilns. Project Meeting. Adelaide: Private communication.

Mullinger, P. and Jenkins, B. (2008). Industrial and Process Furnaces, Principles, Design and Operation, Butterworth Heinemann - Elsevier Ltd.

Murthy, M. S., Harish, B. R., Rajanandam, K. S. and Kumar, K. Y. A. P. (1994). "Investigation on the kinetics of thermal decomposition of calcium carbonate." Chemical Engineering Science 49(13): 2198-2204.

Nangia, V. K., Grewal, N. S. and Rao, B. S. (1988). "Normal total emittance of limestone." International Communications in Heat and Mass Transfer 15(5): 681-687.

Nathan, G. (2002). Electrical efficiency of crushing and screening plants. Project Meeting Private communication. Adelaide.

Neumann, A. and Groer, U. (1996). "Experimenting with concentrated sunlight using the DLR solar furnace." Solar Energy 58(4-6): 181-190.

Nostell, P. (2000). Preparation and optical characterisation of antireflection coats and reflector materials for solar energy systems. Faculty of Science and Technology - Solid State Physics. Uppsala, Uppsala University: Dissertation, 67.

Oates, J. A. H. (1998). Lime and limestone : Chemistry and technology, production and uses. Weinheim, Germany, Wiley-Vch.

Oates, J. A. H. (2001). Private communication: Calcimatic kilns. R. Craig. Adelaide, Australia - Buxton, Derbyshire, United Kingdom.

Optical Coating Laboratory Inc (2003). Metallic mirrors. Metal based coatings, Self Published: 10.

Oriel Instruments (1998). The Book of Photon Tools, Thermo Electron Corporation.

OSRAM (1996). XBO Theatre Lamps - Technology and Applications: 43.

Paul Scherrer Institute and QualiCal (2000-2003). 2000-2003 Research Program: The solar production of lime. Villigen, Switzerland, Paul Scherrer Institute. 2000 - 2003.

Pimentel, D., Rodrigues, G., Wane, T., Abrams, R., Goldberg, K., Staecker, H., Ma, E., Brueckner, L., Trovato, L., Chow, C., Govindarajulu, U. and Boerke, S. (1994). "Renewable energy: Economic and environmental issues." Bioscience 44(8).

Primary Industries and Resources of South Australia (2001). Minerals and petroleum South Australia 2001. Adelaide, Government of South Australia.

Radziemska, E. and Lewandowski, W. M. (2005). "The Effect of Plate Size on the Natural Convective Heat Transfer Intensity of Horizontal Surfaces." Heat Transfer Engineering 26(2): 50 - 53.

Rao, T. R., Gunn, D. J. and Bowen, J. H. (1989). "Kinetics of calcium carbonate decomposition." Chemical Engineering Research & Design 67(1): 47.

Renewable Energy Centre (2000). Introduction to renewable energy technologies resource book. Red Hill, Brisbane Institute of TAFE.

Rhine, J. M. and Tucker, R. J. (1991). Modelling of gas-fired furnaces and boilers and other industrial heating processes. London : London ; New York :, British Gas; McGraw-Hill Book Company.

Riedl, A. (2003). Life cycle analysis of lime manufacturing; An environmental comparison of lime calcination using solar energy and fossil fuel combustion. Adelaide, Chemical Engineering, University of Adelaide: 97.

Rose, J. W. and Cooper, J. R. (1977). Technical data on fuel, Scottish Academic Press.

Salman, O. A. and Khraishi, N. (1988). "Thermal decomposition of limestone and gypsum by solar energy." Solar Energy 41(4): 305-308.

Satterfield, C. N. and Feakes, F. (1959). "Kinetics of the thermal decomposition of calcium carbonate." American Institute of Chemical Engineers (A.I.Ch.E) 5(1): 115 - 123.

Sauers, D., Biege Sr, N. and Smith, D. (1993). "Comparing lime kilns." Rock Products (5 Parts).

Schubnell, M., Keller, J. and Imhof, A. (1991). "Flux density distribution in the focal region of a solar concentrator system." Journal of Solar Energy Engineering 113(2, May 1991): 112 - 116.

Schwarzkopf, F. (1970). "A comparison of modern lime calcining systems." Rock Products 73(7): pp68-71,112 &114.

Schwarzkopf, F. (1974). Lime burning technology, Svedala Industries, Kennedy Van Saun.

Searcy, A. W. and Beruto, D. (1978). "Kinetics of endothermic decomposition reactions: 2. Effects of the solid and gaseous products." The Journal Of Physical Chemistry 82(2): 163 - 167.

Selcuk, N., Siddall, R. G. and Beer, J. M. (1975). "A comparison of mathematical models of the radiative behaviour of an industrial heater." Chemical Engineering Science 30(8): 871-876.

Siddall, R. G. (1972). "Flux methods for the analysis of radiant heat transfer." Proc. Fourth Symposium on Flames and Industry: Prediction Methods for Industrial Flames; The Insititute of Fuel: Paper 16.

Siegal, R. and Howell, J. (2001). Thermal radiation heat transfer. New York and London, Taylor and Francis.

Silcox, G. D., Kramlich, J. C. and Pershing, D. W. (1989). "Mathematical model for the flash calcination of dispersed $CaCO_3$ and $Ca(OH)_2$ particles." Industrial & Engineering Chemistry Research 28(2): 155-160.

Sillem, H. (1977). "Size Reduction." Zement-Kalk-Gips 66(11): 550-558.

Simonsen, H. I. and M. K. Azarniouch (1987). "Survey, simulation and evaluation of energy consumption in lime kilns." Pulp & Paper Canada 88(4): 49-52.

Singhal, A. K. (1999). Numerical analysis in thermal design. Handbook of Applied Thermal Design. E. C. Guyer, Taylor & Francis: Part 1: Chapter 7.

Smith, J. M. (1981). Chapter 14. Fluid-solid noncatalytic reactions. Chemical engineering kinetics. J. V. Brown. New York, McGraw-Hill: 638 - 648.

SolarPaces (2001). Concentrating solar power in 2001: 16.

SolarPACES (2002) 29(5-6): 925-933.

Spalding, D. B. (1963). The art of partial modeling. Colloquium on Modeling Principles, 9th International Symposium on Combustion.

Splendor Solis (1532-35). Illuminated alchemical manuscripts. Laboratory Symbolism; Retort Series, The Alchemy web site.

Spitzer, J. (2001). Biomass, bioenergy and greenhouse gas mitigation. ISES 2001 Solar World Congress, Adelaide, Australia, ANZSES.

Stanmore, B. R. and Gilot, P. (2005). "Review--calcination and carbonation of limestone during thermal cycling for CO_2 sequestration." Fuel Processing Technology 86(16): 1707-1743.

Statistics, Australian Bureau of (2001). Population by age and sex. Canberra, Australian Bureau of Statistics: 40.

Steinfeld, A. and M. Epstein (2001). "Light years ahead." Chemistry in Britain 37(5): 30 -32.

Steinfeld, A. and R. Palumbo (2001). Solar thermochemical process technology. Encyclopedia of Physical Science and Technology. R.A.Meyers. Zurich, Academic Press: 237 - 256.

Steinfeld, A. and Schubnell, M. (1993). "Optimum aperture size and operating temperature of a solar cavity-receiver." Solar Energy 50(1): 19-25.

Steinfeld, A., Imhof, A. and Mischler, D. (1992). Experimental investigation of an atmospheric-open cyclone solar reactor for solid-gas thermochemical reactions. ASME, JSES and KSES International Solar Energy Conference, New York, USA, American Society of Mechanical Engineers.

Telfer, M. (1999). Sulphur transformation during pyrolysis of low rank coals and characterisation of Ca based sorbents. PhD Thesis, Department of Chemical Engineering. University of Adelaide, Australia.

Telfer, M., Zhong, Z., Xu, Y., Li, D., Zhang, M. and Zhang, D. K. (2000). "An experimental study of calcination of South Australian Caroline limestone." Development of Chemical Engineering Minerals Process 8(3/4): 245 - 267.

The Australian Cooperative Research Centre for Renewable Energy (A.C.R.C.R.E) (2002). Fact sheet 6 - Hydro Electricity. The Australian Institute of Energy. The Australian Cooperative Research Centre for Renewable Energy. 2002.

The Institute of Fuel (1963). Waste heat recovery. London, Chapman and Hall LTD.

Thring, M.W. (1962). The Science of Flames and Furnaces, 2nd Ed, John Wiley & Sons.

Tillman, D. A. (2000). "Cofiring benefits for coal and biomass." Biomass and Bioenergy 19(6): 363-364.

Touloukian Y. S. (1972), Thermophysical properties of matter: thermal radiative properties - nonmetallic solids, IFI/Plenum vol. 8.

Tucker, R. J. (1990). Evaluation and development of the zone method for modelling metal heating furnaces. Faculty of technology, The Open University: Degree of Doctor of Philosophy.

U.S. Department of Energy (1999). Carbon Sequestration Research and Development, Office of Science and Office of Fossil Energy.

U.S. Department of Energy (2002). Energy efficiency in the power industry, Office of Energy Efficiency and Renewable Energy. 2002.

Ulmer, S., Lupfert, E., Pfander, M. and Buck, R. (2004). "Calibration corrections of solar tower flux density measurements." Energy SolarPACES 2002 29(5-6): 925-933.

UNFCCC (2006). Greenhouse Gas Emissions Data 2006. Highlights from Greenhouse Gas Emissions Data from 1990 - 2004 for Annex 1 Parties, Submitted under the United Nations Framework Convention on Climate Change: 24pp.

Unifrax Fiberfrax Duraboard (1999). Ceramic Fiber Technical Information, Advanced Thermal Supplies PTY LTD.

Vardavas, I. M. and L. M. Cannon (1989). A simple computer model for terrestrial and solar radiation transfer, Australian Government Publishing Services.

Vercammen, H. A. J. and Froment, G. F. (1980). "Improved zone method using Monte Carlo techniques for the simulation of radiation in industrial furnaces." International Journal of Heat and Mass Transfer 23(3): 329-337.

Villermaux, J. (1979). "Les reacteurs chimiques solaires (Solar chemical reactors)." Entropie 15(85): 25-31.

Viskanta, R. and Menguc, M. P. (1987). "Radiation heat transfer in combustion systems." Progress in Energy and Combustion Science 13(2): 97 - 160.

Ward, J., Correia, S. A. C. and Sousa, J. L. V. A. (1999). "Application of multi-zone thermal radiation models to investigate the energy efficiency of a metal reheating furnace under start up conditions." American Society of Mechanical Engineers, Advanced Energy Systems Division 39: 621-626.

Wei, H. and Luo, Y. (1995). "Study on the kinetics of thermal decomposition of $CaCO_3$." Journal of Thermal Analysis 45(1-2): 303 - 310.

Weins, B. (2002). The future of power production, Ben Wiens Energy Science Inc. 2002.

Wentworth, W. E. and Chen, E. (1976). "Simple thermal decomposition reactions for storage of solar thermal energy." Solar Energy 18(3): 205 - 214.

Wingate, M. (1985). Small scale lime burning. London, Intermediate Technology Publications.

Wohlgemuth, N. and Missfeldt, F. (2000). "The Kyoto mechanisms and the prospects for renewable energy technologies." Solar Energy 69(4): 305-314.

World Meteorological Organisation (2002). Common questions about climate change, United Nations Environment Programme. 2001.

Yamamoto, H., Fujino, J. and Yamaji, K. (2001). "Evaluation of bioenergy potential with a multi-regional global-land-use-and-energy model." Biomass and Bioenergy 21(3): 185-203.

Youn, B., Choi, H.J. and Mills, A.F (1995). BHMT. Computer programs for the text 'Basic Heat and Mass Transfer' by A.F.Mills.